Northumbria University
NEWCASTLE

Flexible ZnO thin film-based surface acoustic wave devices for environmental and biomedical sensing applications

Sameer Ahmad Hasan

PhD

2019

Flexible ZnO thin film-based surface acoustic wave devices for environmental and biomedical sensing applications

Sameer Ahmad Hasan

A thesis submitted in partial fulfilment
of the requirements of
The University of Northumbria at Newcastle
for the degree of
Doctor of Philosophy

The research was undertaken in the Faculty
of Engineering and Environment

September 2019

Declaration

I declare that the work contained in this thesis has not been submitted for any other award and that it is all my work. I also confirm that this work fully acknowledges opinions, ideas and contributions from the work of others. Any ethical clearance for the research presented in this thesis has been approved. Approval has been sought and granted by the University Ethics Committee on October 2015.

I declare that the word count of this thesis is 38,893 words.

Name: Sameer Ahmad Hasan

Signature:

Date: 30-09-2019

Acknowledgement

First of all, I would like to express my sincere gratitude and appreciation to my principal supervisor Prof. Richard Fu for the continuous support throughout my PhD project. His guidance helped me in all the time of research and writing of this thesis.

My sincere thanks also go to my co-supervisors Prof. John Dean and Prof. Glen McHale, for their thoughtful comments and recommendations in this research project. I would like to say a special thank you to Dr Hamdi Torun for helping and supporting me throughout my PhD.

I would like to thank many people for their help and support during my study: Prof. Des Gibson, Dr Liz Porteous and Mr Andrew Bunyan from the University of West of Scotland, Dr Michael Cooke from Durham University, and Dr Yifan Li.

Special thanks to my friend and former colleague Dr Chao Zhao for his help and the great time we spent in the lab. Also, I thank Dr Ran Tao for helping me in my research and publications. I would like to express my sincere thanks to all members of the smart material group at Northumbria University. I also would like to thank Dr Pietro Maiello and all the technicians for their help in my research work.

I would like to thank Northumbria University for supporting me in a studentship.

Last but not least, I would like to thank my family: my mom, my brothers, and sisters for supporting me throughout my life. My biggest thanks to my wife for everything, this never would happen without her support.

List of abbreviations

AFM	Atomic force microscope
BAW	Bulk acoustic wave
CMOS	Complementary metal oxide semiconductor
CVD	Chemical vapour deposition
DC	Direct current
FBAR	Film bulk acoustic wave resonator
FEA	Finite element analysis
FPW	Flexural plate wave
FWHM	Full width at half maxima
IDT	Interdigital transducer
LOC	Lab-on-a-chip
MBE	Magnetron beam epitaxy
MEMS	Microelectromechanical systems
NDT	Non-destructive testing
NR	Nanorod
PLD	Pulsed laser deposition
PVD	Physical vapour deposition
PVDF	Polyvinylidene fluoride
QCM	Quartz crystal microbalance
RF	Radio frequency
RH	Relative humidity
RMS	Root mean squared
SAW	Surface acoustic wave
SEM	Scanning electron microscope
SH-APM	Shear horizontal acoustic wave plate mode

SPUDT	Single phase unidirectional transducer
TC	Texture coefficient
TCF	Temperature coefficient of frequency
TEC	Thermal expansion coefficient
TSM	Thickness-shear mode
UV	ultraviolet
UV-VIS	Ultraviolet-visible spectroscopy
XRD	X-ray diffractometer

Abstract

Flexible ZnO thin film on aluminium foil-based SAW devices have been investigated for the first time as sensors for temperature, UV light, and humidity as well as breath and apnoea detection, and these devices were performing sensing while they were placed in flat and bending (curved) positions. Flexible SAW devices offer a promising technology of low cost, highly sensitive and bendable sensors. They also exhibit high potential for wearable, point of care and microfluidics and lab-on-chips applications.

The ZnO thin film was deposited on the aluminium foil and ZnO nanorods were grown on the surface of selected samples. The SAW sensors were fabricated by patterning Au/Cr IDTs with various wavelengths. Film and nanorods possessed the preferred structure and piezoelectric properties. Lamb modes were identified, and they were in a good agreement with the FEA results.

The maximum value of TCF was -773 ppm/K which is among the highest values mentioned in the literature. The sensors showed excellent linearity and repeatability during temperature cycling test. The maximum value of sensitivity to UV light was 63 ppm $(mW/cm^2)^{-1}$. ZnO nanorods enhanced the sensitivity by 1.76 times. The sensors showed excellent repeatability and reliability during UV light cycling in flat, bent-up and bent-down positions.

The maximum values of sensitivity to humidity were 47.7 kHz at 90%RH for nanorod-enhanced device and the maximum frequency shift was -57 kHz. The sensors exhibited good repeatability in response to humidity cycling. Besides, the devices exhibited an excellent response, sensitivity, and reliability for various breath patterns (e.g., healthy breathing, apnoea, slow and fast breathing).

Contents

List of Figures

List of Tables

List of publications

- **S. A. Hasan**, H. Torun, D. Gibson, Q. Wu, M. D. Cooke, and Y. Fu, "Flexible UV sensor based on nanostructured ZnO thin film SAW device," in 2019 IEEE Jordan International Joint Conference on Electrical Engineering and Information Technology (JEEIT), 2019, pp. 85-90.

- R. Tao, W. B. Wang, J. T. Luo, **S. Ahmad Hasan**, H. Torun, P. Canyelles-Pericas, et al., "Thin film flexible/bendable acoustic wave devices: Evolution, hybridisation and decoupling of multiple acoustic wave modes," Surface and Coatings Technology, vol. 357, pp. 587-594, 2019/01/15/ 2019.

- R. Tao**, S. Hasan**, H. Z. Wang, J. Zhou, J. T. Luo, G. McHale, et al., "Bimorph material/structure designs for high sensitivity flexible surface acoustic wave temperature sensors," Scientific reports, vol. 8, p. 9052, 2018. (**A joint first authors)**.

- **S. A. Hasan**, D. Gibson, S. Song, Q. Wu, W. P. Ng, G. McHale, et al., "ZnO thin film-based flexible temperature sensor," in 2017 IEEE SENSORS, 2017, pp. 1-3.

- Y. Liu, J. T. Luo, C. Zhao, J. Zhou, **S. A. Hasan**, Y. Li, et al., "Annealing effect on structural, functional, and device properties of flexible ZnO acoustic wave sensors based on commercially available Al foil," IEEE Transactions on Electron Devices, vol. 63, pp. 4535-4541, 2016.

Chapter One

Introduction

1.1 Research motivation

Flexible electronics and microelectromechanical systems (MEMS) have attracted significant attention as a promising technology for a wide range of new applications such as displays, solar cells, transistors, batteries, and biosensors [1]. Besides, there has recently been a substantial increase in demand for flexible and wearable sensors to provide continuous and real-time monitoring for biomedical and environmental measurements. Moreover, flexible sensors can yield under stress and this allows them to bend or deform without breaking. On the other hand, rigid sensors are brittle and liable to fracture when they are bent, Therefore, they are unable to withstand bending and remarkable stress compared to flexible sensors. Apart from this, they are easily fabricated, simple, inexpensive, and lightweight as well as they possess better mechanical properties, and they can be integrated with microfluidics and lab-on-a-chip applications [2] .

Many types of transduction technologies have been exploited in various sensing platforms such as piezoelectric, optical, electrical, and mechanical devices. Among these, piezoelectric-based transducers have been extensively reviewed as suitable sensors for biochemical, physical, and environmental applications [3, 4]. The principle of piezoelectricity depends on electromechanical transduction by which an electrical signal is generated as a result of applying mechanical stress and vice versa, as seen in Figure 1.1.

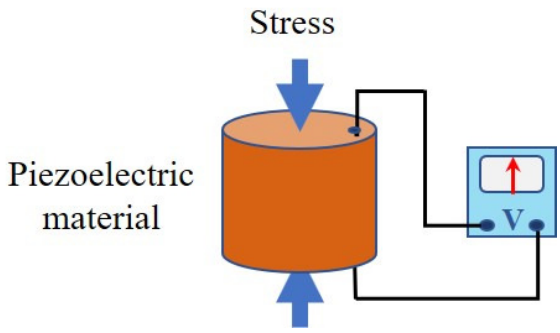

Figure 1.1 Induction of electrical potential by applying stress on piezoelectric material

There are two main categories of piezoelectric materials; those who are naturally occurring such as quartz, and synthetic or engineered compounds such as piezoceramics, thin films (e.g. Zinc oxide), and polymers (e.g. Polyvinylidene fluoride (PVDF)) [5]. Figure 1.2 shows the different types of natural piezoelectric materials.

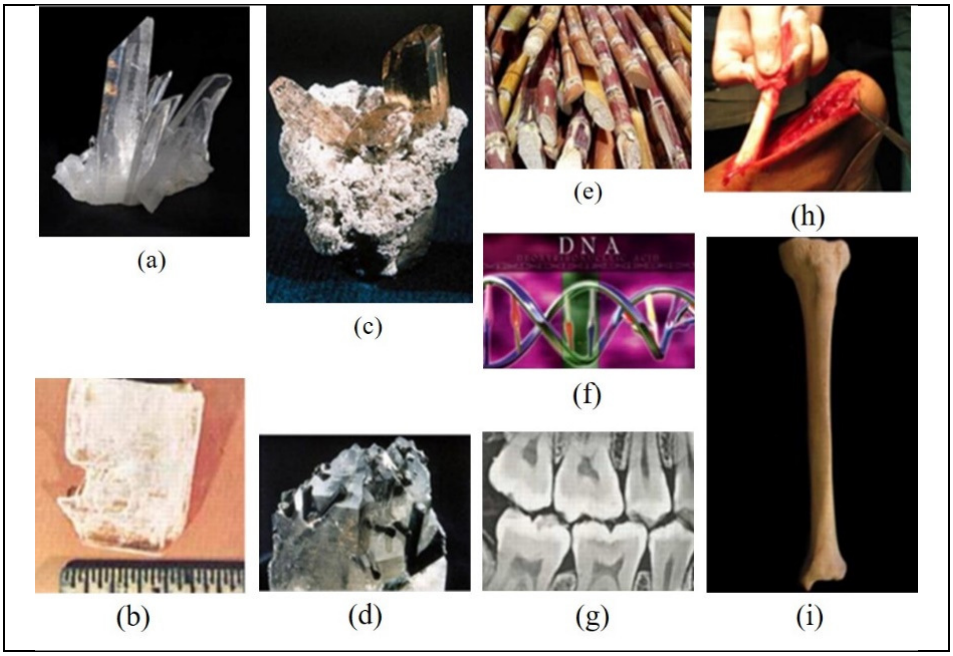

Figure 1.2 Examples of naturally occurring piezoelectric materials
a) Quartz crystal, b) Rochelle Salt, c) Topaz, d) Tourmaline, e) Sugar cane, f) DNA, g) Dentine, h) Tendon and i) Bone [6]

Among a wide variety of piezoelectric materials, ZnO has received considerable interest because it exhibits an excellent combination of semiconducting, piezoelectrical, pyroelectrical and optical properties [7]. Therefore, it has been employed in an enormous number of applications such as electronics, photonics, optoelectronics, acoustic devices and sensors [8].

Furthermore, ZnO is safe, biocompatible, and environmentally friendly, and therefore, it has been considered as the candidate of choice for biomedical applications and represents a suitable replacement for lead-based piezoelectric materials. Also, high quality and appropriately textured thin films can be achieved via epitaxial growth by selecting a suitable technique from a wide range of deposition methods; for example, chemical vapour deposition (CVD), pulsed laser deposition (PLD), magnetron beam epitaxy (MBE), and reactive magnetron sputtering. Among these, sputtering is the most commonly used technique because it is cost-effective and straightforward process. This method includes radio frequency (RF), direct current (DC), and pulsed DC magnetron sputtering systems. Another advantage of ZnO thin films is the possibility for it to be deposited on various rigid and flexible substrates such as silicon, glass, polyimide polymer, and many others [9, 10].

ZnO possesses two crystal structures; the cubic zinc blend, and the hexagonal wurtzite with a tetrahedral coordinate of zinc and oxygen ions. The latter is more popular for ZnO growth, and the preferred orientation for this structure is in the (0002) plane along the c-axis. This form exhibits strong piezoelectric properties along the vertical direction, such as high piezoelectric constant and large electromechanical coupling coefficient [11].

The piezoelectricity of ZnO material has been widely exploited in developing a broad range of acoustic wave devices; for instance, film bulk acoustic wave resonators (FBARs), and a variety of surface acoustic wave and Lamb wave devices. These devices have been extensively employed in sensing applications such as for humidity, temperature, ultraviolet, gas, biochemicals and other biosensors. The basic structure of a ZnO thin film-based SAW sensor consists of a substrate, a sensitive layer and an interdigital transducer (IDT) to excite acoustic wave, as shown in Figure 1.3 [12].

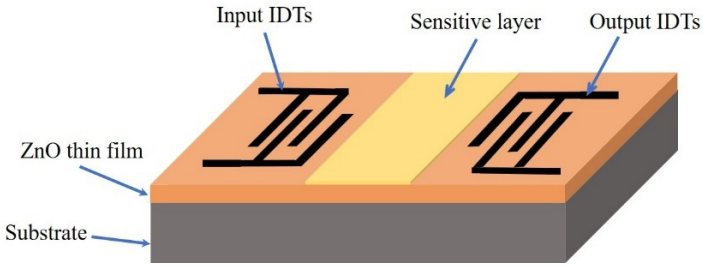

Figure 1.3 Basic structure of ZnO thin film-based SAW sensor which consists of metal IDTs (e.g. Au, Al), functional layer (biomolecules, polymers) and the substrate

Characteristics of high-performance ZnO thin film-based SAW sensors include a high-quality film with strong textured orientation, excellent piezoelectric properties, high Q factor, and high operating (resonant) frequency. Besides, the flexible SAW-based sensors require a substrate that can be bent and deformed easily without degradation in their performance. Plastic and polymer substrates such as polyimide have often been utilised to fabricate flexible ZnO thin film-based SAW sensors. However, those substrates cause severe acoustic wave damping, and they exhibit poor adhesion, lattice mismatching, energy dissipation, and poor film quality, especially for relatively thick films of a few microns [13].

Therefore, a thin metal such as aluminium foil has been used as an alternative option to polymer substrate for ZnO thin film-based sensors. It is commercially available, easy to use and cost-effective [14]. Thin films deposited on aluminium foil showed good adhesion, lower intrinsic stress, and good film quality. Also, the quality of the acoustic wave signal was maintained after several bending cycles as discussed in section 2.5. These devices have been investigated for acoustofluidics applications and in the development of flexible ultrasonic transducers [15]. Furthermore, this type of acoustic wave devices was operated by exciting the Lamb wave modes since this type of wave propagates in a thin plate when its wavelength is larger than the thickness of the substrate. Unlike with Rayleigh waves, Lamb wave-based devices such as the flexural plate wave (FPW) have been widely used in liquid-based biosensing [16].

However, another essential component of the SAW sensor is the sensitive or functional layer, as shown in Figure 1.3. This layer is applied on the surface of the SAW device to absorb or interact with a particular target that results in producing a detectable change in the properties of the acoustic wave such as velocity or amplitude. Hence, the sensitivity and specificity of the sensor are enhanced. A wide variety of materials have been exploited as sensitive layers such as polymers, biological compounds (e.g. antigens), oxide-based materials (e.g. ZnO, TiO_3), and nanomaterials. The ZnO nanorods (NRs) have been frequently used as a popular sensing layer to enhance the sensitivity of the SAW sensor because of their large surface area to volume ratio and the high surface reactivity. Besides, they are mechanically and thermally stable compared to the polymer sensing membranes. The most common growth method to synthesise ZnO NRs is the hydrothermal process due to its simplicity and low cost to make high-quality nanorods [17-19].

However, ZnO thin film on aluminium foil devices has not been investigated in any flexible sensing application. The aluminium foil substrate can be easily deformed, returned to its none-deformed shape, and re-deformed again, and it does not cause acoustic wave attenuation or energy dissipation as does as the polymer substrate. Therefore, it has excellent potential to be used for fabricating SAW sensors for flexible, bendable, and wearable applications.

This thesis aims to develop a SAW sensor based on ZnO thin film on commercial aluminium foil for biomedical and environmental applications which include the sensing of temperature, UV light and humidity and the detection of breath rate and apnoea.

Accordingly, the objectives of this project include:

(1) Depositing ZnO thin films on aluminium foil using a standard and low-cost sputtering method.

(2) Selectively, growing ZnO nanorods using a hydrothermal method after depositing an insulating layer of silicon dioxide.
(3) Designing IDTs to excite the acoustic waves of the desired modes and frequencies.
(4) Characterising the quality of the film using x-ray diffractometry (XRD), scanning electron microscopy (SEM) and atomic force microscopy (AFM).
(5) Performing a finite element analysis to verify the type of vibration modes and their central frequencies in the designed IDT structure.
(6) Fabricating the IDT fingers using a lithography process.
(7) Measuring the frequency response of the SAW sensors.
(8) Investigating the sensing performance of these sensors for temperature, UV light, humidity, and breath applications, at both flat and bending conditions
(9) Using ZnO nanorods to enhance the sensitivity of the sensors to UV light and humidity.

1.2 Thesis outline

This thesis consists of eight chapters. The second chapter reviews the literature and introduces the theoretical background of piezoelectricity in terms of concepts and materials, the ZnO material, its structure and growth methods, acoustic wave devices including bulk acoustic wave and surface acoustic wave, and flexible SAW-based sensors for the sensing of temperature, humidity, UV light and breath rate.

The third chapter explains the detail of experimental methodology using in this research including ZnO thin film deposition and characterisation, the SAW sensors fabrication and characterisation, the growth technique of ZnO nanorods, the sensing process and setup for temperature, UV light, humidity, and breath rate detection.

The fourth chapter discusses the characterisation of the deposited ZnO thin film and the grown nanorods to determine their physical properties. Besides, it presents the simulation

results of the Lamb wave vibration modes and their eigen-frequencies for different SAW wavelengths. Furthermore, the frequency responses obtained experimentally from various SAW devices and the Lamb wave modes are identified and compared to the simulation results.

The fifth chapter studies the temperature coefficient of frequency (TCF) for the flexible SAW sensors and discusses their frequency response in both equilibrium and *in-situ* state conditions. Besides, their real-time and cycling responses in a flexible (curved) position are discussed.

The sixth chapter studies the current-voltage characteristics of the ZnO thin film to determine the changes in surface sheet conductivity as a result of UV light. The frequency response of the sensors at various UV light intensities and different flexible positions are discussed. Also, the influence of temperature on the frequency shift is studied. Sensitivity analysis and results of the sensing performance of the sensors in response to UV light are explained. Besides, the enhancement of sensors sensitivity due to the ZnO nanorods is also discussed.

The seventh chapter discusses the frequency response of the flexible sensors to changes in humidity in both flat and bent positions. Besides, the sensing enhancement due to the ZnO nanorods is discussed. This chapter also explains the frequency response of the sensors to various breath patterns such as normal, fast, and slow breathing, and their sensitivity in the detection of respiratory rate and apnoea intervals.

Finally, the eighth chapter contains the conclusion and makes a recommendation for future work.

Chapter Two

Literature review and theoretical background

2.1 Introduction

An enormous number of technologies have exploited the piezoelectric phenomenon in their applications such as energy harvesting, acoustic wave devices, electronic oscillators, and piezo actuators and sensors. Besides, various piezoelectric materials have recently been discovered which opened the doors for the development of several applications including those flexible and wearable sensors [20, 21]. This chapter reviews the main concepts of piezoelectricity and the properties of commonly used piezoelectric materials with a particular focus on ZnO thin films.

ZnO material has attracted substantial attention due to the unique combinations of excellent piezoelectric and semiconducting properties. It also can be deposited on various types of substrates using a wide range of growth methods which are mostly compatible with semiconductor fabrication processes. Besides, it has been utilised in the fabrication of various kinds of acoustic wave device which have been used for sensing applications [22].

Flexible ZnO thin film-based SAW devices have received a remarkable interest due to the increasing of demand on flexible sensors for bendable and wearable sensing applications as well as lab-on-a-chip [15]. Various flexible materials have been used as substrates for the development of flexible ZnO thin film based-SAW devices such as polymers, plastics, and metal foils. However, the films deposited on polymer substrates exhibit poor quality and thermal and lattice mismatch. Moreover, the propagation of the acoustic wave suffers from severe attenuation [13]. On the other hand, metal foils such as aluminium overcome these

drawbacks, and it has great potential to be a candidate of choice for the next generation of flexible acoustic wave devices.

However, the SAW devices based on ZnO on aluminium foil have not been investigated for sensing application, which is considered to be a gap and an interesting field of research. Therefore, based on this review, a flexible SAW device based on ZnO thin film on a commercial aluminium foil are proposed for the development of flexible sensors for temperature, humidity and ultraviolet light and breathing detection applications. Finite element analysis is needed to verify the design of the SAW devices and their operating modes which is followed by fabrication sensors and study their sensing performance.

2.2 Piezoelectricity

The word piezoelectricity is derived from the Greek phrase ‘piezo’ that means ‘presses’, and it means electricity produced by pressure. The direct piezoelectric effect was reported in the literature for the first time in 1880 by Pierre and Jacques Curie, who observed the generation of surface charges (electricity) when mechanical stress was applied to a variety of crystals. However, the indirect or converse piezoelectric effect was mathematically derived by Lippman , and it was experimentally verified by Curie’s brothers in 1881 when they noticed that those crystals were subject to structural deformation when an electrical potential was applied [23].

2.2.1 The concept of piezoelectricity

This phenomenon occurs as a result of the self-reorientation of dipole moments of the piezoelectric material when a mechanical force such as compression, twisting or expansion is applied. This causes variations in the electric polarization of the molecules, which eventually affects the surface charge density and produces an electrical potential. Likewise, a slight change in the dipole moments occurs when an electrical potential is applied across

the piezoelectric material, and this results in significant deformation of the material structure[6].

Figure 2.1a shows the distribution of the charges in an equilibrium state. The variation in surface charge density due to applying compressive or tensile stress (direct piezoelectricity) is illustrated in Figures 2.1d and 2.1e, respectively. The change in material dimensions; longitudinal and axial strain when the electrical field is applied (converse piezoelectricity) can be seen in Figures 2.1b and 2.1c, respectively.

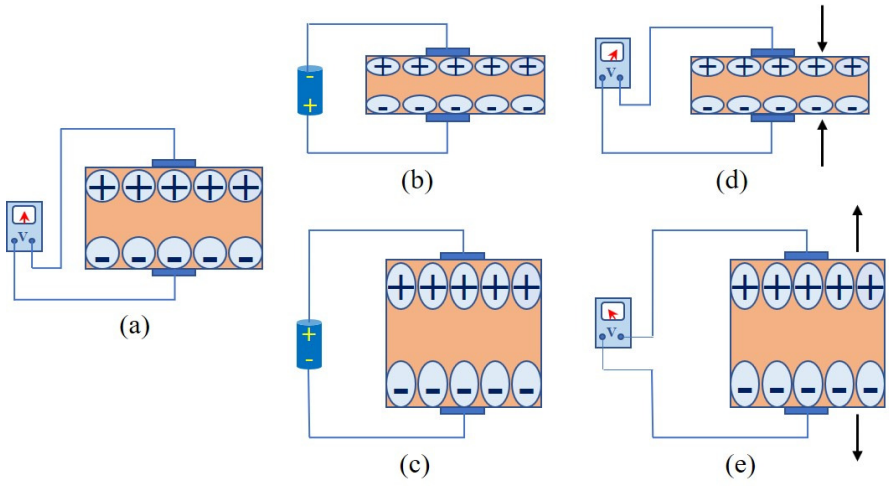

Figure 2.1 Schematic illustration of the piezoelectric phenomenon a) at equilibrium state, b) converse effect with induced longitudinal strain, c) converse effect with the induced axial strain, d) direct effect by applying compressive stress and e) direct effect by applying tensile stress

The polarisation or the total dipole moments occur spontaneously in ferroelectric materials and is reversed when an external electric field is applied. Meanwhile, a pyroelectric material exhibits polarisation that varies with changes in temperature. Therefore, all ferroelectric materials possess piezoelectricity, and the material should be polarised with a net dipole moment vector in order for these phenomena to be exhibited, such as in crystals and polycrystalline materials [24, 25].

The main Figures of merit of piezoelectric materials that determine the performance and the physical properties are as follows:

1. The electromechanical coupling factor (K^2): this is the ability of the piezoelectric material to convert electrical energy into mechanical energy and vice versa (energy transmission coefficient). It is given by the following formula 2.1 [13]:

$$K^2 = \frac{e_{31}^2}{C_{11}\,\varepsilon_{33}} \tag{2.1}$$

where e_{31} is the piezoelectric coefficient, $C_{11}$is the elastic constant of the material, and ε_{33} is the permittivity at a constant strain.

2. The piezoelectric coefficient or strain constant (d): this is related to the generation of surface charges to the applied stress or the induced strain to the applied electrical field. For example, (d_{33}) is the piezoelectric constant when the stress is applied in the vertical direction Z(3) and the polarization occurs in the same direction [26], as shown in Figure 2.2.

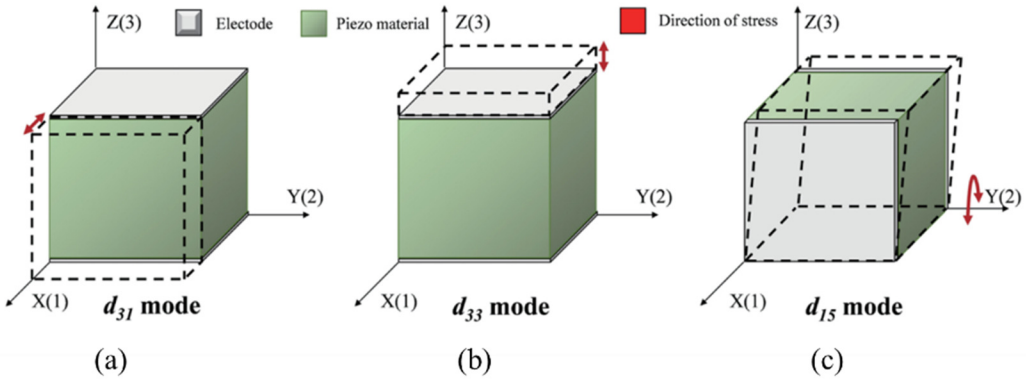

Figure 2.2 Piezoelectric operating modes showing the directions of the displacement and electric field when (a) stress applied in direction X(1) and electrodes placed in Z(3) direction (d_{31} mode), (b) stress applied in direction Z(3) and electrodes placed in Z(3) direction (d_{33} mode) and c) stress applied in direction Y(2) and electrodes placed in Z(3) direction (d_{15} mode or shear mode) [27]

3. Voltage constant or open circuit coefficient (g): this determines the amount of voltage per unit of input mechanical stress or the amount of induced strain per unit of the applied electrical field [28].

2.2.2 Piezoelectric materials

The materials that possess a piezoelectric effect (or converse effect) must be non-centrosymmetric crystals. This structure implies that the material is polarised, and it exhibits the required symmetry for spontaneous polarization that varies when applied mechanical stress [29, 30].

Since the discovery of the piezoelectric effect in quartz by the Curie brothers, other materials such as Rochelle salt (potassium sodium tartrate tetra-hydrate) [31], topaz and tourmaline-group minerals have been investigated and they also exhibit similar phenomenon. These inorganic materials occurred naturally and were the only piezoelectric crystals available until the early twentieth century [5].

The first practical application of piezoelectricity was developed after World War I, which was an ultrasonic transducer made of quartz that produced acoustic waves and was used to detect underwater vessels and submarines. Later, the quartz in these transducers was replaced by Rochelle salt crystals that showed higher electromechanically coupling coefficient, in addition to the ferroelectric properties [32, 33].

On the other hand, most organic compounds and biomolecules have acentric and asymmetric structures, and dipole moments are created due to the presence of polar chemical groups [34]. Thus, the piezoelectric phenomenon has also been discovered in many organic and biological materials such as cellulose (wood), silk, collagen, bone, and DNA [35-39]. This has been exploited in various biomedical implementations by developing biocompatible materials for various sensing applications and tissue regeneration [40, 41].

However, extensive research has been conducted to develop synthetic piezoelectric materials that possess better piezoelectric performance and enhanced physical properties compared to naturally occurring materials [42]. They should also be easily manufactured at low cost, have

small converted energy losses, and be thermally stable, reliable and reproducible [43, 44]. Thus, the first synthetic piezoelectric material was made in the early 1940s from barium titanate ($BaTiO_3$) ceramic that exhibits good ferroelectric and piezoelectric properties [45]. Besides, it exhibits a relatively high dielectric constant depending on its grain size and method of synthesis, and a high electromechanical coupling coefficient with good thermal and mechanical stability [46]. However, ceramic is an inert material and has randomly oriented dipoles, and therefore, a strong electrical field has to be applied at a temperature slightly lower than its Curie point to render it an active piezoelectric material. This process is called poling, where, the domains of dipoles are aligned in the direction of the field and the material becomes permanently polarised as shown in Figure 2.3 [47].

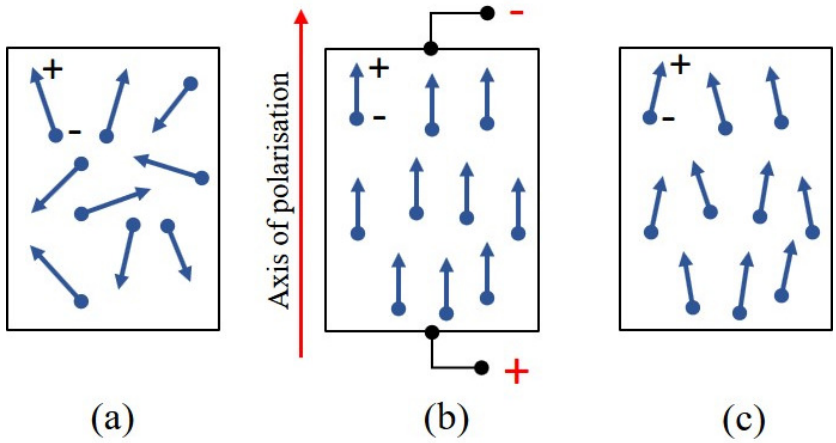

Figure 2.3 Applying external electric field to activate piezoelectricity in ceramic material (poling process) which shows a) randomly oriented charges, b) charges aligned with the applied electrical field and c) charges are nearly permanently aligned after poling

Following the discovery of barium titanate, lead zirconate titanate PZT ($Pb(Zr, Ti)O_3$) ceramic was investigated for its piezoelectric capability by Jaffe in 1954 [48]. It was found that PZT has a higher electromechanical coupling coefficient and Curie temperature, and higher dielectric constant, than those of barium titanate, and it can be easily fabricated and poled at low cost [49, 50]. Due to these excellent piezoelectric properties, PZT has been widely used in sensing applications such as pressure sensors and cantilevers for bio-sensing and energy harvesting [20, 51]. Furthermore, PZT thin films have attracted remarkable attention as they allow the integration of PZT with MEMs and complementary metal-oxide-

semiconductor (CMOS) technology. Exploiting a simple sol-gel method, the PZT can be easily deposited on silicon and other substrates, and it has been utilised in a wide range of actuating and transducing applications [52, 53].

However, the lead oxide-based piezoelectric materials such as PZT have been considered to be environmentally hazardous and toxic materials. Therefore, lead-free piezoelectric materials such as potassium niobate ($KNbO_3$) and bismuth titanate (e.g. $Bi_4Ti_3O_{12}$) families were developed, and they have been used as alternative materials in several biomedical and environmental applications [54, 55]. The first synthetic single crystals of lithium niobate ($LiNbO_3$) and lithium tantalate ($LiTaO_3$) were discovered in the Bell laboratories in 1949 [56]. These two synthesised crystals exhibit exceptional combinations of physical, ferroelectric, piezoelectric, pyroelectric, and optical properties [57, 58]. Hence, they have been candidates of choice in several applications such as SAW transducers due to their large electromechanical coefficients and low acoustic loss, various sensing applications, MEMS, and telecommunications [59-61]. However, the more recent synthetic single crystal langasite, has been investigated for numerous applications since the 1980s. It possesses high piezoelectric properties where its value of the dielectric constant d_{11} is three times greater than that of quartz. It is also thermally stable during high temperature processing because it has no phase transition up to 1470^{o}C. Therefore, it has been used in high temperature bulk acoustic wave (BAW) sensing applications and other SAW resonator devices [62-64].

However, the natural crystals and synthetic piezoelectric materials are rigid, fragile, and incompatible with biomedical and environmental applications. Therefore, extensive research has been conducted to produce flexible and biocompatible materials with high piezoelectric performance properties such as polymers, piezo-composites and thin films [65, 66]. The piezoelectric properties of the polymers were investigated, and they showed a lower

dielectric coefficient and elastic stiffness compared to those of piezoceramics. Besides, they have low density and low acoustic impedance, and this makes them convenient for voltage and liquid-based sensing (bio-sensing) applications [7, 67].

The polyvinylidene-fluoride (PVDF) polymer was first discovered and investigated by Kawai in 1969 [68], and it has since been widely applied in bio-sensing and other flexible applications [69]. Piezoelectric properties have also been identified in polyvinylidene chloride (PVDC) and polyimide polymers, and the latter has been used as a structural material in MEMS applications [70].

Piezoelectric composite materials have attracted substantial attention as they possess the advantages of good piezoelectric properties of piezo-ceramics and the flexibility and strength of polymers [71]. PVDF and polydimethylsiloxane (PDMS) are the most common matrix or filler compound used in polymer composites for various piezoelectric materials such as PZT, $BaTiO_3$, and ZnO [72, 73].

On the other hand, the mechanical and piezoelectric properties of polymers and composites suffer from a number of limitations such as low values of dielectric constant d_{33}, thickness limitations due to the high electric field required in the poling process, a low quality factor, high thermal expansion and low temperature operating point [74, 75].

Thin-film piezoelectric devices have been widely exploited in MEMS applications such as sensing and actuation due to their ease of fabrication, significantly low cost, capability for mass production, and excellent performance [76]. Besides, they can easily be integrated with microsystems, microelectronics, and lab-on-a-chip (LOC) devices by depositing a piezoelectric material such as PZT, ZnO, $LiNbO_3$, aluminium nitride (AlN) and gallium

nitride (GaN) on various substrates such as silicon (Si) [77-81]. Moreover, piezoelectric thin films can be deposited on the regions of the devices where the SAW is required to be generated, whereas the other features and microstructures can be fabricated on the other areas. Thus, complete microsystems can be produced for microfluidics, bio-sensing, and LOC applications [13].

The most common substrates used for thin film deposition are Si, glass, sapphire, polymers, diamond, and some other rigid piezoelectric substrates such as quartz and $LiNbO_3$ [8, 82, 83]. However, polymers such as polyimide have frequently been used in the fabrication of flexible acoustic wave devices for wearable sensing and biomedical applications [84].

Furthermore, among thin-film piezoelectric materials, ZnO and AlN have attracted considerable interest and have been the materials of choice in several kinds of SAW devices used for microfluidics and LOC platforms [85, 86]. Although PZT thin films exhibit superior piezoelectric properties, they have a significant drawback for environmental and biological applications due to its toxicity [87]. Also, the fabrication process for other piezoelectric thin film materials such as $BaTiO_3$, $LiNbO_3$, and $BiFeO_3$ is complex, and the resulting films are of poor quality [88].

ZnO thin film has several advantages over AlN, such as a higher piezoelectric coupling coefficient, ease of fabrication, better film control and quality, lower film stress, and the possibility to grow ZnO nanostructures and nanorods over various acoustic wave devices [89]. Moreover, ZnO is considered to be biocompatible material, and it has attractive physical, electrical, and optical properties [10].

Therefore, in this project, ZnO thin film has been selected as the piezoelectric material for fabricating SAW devices for sensing applications. Next section will discuss in detail the property of the ZnO material.

2.3 ZnO material

Polycrystalline structure of ZnO material has been exploited in a wide range of cosmetics, rubber, and paint industry applications for over a hundred years. Besides, ZnO was utilised for the first time as a semiconductor material in radio sets as a cat's whisker detector in the 1920s. The lattice parameters and other diffraction data of the ZnO crystal were determined in 1935, and its optical properties were investigated in detail in 1954. The piezoelectric effect in ZnO was discovered in 1960, and an early ZnO thin film-based SAW transducer was developed in 1976. The electrical, optical, and piezoelectric properties of ZnO material have attracted substantial attention from the scientific community since the mid-nineties onwards [22, 90].

ZnO possesses a stable and large exciton binding energy of ~60 meV at room temperature and high bandgap energy of ~3.4 eV. Moreover, it exhibits excellent piezoelectric properties and is considered to be bio-safe (biocompatible) and not environmentally toxic. Therefore, it has recently been employed in several applications, such as in the electronics and optoelectronics industry, biomedical applications, sensing, and various acoustic wave-based implementations [91].

2.3.1 ZnO crystal structure

ZnO crystals possess two different structures: wurtzite which is hexagonal, and the cubic zinc blend. The ZnO crystal with wurtzite symmetry is the more stable phase at ambient conditions of pressure and temperature compared to the cubic zinc blend phase. The unit cell of this structure exhibits a hexagonal close-packed (HCP) lattice with two parameters a =

3.25 Å, and c = 5.21 Å, and the ratio c/a is equal to 1.603 in the ideal wurtzite structure. Besides, the lattice has two interconnected sub-lattices of zinc and oxygen ions where each zinc element is connected to tetrahedral coordination of oxygen ions along the c-axis, and vice versa as shown in Figure 2.4 [92].

The hexagonal lattice and the tetrahedral coordination give the asymmetric polar structure of the ZnO crystals and influence the spontaneous polarisation, piezoelectric properties, crystal growth patterns, and intrinsic defects [93].

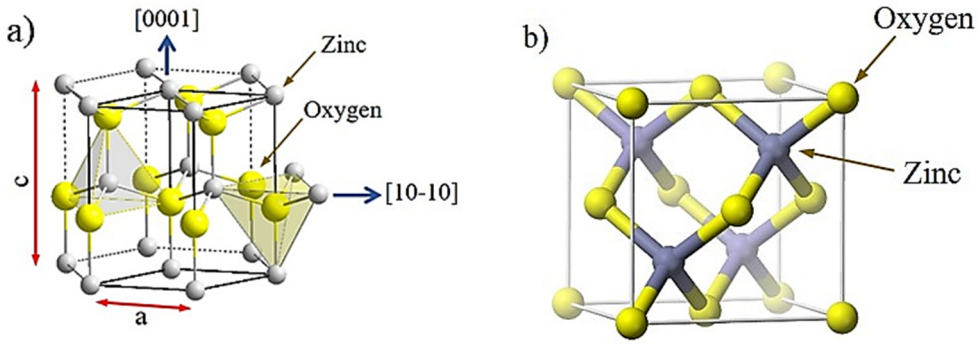

Figure 2.4 The two different structures of ZnO crystal a) wurtzite with tetrahedral coordination and b) cubic zinc blend [94, 95]

The exceptional physical properties of the ZnO material arise mainly from the presence of polar surfaces in its crystal lattice. The ZnO has two polar surfaces in the wurtzite structure, one surface that terminates with zinc ions (Zn^{+}) in the (0001) plane and the other that terminates with oxygen ions (O^{-}) in the $(000\bar{1})$ plane [96], as shown in Figure 2.5

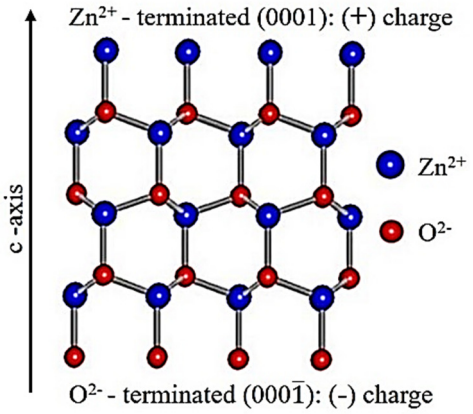

Figure 2.5 ZnO orientation in the polar (0001) plane along the c-axis [97]

The orientation in the polar (0001) plane along the c-axis in the wurtzite symmetry is the most popular structure used to grow ZnO thin films on various substrates. This can be attributed to the lowest surface free energy of this orientation since the distribution of charges in such a configuration results in minimal electrostatic energy and driving the growth in this direction [98]. It is also suggested that the surfaces terminating with Zn ions exhibit higher surface energy compared to the oxygen-terminated surfaces; hence, they are more active in various surface reactions [96].

However, the lattice parameters of ZnO crystals in the grown film can deviate slightly from the ideal case due to the impurities, free charges, film stress, and temperature. Also, the ZnO film is often grown by epitaxial growth, layer by layer on the surface of the substrate. Therefore, it is important to measure the lattice constants or parameters of the thin film since they indicate the quality of the film, the presence of the defects, and the intrinsic stress or strain inside the film [90, 99].

Moreover, variations of the lattice parameters due to defects in the crystal structure may have a profound impact on the symmetry of the crystal. Besides, they affect the polarisation and physical properties of ZnO film, including piezoelectric effect [99].

The lattice parameters of ZnO crystals can be calculated using Bragg equation 2.2, where the diffraction angle θ is obtained from XRD rocking curve [100]:

$$\lambda = 2d\ sin\theta \tag{2.2}$$

where λ is the x-ray wavelength, which is 1.5406 Å for the copper source, d is the inter-planer spacing parameter, and θ is the diffraction angle.

Bragg diffraction occurs when the incident x-ray beam of wavelength (λ) hits a crystal lattice plane where the atoms are ordered in a regular and periodic array, and the planes are separated by a distance (d) as illustrated in Figure 2.6 [101].

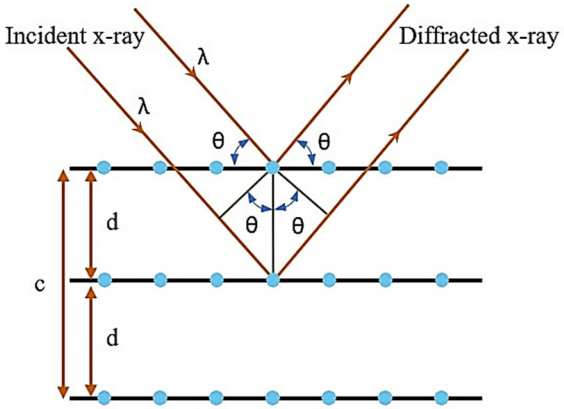

Figure 2.6 X-ray diffraction as a result of hitting atoms in crystal lattice showing diffraction angle θ and lattice parameters d and c

The angle of deviation (2θ) is the angle between the incident and reflected x-ray beams. If the enormous number of ZnO crystallites that make up the thin film have similar orientation, then the X-ray beam will be reflected at a specific value of 2θ that represents the particular plane orientation [101]. Hence, the structure and orientation of ZnO crystals can be identified, and the lattice parameters *a* and *c* for the hexagonal crystals can be calculated using the following equation [102]:

$$\frac{1}{d^2} = \frac{4}{3}\left(\frac{h^2 + hk + k^2}{a^2}\right) + \frac{l^2}{c^2} \tag{2.3}$$

where hkl are the Miller's indices for the cubic crystal lattice, and they can be converted to Miller-Bravais indices (hkil) for the hexagonal structure using the following relationship [102]:

$$h + k = -i \tag{2.4}$$

Thus, from equations 2.2, 2.3 and 2.4, the lattice parameters are calculated using the following simplified equations [103]:

$$c = 2d = \frac{\lambda}{\sin\theta} \tag{2.5}$$

$$a = \frac{1}{\sqrt{3}} \frac{\lambda}{\sin\theta} \tag{2.6}$$

2.3.2 Mechanical properties of ZnO

The mechanical properties of a material determine its behaviour and responses to internal and external forces regarding stress (σ) and strain (ε). Elasticity is one of the essential properties of piezoelectric material and describes its mechanical response and the nature of the interactions between atoms and bonds within the material. The conventional parameters that are frequently used to characterise the elastic properties of materials are Young's modulus (Y), Poisson's ratio (ν), bulk modulus (B) and shear modulus. However, these elastic moduli depend on the elastic constants of the material, which is given by Hook's Law that relates applied stress to material strain as in the following generalised formula [104]:

$$\sigma_{ij} = C_{ijkl}\varepsilon_{kl} \tag{2.7}$$

where σ_{ij} is the applied stress, ε_{kl} is the resulting strain, and C_{ijkl} is the constant of the elastic stiffness of the material.

The standard method for the determination of the elastic constants of an anisotropic material such as ZnO is to study the elastic acoustic wave propagation (sound velocity) in the crystal or solid material. However, the elastic constants are mathematically expressed as a matrix of stiffness tensors, and they rely on the lattice structure and the symmetry of the crystal. Therefore, the wurtzite hexagonal structure of the ZnO crystal possesses five independent elastic stiffness constants along the c-axis (z-axis). These are C_{11}, C_{33}, C_{12}, C_{13}, and C_{44}, as shown in the stress-strain relationship below [104]:

$$\begin{pmatrix}\sigma_{xx}\\ \sigma_{yy}\\ \sigma_{zz}\\ \sigma_{yz}\\ \sigma_{zx}\\ \sigma_{xy}\end{pmatrix} = \begin{pmatrix}C_{11} & C_{12} & C_{13} & 0 & 0 & 0\\ C_{12} & C_{11} & C_{13} & 0 & 0 & 0\\ C_{13} & C_{13} & C_{33} & 0 & 0 & 0\\ 0 & 0 & 0 & C_{44} & 0 & 0\\ 0 & 0 & 0 & 0 & C_{44} & 0\\ 0 & 0 & 0 & 0 & 0 & C_{66}\end{pmatrix}\begin{pmatrix}\varepsilon_{xx}\\ \varepsilon_{yy}\\ \varepsilon_{zz}\\ \varepsilon_{yz}\\ \varepsilon_{zx}\\ \varepsilon_{xy}\end{pmatrix} \quad (2.8)$$

The sound velocity of the longitudinal mode is used to determine the elastic constants C_{11} and C_{33} in the [1000] and [0001] direction, respectively. Whereas, measurements of the sound velocity of the transverse modes are used to determine C_{66} where this elastic constant is given by the following formula due to crystal symmetry [90]:

$$C_{66} = \frac{C_{11-}\ C_{12}}{2} \quad (2.9)$$

Furthermore, the combination of all elastic constants, including the remaining stiffness modulus C_{13}, is found in the sound velocity of the propagating modes along the less symmetrical direction such as [0011]. However, in general, the sound velocity (v) in a material is given by the following equation [90]:

$$v = \sqrt{\frac{C_{ij}}{\rho}} \quad (2.10)$$

where ρ is the material density. Thus, mechanical properties such as bulk modulus, Poisson's ratio, Young's modulus, and shear modulus for an anisotropic material can be estimated a proximally from the elastic stiffness constants using the equations 2.11 - 2.14 [105].

$$Bulk\ modulus\ (B) = \frac{(\ C_{11} + \ C_{12})C_{33} - 2C_{13}^2}{C_{11} + \ C_{12} + 2C_{33} - \ 4C_{13}} \quad (2.11)$$

$$Poisson's\ ratio\ (v) = \frac{C_{13}}{(\ C_{11} + \ C_{12})} \quad (2.12)$$

$$Young's\ modulus\ (Y) = \ 3\mathrm{B}(1 - 2\mathrm{v}) \quad (2.13)$$

$$Shear\ modulus\ (G) = \frac{Y}{2(1+v)} \quad (2.14)$$

Table 2.1 shows a summary of the elastic stiffness constants and the mechanical moduli of the ZnO wurtzite material.

Table 2.1 Mechanical properties of ZnO material in wurtzite structure [22, 90]

Bulk modulus (GPa)	Poisson's ratio (GPa)	Young's modulus (GPa)	Shear modulus (GPa)	Elastic stiffness constants (GPa)					
				C11	C12	C13	C33	C44	C66
142.4	0.36	111.2	40.9	209	120	104	216	44	44

The piezoelectricity of the ZnO material arises as a result of the lack of symmetry in its combined hexagonal and tetrahedral crystal structure. Therefore, wurtzite ZnO naturally exhibits a spontaneous polarisation, and it does not need poling after sputtering deposition [22]. Furthermore, the piezoelectric constants and the electromechanical coupling coefficients of ZnO material are much higher in comparison to those for other semiconductors with a similar structure such as AlN and GaN. The electrical components of polarization (P) that result from strain or applied stress (direct effect) are given by the following equation [90] :

$$P_i = e_{ijk}\,\varepsilon_{jk} = d_{ijk}\,\sigma_{jk} \tag{2.15}$$

where *Pi* is the electrical polarisation, e_{ijk} are the piezoelectric strain coefficients, and d_{ijk} is the piezoelectric stress coefficient. However, d_{ijk} is also related to the electrical potential (*E*) applied to the induced strain (converse effect) as the equation below [90].

$$\varepsilon_{ij} = d_{ijk}\,E_k \tag{2.16}$$

Hence, the ZnO material has only three independent piezoelectric tensors due to the wurtzite phase and the symmetrical hexagonal structure of the ZnO crystal. These piezoelectric constants are d_{31}, d_{33} and d_{15} [106].

The constant d_{31} describes the piezoelectric response along the c-axis when the mechanical stress is applied perpendicular to this axis, and it has a value of about -5.12 pC/N. The coefficient d_{33} represents the piezoelectricity when the piezoelectric response and the applied stress both occur along the c-axis, and this constant has the highest value of about 12.3 pC/N. The last constant d_{15} is the piezoelectric response perpendicular to the c-axis induced by shear stress, and it has a value of -8.3 pC/N [11]. The highest piezoelectric performance is obtained when mechanical stress or force is applied directly along the c-axis as given by the piezoelectric coefficient d_{33}. Therefore, the ZnO thin film orientation in the (0002) plane along the c-axis is preferred for high piezoelectric efficiency [107]. Table 2.2 shows a comparison of values of the piezoelectric constant d_{33} for different piezoelectric materials.

Table 2.2 Comparison of piezoelectric coefficients of various piezoelectric materials [13]

Material	ZnO	AlN	GaN	PZT	128° cut $LiNbO_3$	36° YX-cut $LiTaO_3$	ST-cut Quartz
Piezoelectric constant d_{33} (pC/N)	12	4.5, 6.4	4.5	289 - 380, 117	12	12	2.3 (d_{11})

The effective piezoelectric constant of ZnO material exhibits a higher value than those of AlN, GaN, and Quartz, but it is much lower than that of PZT, and it is comparable to those of $LiNbO_3$ and $LiTaO_3$.

2.3.3 ZnO film growth

Many growth techniques have been developed in order to deposit high-quality thin films of ZnO material on diverse types of substrates. The most common deposition methods include pulsed laser deposition (PLD), chemical vapour deposition (CVD), metal-organic chemical vapour deposition (MOCVD), the sol-gel process, molecular beam epitaxy (MBE), and direct current (DC) and radiofrequency (RF) magnetron sputtering [19]. The determination of the suitability of a deposition technique depends on several criteria such as the desired

film quality, the applications concerned such as transducers, sensors, or optical devices and its requirement for particular piezoelectric performance, the temperature involved in the process, and the cost and availability of the necessary machine [13].

The PLD method uses a high-power pulsed laser that is guided to the zinc target and causes the evaporation of material from the surface of the source. The zinc vapour reacts with oxygen gas creating a plume of high energy and reactive particles that extend toward the surface of the substrate. This technique is not popular in industrial applications as it is expensive, and the deposition covers only a small area, although the film has good crystallinity and quality and the deposition occurs at low substrate temperature [16, 99].

In the CVD method, the ZnO material in the vapour phase is delivered by a carrying gas to the growth site where a chemical reaction occurs at the surface of the substrate. The deposition rate of this process is considered to be relatively low, is not needed a vacuum, and it takes place at a high temperature between 300-800 ^{o}C that might be an issue for some materials such as polymers. However, this technique produces high-quality epitaxial film layers with the possibility of large-scale production. Likewise, MOCVD has a similar process to CVD except that the ZnO precursor is replaced by a metal-organic compound such as diethyl and dimethyl metals that are highly volatile at relatively lower temperatures [16, 95, 108, 109].

Another chemical reaction-based deposition technique is the sol-gel process. This involves the use of a colloidal solution (sol) of organic metal such as zinc acetate dihydrate as a precursor that undergoes several chemical steps until it becomes relatively rigid (gel) and porous. This method is simple and cost-effective, occurs at low temperature and needs no vacuum. However, the grown film suffers from poor crystal quality and small grain size, and it requires high-temperature post-deposition annealing [17, 18].

In contrast, the MBE and magnetron sputtering methods are examples of physical vapour deposition (PVD) techniques that require vacuum and plasma gas for their operation. A high-purity zinc target is used as a source, and the oxygen gas is introduced at a specific flow rate inside the deposition chamber to oxidise the zinc molecules. MBE provides an *in-situ* analysis of the surface of the thin film during the deposition process, thus, permitting accurate control of the parameter involved. Besides, it is possible to produce thin films of precise thickness which have extremely high-quality crystalline structures due to the atomic layer growth and real-time dynamic control. However, this process has several drawbacks such as slow deposition rates, the requirement of ultra-low pressure (high vacuum), film contamination, and high cost. It is also not compatible with MEMS processes [17, 94, 99].

On the other hand, the reactive magnetron sputtering technique has been frequently used as the preferred method for ZnO film deposition. It is a simple and flexible process which operates at low temperature (room temperature). The deposition rate is reasonably high, and the process is cheap and highly scalable. The deposited film possesses an excellent quality which is compatible with MEMS processing. The RF magnetron sputtering system is operated in vacuum condition by using an alternating electrical potential between the substrate and the target at radio frequency levels. This method is suitable for most materials, such as metals, semiconductors, and insulators. The alternating power eliminates the charges that accumulate at the surface of the insulator and prevents the formation of arcing that would influence the deposition process and crystal quality. The deposition has a relatively slow rate, requires significantly high voltages (KV) as well as it is costly. However, the deposited film has a smooth texture and excellent quality [110-112].

In contrast, the DC magnetron sputtering technique is carried out by biasing the targets with a specific DC electrical potential and introducing a mixture of argon and oxygen gases with

a specific ratio inside the vacuum chamber. This method is limited to conducting materials due to the build-up of charges at the surface of the target that could halt the sputtering process completely. It has frequently been used to deposit ZnO thin films over various substrates and for different applications. Hence, it is important to optimise the deposition parameters of the sputtering process in order to produce thin films with the desired quality and thickness. RF power is usually applied for a brief time (~ 5 -15 minutes) to clean any residues or contamination from the surface of the target before starting deposition. This process is cheap, easy to control and offers higher deposition rates and consistent film quality [113-115].
However, an alternative method to the DC and RF sputtering techniques is pulsed DC magnetron sputtering which provides a solution to problems of charge accumulation and arc formation at relatively low cost and with high deposition rates. In this technique, pulsed DC power is applied to the target that is switched periodically between the ground and positive potential at a frequency of 20 to 350 kHz. This technique reduces arcing issue but does not eliminate it. Other advanced methods have recently been developed to provide better conditions for thin film deposition, such as microwave-assisted pulsed sputtering and high-power impulse magnetron sputtering (HPiMS) [13, 116, 117].

Furthermore, the mechanism of the sputtering process involves ion bombardment on the surface of the substrate where the ZnO film is grown. This results in the generation of some defects, and it influences the properties of the film, such as crystal orientation, texture, grain size, and intrinsic stress. Hence, extensive research has been conducted to study the impact of each sputtering parameter on the properties of ZnO film; for example, the temperature of the substrate, the plasma power, gas ratio and flow rates, bias voltage, vacuum and gas pressures, and the annealing process [118-121].

On the other hand, the selection of the substrate is another important issue in the deposition of ZnO thin film, since the matching between the lattice parameters of the substrate and the

film is strongly associated with crystal growth and the film quality [122]. Lattice mismatch may result in the induction of film strain, epitaxial growth defects, decreased crystallite size, and film dislocation [123]. Hence, the hetero-epitaxial growth of ZnO thin films in the wurtzite structure has been successfully deposited on various substrates such as sapphire [124, 125], GaN [126], silicon [127], glass [128], Al_2O_3 [129], SiC [130], ITO/glass [131], ZnO:Al/glass [131], GaAs [132], $LiNbO_3$ [133], $LiTaO_3$ [134], quartz [135], and diamond [136]. The ZnO material has also been grown on polymer substrates such as Kapton (polyimide) [137], polyethylene terephthalate (PET) [138], and naphthalate (PEN) [139] for wearable and flexible applications [140].

2.3.4 ZnO film characterisation

Several methods have been exploited to characterise the deposited ZnO thin film to determine its physical properties such as texture, crystalline structures and orientation, grain size, stress, strain, film thickness, piezoelectric coefficients, and optical and electrical properties. These characterisation methods include Raman spectroscopy, XRD, SEM, AFM, ultraviolet-visible spectroscopy (UV-VIS) and semiconductor characterisation tools such as four-point probe method [141-144].

The ZnO thin film can be grown in different types of textures according to crystal orientation. Columnar microstructures are grown along the c-axis and perpendicular to the substrate, and this is the preferred orientation for high piezoelectric performance. In pyramid and polygon like-structures, the c-axis is parallel to the substrate, [145] as illustrated in Figure 2.7.

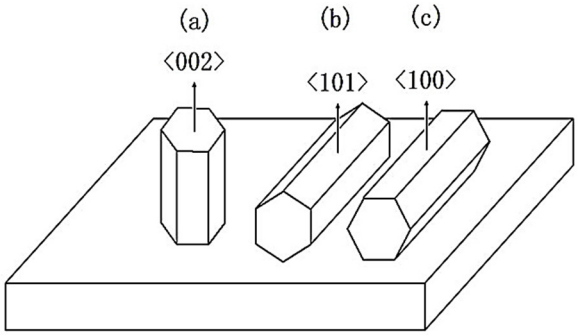

Figure 2.7 Different crystal orientations of ZnO hexagonal structure a) columnar, b) pyramid and c) polygon microstructures [146]

The texture of the preferred (0002) orientation is characterised using the formula for the texture coefficient TC (%) as shown below [147]:

$$\text{TC}\ (\%) = \frac{(0002)\ peak\ intensity}{\sum peak\ intesnity\ (observed\ in\ ZnO)} * 100\% \qquad (2.17)$$

Hence, the higher the TC (%) value, the more the textured ZnO thin film corresponds to the (0002) orientation.

Furthermore, the relationship between the thickness of the ZnO thin film and the grain size in terms of piezoelectric properties has been investigated. Research suggests that the thicker films possess larger grain size and higher piezoelectric coefficients [110, 148, 149]. The grain sizes of a ZnO thin film and its nanostructures are estimated using Scherrer's formula [150-152].

$$D = \frac{k\lambda}{\beta \cos\theta} \qquad (2.18)$$

where D is the grain size, k is a dimensionless number called shape factor or Scherrer's constant (~0.9), λ is the x-ray wavelength (for a copper source is 0.15406 nm), β is the full width at half maxima (FWHM) of the peak corresponding to Bragg's diffraction angle θ [153].

On the other hand, the physical properties of ZnO thin film are influenced by the residual (intrinsic) stress in the film [154]. This stress arises as a result of many factors such as lattice misfit, thermal expansion mismatch between the film and the substrate and the conditions of the deposition process [155]. MEMS devices based on ZnO thin film with large values of intrinsic stress exhibit poor performance and low yield, and are less reliable in practical applications [156]. Hence, the residual stress (σ_r) of the ZnO thin film is calculated based on the biaxial strain (ε_{zz}) model as per the following two equations [157]:

$$\varepsilon_{zz} = \frac{d - d_0}{d_0} \tag{2.19}$$

$$\sigma_r = \frac{2C_{13} - (C_{11} + C_{12})C_{33}}{C_{13}} . \varepsilon_{zz} \tag{2.20}$$

where d is the calculated lattice parameter from XRD (peak 0002), d_0 is the lattice parameter of the ZnO bulk, and C_{ij} are elastic stiffness constants.

However, strain and stress are induced due to the defects in the film crystallites, and they cause a broadening of the XRD peak of the (0002) orientation plane. Therefore, they can be estimated using the XRD peak shift as per the following equations [158, 159].

$$\varepsilon_{zz} = \frac{\beta cos\theta}{4} \tag{2.21}$$

$$\sigma_r = \frac{Y}{2\nu} \frac{2(\theta - \theta_0)}{2\tan\theta_0} \tag{2.22}$$

where θ_0 is the Bragg's diffraction angle of the stress-free bulk ZnO.

Surface properties of thin films such as surface roughness are further important parameters that affect the efficiency of ZnO thin film-based applications. In particular, higher surface roughness has a negative impact on SAW propagation, resulting in increases in its dispersion,

scattering and attenuation. The significance of this influence also increases with the phase velocity of the SAW [160-162].

Thus, for optimal piezoelectric performance in practical applications, it is required that the ZnO possesses a single crystal structure or a strong textured thin film with minimal defects, the appropriate thickness, good stoichiometry and low roughness (i.e. a smooth surface) [19].

In this project, the DC reactive magnetron sputtering method was used to deposit a high-quality thin film of ZnO material because of the availability of the equipment, the low cost and the simplicity of the process, and the possibility to deposit films over a large area at room temperature.

2.3.5 ZnO nanostructures including nanorods

ZnO nanostructures have recently attracted considerable attention due to the ease and low cost of the fabrication process, and they are a promising technology for enhancing a sensor's sensitivity, response, and performance [163]. ZnO nanostructures have been exploited in several sensing applications, such as gas, chemical, pH and UV sensing and biosensing [164]. However, the chemical and the physical properties of ZnO nanostructures are affected by their morphology and sizes [165]. Therefore, various shapes of ZnO nanostructures such as rods [166], wires [167], spheres [168], particles [169], composites [170] and tubes [171] have been grown. These various morphologies provide different characteristics over their surface-to-volume ratios and diverse options for spatial structures that play a vital role in enhancing sensing performance [172].

The critical advantage of ZnO nanostructures is their highly reactive surface area and the high surface-to-volume ratio. These are available for the effective adsorption of other molecules and to respond to small variations and low analyte concentrations. ZnO

nanostructures also have excellent piezoelectric properties that make them an attractive candidate for highly sensitive mechanical sensing applications such as in pressure sensors. Furthermore, their surface possesses high electron mobility which contributes to the modulation of surface conductivity and has been utilised in electrochemical and optical (e.g. UV light) sensing [173].

Researchers have found that, among all the morphologies of ZnO nanostructures, devices based on ZnO nanorods, porous nanostructures, and those with high surface area exhibit excellent sensing performance, rapid responsiveness, higher sensitivity and better optical properties [174-176]. These ZnO nanostructures have been grown on various substrates such as silicon [177], glass [178], sapphire [179], and PET polymer [180] using several synthesis techniques.

The most prevalent methods of growing vertically aligned and high aspect ratio ZnO nanorods are the CVD method [181], vapour liquid-solid (VLS) technique [182], electrochemical deposition [183], sol-gel [184], PLD method [185], chemical bath deposition [186] and the hydrothermal synthesis process [187]. A thin film of ZnO seed layer must be deposited on all the substrates before growing the nanorods, and this layer provides nucleation sites for the subsequent growth of the nanorods [188].

The hydrothermal process is the most popular method used for the anisotropic crystal synthesis of ZnO nanorods in aqueous solution. Andres-Verges et al. exploited this technique to grow ZnO nanostructures for the first time in 1990 [189]. A decade later, Vayssieres et al. reported the use of this method to control the fabrication of ZnO nanowires on glass and silicon substrates through the thermal decomposition of methenamine and zinc nitrate ($Zn(NO_3)_2$ compounds [190]. This method is simple, does not need a complicated set-up, and is cost-effective, environmentally friendly and surface independent. Moreover, various

properties and morphologies of ZnO nanorods can easily be synthesized by tuning growth parameters such as seed layer, the concentration of precursor solution, growth time, and the temperature and pH of the solution [191-194]. On the other hand, as a solution-based method, the hydrothermal process may yield poor quality ZnO crystals with significant defects in nanorods [195, 196].

The chemical equations 2.23 and 2.24 summarize the reaction that takes place in an aqueous solution using ammonia to control the pH of the solution and with zinc nitrate as the precursor for zinc ions. Methenamine, which is also called hexamethylenetetramine (HMTA) ($C_6H_{12}N_4$) is a water-soluble compound that is thermally degraded and releases hydroxyl groups which react with zinc ions to form ZnO as in equation 2.25 [197, 198].

$$C_6H_{12}N_4 + 6H_2O \leftrightarrow 6HCHO + 4NH_3, \quad (2.23)$$

$$NH_3 + H_2O \leftrightarrow NH_4^+ + OH^-, \quad (2.24)$$

$$2OH^- + Zn^{2+} \rightarrow ZnO(s) + H_2O, \quad (2.25)$$

2.4 Acoustic wave devices

Acoustic waves are mechanical waves that propagate through a material with a velocity which depends on its elastic properties. There are several types of acoustic wave, such as the bulk acoustic wave that propagates through bulk material, the surface acoustic wave or Rayleigh wave that travels along the surface of the piezoelectric material, the Stoneley wave which propagates in the interface of two elastic materials and Lamb waves that occur in a plate with a thickness comparable to or less than their wavelengths [199].

2.4.1 Bulk acoustic wave

The earliest and most well-known BAW device is the quartz crystal microbalance (QCM) that utilises the thickness-shear mode (TSM) for its operation. The QCM device has been

extensively exploited in various liquid-based sensing applications, particularly in the fields of biomedicine and biochemistry [200]. The QCM device has a resonator configuration that is composed of a thin plate of AT-cut quartz sandwiched between two electrodes. The sensing principle of the QCM was explained by Sauerbrey in 1959 [108], and it is based on the gravimetric method of mass change. When a molecule is adsorbed or attached to the surface of the QCM, it causes a change in resonant frequency due to the increase in the overall weight of the QCM. The change in frequency can be estimated using the Sauerbrey equation [201, 202]:

$$\Delta f = -\frac{2f_0^2}{A\sqrt{u_q \rho_q}}\,\Delta m \tag{2.26}$$

where Δf, f_0, A, u_q, ρ_q and Δm are the change in resonant frequency (Hz), the resonant frequency (Hz), the active area of the crystal, the shear modulus of the AT-cut quartz ($g.cm^{-1}.s^{-2}$), the density of the quartz (g/cm^3), and the mass change (g) respectively. However, QCM resonators possess a lower sensitivity to mass loading because of their low operating frequency at 5–30 MHz. Moreover, there is a limitation to the enhancement of sensitivity when the resonant frequency increases since the devices become very thin and fragile. Moreover, the thick and bulk structure of the QCM makes it difficult to be integrated with electronics and microfluidics platforms where scaling and miniaturisation capabilities are required [203-205].

BAW devices possess another type of operating mode called shear horizontal acoustic wave plate mode (SH-APM) where the electrodes are replaced by IDTs deposited on one side of the crystal surface. The SH-APM sensors are relatively thinner where the acoustic energy is confined between the two surfaces of the plate. Therefore, the IDT site must be isolated from contact with the liquids and the sensing occur on the other side of the crystal. SH-APM sensors possess higher resonant frequency than that of QCM, and hence they are more

sensitive to mass loading. However, these devices are expensive and hard to manufacture, and IDTs suffer from corrosion due to their immersion in liquids [206, 207].

Recently, film bulk acoustic wave resonators have attracted substantial attention for sensing and biosensing applications due to their small size, high sensitivity, good linearity and reliability, and low cost [204]. They have also been broadly investigated as an alternative candidate for the high-frequency applications at more than GHz level rather than surface acoustic wave devices. The structure of the FBAR consists of a piezoelectric thin film such as ZnO, AlN or PZT deposited between a top and bottom electrode where the film is separated from the substrate by an isolation layer such as SiO_2 as shown in Figure 2.8.

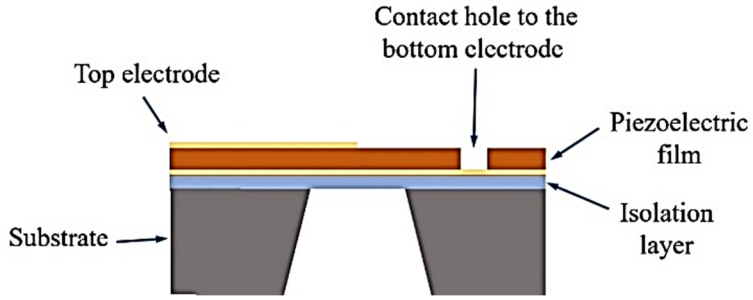

Figure 2.8 Cross-sectional schematic of main components of FBAR structure

Thus, FBAR sensors can be easily integrated with CMOS devices and for microfluidics applications. However, the type of the excited acoustic wave mode (longitudinal or shear thickness) is determined by the structural and the physical properties of the piezoelectric thin film [208-211].

2.4.2 Surface acoustic wave

The propagation of the SAW along the free surface of a semi-infinite elastic solid was first explained by Lord Rayleigh in 1885, and later the SAW was frequently referred to as the Rayleigh wave or mode [212]. This elastic wave travels along the surface of a piezoelectric substrate where most of its acoustic energy is confined and decaying exponentially with

depth into the material until it becomes negligible after penetration by more than few wavelengths [213]. The Rayleigh mode consists of a combination of longitudinal and vertical shear (transverse) components that couple at the surface of the piezoelectric material. It results in a retrograde elliptical and trajectory motion of the particles normal to the surface plane and along the direction of propagation, as shown in Figure 2.9 [214].

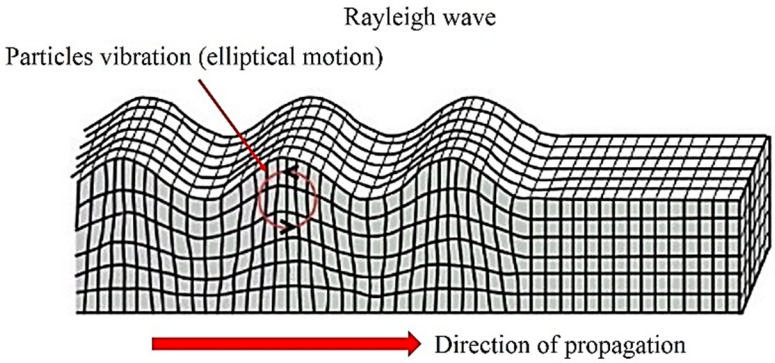

Figure 2.9 The direction of propagation and particles vibration of the Rayleigh wave [214]

The practical utilisation of SAW devices was launched with the development of interdigital transducers by White and Voltmer in 1965 [215]. Subsequently, SAW devices have been exploited in a wide range of electronics and sensing applications such as telecommunications, automotive and biosensing [216]. IDTs possess an inter-crossing design that consists of periodic fingers (electrodes) of two comb-shaped arrays, as illustrated in Figure 2.10. They are composed of a conductive material such as gold or aluminium that is deposited on the surface of the piezoelectric substrate [217].

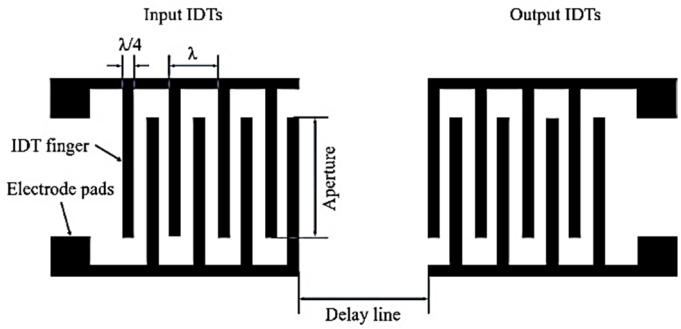

Figure 2.10 The structure and configuration of metal IDTs (e.g. Al or Au) in a delay line SAW device

The function of the input IDTs is to convert the electrical signal into SAWs, and then these SAWs propagate along the surface of the piezoelectric material through the delay line and are converted back into an electrical signal by the output IDTs [218, 219]. The most popular materials for IDTs are aluminium (Al) and gold (Au) due to their high Q factors and low resistivity [220].

However, other materials have also been exploited to fabricate IDTs; for example, tungsten (W), nickel (Ni), platinum (Pt), tantalum (Ta) [221-223]. Besides, materials like chromium (Cr) and titanium (Ti) have been deposited on the substrate to improve the adhesion between the piezoelectric material and the IDTs [224, 225]. In addition to the delay line configuration, SAW devices can also be constructed in a one-port resonator design, as shown in Figure 2.11 [226].

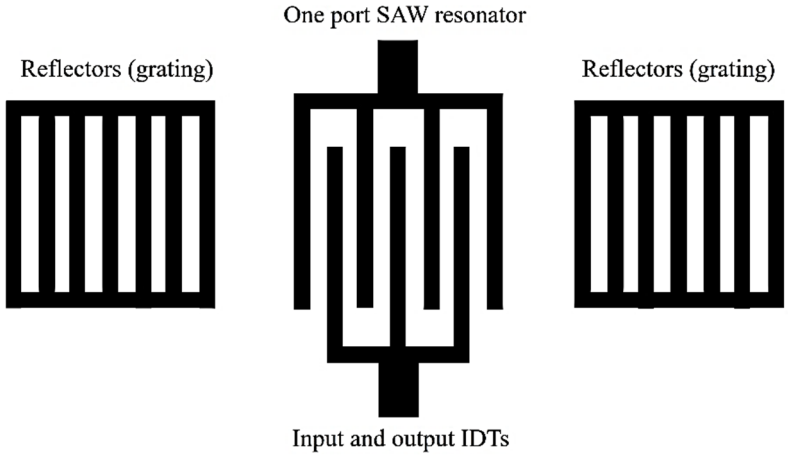

Figure 2.11 The structure and configuration of the IDTs in a One-port SAW resonator

The configuration of the SAW device and the IDT design are selected according to the application involved; for instance, biochemical SAW sensors usually possess a delay line structure where the region between the two IDTs in a pair is coated with a sensitive layer [227]. The resonant or central frequency is the main parameter of the SAW device, and it is determined by the velocity of the acoustic wave (v_0) in the piezoelectric substrate and the design wavelength (λ_0) of the SAW device. The following equations 2.27- 2.29 are used to

calculate the central frequency (f_0), the finger and spacing widths, and the number of IDT fingers (N) respectively when designing the SAW device [228-230]:

$$f_0 = \frac{v_0}{\lambda_0} \tag{2.27}$$

$$Finger\ width = spacing = \frac{\lambda_0}{4} \tag{2.28}$$

$$N = \frac{2f_0}{band\ width} \tag{2.29}$$

Furthermore, the design shown in Figure 2.12 is called bidirectional since the IDTs are symmetrical, and the exciting SAWs are propagated in both forward and backwards directions. This structure results in the loss of acoustic wave energy, increase insertion loss and side lobes. Therefore, unidirectional IDTs have been developed by adding internal reflectors to excite the SAW towards one direction and thus overcoming these issues [231]. Figure 2.12 shows an example of unidirectional IDT called a single-phase unidirectional transducer (SPUDT) that was proposed for the first time in 1976 by Hanma and Hunsinger which has been frequently used in sensing applications [232, 233].

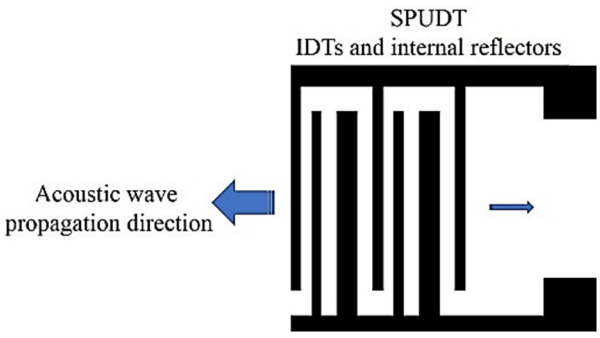

Figure 2.12 The structure and configuration of the SPUDT design

In this project, the bidirectional and the SPUDT configurations were used to design the IDTs of the SAW devices with varied wavelengths for sensing applications. However, there are several other types of IDT designs for acoustic wave devices that have been discussed in detail in the references [13] and [234].

Thus, the basic layout of the SAW sensor consists of the IDTs deposited on the surface of the piezoelectric material either in one-port or delay line configuration. However, several types of SAW modes can be generated according to the crystal orientation of the piezoelectric material or the crystal cut angle. For example, a Rayleigh wave is generated in 128^{o} Y-X $LiNbO_3$ and Y-Z $LiTaO_3$ materials, whereas a shear horizontal SH- SAW can be excited in 36^{o} Y-X cut $LiTaO_3$ and 64^{o} Y-X cut $LiNbO_3$ [235].

Unlike the Rayleigh wave, the SH-SAW propagates parallel to the surface plane of the piezoelectric substrate and normal to the propagation direction. Thus, SH-SAW sensors have been employed in liquid sensing due to the absence of the longitudinal component of the acoustic wave and their higher operating frequency compared to the BAW [236, 237]. Likewise, Love wave propagates in a similar way to the SH-SAW, but it is confined to a guided layer deposited on the top of the device, and it has different properties than the substrate such as slower shear wave velocity [238]. Furthermore, the SH-SAW can be excited in ZnO thin film devices such as those made with ZnO/SiO_2/Si by growing the ZnO film in the (110) or (100) orientations where the c-axis is parallel to the substrate surface [239].

On the other hand, the excited acoustic wave modes, and their properties in c-axis oriented ZnO thin film devices can be determined according to the designed wavelength (λ_0) and the total device thickness (H). The Rayleigh mode can be excited in the device of a wavelength is comparable to or smaller than its thickness, and Lamb wave modes are generated when the thickness of the device is much smaller than their wavelength [112]. However, coupled modes of longitudinal and shear waves have also been realised when the ZnO thin film is deposited at an inclined angle or in a c-axis zig-zag structure [240-242].

2.4.3 Lamb wave

The first publication that described the propagation of a Lamb wave was reported by H. Lamb in 1917, and it was later given his name [243]. Extensive experimental investigations were subsequently conducted by Worlton in 1961 to understand the characteristics of the Lamb wave [244].

Similar to the Rayleigh wave, the Lamb wave results from a superposition of both longitudinal and transverse components and its characteristics are constrained by the elastic properties of the substrate boundaries. Furthermore, it propagates across a thin plate with a thickness less than the device wavelength or penetration depth. Hence, it can be described as two Rayleigh waves travelling along each side of the plate which propagate freely when the plate is thicker, or when the wavelength becomes equal to or smaller than the plate thickness [245]. However, the Lamb wave possesses both symmetric (S) and antisymmetric (A) modes, as shown in Figure 2.13.

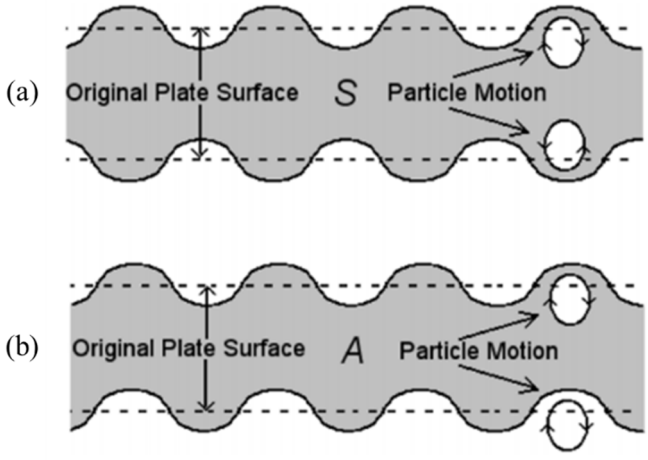

Figure 2.13 The modes of vibrating ad particle displacement of Lamb wave (a) symmetric (S), (b) antisymmetric modes (A) [246]

The symmetry of these modes is related to the direction of displacement and the motion of the particle with respect to the median of the plate. The displacement of particles in the S mode is in-plane (compressional) while it is out-of-plane (flexural) for the A mode.

Mathematical descriptions of the S and A modes are given by equations 2.30 and 2.31 respectively [247]:

$$\frac{\tanh(sd)}{\tanh(qd)} = \frac{4k^2 qs}{(k^2 + s^2)^2} \tag{2.30}$$

$$\frac{\tanh(sd)}{\tanh(qd)} = \frac{(k^2 + s^2)^2}{4k^2 qs} \tag{2.31}$$

where d is the half-thickness of the plate and s and q are given by equations 2.32 and 2.33 respectively:

$$\mathrm{s} = \sqrt{k^2 - k_T^2} \tag{2.32}$$

$$\mathrm{q} = \sqrt{k^2 - k_L^2} \tag{2.33}$$

where k is the wavenumber, and k_T and k_L are the transverse and longitudinal wavenumbers of the solid material. Thus, an infinite number of simultaneous Lamb wave modes are excited and are superposed on each other across the plate surfaces to become definite guided waves. The velocity of the Lamb wave is highly dispersive since it depends on both the wave frequency and the thickness of the plate. Therefore, the relationship between the velocity of Lamb wave modes, their frequency, and thickness is dispersive one [248]. The phase velocities of the zero-order antisymmetric (A0) and symmetric (S0) modes can be estimated using the following equations [249].

$$V_{A0} = \frac{2\pi h}{\lambda} \sqrt{\frac{Y}{12(1 - v^2)\rho}} \frac{1}{\sqrt{\frac{\pi^2 h^2}{3\lambda^2} + 1}} \tag{2.34}$$

$$V_{S0} = \sqrt{\frac{Y}{(1 - v^2)\rho}} \tag{2.35}$$

where h, λ, Y, v, ρ are the plate thickness, the wavelength of the Lamb wave, Young's modulus, Poisson's ratio, and the density of the piezoelectric material respectively. Thus, the phase velocity of the A0 mode exhibits a direct relationship with the thickness of the plate at low-frequency levels, and it is frequently described as a flexural plate wave. In

contrast, the plate thickness has no effect on the wave velocity of the S0 mode in a very thin plate. Hence, the S0 mode becomes dispersionless and possesses a higher velocity than a SAW propagating in the same material. Furthermore, as the thickness of the plate approaches zero asymptotically, the S0 mode changes to a longitudinal wave, and the A0 mode continues to decrease to zero. On the other hand, for a high-frequency regime, the wave velocity of the Lamb wave modes moves toward the velocity of the Rayleigh wave until they eventually become Rayleigh wave or higher-order modes. Likewise, this also occurs when the plate thickness is increased compared to the device wavelength [13, 249, 250].

Lamb wave sensors exploit the different characteristics of symmetric and antisymmetric modes. For example, the A0 mode is dispersive, and its phase velocity is strongly dependent on plate thickness which permits operation at various resonant frequencies. Thus, with very thin plates, the phase velocity of the A0 mode (FPW) becomes lower than the velocity of the acoustic wave in the liquid, and the plate acts as a guided layer. This results in the concentration of the acoustic energy at the surface of the plate, and it is prevented from dissipating to the liquid medium. Therefore, FPW-based sensors have been employed in several chemical and biomedical sensing applications, and they exhibit a high sensitivity compared to other gravimetric acoustic wave devices [251-253]. On the other hand, the S0 mode propagates at a phase velocity higher than that of A0 mode with a strong longitudinal component. Nevertheless, the leakage of the acoustic energy in a liquid environment is small because the in-plane motion of the particles retains the S0 mode in the plate and displacement occurs parallel to the surface [254].

The conventional structure of Lamb wave sensors consists of a thin membrane of piezoelectric material such as ZnO, AlN and GaN deposited on a substrate (e.g. silicon), and a pair of IDTs are used to excite the Lamb waves as shown in Figure 2.14 [255-257].

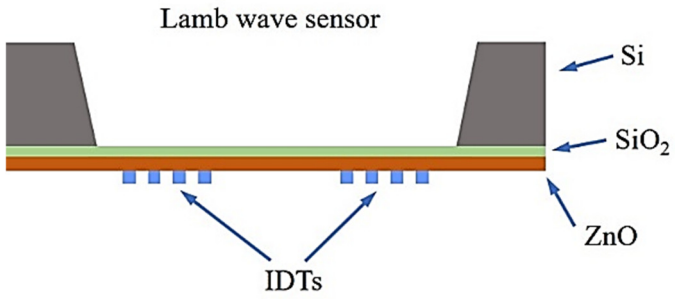

Figure 2.14 Cross-sectional schematic of main components of Lamb wave-based sensor

These FPW-based devices have been primarily used as biosensors; for example, in the detection of proteins, immunoglobulins, volatile organic compounds, and carcinoembryonic antigen (CEA) and bacterial growth monitoring [253, 258-262]. Besides, the higher-order modes of FPW devices have been used in viscosity and density sensing applications [263]. However, FPW sensors are subject to several limitations and drawbacks, such as the thin membrane which makes the device more fragile, the occurring of coupling loss due to the use of the IDTs to excite the Lamb waves, and temperature sensitivity [264]. On the other hand, as the plate thickness is increased, the phase velocity of the A0 mode increases and this results in the partial leakage of acoustic energy into the liquid. Therefore, the FPW has been investigated for microfluidics applications such as pumping and mixing [265, 266].

2.5 Flexible SAW sensors

Flexible microsystems have attracted remarkable attention due to the significant advantages of bendable electronics and MEMS devices compared to rigid ones, owing to their lightweight, low cost, and capability to be adapted for various irregular surfaces and their easy integration with other systems. Recently, a broad range of flexible applications has been developed, such as wearable sensors, displays, eyeball cameras, memories, transistors, and microfluidic platforms. Therefore, flexible SAW devices have been intensively studied for the great potential to be employed in sensing applications [267, 268].

Thin-film piezoelectric materials such as ZnO and AlN have an advantage in that they can be deposited on a flexible substrate such as polymers, plastics, and metal foils in the fabrication of flexible SAW-based sensors. For example, ZnO thin film has been deposited on polyethylene terephthalate (PET) and Kapton polyimide (PI) polymer substrates for temperature and humidity sensing, energy harvesting, strain sensing, and microfluidics applications [267, 269-273]. Meanwhile, ZnO thin film-based strain sensors have been fabricated on ultra-thin flexible glass [274, 275].

However, polymers exhibit several drawbacks as a flexible substrate for SAW-based sensors, such as the significant acoustic wave attenuation, energy dissipation, lattice and thermal mismatching and poor adhesion with thin films. Therefore, flexible SAW devices based on ZnO/aluminium foil have been investigated as a potential candidate to overcome these limitations. Aluminium foil possesses excellent flexibility, bendability and deformability, with the capability to be fixed with any kind of surface (flat, curved, irregular) or shape. Besides, it is widely available commercially at low cost, is easy to use, and it can withstand the high-temperature annealing process better than polymer substrates, and it is suitable for mass production [13, 14].

Liu et al. fabricated the first ZnO/Al foil-based SAW devices with various wavelengths using commercial aluminium foil with 50 μm thickness and ZnO thin film five μm thick. Flexibility of the devices was demonstrated by substrate bending characterisation method where a device was bent to different angles with different strains. The results showed that a weak S21 signal could be detected after bending the device to a large strain of 1.375% a bending angle of 90^{o} and it recovered its complete amplitude when returned to a flat position. Moreover, the fatigue and cycling performance of the devices were evaluated by a standard bending test using a mechanical bending vise where steel tubes with different diameters were placed under the device at the bending centre. The device was then taken out and straightened

again. The results showed that the amplitude of the S21 signal decreased by 0.9% - 23% after 2000 bending cycles with a fixed strain of 0.6% indicating good fatigue resistance [15]. Another study was then conducted to investigate the effect of annealing on the properties of ZnO/Al foil-based SAW devices. It is found that the devices could withstand the annealing temperatures up to 500 ^{o}C, where the optimal value for the best physical properties and performance was 350 ^{o}C [276]. This type of ZnO/Al foil device has been utilised to develop a flexible ultrasonic transducer with an operating frequency between 15–30 MHz. The performance of this transducer was demonstrated for non-destructive testing (NDT) in both flat and curved positions and it showed a satisfactory sensitivity [277]. However, the SAW devices based on ZnO/Al foil have not yet been utilised in sensing or biosensing applications, but the door is open for further investigations.

2.5.1 SAW-based temperature sensing

Recently, numerous devices have been investigated for temperature sensing using various physical mechanisms. These include resistor temperature detectors, field-effect transistors, thermocouples, thermistors, optical sensors, infrared sensors and mercury thermometers [278]. The most commonly used sensors for temperature monitoring in biomedical applications are thermocouples and thermistors as they are capable to detect a change of temperature as low as 0.5 ^{o}C [279]. Thermocouples have a wide dynamic range of -200 to +1200 ^{o}C with a sensitivity of 41 μV/ ^{o}C, but they suffer from a non-linear low output signal and low signal to noise ratio [280].

However, the demand for flexible temperature sensors in the environmental, industrial, and medical sectors has substantially increased for reasons of safety, better functionality, real-time monitoring, and operation in harsh and hazardous conditions. For example, flexible temperature sensors have been used in medical applications for the long-term monitoring of patient temperature. Different types and technologies have been employed for flexible

temperature sensing in this field. Most of these sensors are polymer-based, and they exploit changes in resistance as a function of temperature [281, 282]. Piezoresistive sensors based on PVDF polymer have been popular candidates for flexible temperature sensing utilising the piezoelectric effect to generate electricity as a response to variation in temperature [283, 284].

SAW-based temperature sensors have a significant advantage over other technologies because of their capability to operate wirelessly and thus remotely and passively or battery-free. Besides, they exhibit good sensitivity, reliability, robustness, low cost and small size, and are easily integrated with other sensors [285, 286].

The dependence of acoustic wave phase velocity on temperature is a well-known phenomenon in piezoelectric and pyroelectric materials, including ZnO thin films [287]. The most important parameter that determines the functionality, thermal stability and performance of a SAW device is the temperature coefficient of frequency (TCF). It is defined as the relative or rate of change in resonant frequency (f_0) with temperature (T), and it is given by the following equation [288] :

$$TCF = \frac{1}{f_0}\frac{df}{dT}\ (ppm/K) \tag{2.36}$$

However, the temperature has a direct influence on the device material's elastic stiffness constants (C_{ij}), density (ρ), and temperature coefficient of expansion TEC (α). Therefore, equation 2.36 can be rewritten concerning the phase velocity (v_p) and TEC of each material in the SAW device with a particular thickness (H) as follows [289]:

$$TCF = \frac{1}{v_p}\frac{dv_p}{dT} - \frac{1}{H}\frac{dH}{dH} = \frac{1}{v_p}\frac{dv_p}{dT} - \alpha \tag{2.37}$$

Thus, a high TCF value is desirable for temperature sensing, and this can be achieved by either increasing the resonant frequency to increase the accuracy and resolution, and this requires complicated and expensive electronic circuitry or selecting a substrate with a high TEC such as aluminium, where $\alpha = 23.6$ ppm/K.

On the other hand, reducing the TCF value of the SAW sensor or compensating for the temperature during chemical, biomedical, environmental, and physical sensing applications is important to achieve thermal stability. Therefore, a layer of silicon dioxide (SiO_2) which has a positive TCF is usually added to the structure of SAW devices to counter the effect of the negative TCF values of most piezoelectric materials [290-292].

An early SAW-based temperature sensor was developed in 1969 by Hewlett-Packard. It was made of a bulk wave Y-cut quartz resonator that utilised the TSM mode at a resonant frequency of 28 MHz. The sensor exhibited a sensitivity of 5 ppm/^{o}C over a temperature range of -80 to +250 ^{o}C. In 1976, Reeder and Cullen developed a SAW pressure and temperature sensor by fabricating IDTs on a miniature diaphragm created in Y-cut crystalline quartz. Sensing performance was investigated in the temperature range from -50 to +100 ^{o}C, and a sensitivity of 130 ppm/^{o}C was found [293]. Borrero et al. reported the development of a SAW device for temperature, pressure, and impedance sensing. The sensor had a one-port resonator structure and was fabricated on a 128^{o} YX $LiNbO_3$ rigid substrate. The performance results showed a linear relationship between the frequency shift and temperature change in the range of 50 – 200 ^{o}C with a sensitivity of 87.81 ppm/^{o}C [294]. Recently, various SAW-based sensors have also been exploited for high temperature sensing up to 1000 ^{o}C, and some of them can operate wirelessly such as langasite (LGS) [295], AlN/GaN/sapphire [296], AlN/Si [297], and AlN/quartz [298].

The previous examples of SAW sensors were fabricated on rigid substrates, and they lack flexibility. Jin et al. reported the development of a flexible SAW resonator by depositing a ZnO thin film of varied thickness from 1.7-4.0 μm on a Kapton polyimide polymer 100 μm thick. The Rayleigh and Lamb wave modes were excited at different resonant frequencies according to the designed wavelengths of each device, and they were used to perform temperature sensing. The results showed that the TCFs of the Rayleigh and Lamb modes were -442 and -245 ppm/k, respectively, and they were constant for the various device thicknesses and wavelengths. It was suggested that these values are higher than those obtained for the Rayleigh mode of ZnO/Si (~67 ppm/k) and $LiNbO_3$ substrate (~ 70-80 ppm/k) [269]. Another SAW-based temperature sensor was developed by depositing a ZnO thin film of 3.5 μm thickness on a Kapton polyimide substrate. The wavelength of the device was 12 μm, and the Rayleigh wave was excited at 132 MHz and Lamb wave at 427 MHz. The TCF values were -423 ppm/K and -258 ppm/K corresponding to the Rayleigh and Lamb modes, respectively [270]. These findings are comparable to those obtained in reference [269].

Table 2.3 shows a summary of the sensitivity values of the SAW based temperature sensors.

Table 2.3 Summary of the sensitivity values of the SAW based temperature sensors

Sensor structure	Mode of operation	Sensitivity ppm/K	comments
Y-cut quartz	TSM	5	None-flexible
Y-cut crystalline quartz	TSM	130	None-flexible
128° YX $LiNbO_3$	SAW	87.81	None-flexible
ZnO/Si	Rayleigh wave	67	None-flexible
ZnO/$LiNbO_3$	Rayleigh wave	70 - 80	None-flexible
ZnO/Polyimide	Rayleigh wave Lamb wave	423 258	Flexible
ZnO/Polyimide	Rayleigh wave Lamb wave	442 245	Flexible

2.5.2 SAW-based ultraviolet (UV) sensing

Ultraviolet (UV) light has been used in numerous critical applications such as defence warning systems in the military, medicine and healthcare, astronomy, communications, and a variety of environmental implementations such as water purification. Therefore, the detection and monitoring of UV light have received considerable attention during the development of highly sensitive and reliable sensors. UV light spectra have wavelengths that range from 100 to 400 nm, and a photon energy range of 3.1-12.4 eV. The UV light is classified into four bands according to wavelength, namely UV-A (315-400 nm), UV-B (285-315 nm), UV-C (200-280 nm) which is absorbed by the ozone layer of the earth, and V-UV or far UV (10-200 nm). Hence, there has been a particular focus on the UVA and UVB bands (3.1-4.43 eV) since they can be transmitted through the air and could cause direct harm to human health [299, 300].

The most fundamental UV light detector is thermopile which converts thermal energy into electrical energy, and it provides the basis for calibrating all other types of UV light sensors. Thermopile is stated to be linear in the range from 1 $\mu W/cm^2$ to 100 mW/cm^2. However, the main drawback of thermopile is fragility, but the most recent devices have become more robust and resistant to both mechanical and temperature shock [301].

The other category of UV light detectors is based on photon interaction which has been frequently used in various applications. There are two main kinds of such detectors, vacuum detectors (photomultiplier tubes) and solid-state detectors which is based on semiconductor materials such as ZnO, TiO_2, and SnO_2. The photoconductivity and photovoltaic detection are the two mechanisms of UV light sensing using the semiconductor devices such as Schottky photodiode, phototransistors, and metal-semiconductor-metal (MSM) photoresistors [302, 303]. The photocurrent generated from Schottky detector under UV illumination was about 120 nA without applying any external bias and it has a fast switching

time of less than 30 ms [304]. However, Schottky UV detectors have several advantages such as high responsivity, high quantum efficiency, low dark current, short response time and possible zero-bias operations [305].

SAW-based UV sensors have received significant attention due to their distinctive features such as high sensitivity, reliability, reproducibility, rapid response, and low cost. Furthermore, ZnO thin film is considered to be a popular material for UV photodetection due to its excellent optical and piezoelectrical properties. It has a bandgap energy of 3.37 eV and a large exciton binding energy of 60 meV at room temperature. Therefore, it interacts with UV light whose photon energy is higher than that of its bandgap by creating electron-hole pairs. Hence, ZnO thin film-based SAW devices have dominated the development of UV sensors rather than other piezoelectric materials, and they exhibit high sensitivity to UV light [306, 307].

The mechanism of ZnO thin film devices for UV detection is based on the chemisorption of oxygen molecules at the surface of the SAW device. In the absence of UV irradiation, the surface of the ZnO thin film has free electrons due to intrinsic defects of the film. Therefore, oxygen molecules from the atmosphere become adsorbed onto the surface and confine these free electrons to form negatively charged ions as per equation 2.38, and this creates a less conductive depletion region [308, 309].

$$O_{2\,(gas)} + 2\,electron^{-} \rightarrow O^{2-}_{2\,(adsorbed)} \qquad (2.38)$$

Illumination of the sensor surface with UV light results in the generation of electron-hole pairs where the holes recombine with the electrons adsorbed by oxygen ions. This process releases the oxygen molecules back to the atmosphere as per equation 2.39, which increases the surface sheet conductivity (σ_s) of the sensor along with a decrease in the depletion area [308, 309].

$$2Hole^{+} + O_{2\,(adsorbed)}^{2-} \rightarrow O_{2(gas)} \tag{2.39}$$

Thus, UV light illumination on the ZnO thin film SAW sensor causes an acoustic-electric response where the change in the surface sheet conductivity results in a change in phase velocity and the amplitude of the acoustic wave. These effects are expressed as in the following equations [310]:

$$\frac{\Delta v}{v_0} = -\frac{k^2}{2}\frac{\sigma_s^2}{\sigma_s^2 + v_0^2 C_s^2} \tag{2.40}$$

$$\Delta\Gamma = \frac{k^2}{2}\frac{v_0 C_s \sigma_s}{\sigma_s^2 + v_0^2 C_s^2} \tag{2.41}$$

where Δv is the change of acoustic wave velocity, v_0 is the unperturbed velocity at the free surface, k^2 is the electromechanical coupling coefficient, σ_s is the surface sheet conductivity, C_s is the capacitance per unit length of the surface, and $\Delta\Gamma$ is the change of signal amplitude (the insertion loss). However, equation 2.40 can be rewritten with respect to the change in resonant frequency ($v = \lambda f$) as follows:

$$\frac{\Delta f}{f_0} = -\frac{k^2}{2}\frac{\sigma_s^2}{\sigma_s^2 + v_0^2 C_s^2} \tag{2.42}$$

This indicates that the increase in the surface sheet conductivity results in a downshift of the resonant frequency and an increase in insertion loss.

However, several SAW-based UV sensors have been developed by depositing the ZnO thin film on various rigid substrates such as sapphire, $LiNbO_3$, quartz, $LiTaO_3$, and silicon, as shown in Table 2.3. Most ZnO thin film-based SAW UV sensors operate in Rayleigh wave mode due to the strong longitudinal component that confines the acoustic energy at the surface of the device, resulting in high sensitivity to electro-mechanical changes occurring at the surface [306]. Among all the Rayleigh wave-operated devices shown in Table 2.3, the highest UV sensitivity has been obtained for the ZnO/$LiNbO_3$ structure developed by

Sharma and Sreenivas [311]. Besides, the use of ZnO nanorods leads to a considerable enhancement in sensitivity to UV light.

Table 2.4 Summay of SAW UV sensors based on ZnO thin film deposited on differet rigid substrates

Substrate	Mode	Resonant Frequency (MHz)	UV intensity (mW cm^{-2})	Frequency Shift (kHz)	Sensitivity ppm (mW $cm^{-2})^{-1}$	comments	Reference
Silicon	Rayleigh	63.2	0.6	1.4	36.92	-	[312]
		59.75	0.6	8.3	231.52	With NRs	
	Rayleigh	180.71	0.6	12	110.67	-	
		174.5	0.6	27.4	261.7	With NRs	
	Sezawa	271.83	0.6	25	153.28	-	
Quartz	Rayleigh	41.2	19	45	57.49	-	[313]
$LiNbO_3$	Rayleigh	37	40	170	114.87	-	[311]
Sapphire	Sezawa	711.3	2.32	1360	824	-	[314]
Silicon	Sezawa	842.8	0.551	1017	2190	-	[315]
Quartz	Rayleigh	200.08	0.048	0.3	31.3	-	[316]
		200.02	0.048	0.9	93.7	With NRs	

The sensitivity is significantly increased when using the Sezawa wave as an operating mode because it has a higher phase velocity compared to the Rayleigh wave. Moreover, the sensitivity increases with a resonant frequency, and this indicates that the use of higher wave modes would result in better sensing performance [306, 317].

Wang et al. have reported on the performance of a Rayleigh mode UV sensor based on annealed ZnO thin film deposited on a glass substrate. The device had the merit of transparency and exhibited a sensitivity of 43 ppm (mW $cm^{-2})^{-1}$ [318].

Ciplys et al. developed a GaN/sapphire-based SAW oscillator with an operating frequency of 200 MHz for UV light detection in the range of 330-600 nm. An evaluation showed that

the maximum shift was obtained at UV light with a wavelength of 365 nm, and this dropped to zero above 400 nm [319].

However, the SAW-based UV sensors shown in Table 2.3 were fabricated on rigid substrates. He et al. have reported the development of flexible SAW-based UV light detectors made by depositing a ZnO thin film on a polyimide polymer substrate. The Rayleigh and Lamb wave modes were excited at 75.7 MHz and 254.3 MHz, respectively. The sensor exhibited values of the sensitivity of 111.3 and 55.8 ppm $(mW\ cm^{-2})^{-1}$ corresponding to Rayleigh and Lamb modes, respectively [320].

2.5.3 SAW-based humidity sensing

Relative humidity (RH) has been used in various applications more often than absolute humidity (AH) because the sensing process is then easier, more cost-effective, and simpler. The relative humidity is defined as the ratio of the partial pressure of water vapour to the saturation vapour pressure at a specific temperature. In other words, RH sensing measures the ratio of the amount of vapour in the atmosphere compared to the maximum amount of vapour represents saturation in the atmosphere. Humidity sensing and monitoring have been received great interest due to its importance in agriculture, and the food industry, process control, scientific research laboratories, and environmental and biomedical applications. Humidity sensors can be classified according to the different transduction mechanisms involved as optical, gravimetric, capacitive, resistive, piezoresistive, or magnetoelastic [321-323].

The mechanism principle of RH sensing relies on the water vapour adsorption (chemisorption or physisorption) at the surface of the sensor which results in changing in its resistance, capacitance, or conductance. However, capacitance RH sensors have been frequently used in a wide range of commercial, industrial, and weather telemetry applications. The basic structure of a capacitive RH sensor is composed of a dielectric

polymer film sandwiched between two metal electrodes. Thus, it responds to change in RH by varying the permittivity of the dielectric material which is proportional to the ambient vapour change. It has an excellent linear response in the range of 10% to 90% RH with a resolution of 1% [322] .

Conventional gravimetric-based devices used for humidity sensing include QCM, FBAR, SAW, and microcantilever-based resonators [324]. SAW devices have been widely employed as humidity sensors in various applications due to their high sensitivity to mass loading, [325]. However, changes in the acoustic velocity of the thin film-based SAW humidity sensor occurs for various reasons such as the effect of mass loading, a change in the surface sheet conductivity of the thin film, and changes in elasticity [326]. The delay line area of the SAW-based humidity sensor is usually coated with a thin membrane of moisture-sensitive material such as polymers, ZnO nanostructures, and graphene oxide to increase sensor sensitivity [324].

Nomura et al. described a humidity sensor based on a polymer/$LiNbO_3$ SAW device. A hygroscopic conductive polymer was applied to the surface of the delay line of the 128º YX $LiNbO_3$, which acts as a layer sensitive to humidity. The sensor exhibited a linear response in the range of 40-80%RH [327]. Caliendo et al. developed a SAW-based humidity sensor by coating a quartz substrate with a sensitive membrane of polyphenylacetylene (PPA) polymer. Both Rayleigh and surface transverse wave modes were excited and used for humidity sensing. The results showed that the sensor possessed good sensitivity and reproducibility over a humidity range of 0-80%RH at various temperatures from 20 to 50 ºC [328]. Li et al. reported on the development of a SAW-based humidity sensor made by electro-spraying a sensitive film of silicon-containing polyelectrolyte polymer to the delay line of a two-port ST-X cut quartz resonator operating at 433 MHz. The sensor exhibited a sensitivity of -0.4 kHz/%RH over a humidity range of 11-97 %RH [329].

ZnO thin film and nanostructures have also been exploited as a sensitive membrane for SAW-based humidity sensors. Guo et al. fabricated a Love mode humidity sensor by depositing ZnO thin film of various thicknesses on a 42^{o} YX $LiTaO_3$. The device with a thickness of 250 nm exhibited the best humidity sensing performance, with a frequency shift of 65 kHz at 90%RH. Therefore, this device was selected to grow ZnO nanorods, and sensitivity was almost doubled [330]. Chung and Hong designed a SAW humidity sensor based on ZnO/AlN/Si with an operating frequency of ~125.8 MHz. The maximum frequency shift was 160 kHz, with a change in RH from 10 to 90% RH [331]. A humidity sensor with ZnO nanorods/AlN/Si-based SAW was proposed by Hong et al. It was suggested that the perturbation in the SAW due to the change in humidity resulting from mass loading and changes in the surface sheet conductivity of the ZnO nanorods. The frequency shift was approximately 750 kHz over an RH range of 10- 90%, which is significantly higher than that of ZnO thin films (~110 kHz) [332].

SAW humidity sensors based on a graphene oxide functional layer have recently been investigated due to their considerable advantages such as fast response, high sensitivity, large surface-area-to-volume ratio, and lower hysteresis. The graphene oxide can be deposited on the surface of various SAW devices such as those made using ZnO/glass, AlN/Si, and $LiNbO_3$ [333-335]. Furthermore, graphene oxide has been exploited in the development of flexible SAW humidity sensors fabricated by depositing different thicknesses of graphene oxide on ZnO/polyimide SAW devices with various wavelengths. The A0 and S0 modes were identified at 150 MHz and 395 MHz, respectively. The results suggest that the A0 and S0 modes exhibited values of the sensitivity of 145.83 ppm per %RH and 89.35 ppm per %RH at 85%RH, respectively. The sensor also showed reasonable performance and good reliability when it was bent [336]. This type of device has been further investigated with temperature compensation to exclude the effect of changes in temperature [271].

A Lamb wave-based humidity sensor was reported by Sato and Yamamoto. The device was composed of a polyamide/ZnO/silicon nitride structure, and a zero-order antisymmetric mode with a resonant frequency of 8.4 MHz was used for humidity sensing in the range of 20-60%RH. It was suggested that the change in phase velocity of the Lamb wave was due to the increase in density and decrease in elastic stiffness of the polyamide polymer. Besides, the sensitivity of the Lamb wave was six times larger than that of the Rayleigh wave for the same polyimide thickness and phase velocity [337].

He et al. described flexible SAW humidity sensors based on ZnO thin film on a polyimide substrate where ZnO was used as a moisture-sensitive layer. The sensor showed the highest sensitivity of 34.7 kHz/10%%RH at 80%RH at a central frequency of 132.1 MHz. However, the sensitivity dropped as the resonant frequency decreased. However, it was suggested that the nonlinear behaviour of the sensor could have resulted from the contact angle (between 20^{o}–70^{o}) of the ZnO surface and the absorption of water by the polyimide substrate. As the humidity increased, a thin layer of the absorbed moisture may have covered the sensing area, and it increased the absorption of more water [338].

The summary of the above SAW based humidity sensors is shown in Table 2.5.

Table 2.5 Summary of SAW based humidity sensors

Device structure	Resonant frequency (MHz)	Frequency shift (kHz)	Sensitivity	Comments
Polymer/$LiNbO_3$	30	-	20 m/s per 10%RH	Linear from 40% to 80%
Polymer/Quartz	433	7.5	-0.4 kHz per %RH	In the range of 11% - 97%
ZnO/$LiTaO_3$	-	65	-	In the range of (20% - 87%)
ZnO/AlN/Si	125	160	-	In the range of (10% - 90%)
ZnO NRs/AlN/Si	123.5	750	-	In the range of (10% - 90%)
Graphene oxide /AlN/Si	392	-	182.51 kHz per %RH	In the range of (90% - 95%)

Graphene oxide /ZnO/glass	225	-	265.18 kHz per 5%RH	In the range of (0.5% - 85%)
Graphene oxide /ZnO/polyimide	150 395	-	145.83 ppm per %RH 89.35 ppm per %RH	At 85%RH
Polyimide/ZnO/Si_3N_4	8.4	-	0.725 kHz per %RH	In the range of (20% - 60%)
Flexible ZnO/polyimide	132.1	-	34.7 kHz per 10%RH	In the range of (5% - 87%)

2.5.4 SAW-based breath sensing

Breathing is a vital physiological function in keeping human and other living organisms alive. The breathing process involves bringing air containing oxygen from the atmosphere into the lungs by inhalation so that gas exchange can take place, and this is followed by the exhalation of the air containing carbon dioxide out of the lung. Breathing in the respiratory cycle includes the entire process from inhalation to exhalation. The respiratory rate has been considered to be an important vital sign that provides fundamental information about some severe illnesses.

Meanwhile, the tidal volume is the amount of air inhaled in one breath, and both processes play a crucial role in the metabolism of the human body [339]. The regular or quiet respiratory rate of healthy adults is between 12 to 20 breaths per minutes (bpm) and breathing below this range is called slow breathing or bradypnea while breathing at a higher rate is called fast breathing or tachypnoea. Several types of breath sensors have been developed for the monitoring of respiratory rate and apnoea (cessation of breathing) detection. These sensors can be divided into two main groups; contact devices that make direct contact with the human body, and non-contact devices that include radar (Doppler) and optically based respiratory rate monitoring [340].

The mechanisms by which the contact-based sensors use to measure the breathing rate are categorised according to the place in the body where the sensor is positioned. Respiratory

transducers can use airflow, or the temperature, humidity, or components of air, chest wall movement and respiratory sounds to detect breathing rates and patterns [339]. Therefore, various respiratory sensors have been investigated for breath detection. For example, there is a graphene-based resistive sensor for humidity sensing [341], chest wall and abdominal movement detectors that include capacitive, magnetometry, strain, and piezoresistive sensors [342-347], and bio-acoustic sensors which detect the sound of the airflow [348]. Sezen et al. reported the development of a MEMS microphone for the detection of breath sounds, and this was integrated with a SAW device for wireless telemetry [349].

Selyanchyn et al. described a QCM-based breath sensor which detects changes in humidity on the sensor surface. The QCM was coated with a moisture-sensitive layer of porphyrins and was fixed in a chamber to which the breath outlet of a face mask was connected. The proposed sensor exhibited excellent performance in detecting respiratory rate in various dynamic breath patterns [350].

Jin et al. developed a flexible SAW-based respiratory sensor for the detection of sleep apnoea syndrome. The sensor was fabricated by depositing ZnO thin film on polyimide (PI) substrate, and it had a central frequency of 170.94 MHz. Also, a $LiNbO_3$ based-SAW sensor with an operating frequency of 436.5 MHz was made for comparison purposes. The sensors were placed on the upper lip below the nose where they were exposed to exhaled air, and the breath rate was monitored in forms of changes in humidity. The evaluation showed that the sensitivity of the flexible ZnO/PI sensor was 2.7 MHz/50%RH, while it was only 0.36 MHz/50%RH for the other sensor. Both sensors exhibited excellent repeatability for breathing and apnoea detection [351].

The previous studies which used polymer substrates suffered from issues such as poor film quality and acoustic wave attenuation. Besides, those devices based on ZnO thin film on

aluminium foil have not been investigated for sensing applications. Thus, ZnO thin film on commercial aluminium foil is proposed for the development of flexible sensors for temperature, UV light, and humidity as well as breathing detection. A finite element analysis (FEA) was carried out and discussed in the next section.

2.6 Summary

The piezoelectric effect occurs when electric charges are observed as a result of the application of mechanical stress. The piezoelectric material has to possess a spontaneous polarisation to exhibit piezoelectricity. There are two main types of piezoelectric materials, the naturally occurring such as quartz and synthetic material such as ceramics. However, ZnO thin film has been widely used as a piezoelectric material due to its excellent piezo-electrical, semiconducting, and optical properties.

ZnO possesses a large exciton binding energy of ~60 meV at room temperature and bandgap energy of ~3.4 eV as well as excellent piezoelectric properties. Besides, it is considered to be safe to human and environmentally. Moreover, ZnO thin films and nanostructures can be grown in various substrate using different techniques. ZnO thin based acoustic devices have been developed and exploited in various sensing applications. The demand for flexible and bendable microsystems, including SAW devices for wearable applications have been substantially increased. Polymers offer a solution for the development of flexible SAW devices, but they cause substantial acoustic attenuation, and they exhibit thermal and lattice mismatching with ZnO thin film.

Aluminium foil was proposed in the literature as an alternative substrate to polymer, and it has been used to develop flexible SAW devices and ultrasonic transducer. However, this type of SAW devices has not been utilised in any sensing applications.

Thus, to overcome this gap, flexible SAW devices based on ZnO thin film on commercial aluminium foil are proposed to perform sensing of temperature, humidity, and UV light and for the detection of breathing rate and apnoea. The design of IDTs was selected based on the literature to excite Lamb wave modes. Next chapter is the experimental methodology which discussing the fabrication process and set up for each sensing parameters.

Chapter Three

Experimental methodology

3.1 ZnO thin film deposition and characterisation

ZnO thin film was deposited on aluminium foil using the physical vapour deposition (PVD) technique. A direct current (DC) reactive magnetron sputtering system (Nordiko) with two rectangular zinc targets of 99.99% purity was used for the deposition process to produce films with high quality as shown in Figure 3.1. A commercial aluminium foil roll of 50 µm thickness was used as the substrate for ZnO thin film deposition. The foil was cut into small pieces of 10 × 10 cm which was fixed on glass wafers before being put onto the sputtering machine holders. Some foil samples were attached to the holders with Kapton taps, as shown in Figure 3.1b, and they were cut using scissors after the deposition into small pieces for the lithography process. The surface of the foil was cleaned with acetone followed by ethanol, and then it was rinsed with deionised (DI) water and dried with nitrogen.

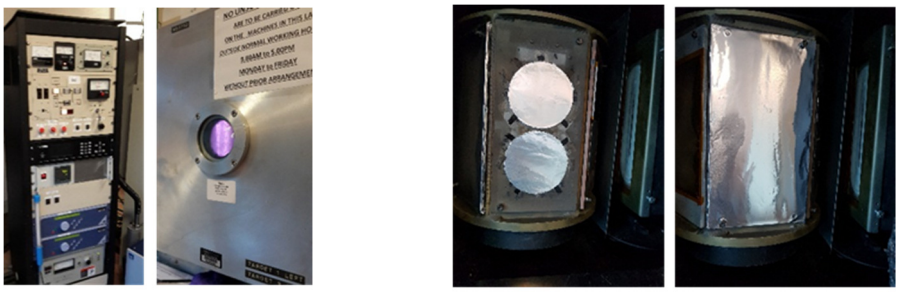

(a) (b)

Figure 3.1 Nordiko sputtering system, a) the machine control panel and chamber, and b) the rotary cylinder-type holder inside the chamber where aluminium foil samples are fixed

The chamber of the sputtering machine has a large rotary cylinder-type holder in the middle where six holders with aluminium foil samples were placed at a distance of 20 cm from the targets. The holder was rotated at a speed of 4 rpm. A few glass slide samples were also added for characterisation purposes. The vacuum pump was turned on, and a chamber pressure of ~3.75 mTorr was maintained during the deposition process. A pre-deposition cleaning process was performed for five minutes by applying a forward bias of radio

frequency (RF) power of 200 watts, and a reverse power of zero watts. The argon (Ar) gas flow rate was ten sccm (standard cubic centimetre per minute).

The deposition process was performed by flowing the oxygen gas into the chamber to oxidise the zinc metal to form the ZnO compound. The parameters of the process were optimised by biasing the two zinc targets with a DC power of 400 watts and varying the flow rates of Ar gas from 3-8 sccm and O_2 from 5-15 sccm. The optimal parameters for deposition were selected based on film quality and the desired thickness. Film structure, crystallinity and thickness were evaluated after the deposition, and the parameters were adjusted according to the results of film characterisation. Therefore, the final deposition parameters were adjusted by setting the flow rate of Ar gas to 6.5 sccm, and of O_2 to 13.0 sccm, with the DC bias power kept of 400 watts. There was no intentional heating of the substrate, and the maximum monitored temperature throughout the deposition process reached 55 ^{o}C. Hence, the deposition rate achieved was about ~0.3 µm/hour and the total deposition period lasted for 15 to 18 hours. Figure 3.2 shows a sample of as-deposited ZnO thin film on aluminium foil fixed on a glass wafer.

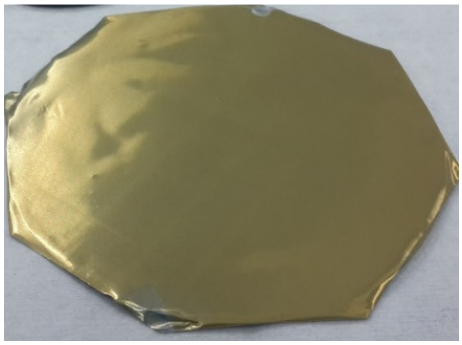

Figure 3.2 as-deposited ZnO thin film on aluminium foil. The sample is fixed on a glass wafer

ZnO thin film was characterised using a scanning electron microscope (SEM) for surface morphology and cross-section. The film structure, orientation and crystallinity were characterised using XRD analysis. The surface roughness of the deposited ZnO thin film on aluminium foil was characterised using AFM.

3.2 Surface acoustic wave device fabrication and frequency response characterisation

The ZnO thin film-based SAW device on flexible aluminium foil substrate was fabricated using conventional lithography and lift-off processes as illustrated in Figure 3.3.

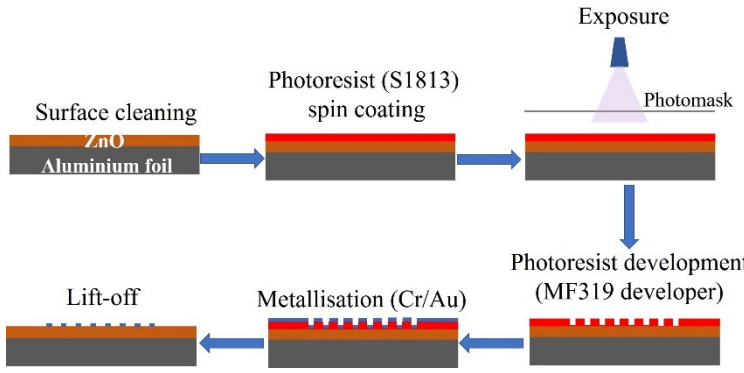

Figure 3.3 The fabrication process of IDTs using lithography and lift-off methods

The samples were prepared for IDT patterning and fabrication by cutting the foil into small pieces and fixing them over glass wafers. However, some foil samples were mounted onto glass wafers before ZnO deposition, and they were used directly for the lithography process. The samples were cleaned using acetone, ethanol, and DI water, and dried with nitrogen gas. A positive photoresist S1813 from Rohm and Haas Company was spin-coated onto the surface of the ZnO/Al-foil samples, and it was spun using a Laurell 650M spin coater. The initial rotational speed was 10 rpm for 10 seconds, followed by a constant acceleration rate of 3,700 rpm for 60 seconds. The samples were placed on a hot plate for soft baking where the temperature was increased to 95 ^{o}C for a longer time of 10 minutes compared to the standard baking time because the glass wafer is acted as a barrier to heat transfer from the hot plate to the substrate. An exposure dose of 90 mJ was applied to the samples using an EVG620 mask aligner followed by immersing them in MF319 developer solution for 1 minute to develop the S1813 photoresist. The samples were rinsed with DI water and dried using filtered dry nitrogen.

Two different masks were used to pattern the IDTs: mask (A) and mask (B) as shown in Figure 3.4a and 3.4b, respectively.

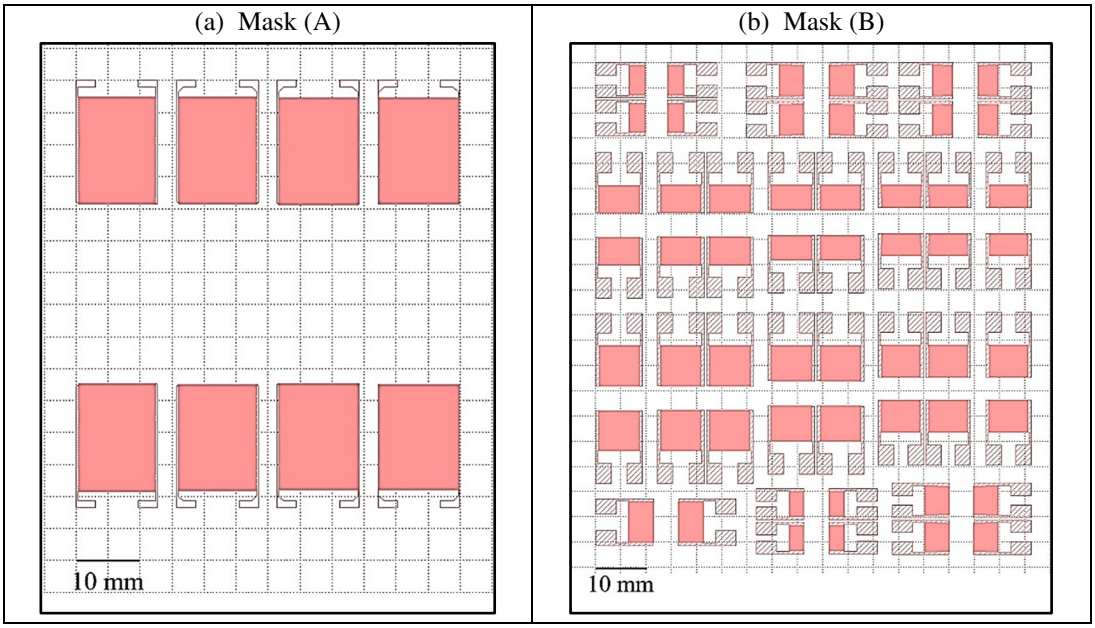

Figure 3.4 The design and configuration of IDTs in two different layouts a) mask (A); b) mask (B)

The basics of IDT design were discussed in section 2.4.2. Mask (A) has a dimension of 4 × 4 inches, and it consists of four pairs of SAW devices with wavelengths of 100 µm, 200 µm, 300 µm and 400 µm. The IDTs have a bidirectional design with an aperture width of 12 mm and a delay line distance of 28 mm. The complete specifications of the mask (A) are summarised in Table 3.1.

Table 3.1 Specifications of the IDTs of mask (A)

Device	Wavelength λ (µm)	Number of IDTs (mm)	Aperture width (mm)	Delay line (mm)	IDTs type
1	100	337	12	28	Bidirectional
2	200	166	12	28	Bidirectional
3	300	110	12	28	Bidirectional
4	400	84	12	28	Bidirectional

Each device in the mask (A) occupies an area of 17 × 12.7 mm for the single port IDTs, and the total area of a single pair of devices including the delay line region is 62 x 12.7 mm. On the other hand, the devices in the mask (B) have a smaller area, where the largest dimensions

of the single port IDTs is 7 × 9 mm for the device with a wavelength of 160 µm and the size of a single pair of the devices is 19 × 9 mm. The delay line region has a length of 5 mm which is 5.6 times less than that of the mask (A), and this will reduce the return loss of the acoustic wave during propagation in the two-port device configuration.

The transferrable IDT patterns inside the 4-inch area of the mask (B) have three design wavelengths of 160 µm, 100 µm and 64 µm. Besides, other IDT patterns at the edges of the mask have design wavelengths of 32 µm, 40 µm, 80 µm, 100 µm and 200 µm. The IDT was designed in two types: single-phase unidirectional transducers (SPUDTs) and bidirectional structures. Table 3.2 shows the full specifications of the SAW devices and the IDT types in the designed mask.

Table 3.2 The specifications of the IDTs of mask (B)

Device	Wavelength λ (µm)	Number IDTs	Number of reflectors	Aperture width (mm)	Delay line (mm)	IDTs type
1	160	70	-	8	5	Bidirectional
2	100	100	-	8	5	Bidirectional
3	64	70	70	8	5	SPUDT
4	160	100	-	8	5	SPUDT
5	100	140	-	8	5	SPUDT
6	64	200	-	8	5	SPUDT
7	32	100	-	6	5	Bidirectional
8	100	50	50	6	5	SPUDT
9	40	100	100	6	5	SPUDT
10	200	50	-	8	5	Bidirectional
11	40	135	-	8	5	Bidirectional
12	80	30	30	8	5	Bidirectional

The surface of the substrate (aluminium foil) is very rough, and it contains scratches that influence the patterning process. Therefore, the developed structures of the IDT patterns were checked under an optical microscope for any defects before metallisation. The Moorfield electron beam evaporation cluster system with a base pressure of ~2.0 E-7 mbar was used to deposit 80 nm of a chromium layer and 120 nm of gold. Then the samples were placed in a water tank and soaked in an acetone solution for a few minutes before conducting

a lift-off using an ultrasonic bath. However, extra mechanical rubbing with acetone was performed over the IDT patterns to remove unstripped photoresists where they had stuck in deep scratches. Finally, the samples were rinsed using ethanol and DI water and dried with nitrogen. Figures 3.5a and 3.5b show SAW devices after IDTs patterning using masks (A) and (B), respectively.

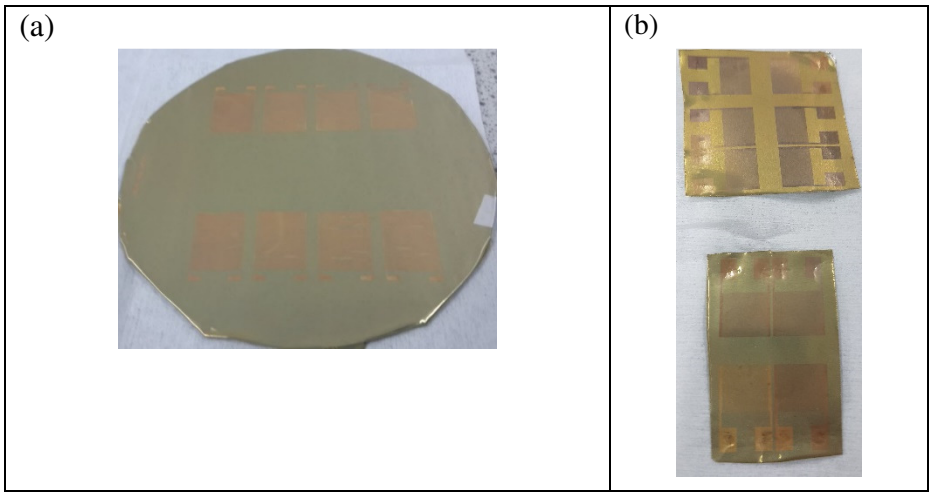

Figure 3.5 Examples of fabricated SAW devices using a) mask (A) and b) mask (B)

The minimum linewidth (the minimum line or space that can be resolved) of the IDT is equal to 25 μm for the device of wavelength of 100 μm which is considered to be large for lithography process compared to CMOS fabrication (the minimum linewidth is a nanoscale). However, the non-uniform and high surface roughness (~261.1 nm) and the existence of defects (e.g. scratches) on the surface of aluminium foil influence the yield of fabrication, increase IDTs defects (e.g. damage of IDT) and tolerance. This cannot be predicted or avoided due to the random defects and non-uniform roughness of the surface of aluminium foil. Therefore, the samples were examined under optical microscope for any apparent defects in the IDTs before performing metallisation which improves the yield of fabrication and produce SAW devices with good acoustic signal.

The frequency spectra of the SAW devices were characterised using a vector network analyser (Agilent E5061B) and a Keysight N9913A Fieldfox handheld analyser. The S-

parameters of each SAW device, the insertion loss of the reflection (S11) and the return loss of the transmission (S21) signals were recorded. The various resonant frequencies and Lamb wave vibration modes were identified and compared with simulation results.

3.3 Nanorods growth and characterisation

The SAW device with a wavelength of 160 µm was selected to grow the ZnO nanorods between the delay line regions using the hydrothermal technique. The process was conducted by growing the nanorods on the top of the thin film without depositing an insulating layer or a seed layer. A precursor solution with a concentration of 60 mM was prepared in a large flask by adding 11.36 mg of zinc nitrate powder ($Zn(NO_3)_2$, ≥ 99.0% purity, molar mass 189.36 g/mol) from Sigma-Aldrich to one litre of DI water. The solution was further diluted to a final concentration of 25 mM, and it was kept in a sealed container, as shown in Figure 3.6. The pH value of this solution was adjusted to 10.3 by adding drops of ammonium hydroxide (NH_4OH, ≥ 99.99%) obtained from Sigma Aldrich, and the pH was monitored using a pH meter.

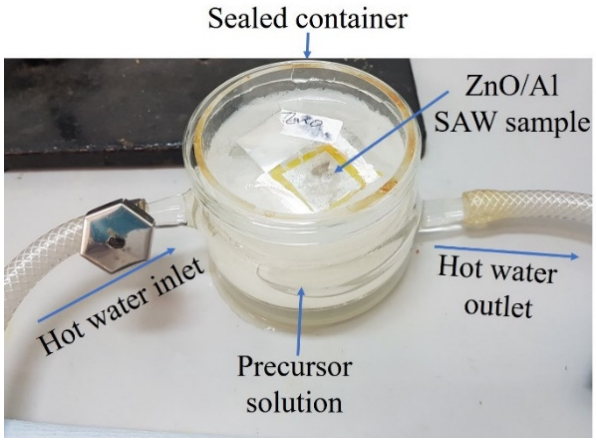

Figure 3.6 Experimental set-up for ZnO nanorods growth by hydrothermal process

This method was modified from the standard hydrothermal process mentioned in the literature by which no other materials such as methenamine were added to the solution. The SAW device was suspended upside down on the surface of the solution where the ZnO thin

film was in contact with the solution, and the IDTs were covered by Kapton tape. The container was placed in a fume cupboard and connected to a water bath heater where the temperature was set at 85 ^{o}C, and the device was kept in the solution for 4 hours before being rinsed with DI water to remove any reaction residue.

Furthermore, another SAW device with a wavelength of 160 µm was prepared for nanorods growth by depositing an isolation layer of 150 nm silicon dioxide (SiO_2) on the surface of ZnO thin film using plasma-enhanced CVD method. The importance of this layer is to separate ZnO thin film from nanorods. A seed layer of 30 nm of ZnO was further deposited on the SiO_2 layer to act as nucleation sites for growing ZnO nanorods.

The surface morphology and cross-section of the grown nanorods were characterised using SEM. The frequency spectra of the SAW device before and after growing the nanorods were obtained by recording the S21 signal using the network analyser.

3.4 Temperature sensing using flexible ZnO thin film-based SAW device

The flexible ZnO thin film-based SAW devices with the wavelengths of 100 µm, 160 µm, 200 µm, 300 µm and 400 µm were investigated for temperature sensing. They were mounted on a printed circuit board (PCB) in a flat and bent position. The pads of the devices were connected by thin copper wires using the silver paste, as shown in Figure 3.7.

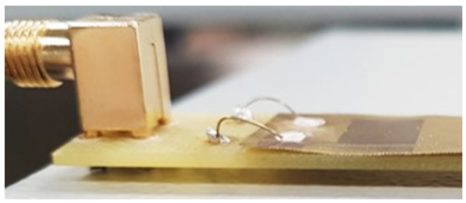

Figure 3.7 SAW device with a wavelength of 160 µm mounted on a PCB in a flat position

The acoustic signals (Lamb waves) were excited using the vector network analyser. The antisymmetric and symmetric zero ordered vibration modes were characterised and identified based on the simulation results discussed in section 4.4. The devices were placed

inside a closed oven (Carbolite), and they were connected to the network analyser that was controlled by LabVIEW software, as shown in Figure 3.8. The oven has a built-in fan to assist in air circulation and to distribute the heat homogeneously inside the oven. A digital temperature sensor (SHT71) from Sensirion was attached to the SAW devices to monitor changes in temperature at the surface of the device.

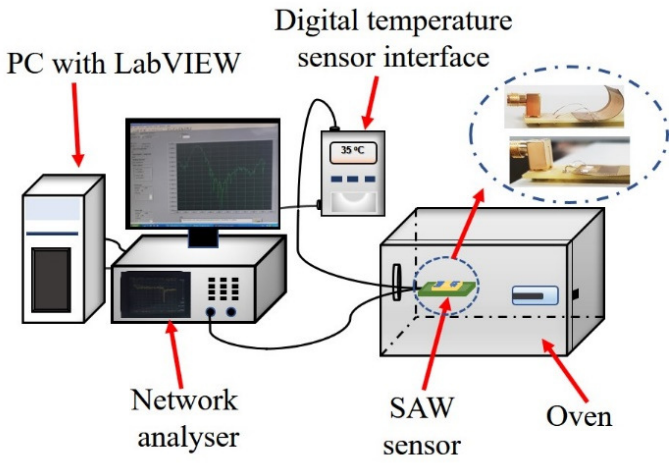

Figure 3.8 Schematic of experimental set-up for sensing temperature in equilibrium condition

The TCF values of the A0 and S0 vibration modes of the SAW devices of various wavelengths were calculated using equation 2.36. The initial temperature ($T_{initial}$) and resonant frequency ($f_{initial}$) were recorded before the temperature was increased. The temperature was controlled by adjusting the set point of the digital controller of the oven where it started to rise until it reached the pre-set point and then held this value. The values of final resonant frequency (f_{final}) and temperature (T_{final}) were subsequently obtained in the equilibrium condition state when the temperature was stable at this value, implying that no further heat transfer occurred. The actual changes in temperature and resonant frequency were calculated using the following relationships:

$$\Delta T = T_{final} - T_{initial} \tag{3.1}$$

$$\Delta f = f_{final} - f_{initial} \tag{3.2}$$

Those calculated values were substituted in equation 2.36 to find the TCF values for each device at various vibration modes.

Furthermore, the real-time responses of the devices were examined by adjusting the pre-set point of the temperature to 50 ^{o}C. Then, the temperature was slowly increased until it reached the set-point, which decreased to the original value after it had been held at the maximum point for a few minutes. The changes in resonant frequency and temperature were recorded at the same time for the whole cycle when the temperature was increasing, stable and decreasing. The resonant frequency was initially obtained for three minutes before the temperature was increased in order to eliminate any external factors that may have influenced the measurements of frequency.

The SAW device with a wavelength of 400 µm was selected for real-time investigation in the bent-down position because it exhibits the highest TCF value among all of the devices, as shown in Figure 3.9. Similarly, the resonant frequency was recorded at the same time when the temperature was increasing to 50 ^{o}C and decreasing back to the original value for one cycle.

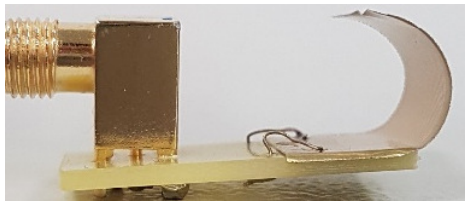

Figure 3.9 SAW device with a wavelength of 400 µm mounted on PCB in a bent-down position. The radius of curvature is 5 mm.

The temperature sensing in the *in-situ* condition was also carried out using a Peltier system and selecting two SAW devices with wavelengths 160 µm and 200 µm. These devices have a different structure of IDTs, and they were attached to the surface of the Peltier plate using highly thermally conductive silicone grease obtained from the Farnell Company. The Peltier system was controlled manually by adjusting the input voltage of a DC power supply. A double-pole switch was used to change the input polarity of the Peltier system, allowing one

side to heat up and the other side to cool down. Hence, the temperature of the top plate where the SAW device was placed, was increased, or decreased quickly without changing the input voltage that was fixed at 5 V. The reference sensor (SHT71) was attached to the surface of the SAW devices to measure their actual temperature as shown in Figure 3.10.

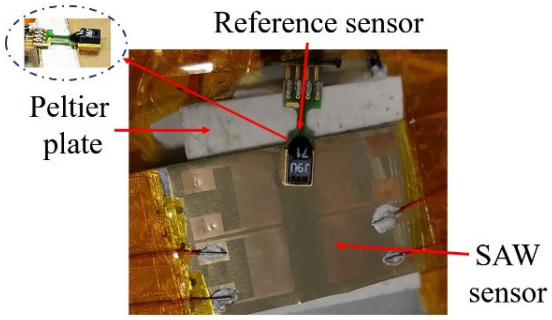

Figure 3.10 SAW device fixed on a Peltier plate in a flat position for sensing of temperature in *in-situ* condition

The changes in resonant frequency and the corresponding values of temperature were recorded simultaneously, and the TCFs for both devices were calculated accordingly for the A0 and S0 vibration modes. Likewise, the real-time response of the SAW devices was obtained by setting the input voltage to about 15 V, allowing the temperature to increase quickly to ~55-60 ^{o}C within 15 seconds. Then, the temperature was decreased by switching the polarity of the input voltage using the double-pole switch to let the upper surface of the Peltier system to cool down quickly.

The device with the wavelength of 160 µm was selected for flexible sensing by obtaining the frequency response to temperature change for one cycle when the device was placed in bent-up position using a semi-circular metal holder with a radius of 10 mm as shown in Figure 3.11. The metal holder was attached to the surface of the Peltier system with silicone grease.

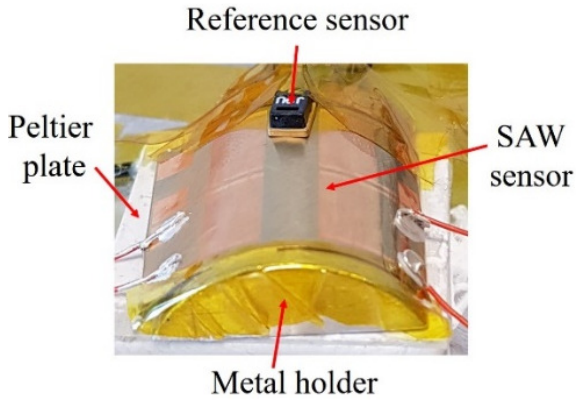

Figure 3.11 SAW device fixed on a Peltier plate in bent-up position for sensing of temperature in *in-situ* condition. The radius of curvature is 10 mm.

The real-time cycling response was further investigated for both devices in a flat position by setting the input voltage of the Peltier system to 5 V, and the input polarity was changed to heat up and cool down the surface of the Peltier plate over five cycles. The cycling response of the device with a wavelength of 160 µm was also obtained when the device was placed in a bent-up position.

3.5 Ultraviolet (UV) sensing using flexible ZnO thin film-based SAW device

The flexible SAW devices based on ZnO thin film on the aluminium foil substrate with wavelengths of 200 µm and 160 µm were selected for a study of their performance as UV light sensors. The ZnO nanorods were further grown on the delay line region of the SAW device with a wavelength of 160 µm using the hydrothermal process mentioned in section 3.3. The frequency spectra of the SAW devices were characterised using the handheld network analyser for both the reflection (S11) and transmission (S21) signals.

Two types of UV light-emitting diode (LED) systems were used as UV light sources: the CS2010 from Thorlabs and BlueWave LED DX-1000 from Dymax. Both sources have adjustable exposure times and intensities. However, the CS2010 source has an output wavelength of 365 nm, and it was used to deliver the low UV intensities (low power source)

since it has a minimum value of 25 mW/cm^2 at a source-to-sample distance of 20 mm. On the other hand, the output wavelength of the DX-1000 is 385 nm, and it was exploited to deliver high UV light intensity levels (high power source) as the minimum exposure intensity is 1.4 W/cm^2 at 25.4 mm.

The SAW devices were kept at a fixed distance of 60 mm from the CS2010 UV light source, and at 100 mm from the DX-1000 LED source. The UV light intensity in both sources is controlled by a knob that delivers the UV light in percentage levels from 1.0 to 100 % in steps of 1%. Therefore, an external photodiode power sensor (Thorlabs S120VC) was used to measure the corresponding surface power density in Watts per centimetre squared (W/cm^2) at each percentage level. Thus, the actual UV light intensities delivered while the devices were placed at the fixed distance and position were obtained.

The changes in temperature of the SAW device due to exposure to UV light were monitored by fixing the digital sensor SHT71 on the surface of the device. The Sensirion EK-H4 viewer software connected to the sensor interface via a USB cable was used to record real-time variations in temperature during UV light irradiation. The SAW device was fixed in flat, bent-up and bent-down positions with a bending radius of 10 mm, as shown in Figure 3.12.

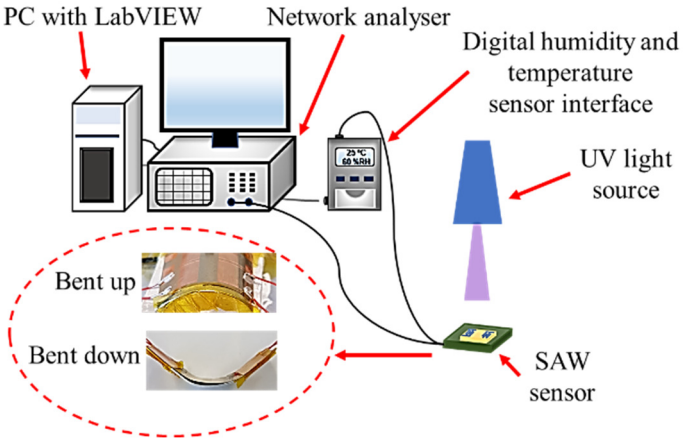

Figure 3.12 Schematic of the experimental set-up for UV light sensing while the devices were placed in flat, bent-up and bent-down positions

The changes in the electrical conductivity of the ZnO thin film as a result of exposure to UV light was also investigated. The current-voltage (I-V) characteristic curve was obtained for

the ZnO film using a Keithley 2400 source meter. Two probes were connected to the IDT pads, and the current was measured by sweeping the voltage from 0-10 V. A LabVIEW software application was used to control the source meter and record the measurements. In addition, the ZnO thin film-based SAW devices were placed at the fixed distances from the two UV light sources and the current induced was measured at different intensities of UV light exposure by sweeping the voltage from 0 to 5 V.

The frequency response of the flexible SAW devices to UV light irradiation was obtained using the reflection (S11) signal while the devices were kept in a flat position using the two UV power sources. The Keysight N9913A vector network analyser was used to characterise the resonant frequencies of the SAW devices. The network analyser was controlled by a LabVIEW based software application through a network cable.

The frequency response and the temperature of the SAW device were recorded simultaneously at different UV light intensities. The measurements were obtained initially when the UV light was switched off for 20 seconds in order to check the stability of the sensors against environmental factors. Then, the recordings were continued when the UV light was turned on for 20 seconds and when the UV light was switched off again for another 20 seconds, thus giving a one-minute cycle.

The UV light sensing performance of the two flexible SAW devices with wavelengths of 160 µm and 200 µm was then studied for different vibration modes and various UV light intensities. The frequency shifts resulting from the exposure to UV light was measured. The real-time cycling response of the SAW devices was also investigated by adjusting the UV light intensities to 16 mW/cm^2 and 240 mW/cm^2 when the low and high-power UV light sources were used, respectively. The frequency responses of the A0 modes of both devices were recorded for five cycles by switching the UV light on for 20 seconds and switched it off for 20 seconds.

The frequency responses of the two SAW devices to UV irradiation were obtained when the devices were placed in a bent-up and bent-down positions with a curvature radii 10 mm. The low-power UV light source was only used to study the sensing performance of the devices in a flexible position since the UV irradiation of the high-power source led to significantly increased temperature. The frequency shift was obtained in the one-minute cycle for different vibration modes in both bent positions at various UV light intensities. The real-time cycling responses of the bent devices were also investigated by setting the UV light intensity to 16 mW/cm^2 for five cycles. The SAW device of wavelength 160 µm was further investigated for UV light sensing by considering the S21 signal to determine the resonant frequency before and after the nanorods were grown. The frequency shift of the different vibration modes was obtained when the device was placed in the flat position, and it was irradiated by the low-power UV light source. The cycling response was also obtained by recording the frequency shift of the A0 mode when the nanorods-enhanced SAW device was exposed to 16 mW/cm^2 of UV light irradiation for five cycles.

3.6 Humidity, breath, and apnoea detection using the flexible ZnO thin film-based SAW device

The flexible SAW device with a wavelength of 160 µm was further investigated as a humidity sensor. The frequency response of the device was characterised using the handheld network analyser, and the vibration modes were identified based on the simulation results, as mentioned earlier. The humidity chamber was designed using SolidWorks software, and it was made by the 3D printing facility. The chamber has a cylindrical shape with a radius of 50 mm and a height of 150 mm, as shown in Figure 3.13.

Figure 3.13 3D printed cylindrical shaped chamber for humidity sensing

Besides, it has two small holes in the base and top covers; one to introduce the dry nitrogen gas into the chamber and the other one to act as an outlet for the gas. The humidity set-up consists of two large bottles, one of them was filled with deionised (DI) water, and a central source of dry nitrogen as well as two flow meters connected to the bottles which can be adjusted either electrically or manually as seen in Figure 3.14.

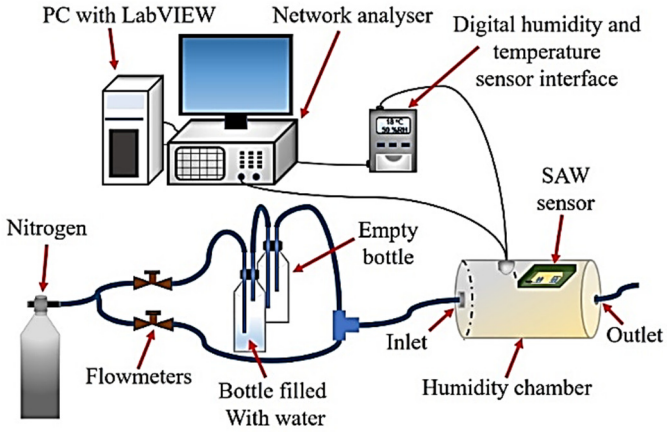

Figure 3.14 Schematic of the experimental set-up of humidity sensing

The humidity inside the chamber was controlled by adjusting the flow rate of the nitrogen gas that passed through the bottles carrying the water vapour into the chamber. Relative humidity and temperature were measured using the SHT71 reference sensor. The frequency response of the device was recorded at the desired value of humidity and when the humidity was maintained at a stable level for 2-3 minutes. The dry nitrogen was purged inside the chamber until the relative humidity dropped to 1%, and then the humidity was increased to 90% for several cycles, and corresponding temperature changes were obtained accordingly.

The frequency shifts of the various vibration modes were recorded when the relative humidity was adjusted to 1%, 20%, 40%, 60%, 80% and 90% using the S11 and S21 signals to determine the resonant frequencies. The SAW device was mounted on a particular holder in a flat and bent-down position, the radius of the curvature is 50 mm as shown in Figure 3.15, where the frequency responses to different humidity levels were obtained.

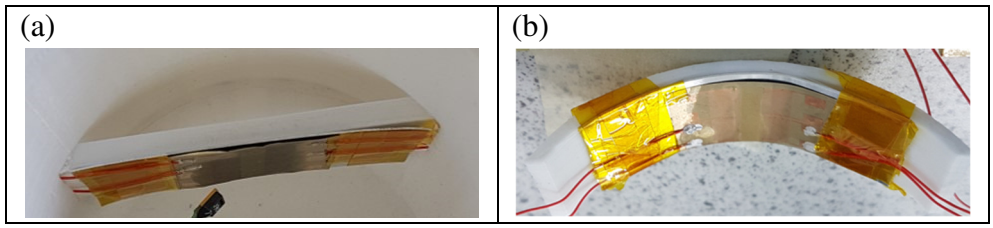

Figure 3.15 SAW device mounted on holders for humidity sensing in a) flat and b) bent-down position with curvature radius of 50 mm

The real-time cycling responses was investigated by recording the frequency shift of the fundamental (A0 and S0) modes to the changes in relative humidity for five cycles when the device was placed in the flat and bent-down positions. Moreover, the cycling response was obtained for the nanorods-enhanced SAW device when the humidity was varied over several cycles.

The SAW device was further investigated for the monitoring of respiratory rate and apnoea by exposing the device to the exhalation stream. The device was placed at a distance of 50 mm from the mouth of a volunteer, where the exhaled air flowed in parallel over the device to minimise the pressure effect, as shown in Figure 3.16. The SHT71 reference sensor was fixed on the top of the SAW device to measure the changes in temperature and humidity due to the breathing cycles.

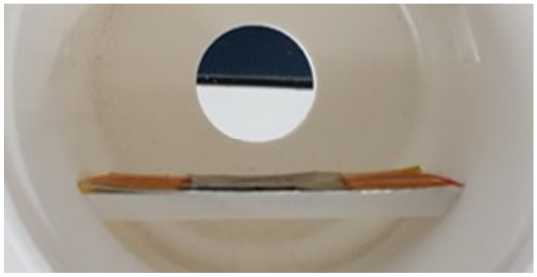

Figure 3.16 SAW device fixed in a flat position inside a breath chamber for the detection of respiratory rate and apnoea

The volunteer was instructed to breathe in different patterns: regular and healthy, irregular, holding a breath (apnoea), and breathing slowly (bradypnea) and quickly (tachypnoea). The normal respiratory rate is defined when the number of the breaths per minute is 12 to 20 breaths/min while resting. Therefore, breathing below this range is considered to be bradypnea, and tachypnoea when it is above the normal range.

Thus, the frequency responses of the fundamental (A0 and S0) Lamb wave modes were recorded using the handheld network analyser, and the respiratory rate was counted manually when the volunteer was breathing. The performance of the SAW device in detecting respiratory rate and apnoea for various breath patterns was investigated when the device was placed in the flat and bent positions. The frequency response of the SAW device with the grown nanorods was further studied to show enhancement in breathing monitoring, and the results were compared with those for the SAW device without nanorods.

3.7 Finite element analysis of SAW device based on ZnO thin film on aluminium foil

SAW device based on ZnO thin film on aluminium foil has a double layer structure which Lamb waves are excited when the wavelength is the designed to be much larger than the thickness of the two layers. Thus, finite element analysis was exploited using COMSOL software to predict the eigen-frequency values and vibration modes patterns for the proposed SAW devices with five different wavelengths. The simulation was performed by

investigating the mechanical displacement occurring as a result of the application of an electrical potential to the piezoelectric material (ZnO) in a two-dimensional (2D) model as shown in Figure 3.17 [112, 113].

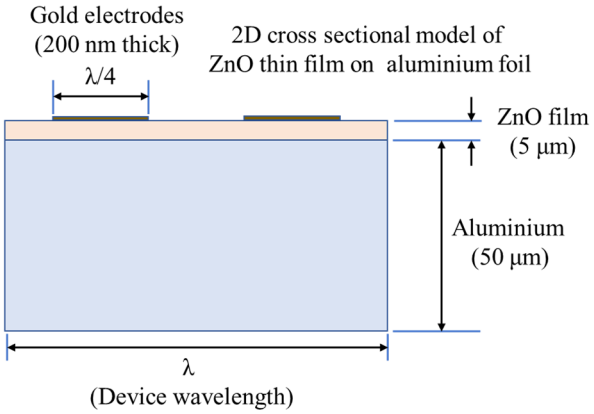

Figure 3.17 Geometry of a 2D cross-sectional model of ZnO thin film on aluminium foil

The geometry of the 2D model consists of a double layer structure of ZnO and aluminium materials, and their heights are equal to 5 μm and 50 μm, respectively. The width of the model represents one wavelength (λ) which is varied according to the different designed wavelengths (100 μm, 160 μm, 200 μm, 300 μm, 400 μm). Gold material was assigned to one pair of IDTs, and infinite boundary conditions were applied.

The propagation of the acoustic wave in a piezoelectric material is represented by the relationship between stress, strain, and electric field and displacement given by the following equations [113] :

$$T_{ij} = C^{E}_{ijkl} S_{kl} - e_{ijk} E_k \tag{3.3}$$

$$D_i = e_{ijk} S_{kl} + \varepsilon^{S}_{ik} E_k \tag{3.4}$$

where T is the stress tensor, C^E is the elastic matrix (N/m^2) on constant electric displacement condition, S is the strain tensor, e is the piezoelectric coupling constant matrix (C/m^2), E is the vector of electric field, D is the vector of electrical displacement (C/m^2), and ε is the permittivity matrix (F/m) on strain constant condition.

Thus, the electric potential (V) and the displacement (u) in the direction (x) can be obtained by solving the Newton and Maxwell equations related to formulas 3.3, and 3.4 and the solutions are given in the following equations [112]:

$$\sum_{ijk} C_{ijkl}^{E} \frac{\partial^2 u_l}{\partial x_j \partial x_k} + \sum_{jk} e_{kij} \frac{\partial^2 V}{\partial x_j \partial x_k} = \rho \frac{\partial^2 u_i}{\partial t^2} \tag{3.5}$$

$$\sum_{kl} e_{jkl} \frac{\partial^2 u_l}{\partial x_j \partial x_k} - \sum_{jk} \varepsilon_{jk}^{s} \frac{\partial^2 V}{\partial x_j \partial x_k} = 0 \tag{3.6}$$

where i, j, k, l = 1, 2, and 3 and ρ is the density.

A polarisation voltage value of 1 V is assigned to one of the gold electrodes, while the other is assigned to be ground. A zero charge/symmetry is applied to the top surface, and all the boundaries are considered to be stress-free since the device is designed to operate in Lamb wave modes. A periodic boundary condition was also applied to the left and right boundaries. The model was meshed using extra fine triangular mode, as shown in Figure 3.18.

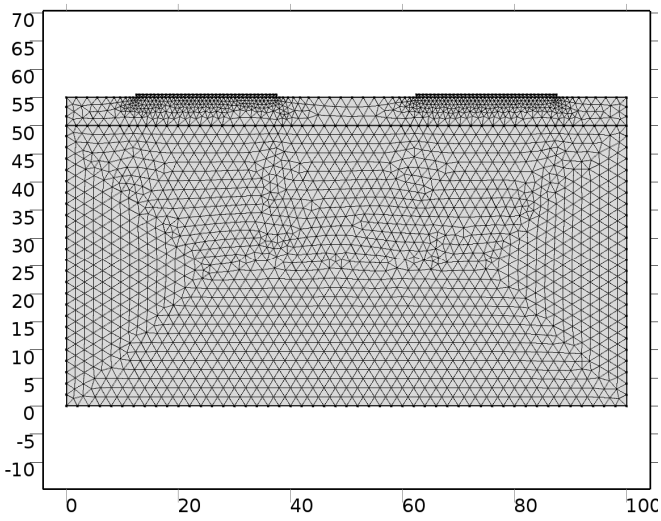

Figure 3.18 Image of the meshed 2D cross-sectional model of the ZnO thin film-based SAW device

The structure of ZnO thin film is considered to have *c*-axis orientation with in-plane isotropic and ideal material properties. The material parameters of ZnO thin film and aluminium, which are used in the simulation, are summarised in Table 3.3.

Table 3.3 The parameters of ZnO thin film and aluminium that used in the simulation [1]

Material	Young's modulus Y (GPa)	Poisson's ratio υ	Piezoelectric constant e_{33} (c/m^2)	Relative dielectric constant ε	Density ρ (kg/m^3)
ZnO	120	0.44	1.32	10.204	5680
Al	70	0.35	-	-	2700

Chapter Four

ZnO thin film and flexible SAW device characterisation

4.1 Introduction

ZnO thin film is deposited on aluminium foil using a DC magnetron sputtering system ready with high purity Zn targets. Besides, ZnO nanorods are grown on the surface of the λ=160 μm device using the hydrothermal technique. A high-quality ZnO thin film is obtained by optimising process parameters such as bias voltage and gas flow rates. The piezoelectric properties are highly associated with the structure and orientation of ZnO thin film crystallites as well as the adhesion with aluminium substrate. Therefore, surface morphology and cross-section of the ZnO thin film and nanorods are characterised by SEM. XRD rocking curve is also obtained, which shows the structure, orientation, and crystallinity of the thin film. AFM results of surface roughness are important due to their effect on acoustic wave propagation and attenuation.

Furthermore, the frequency responses of ZnO thin film-based SAW devices are characterised in various flat, bent-up and bent-down positions. Bending the devices causes resonant frequency shift due to the strain and the defects generated in the thin film. The resonant frequencies are obtained, and the various vibration modes are identified based on the eigen-frequencies predicted from simulation results.

However, the surface of commercial aluminium foil possesses high roughness as well as has several defects and scratches which influences the fabrication of the IDTs, and hence the quality of the acoustic wave.

4.2 Characterisation of the ZnO thin film on aluminium foils substrate

The SEM topographical image of the ZnO thin film on aluminium foil is shown in Figure 4.1. The surface morphology of the deposited film showed a dense granular pattern composed of large ZnO grain-like structures with an average diameter of ~350 nm. The film was compact and did not show any apparent defects or significant cracks on the surface.

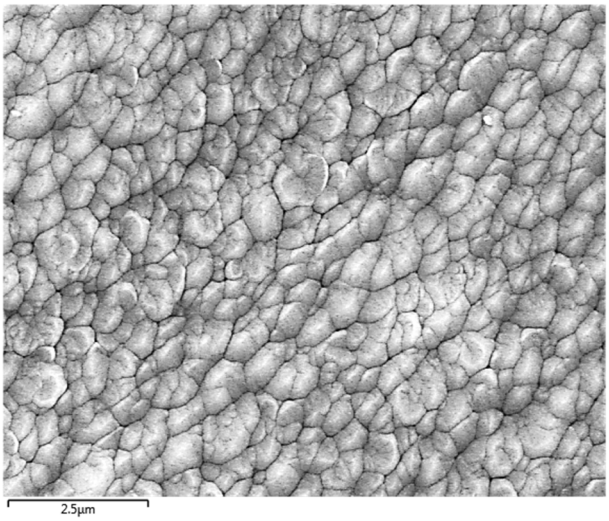

Figure 4.1 SEM surface topographical image of the ZnO thin film deposited on aluminium foil substrate using DC reactive magnetron sputtering

Figure 4.2 shows an SEM cross-sectional image of the ZnO thin film on the aluminium foil substrate. It shows that the ZnO film has a thickness of about ~8.5 µm, and it was vertically aligned in highly oriented columnar structures of nanocrystals perpendicular to the aluminium substrate. However, the sample was mechanically torn by hand for the cross-sectional image to avoid any severe damage to the film at the edge to be scanned. Therefore, the image does show some cracks and defects.

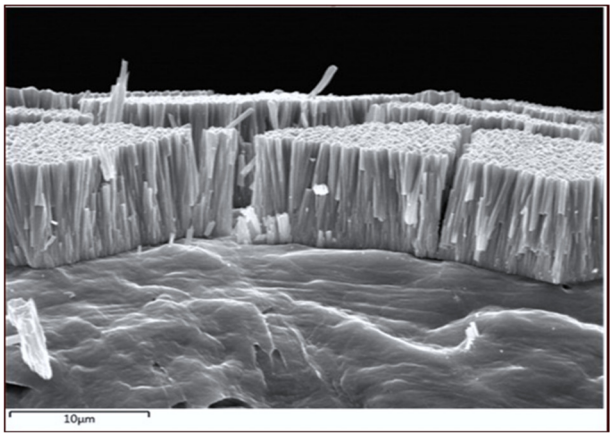

Figure 4.2 SEM cross-section image showing the ZnO thin film deposited on an aluminium foil substrate

The AFM image of a scanned area of 100 × 100 µm reveals that the surface texture of the ZnO film-based device was irregular, rugged, and curled, as shown in Figure 4.3. There are mechanical grinding patterns formed during the foil fabrication process. Further analysis showed that the root-mean-squared (RMS) value of the surface roughness (Rq) is 261.1 nm. This value is considerably high compared to the ZnO thin films deposited on rigid and smooth substrates such as silicon and glass. The values of RMS roughness reported for this type of substrates using sputtering method were in the range of less than a nanometre to 75 nm [16, 111, 153]. This can be mainly attributed to the use of a thin commercial aluminium foil as a substrate which is expected to have a non-homogeneous surface with defects and irregularities.

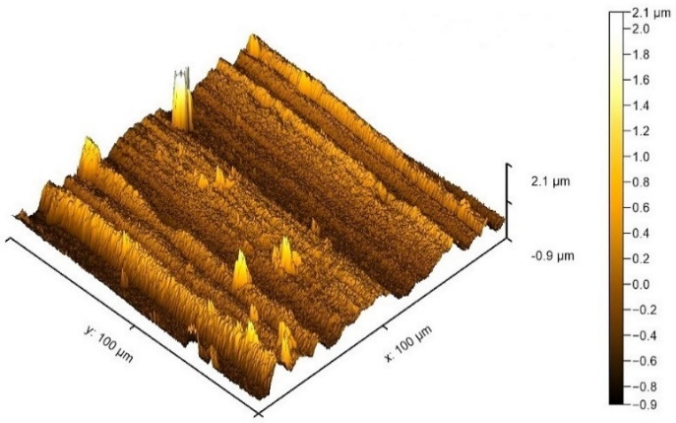

Figure 4.3 AFM image of the ZnO thin film deposited on an aluminium foil substrate

Therefore, the texture of the ZnO film is non-uniform as it conforms to the surface of the aluminium foil substrate, and this directly influences the characteristics of the excited acoustic waves and the overall performance of the ZnO thin film surface acoustic wave-based sensors.

The ZnO thin film was further characterised using XRD to study the film's crystallinity, and the results are shown in Figure 4.4. The XRD analysis reveals that there is a sharp peak at a diffraction angle (2θ) of 34.2° corresponding to the orientation of the ZnO crystals in the (0002) plane along the c-axis and perpendicular to the substrate. The angle is slightly lower than that of the ZnO bulk as obtained from the XRD JCPDS card #75-1533 where the $2\theta_0$ value is ~34.29 °. This shift in diffraction angle is primarily due to the intrinsic or residual film stress that is resulted from defects generated during the deposition process. The intrinsic stress was estimated using equation 2.22, where Young's modulus (Y) and the Poisson ratio (ν) of the bulk ZnO were considered to be 124 GPa and 0.3 respectively [241]. The film possessed a relatively lower compressive stress of -0.52 GPa compared to the non-annealed samples mentioned in a previous study [276]. This could be due to the elastic and flexible nature of the aluminium foil substrate that relieves some of the residual stress of the deposited film.

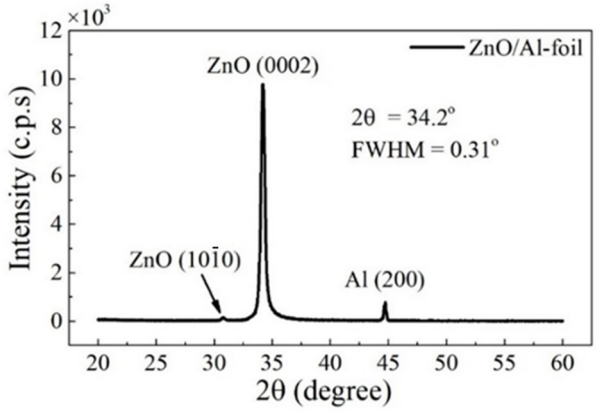

Figure 4.4 XRD analysis of the ZnO thin film deposited on an aluminium foil substrate.

The full-width half maximum (FWHM) value of the diffraction angle of 34.2º is 0.31º (5.41 mRad), indicating a small dispersion of the ZnO crystallites around the (0002) plane orientation. The mean grain size of the ZnO crystallites at the (0002) peak was estimated using Debye-Scherrer's equation (2.18). The result showed that the average crystallite size of the ZnO deposited thin film was 28 nm for the (0002) orientation. This value is comparable to those reported in the reference [153], and to that of the annealed sample in the reference [276] for high-quality ZnO film.

A very low-intensity peak can also be observed at 2θ of 30.78 º, corresponding to ZnO crystals orientation in the $(10\bar{1}0)$ plane compared to the reference diffraction angle of the XRD JCPDS card #75-1533. The estimated texture coefficient (TC %) of the ZnO (0002) orientation was calculated using equation 2.17. Results showed that the ZnO crystal orientation in (0002) plane was dominant over that of the other texture, with a TC% value of 98.5%.

XRD analysis results showed that the grown ZnO film has wurtzite or hexagonal crystalline structure with the preferred (0002) plane orientation. This is particularly important for the piezoelectric properties and the performance of ZnO thin film-based surface acoustic wave devices, as discussed in section 2.3.

Thus, the quality of ZnO thin film is mainly determined by the crystal structure and orientation of ZnO crystallites which they should be possessed a wurtzite shape and orientation plane of (0002). This structure showed the highest piezoelectric coefficients values along the c-axis compared to other crystals structures and orientation. This is important for better piezoelectric performance (converting mechanical stress into electrical potential) and the quality factor of the generated SAW. The existence of defects such as cracks, impurities, and low TC% of the orientation plane of (0002) (e.g. different crystal

orientations) have a great impact on film quality, hence the piezoelectric properties. For example, they have a negative influence on electromechanical coupling coefficient, piezoelectric coefficients, and the generation and propagation of the SAW. The sensing performance of the devices depends on the properties of the SAW; therefore, low film quality and defects may cause acoustic signal attenuation and low-quality factor and operating frequency which eventually decrease sensors sensitivity and performance.

4.3 Characterisation of ZnO nanorods grown on the surface of the ZnO thin film-based SAW devices

The ZnO nanorods were grown on the delay line region of the SAW device with a wavelength of 160 μm using the hydrothermal process. The growth process was carried out by using a precursor solution of zinc nitrate 25 mM, where the pH was adjusted to 10.3 by adding some drops of ammonium hydroxide, and then the solution was heated to 85 ^{o}C and left for 4 hours. The full experimental method has been discussed in detail in section 3.3.

Figure 4.5 shows the SEM image of the ZnO NRs that were grown directly over the ZnO thin film without depositing an insulating layer between the ZnO thin film and NRs. The results showed that the ZnO NRs had coated the whole area with high and uniform densities of columnar structures perpendicular to the surface of the ZnO thin film. The ZnO NRs had a similar appearance of the ZnO thin film as there were no apparent gaps between the nanorods. Also, they did not possess rod-like shaped nanostructures, and it was difficult to distinguish between the ZnO thin film and the grown ZnO NRs. Hence, it was clear that growing ZnO NRs directly over the surface of the ZnO thin film resulted in the formation of porous ZnO layer instead of actual ZnO NRs. This can be attributed to ZnO thin film which provides a high density of active nucleation sites and a suitable surface property such as surface roughness and crystallites sizes for growing nanorods.

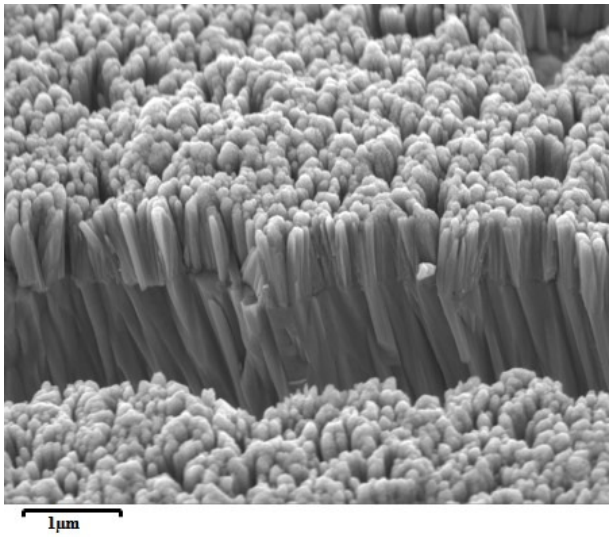

Figure 4.5 SEM topographical image of the ZnO nanorods that grown on the ZnO thin film-based SAW device without SiO_2 and seed layers

Therefore, the surface of the ZnO thin film was first coated with an insulating layer of silicon dioxide (SiO_2) with a thickness of 150 nm to separate the ZnO thin film from the nanorods, followed by the deposition of a 30 nm of ZnO seed layer to provide the required nucleation sites for nanorods. Figure 4.6 shows the SEM topographical image of the ZnO NRs grown on the seed layer over the top surface of the ZnO thin film. The SEM morphological image revealed that the ZnO NRs exhibited a highly- packed density over the surface of the ZnO thin film with a homogenous distribution and no apparent defects. Moreover, the grown ZnO NRs can be easily distinguished since they exhibited well-defined rod-like shaped nanostructures, and the gaps between the nanorods are clearly noticeable.

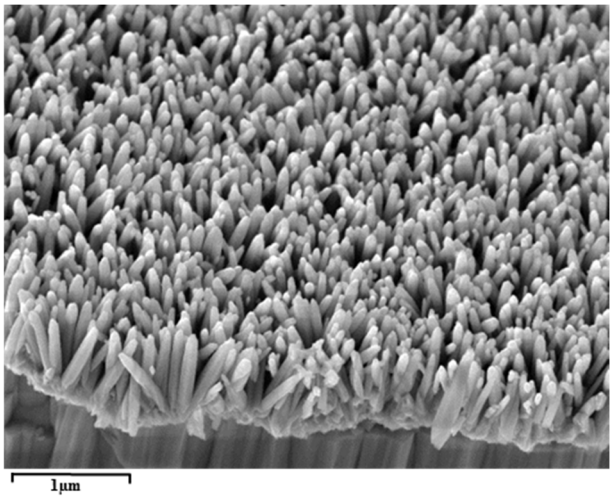

Figure 4.6 SEM topographical image of the ZnO nanorods grown on the ZnO thin film with a layer of 150 nm thick SiO_2 and a seed layer of 30 nm thick ZnO

Furthermore, the ZnO NRs were equal in length, and they were aligned vertically in columnar structures perpendicular to the ZnO thin film, as shown in Figure 4.7. The ZnO NRs showed excellent adhesion to the substrate, and there were no dislocations or apparent defects. The average length and the diameter of the ZnO NRs were 900 nm and 65 nm, respectively.

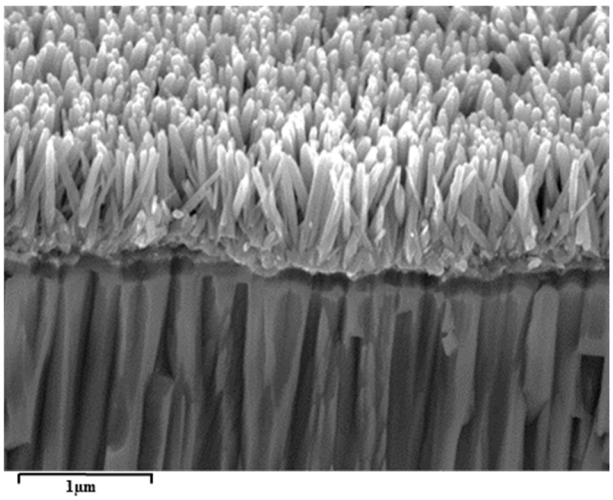

Figure 4.7 SEM cross-section image for the ZnO nanorods grown on the ZnO thin film with a layer of 150 nm thick SiO_2 and a seed layer of 30 nm thick ZnO

The XRD analysis and the corresponding JCPDS reference cards of the ZnO NRs grown on the 30 nm ZnO seed layer and 150 nm SiO_2 insulating layer can be seen in Figure 4.8. An intense peak is found at a diffraction angle (2θ) of 34.35^o corresponding to the ZnO orientation in the preferred plane (0002) along the c-axis and perpendicular to the substrate, and another peak at 2θ of 31.8^o corresponds to the ZnO orientation in the plane (1010) as per the XRD JCPDS card# 75-1533.

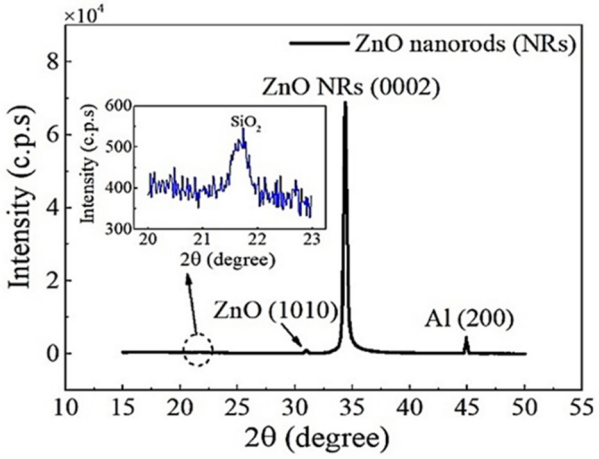

Figure 4.8 XRD analysis of the ZnO NRs grown on the ZnO thin film with a layer of 150 nm thick SiO_2 and a seed layer of 30 nm thick ZnO. The insert shows the rescale plot of the peak at 2θ of 21.73°

The peak at 2θ of 34.35° is likely to be a combined peak of ZnO NRs and the ZnO thin film, and this reveals that the overall ZnO crystal orientation in the (0002) plane is dominant in the whole device structure. However, there is a small peak with very low intensity at 2θ of 21.73° corresponding to the SiO_2 material based on XRD JCPDS card# 52-0650. Besides, the aluminium (200) orientation can also be observed at 2θ of 44.85°.

Thus, the ZnO NRs grown on the surface of the ZnO thin film-based SAW devices possess the structural properties that are expected to enhance the sensing performance of the device because of the high surface-to-volume ratio.

The crystal orientation of ZnO drives the growth of the nanorods in a columnar structure which gives the rod-like shaped nanostructures that aligned vertically and perpendicular to the ZnO thin film and results in a uniform distribution of the nanorods. Besides, the high aspect ratio (small diameter and long length) increases the surface-to-volume ratio as well as the spaces between the nanorods that allows the targets (e.g. humidity or photons) to penetrate and interact with the nanorods. Therefore, the amount of the targets binding and interacting with the nanorods increases which causes enhancement to the detectable signal, hence the sensitivity of the SAW sensors.

4.4 Eigen-frequency and modes of vibrations based on COMSOL simulation

The eigen-frequency values and vibration modes patterns of the Lamb wave modes were evaluated by FEA using COMSOL software, as discussed in section 3.7. Figure 4.9 shows an example of the FEA simulation results for the total displacement of the cross-section of the SAW device at a wavelength of 160 µm.

The X-axis of the plots represents the IDT period or a one-wavelength (λ = 160 µm) unit cell. The Y-axis shows the total device thickness (H = 55 µm), and the surface of the 2D cross-section represents the total displacement in the XY plane. The A0 and A1 modes are shown in Figure 4.9a and 4.9c, whereas, the symmetric S0 and S1 modes are plotted in Figures 4.9b and 4.9d, respectively. The deformation of the device or the structural displacement and the acoustic wave propagation occurred throughout the whole device thickness have shown the excitation of Lamb wave modes.

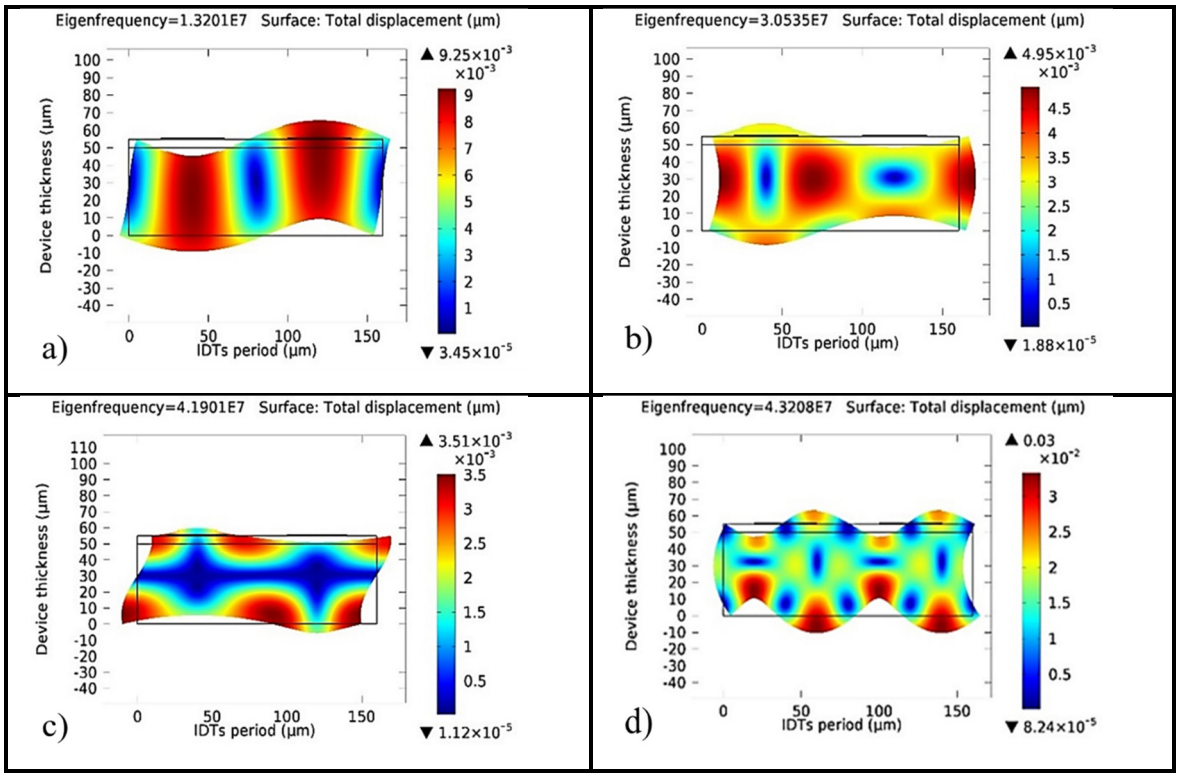

Figure 4.9 The eigen frequencies and shape of deformation (displacement) obtained from COMSOL simulation of a 2D cross-sectional model of the ZnO thin film on aluminium foil with a wavelength of 160 µm showing the various types of Lamb wave vibration modes a) A0, b) S0, c) A1 and d) S1

The acoustic wave modes are determined by the ratio between the total thickness of the device and the designed wavelength. When the ratio of the wavelength to device thickness (λ/H) > 1, then Lamb wave is dominant, and if the (λ/H) ratio < 1, Rayleigh wave can be observed as the first excitation mode [352]. Therefore, it is clear that the Lamb wave modes were dominant in all devices of wavelengths of 100 µm, 160 µm, 200 µm, 300 µm, and 400 µm as per the FEA results summarised in Table 4.1.

Table 4.1 FEA simulation results showing the vibration modes and the corresponding eigen-frequencies for ZnO thin film/aluminium foil devices of various wavelengths

Mode	Device wavelength (µm)				
	100	160	200	300	400
A0	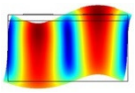 24.22 MHz	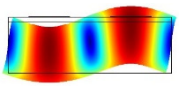 13.2 MHz	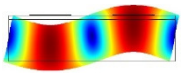 9.58 MHz	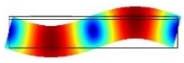 5.06 MHz	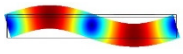 3.09 MHz
S0	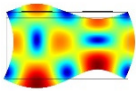 38.88 MHz	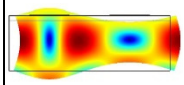 30.53 MHz	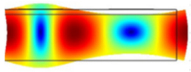 25.64 MHz	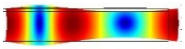 17.73 MHz	 13.44 MHz
A1	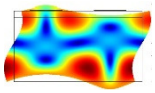 55.60 MHz	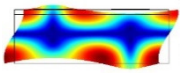 41.9 MHz	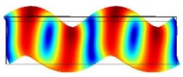 24.31 MHz	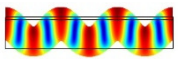 24.26 MHz	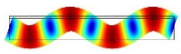 9.62 MHz
S1	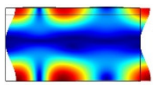 62.42 MHz	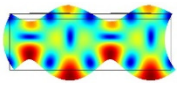 43.21 MHz	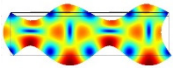 39.17 MHz	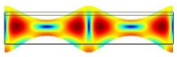 31.94 MHz	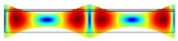 25.52 MHz

The simulation results give a prediction of the vibration patterns of the zero-ordered (A0 and S0) and the first-ordered (A1 and S1) Lamb wave modes, and the corresponding resonant frequency (eigen-frequency) value at which each mode is excited. Moreover, the FEA results show that the resonant frequency of the vibration mode was decreased with increasing wavelength.

4.5 The frequency response of the ZnO thin film-based SAW devices

Based on the simulation results, the ZnO thin film-based SAW devices of the wavelengths of 100 µm, 160 µm, 200 µm, 300 µm, and 400 µm were fabricated using the lithography and lift-off processes. The frequency responses of these devices were obtained using a vector network analyser where the reflection (S11) and transmission (S21) signals were used to determine the resonant frequency.

Hence, the frequency spectra of the SAW devices of wavelengths 100–400 µm using S11 signal are shown in Figure 4.10. The results show that the Lamb wave modes were excited in the four devices of different wavelengths, as predicted in the simulation.

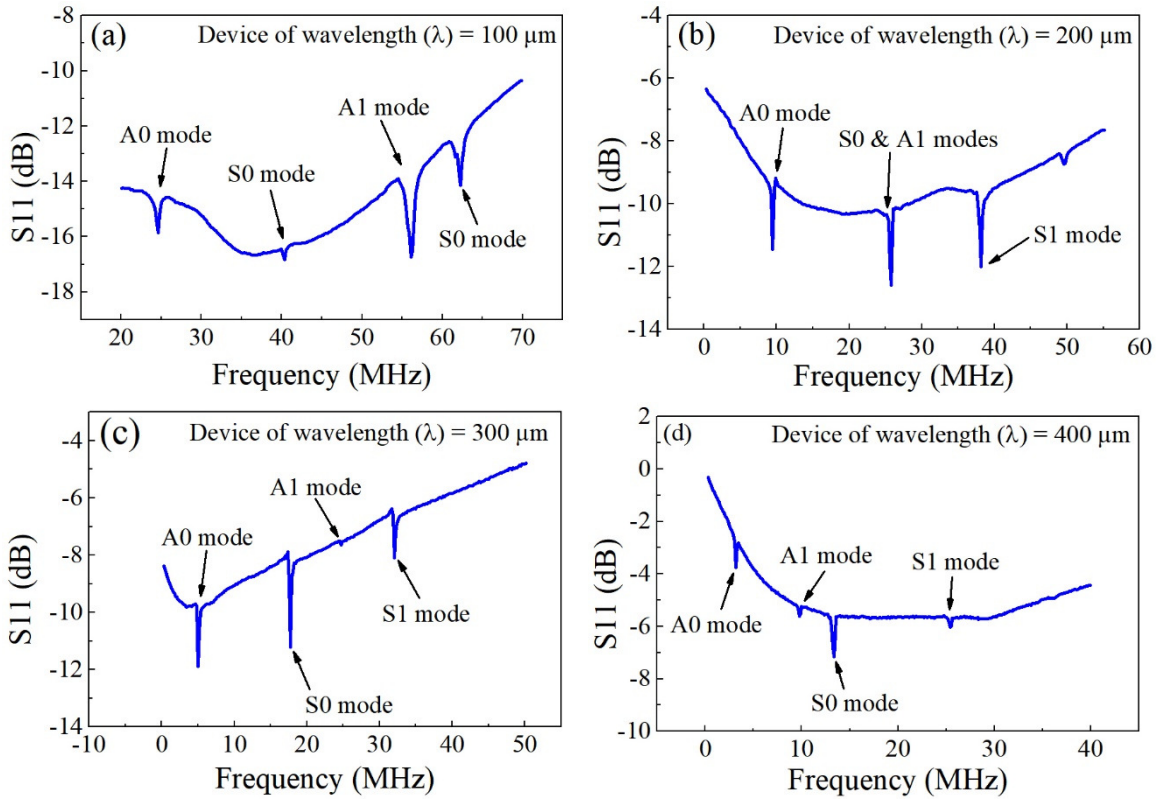

Figure 4.10 Frequency spectra of the SAW device of various wavelengths a) 100 µm, b) 200 µm, c) 300 µm, and d) 400 µm. S11 signal was used to determine the resonant frequency

The frequency responses of the fundamental modes (A0 & S0) were then further characterised, and the S21 signals are plotted in Figure 4.11. The results show that the (S21) signals have main lobe peaks at the central frequency values as well as multiple sides' lobes

that vary in number and magnitude. The side lobes mainly result from IDT defects arising during the fabrication process due to the high surface roughness and waviness of the substrate leading to IDT pairs mismatching, in addition to the internal reflections of the acoustic signals.

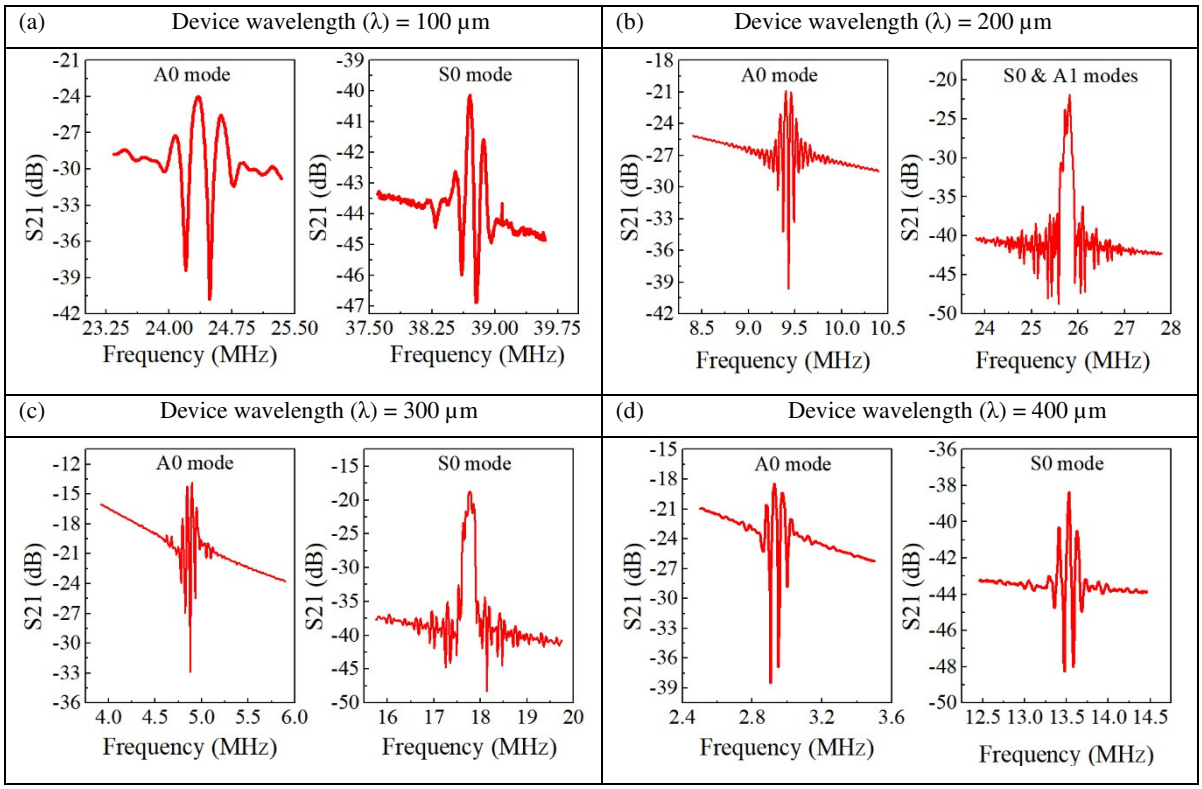

Figure 4.11 Frequency spectra of SAW devices of various wavelengths a) 100 µm, b) 200 µm, c) 300 µm, and d) 400 µm. S21 signal was used to determine the resonant frequency

It was observed that the transmission (S21) signals exhibited low values of insertion losses that varied from -13.5 to -43.7 dB. Besides, the S0 modes possessed lower insertion losses compared to those of the A0 modes for the same wavelength since this mode is extensional and less dispersive compared to A0 mode. The central frequency values of the main lobes are comparable to the resonant frequency results obtained for S11 signal but with slight variations, as shown in Figure 4.12.

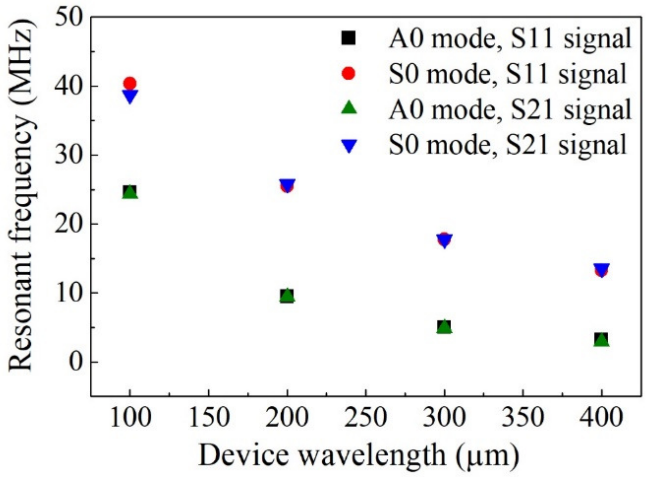

Figure 4.12 The agreement of resonant frequency results of reflection (S11) and transmission (S21) signals of A0 and S0 modes

The other SAW device with the wavelength of 160 μm was considered for growing ZnO nanorods on its delay line region, and the frequency response was characterised before and after the growth of the nanorods. Hence, the frequency spectrum of the S11 signal was obtained to identify the resonant frequencies and the corresponding vibration modes, as shown in Figure 4.13. The four Lamb wave modes A0, S0, A1 and S1 were clearly observed in the spectrum according to the results obtained by simulation.

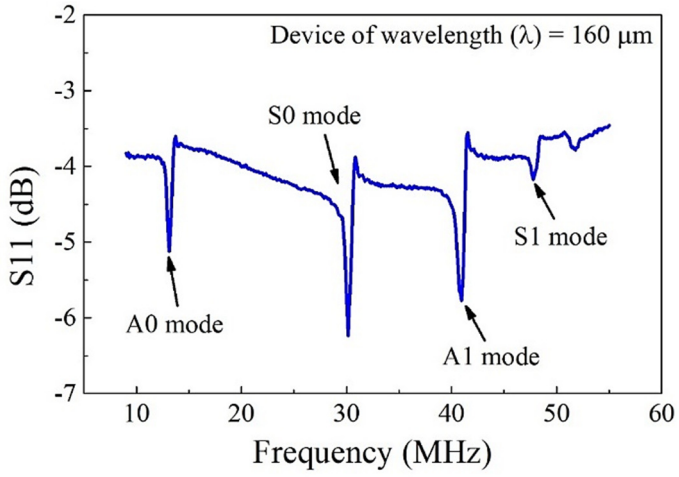

Figure 4.13 Frequency spectra of the SAW device of the wavelength of 160 μm. The S11signal was used to determine the resonant frequency

Furthermore, the frequency response of the fundamental modes using the S21 signal was further investigated before and after growing the ZnO nanorods, as shown in Figure 4.14a and 4.15b, respectively. The main lobe of the S21 signals of the A0 and S0 modes for the SAW device without ZnO nanorods exhibited two consecutive and identical peaks where

the insertion losses of the two modes were nearly the same. However, the shapes of these two peaks were less identical, and they showed a slight change in insertion loss when the ZnO nanorods were grown on the surface of the device. This can be attributed to the perturbation of the acoustic wave propagation due to mass loading caused by the grown nanorods.

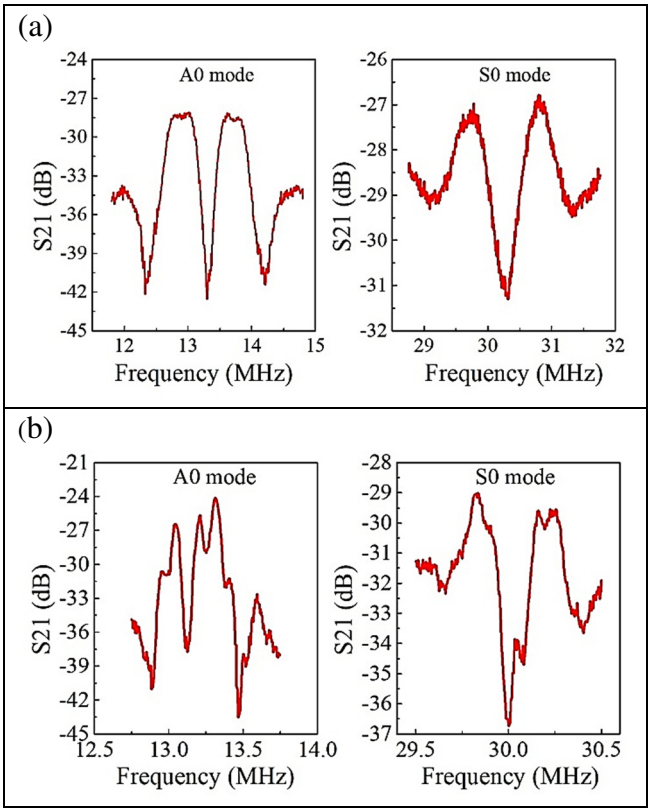

Figure 4.14 Frequency spectra of the SAW devices of the wavelength of 160 µm
a) without ZnO nanorods and b) with ZnO nanorods

Results show that the measured resonant frequencies of the devices of various wavelengths exhibited excellent agreements with those obtained by FEA, as shown in Figure 4.15. It shows that the resonant frequency was decreased with device wavelength in both measured and simulation results. There was a slight variation between the simulation and the experimental values due to film defects and the fabrication process.

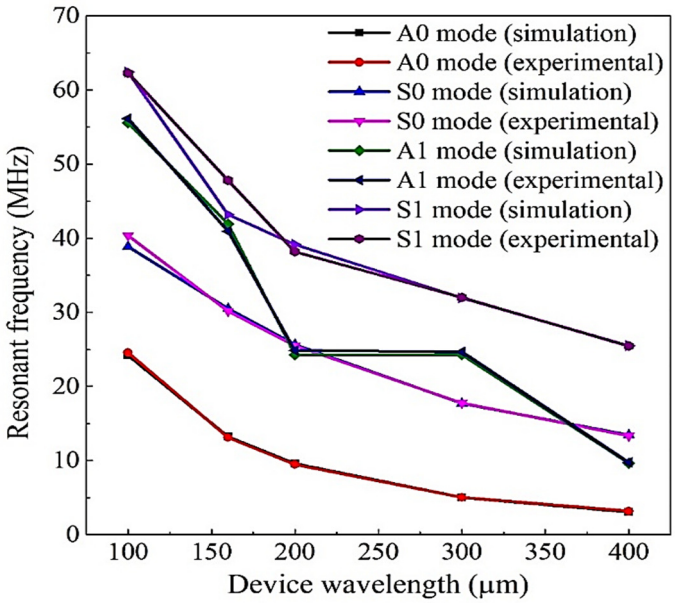

Figure 4.15 The agreement between the values of resonant frequencies obtained expeirmentally and from simulation for Lamb wave modes A0, S0 and A1

4.6 The frequency response of the ZnO thin film-based SAW devices in bent positions

Flexible ZnO thin film-based SAW devices were placed in a bent-up and bent-down positions to perform as flexible sensors. Bending the SAW devices generates some defects and cracks in ZnO thin film as well as induces film strain, which eventually influences the propagation of the acoustic wave.

Figure 4.16 shows the frequency response of the fundamental Lamb wave modes of the SAW devices with wavelengths of 160 μm and 200 μm, when they were placed in a bent-up and bent-down positions with curvature radii of 10 mm and 50 mm, respectively. It shows that the resonant frequencies were shifted to lower values when the devices were bent. This shift was more significant in the bent-up position than that of the bent-down position since more cracks are likely to be produced due to tensile strain. On the other hand, the insertion loss was slightly affected when the device was bent-down compared to its original value in a flat position, whereas it was increased when the device was bent-up. This was much significant

for S0 mode because it propagates in a higher frequency and closes to the surface. Thus, the acoustic wave signal continued to propagate and be detectable despite the strain and film defects generated due to bending of the devices. This is particularly important for flexible SAW sensors when performing sensing in bending conditions.

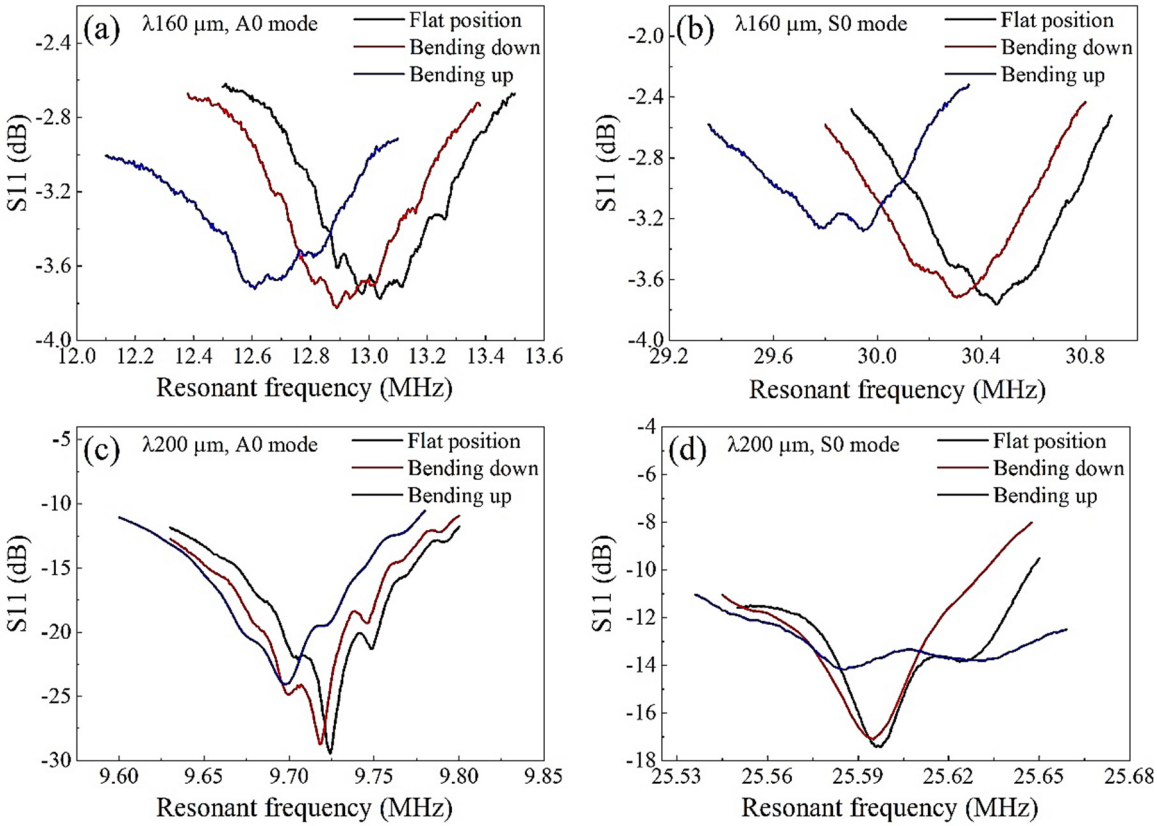

Figure 4.16 Frequency spectra of SAW devices in flat, bent-up and bent-down positions with wavelengths of a) 160 µm, A0 mode, b) 160 µm, S0 mode, c) 200 µm, A0 mode, and d) 200 µm, S0 mode

High-quality ZnO thin film is an essential requirement for the piezoelectric performance of the SAW device, and it is influenced by the deposition process and the properties of the substrate. The IDTs also play a vital role in exciting the acoustic wave modes, since the electrical potential is applied to the piezoelectric material (ZnO thin film) through them. Moreover, the accuracy of the wavelength of the SAW device is highly associated with the precision of the lithography process of the IDTs. Thus, fabricating IDTs with a thickness of ~150 nm and a length of ~9 mm over a non-uniform surface and a substrate with high surface roughness such as aluminium foil can be considered to be a significant challenge.

Figures 4.17a and 4.17b show microscopic images of the IDTs defects such as broken IDTs during the lithography and lift-off process, and the mismatching of the period (λ/4) because the dimensions of the fingers and the inter-spaces widths are different. Figures 4.17c and 4.17d show the IDT patterns on the aluminium foil and silicon substrates, respectively. It is clear that the silicon substrate exhibited distinct IDT patterns without apparent defects, whereas the surface of the aluminium foil substrate showed some defects and scratches that caused severe damage to the IDT patterns.

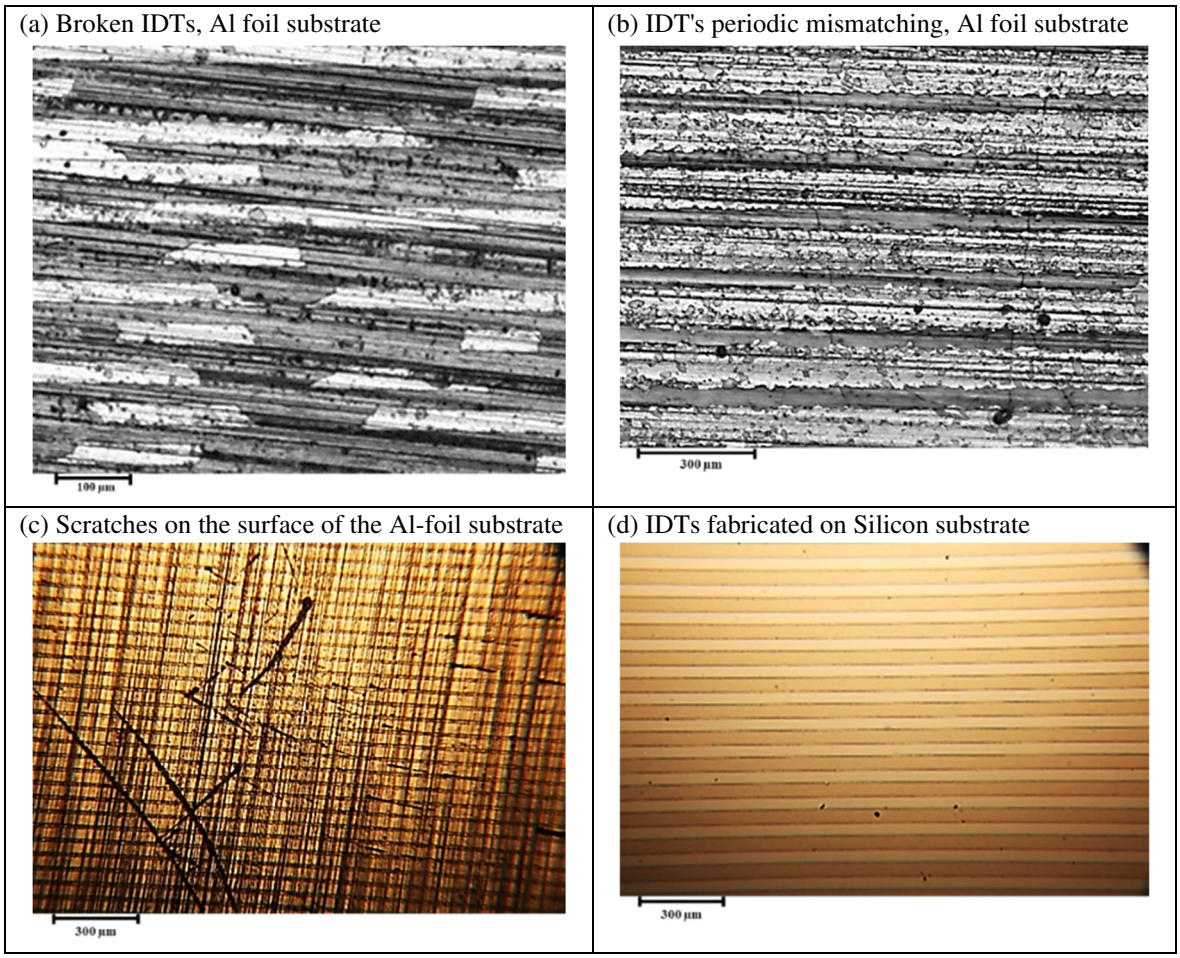

Figure 4.17 Microscopic images of the IDTs of fabricated SAW devices showing a) broken IDTs, b) IDT periodic mismatching, c) scratches on the Al foil substrate and d) IDTs fabricated on silicon substrate

The scratches shown in figure 4.17c cause severe defects in ZnO thin film and nanorods and damage to the IDTs which eventually result in low quality and attenuation of the surface acoustic wave and degradation in sensing performance of the devices.

4.7 Summary

The surface morphology of ZnO thin film showed large ZnO grain-like structures with an average diameter of 350 nm. The results of the cross-section image showed that the ZnO thin film was vertically aligned in columnar structures of nanocrystals perpendicular to the substrate. The XRD results reveal that the ZnO crystals exhibited a strong texture in the orientation of (0002) plane along *c*-axis with texture coefficient (TC%) of 98.5%. Furthermore, the film possessed low compressive stress of -0.52 GPs, which is suggested that the elastic and flexible nature of the aluminium foil substrate relieves some of the residual stress of the deposited film. These results suggested that the ZnO thin film possessed the preferred orientation and structure for high piezoelectric coefficients.

The ZnO nanorods showed highly packed density of well-defined rod-like shaped nanostructures, and they were aligned vertically and perpendicular to the ZnO thin film. The average length and diameter of the ZnO NRs were 900 nm and 65 nm, respectively.

The simulation results for the vibration modes of ZnO thin film SAW devices showed that the structural displacements occurred throughout the whole device thickness which indicates the excitation of the Lamb wave vibration modes. The Eigen frequencies were identified for these vibration modes for all designed wavelengths. Hence, the frequency responses obtained experimentally were compared with the corresponding simulation results, and they were in good agreements. Furthermore, the resonant frequency of the acoustic signals was downshifted, and the insertion loss was increased when the devices were placed in bent positions.

Chapter Five

Temperature sensing using the flexible ZnO thin film-based SAW device

5.1 Introduction

The demand for flexible temperature sensors has remarkably increased due to the need for monitoring the temperature in real-time as well as for health and safety in harsh and hazardous conditions. Therefore, ZnO thin film on aluminium foil-based SAW devices was investigated as flexible temperature sensors. Motivated by their double-layer structure which aluminium foil possesses a high value of thermal expansion coefficient (TEC) and other elastic properties, and the excellent piezoelectric properties of ZnO thin film. Moreover, these devices are operated in Lamb wave modes which propagate through the whole device thickness. Thus, their phase velocities are influenced by changes in the physical properties of both aluminium foil and ZnO thin film.

In this study, the temperature coefficient of frequency (TCF) of various ZnO thin film-based SAW devices and vibration modes are investigated in an equilibrium condition when thermal exchange reaches to a steady-state level, and no further increase in temperature has occurred. Therefore, the devices of wavelengths of 100 μm, 160 μm, 200 μm, 300 μm, and 400 μm are placed inside a closed oven which temperature is adjusted by the digital controller as discussed in section 3.4. The importance of TCF is that the higher value of TCF is more sensitive to changes in temperature.

On the other hand, temperature sensing in the *in-situ* condition is investigated using a Peltier system which temperature is adjusted quickly, and real-time response is obtained. Frequency responses of SAW devices with wavelengths of 160 μm and 200 μm are recorded

when the devices are placed in flat and bent-up positions over several cycles of changing temperature.

5.2 Equilibrium condition temperature sensing

5.2.1 TCF of a flexible SAW device

The resonant frequencies of SAW devices with varying wavelengths (λ); 100- 400 µm were recorded at various temperatures for different vibration modes. Hence, the frequency shifts that were resulted from the temperature change were obtained. Figures 5.1a and 5.1b show a linear relationship between the resonant frequency shift and the change in temperature for A0 and S0, respectively.

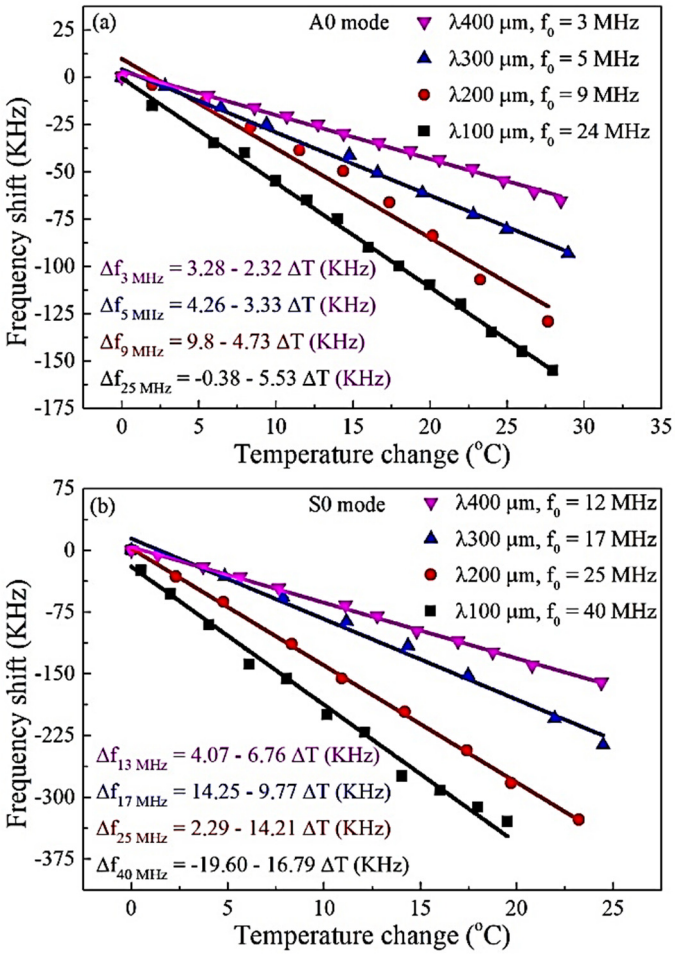

Figure 5.1 The relationship between frequency shift and temperature change of different SAW device's wavelengths (λ) and various resonant frequencies (f_0) for a) A0 and b) S0 vibration modes

The resonant frequencies for all vibration modes were decreased when the temperature increased. This can be attributed to changes in the stiffness constant, elastic properties, thermal expansion coefficient and density of the materials the SAW devices are made.

The S0 modes showed higher frequency shifts than those of the A0 modes for the same temperature change and device wavelength. For instance, the frequency shifts for the SAW device with a wavelength of 100 µm at 20 ^{o}C were -335 kHz and -110 kHz corresponding to S0 and A0 respectively. Thus, the S0 mode showed ~3 times the size of a shift greater than that of the A0 mode, and this is due to the higher value of resonant frequency of the S0 mode which results in larger detectable shifts in frequency (higher resolution).

Furthermore, the values of slopes of these curves represent the rate of the change in resonant frequency relative to temperature change ($\Delta f/\Delta T$). The slopes also decreased with an increase in resonant frequency for the same mode. The TCFs were calculated using the $\Delta f/\Delta T$ results for all the corresponding resonant frequencies and vibration modes using equation 2.36 (in section 2.5.1). The obtained TCF values are shown in Figure 5.2 as a function of resonant frequency for the A0 and S0 modes.

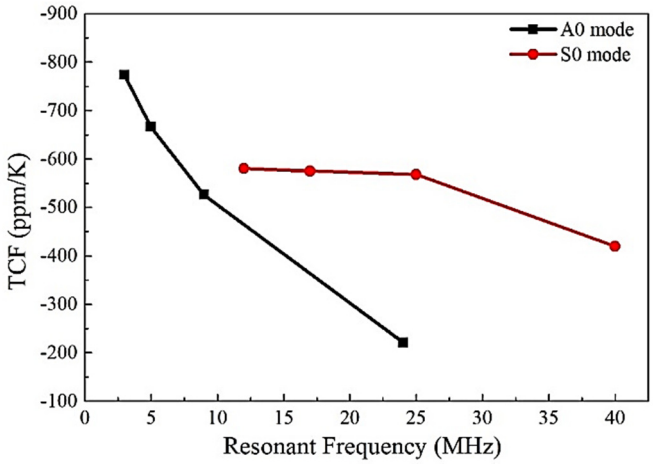

Figure 5.2 The relationship between TCF values and resonant frequencies for A0 and S0 modes

All the TCF results have negative signs since the resonant frequency of the SAW devices shifts to lower values when the temperature increases. The maximum absolute value of TCF

was 773 ppm/K at a resonant frequency of 3 MHz (A0 mode) of the device with a wavelength of 400 µm. In general, a substantial value of TCF is desired for SAW-based temperature sensors for then to exhibit better performance and sensitivity. This is among the highest TCF values (sensitivity) that has been obtained compared to those flexible SAW devices discussed in section 2.5.1 and summarised in table 2.3. Moreover, it is exceptionally high in comparison to the values of sensitivity of rigid substrates such as silicon (TCF ~ 20- 50 ppm/K) [352].

Furthermore, the absolute values of TCFs decreased with increases in frequency. In the case of A0 modes, TCFs decreased significantly when the resonant frequency was increased. They were decreased only gradually with slight variations for the S0 mode which exhibited relatively stable TCF values against different resonant frequencies before dropping markedly at 40 MHz.

On the other hand, the relationship between the TCF and device wavelengths is illustrated in Figure 5.3. The absolute values of TCFs increased with device wavelength, assuming that the thickness of the devices (H) was the same for all samples. Moreover, the TCFs for the S0 modes of the SAW devices with wavelengths of 100 µm and 200 µm were higher than those for the A0 mode, but they remained at similar levels for wavelengths greater than 200 µm. In contrast, the TCF results for the A0 mode continued to increase, and they possessed higher values than those of the S0 mode for devices with wavelengths of 300 µm and 400 µm. Thus, the A0 modes showed significant variations in response to temperature change than the S0 mode of various wavelengths and resonant frequencies.

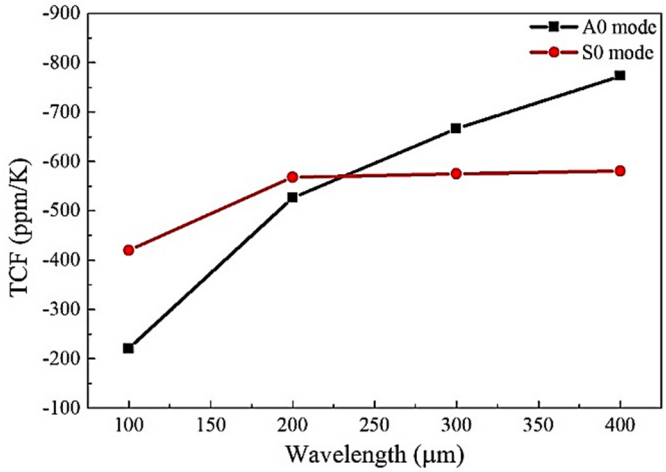

Figure 5.3 The relationship between TCF values and wavelengths of SAW devices for A0 and S0 modes

Thus, increasing device wavelength results in increasing the absolute value of TCF. However, there are some limitations to increasing the wavelength further in order to make SAW devices with higher TCFs. For example, the IDTs will occupy a larger area on the surface of the SAW device, and this will increase the overall size of the sensor. Also, it will reduce the resonant frequency of the fundamental A0 and S0 vibration modes to several kilohertz or a few megahertz resulting in reduced sensor accuracy, resolution, and precision.

Another SAW device with a wavelength of 160 μm was also examined for temperature sensing, and the frequency change of the fundamental modes as a function of temperature can be seen in Figure 5.4.

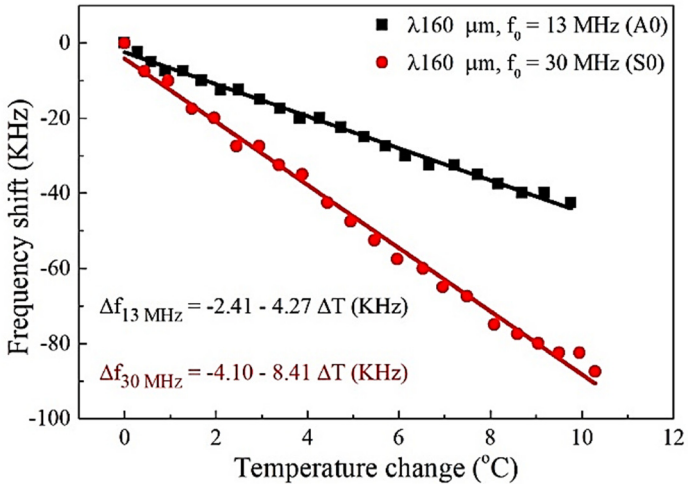

Figure 5.4 The relationship between frequency shift and temperature change of the SAW device of wavelength of 160 μm for A0 and S0 vibrating modes

The figure shows that the frequency shift has a linear relationship with temperature, and the rate of change in resonant frequency (Δf/ΔT) of the S0 mode is higher than that of the A0 mode. These results reflect the same response trend as obtained for the devices with wavelengths of 100-400 µm. The calculated TCF values for both fundamental vibration modes are summarised in Table 5.1.

Table 5.1TCF values of A0 and S0 mode for SAW device of wavelength of 160 µm

Vibration mode	Resonant frequency (MHz)	TCF (ppm/K)
A0	13	-315
S0	30	-288

The results show that the TCF values also have a negative sign as the resonant frequency decreased when the temperature increased. However, it was noticed that these values are less than those of the TCFs shown in Figure 5.2 except for the TCF of the A0 mode at 24 MHz for the device with a wavelength of 100 µm.

The TCF value of the SAW device is influenced by several factors, such as temperature and the thermal expansion coefficient (TEC) of the materials in its structure. The design of the SAW device consists of a bilayer of ZnO thin film and aluminium foil as the substrate. Therefore, this structure tends to be bent when the temperature increases due to mismatching in TEC between the aluminium foil and the ZnO thin film. This deformation has a significant impact on strain values of the device. However, aluminium foil has a TEC value of 23.6 ppm/K which is much larger than that of the ZnO whose TEC is only 4.7 ppm/K [352], and has smaller Young's modulus. It deforms and expands more easily compared to ZnO thin film. Therefore, it has a significant contribution to strain induction due to the large thermal expansion. Furthermore, increased temperature causes an increase in a strain which

decreases Young's modulus, and this results in decreasing phase velocity of the fundamental modes of Lamb wave as per equations 2.34 and 2.35. Thus, the resonant frequency was decreased when the was temperature increased, and the high TCF values obtained for the SAW devices are mainly attributed to the elastic and thermal properties of the aluminium foil substrate.

However, the Lamb wave mode is converged toward the Rayleigh wave mode at high-frequency levels or when high order Lamb mode is excited, or when the wavelength of a SAW device becomes smaller. In this case, acoustic waves propagate mostly at the top surface and confined in ZnO thin film which explains the decrease in TCF readings because of the lower TEC value of ZnO film. Besides, the S0 mode is less dispersive compared to the A0 mode, and therefore, it shows relative stable TCFs for low frequencies, because the TCF had decreased significantly at high frequency.

5.2.2 Real-time response of flexible SAW devices to temperature change

The frequency responses of the SAW devices in real-time were obtained for one cycle in order to investigate their stability and sensing performance in response to the temperature change in an equilibrium condition. The temperature was increased slowly and gradually to about ~50 ^{o}C to achieve a steady state of thermal equilibrium, and then it was held for a few minutes before it being reduced again. Changes in resonant frequencies were recorded continuously during temperature increase. The obtained real-time frequency shifts of the fundamental modes for the SAW devices with wavelengths of 400 µm and 160 µm are shown in Figure 5.5.

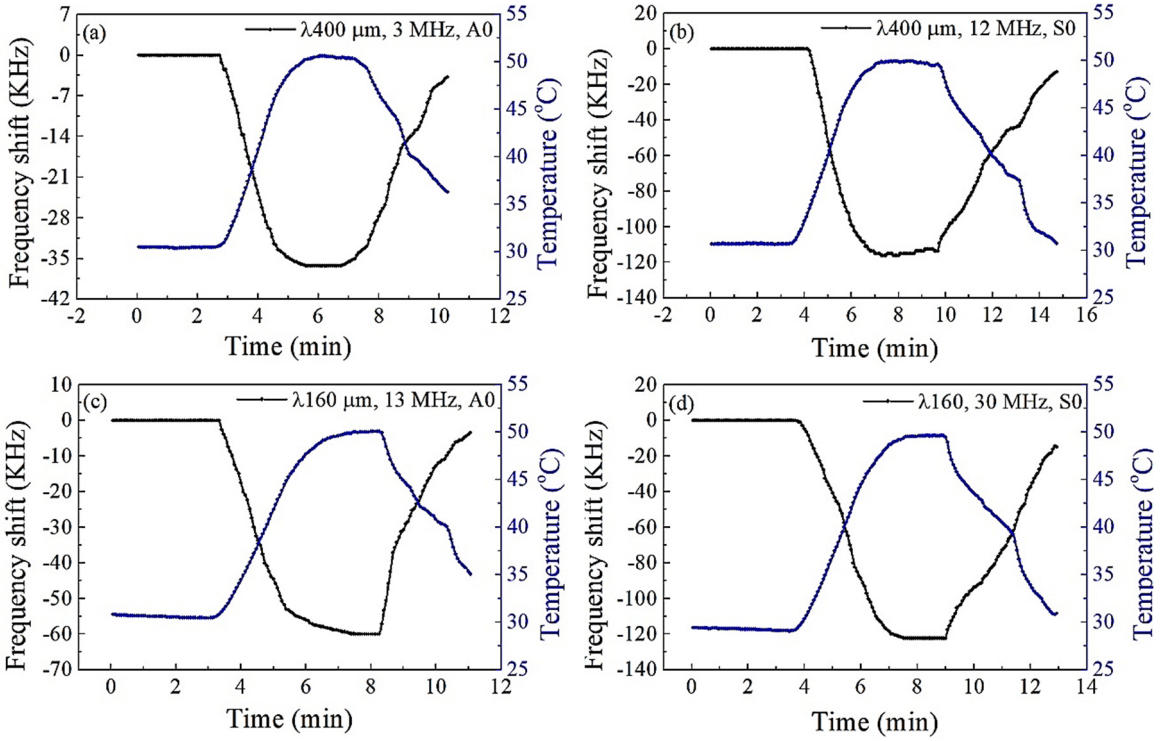

Figure 5.5 Real time response showing the changes in frequency shifts in response to temperature changes of SAW devices with wavelengths of a) 400 µm, A0 mode, b) 400 µm, S0 mode, c) 160 µm, A0 mode, and d) 160 µm, S0 mode. The devices were kept in flat position.

No frequency shift was noticed in the first few minutes before turning the oven on (thus start heating the samples) indicating that the sensor was stable against environmental factors. However, the resonant frequency then decreased as temperature increased until it reached a maximum shift where it held the same value when the temperature was stable, and it then increased as temperature decreased. The maximum frequency shift of the A0 mode of the device with a wavelength of 160 µm was 60 kHz, as seen in Figure 5.5c. This value is 1.7 times higher than that of the A0 mode of the device with a wavelength of 400 µm at the same temperature shown in Figure 5.5a. On the other hand, the frequency shifts obtained for the S0 mode for both devices were nearly the same, as shown in Figures 5.5b and 5.5d. This implies that the relatively low TCF values of the A0 and S0 modes of the 160 µm device were compensated by the higher resonant frequency values, resulting in a significant frequency shift. Hence, the sensitivity of the SAW device to temperature change is influenced primarily by the TCF and the values of the resonant frequency.

However, the SAW device with a wavelength of 400 µm, which has the highest TCF was further investigated in a bent-down position, as mentioned in section 3.4. The real-time frequency shifts in response to temperature change for A0 and S0 modes were obtained, as shown in Figures 5.6a and 5.6b, respectively. The frequency response of the fundamental modes exhibited nearly similar performance when the device was bent compared to the flat position. The maximum frequency shifts obtained for the A0 and S0 modes were -30 and -90 kHz respectively at a temperature of 50 °C. These values are less than that of the frequency shift obtained for the device when kept in a flat position by 14-19%. This is likely resulted from cracks in the film and the deformation due to the device being bent. It is suggested that the bimorph structure and aluminium foil relieved the strain and film stress produced by the device being bent and subject to thermal expansion. However, this would not be possible at high temperatures where the bent curvature would change and result in significant resonant frequency fluctuations.

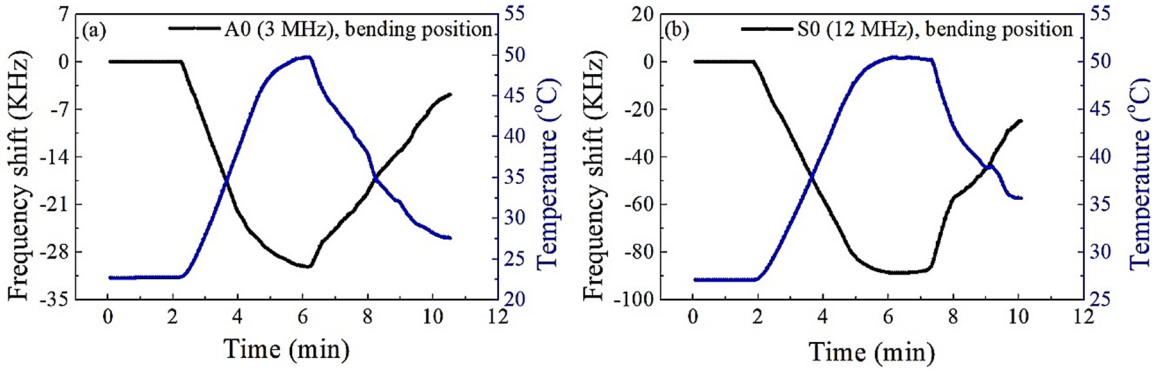

Figure 5.6 Real time response showing the changes in frequency shifts in response to temperature changes of SAW devices with a wavelength of 400 µm for a) A0 and b) S0 modes.
The device was kept in bent-down position

Thus, in order to maximise the sensitivity of the proposed flexible ZnO-based SAW device on aluminium foil, optimal values of TCF and resonant frequency should be carefully chosen. For example, in this study, the S0 mode showed a relatively high absolute value of TCF (571 ppm/k), fewer variations and more stability for a wide range of frequencies (12-25 MHz) and the maximum resonant frequency that held this value was 25 MHz for the device with a

wavelength of 200 µm. This device also has a high TCF value for the A0 mode. Therefore, it was selected for the *in-situ* investigation discussed in the next section

5.3 *In-situ* temperature sensing

The SAW devices with wavelengths of 160 µm and 200 µm were selected for further investigation in an *in-situ* condition where a Peltier system was used to control temperature change. The frequency responses of the fundamental modes of this device were obtained at various temperatures. Figures 5.7a and 5.7b show the linear relationship between resonant frequency shift and temperature change for the SAW devices of 160 µm and 200 µm, respectively.

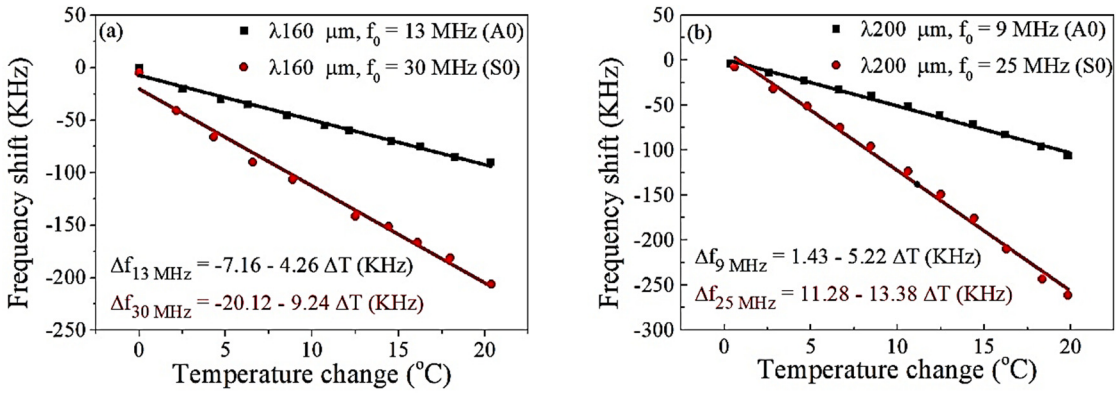

Figure 5.7 The relationship between frequency shifts and temperature change for A0 and S0 modes of SAW devices with wavelengths of a) 160 µm and b) 200 µm.

As in the previous findings, the S0 mode shows a higher rate of frequency shift in response to change in temperature (Δf/ΔT) than that of the A0 mode for the same devices. The Δf/ΔT of both modes of the device with a wavelength of 200 µm is slightly higher than that of the 160 µm device. This is due to the higher TCF of the 200 µm device. However, the high values of resonant frequencies of the 160 µm device kept this difference small.

Figure 5.8 shows a comparison between the values of TCF calculated for these devices in the *in-situ* condition and the values for the same devices in the equilibrium condition. The TCF results are similar to each device in both conditions, and this implies that the devices

possess excellent reliability and repeatability in various environmental conditions. This merit is due to the structure of the SAW devices and the material properties of the aluminium foil substrate such as high TEC and thermal conductivity as well as the characteristics of Lamb wave propagation.

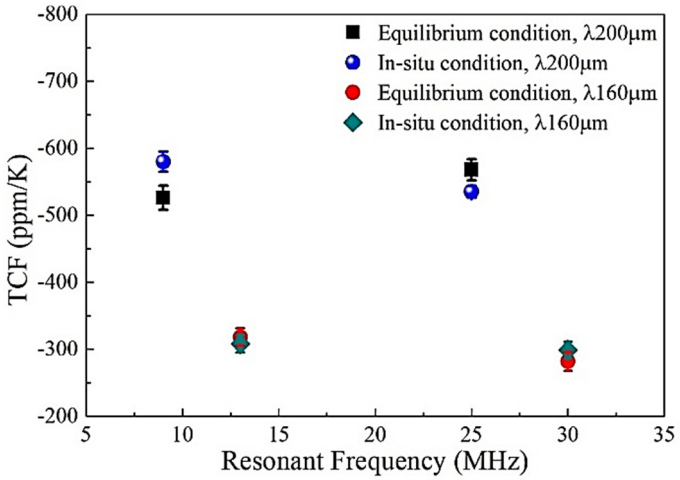

Figure 5.8 The agreement between TCF values obtained in equilbrium and *in-situ* conditions in relation to resonant frequency of SAW devices of wavelengths of 160 μm and 200 μm

The frequency response was obtained for one cycle where the temperature was increased to ~55- 60 ^{o}C within 10- 20 seconds and then decreased again over 15- 20 seconds, as seen in Figure 5.9. The results show that the maximum frequency shifts for the device of wavelength 200 μm were -114 and -385 kHz corresponding to A0 and S0 modes as shown in Figures 5.9a and 5.9b respectively. Meanwhile, they were -90 and -195 kHz for the A0 and S0 modes of the device of wavelength 160 μm as seen in Figures 5.9c and 5.9d.

Moreover, the devices exhibited a fast response time of less than 1.0 second/^{o}C. However, the minimum resolution of the recorded frequency was 1.0 second/spectrum due to the technical limitations of the network analyser and the LabVIEW application, and so it was impossible to measure the exact response time below this value.

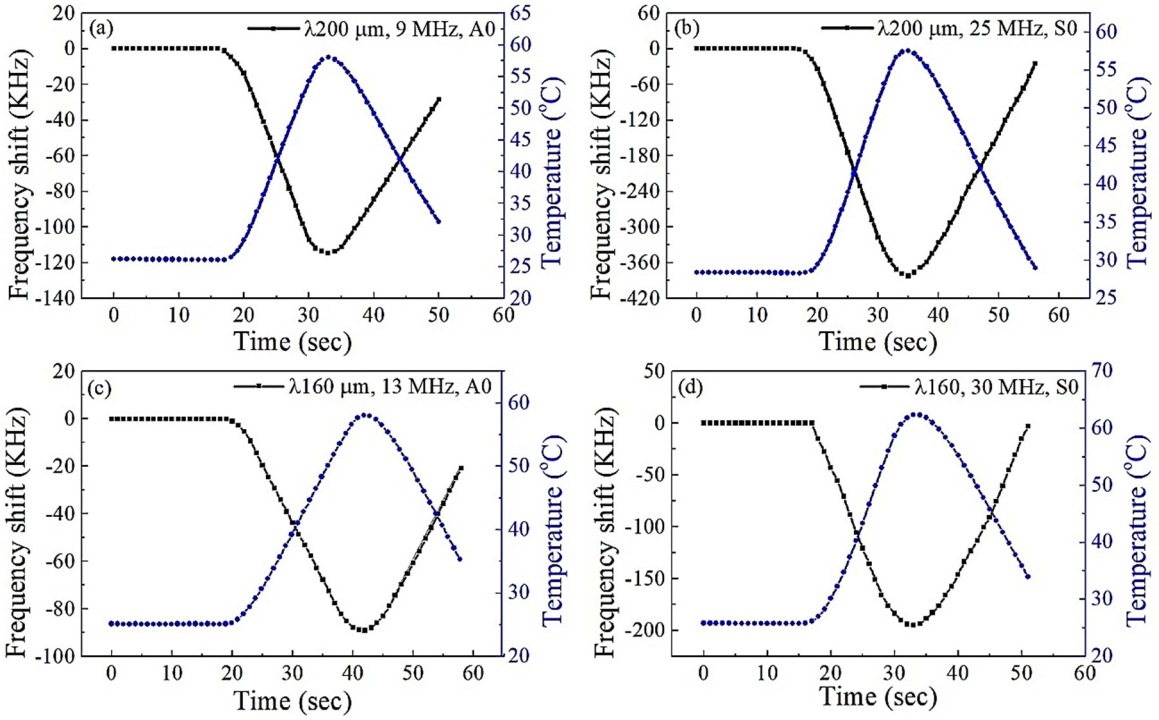

Figure 5.9 Real time response showing the changes in frequency shifts in response to temperature changes of SAW devices with a wavelength of a) 400 µm, A0 mode, b) 400 µm, S0 mode, c) 160 µm, A0 mode and d) 160 µm, S0 mode. The devices were kept in flat position

The SAW device of a wavelength of 160 µm was further investigated in the bent-up position, as shown in Figure 3.11. The frequency responses against temperature changes for the A0 and S0 modes were obtained, as shown in Figure 5.10a and 5.10b, respectively. The results show similar behaviour of the device in flat and bent positions in response to the change in temperature. Although bending the device might cause cracks in ZnO thin film, this had only a minimal influence on the frequency shift comparable to when the device was kept flat. This likely results from the effect of the aluminium foil, which dominates the changes in resonant frequency due to its high value of TEC.

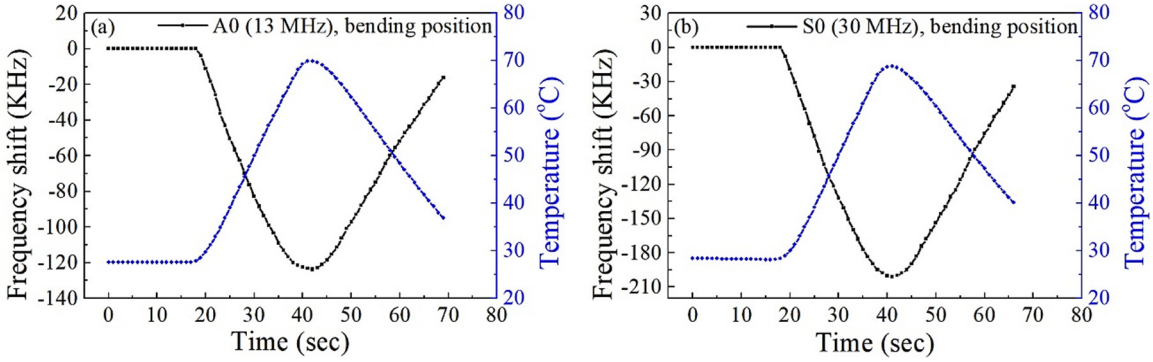

Figure 5.10 Real time response showing the changes in frequency shifts in response to temperature changes of the SAW device with a wavelength of 160 µm for a) A0 mode and b) S0 mode. The device was kept in bent-up position.

The real-time cycling response of the devices was also studied by heating up and cooling down the devices for five cycles, as seen in Figure 5.11. The devices showed a very fast response to temperature change, as the frequency was shifted down immediately when the temperature increased, and it was increased when the temperature decreased. Besides, the resonant frequency shift possessed a positive sign because it shifted upward to a higher frequency when the change in temperature was decreased below 0 °C.

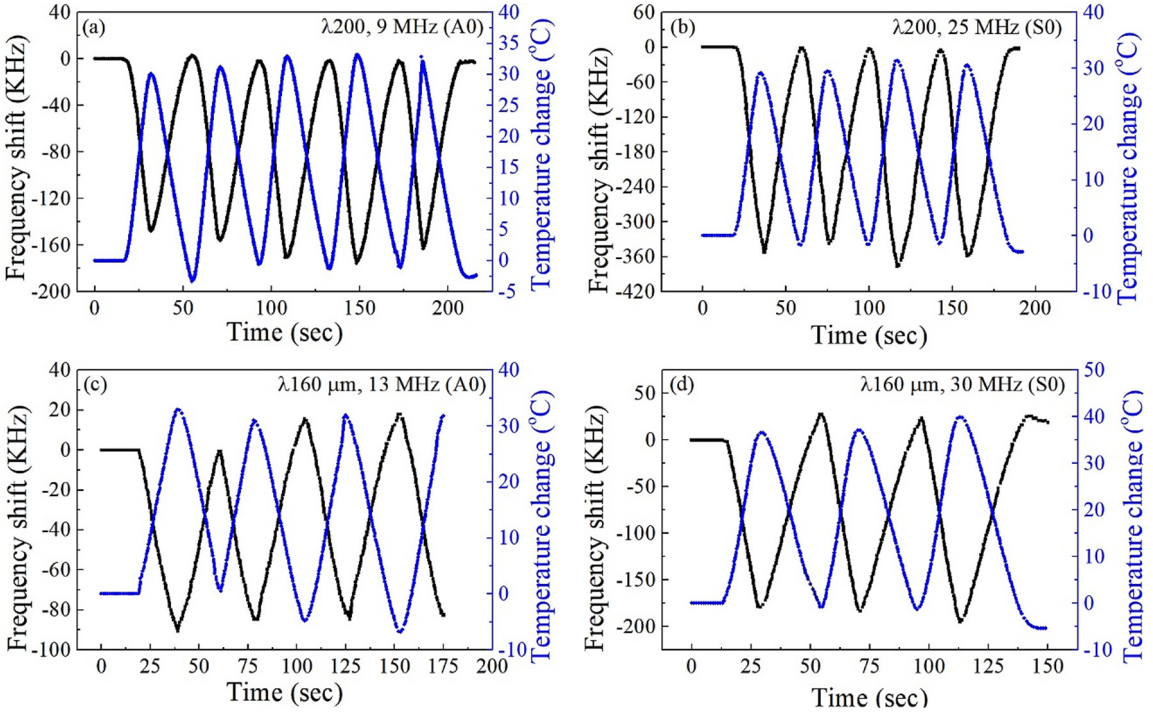

Figure 5.11 Cycling response to temperature change showing the change in frequency shifts of the SAW devices with wavelengths of a) 200 µm, A0 mode, b) 200 µm, S0 mode, c) 160 µm, A0 mode and d) 160 µm, S0 mode. The devices were kept in flat position.

Furthermore, the cycling response of the SAW device of wavelength 160 µm was obtained when the device was bent-up, as shown in Figure 5.12. Likewise, the performance of the SAW when the device was in the bent position showed excellent stability and repeatability over five cycles of temperature change.

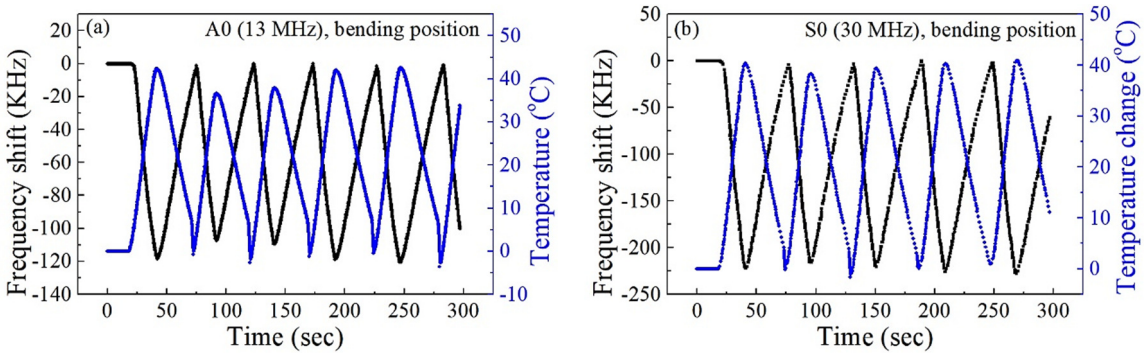

Figure 5.12 Cycling response to temperature change showing the change in frequency shifts of the SAW device with a wavelength of 160 µm for a) A0 mode and b) S0 mode. The device was kept in bent-up positions.

Thus, the performance of the devices exhibited excellent repeatability and reliability over several cycles of changing temperature as shown in Figure 5.13

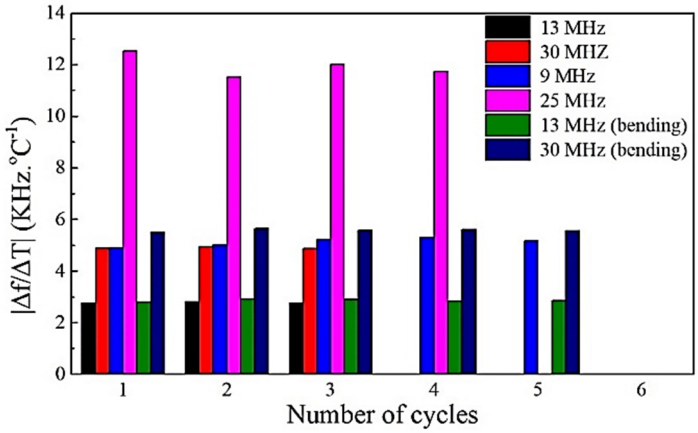

Figure 5.13 The reproducibility and reliability of temperature sensing of the SAW devices at various resonant frequencies in flat and bent-up positions

The variance of frequency change due to temperature change over several cycles was calculated based on the values of (Δf/ΔT) obtained from Figure 5.13. The variance was in the range of 0.19 to 8% for different resonant frequencies which indicates a good reproducibility and repeatability of the SAW device to detect temperature change. The

dynamic range of temperature sensing using the proposed flexible SAW devices was investigated from -5 to 60°C which is considered to be suitable for biomedical applications, but it is much less than that of thermocouples (-200 to +1200). However, these sensors have the advantage of flexibility that allows the detection of temperature while the devices placed in bending positions. The properties of the SAW signal were maintained after several cycles of increasing and decreasing temperature which indicates good film robustness over temperature change.

5.4 Summary

Flexible SAW devices based on ZnO thin film on aluminium foil substrate have been investigated for the first time as temperature sensors while the devices were placed in flat and bending (curved) positions.

The changes in resonant frequencies of various vibration modes for the ZnO/Al SAW devices possess a linear relationship with the change in temperature. Therefore, TCF values were calculated for all flexible ZnO thin film based-SAW devices with various wavelengths and vibration modes. The highest value of TCF was -773 ppm/K for the device with a wavelength of 400 µm, which is considered to be among the highest values of TCF reported in the literature for flexible SAW devices. The lowest TCF value was 288 ppm/K for the λ=100 µm device for the A0 vibration modes. These high readings are due to the high TEC value as well as the elastic properties of aluminium foil. The higher-order modes exhibited larger values of frequency shift and better performance in temperature sensing despite their lower TCF.

Furthermore, the real-time cycling response in *in-situ* condition showed that the devices exhibited excellent linearity to the changes in temperature when they were placed in flat and in bent up positions.

These sensors can be used to detect temperature change in the range of -5 to 60 ^{o}C which is much less than that of thermocouples, but they have the advantage of good linearity and bendability.

Chapter Six

UV sensing using the flexible ZnO thin film-based SAW device

6.1 Introduction

Sensing and monitoring UV light has received a substantial interest since it has been used in various critical applications. The ZnO possesses bandgap energy of 3.37 eV and large stable exciton binding energy of 60 meV at room temperature. Therefore, it has been widely exploited in the development of ZnO thin film-based UV light sensors. The basic principle of ZnO thin film in the detection of UV light is based on changes in surface sheet conductivity of ZnO film as a result of UV illumination which eventually influences acoustic wave velocity as discussed in section 2.5.2.

The flexible SAW devices with wavelengths of 160 µm and 200 µm are used to investigate the sensing performance to UV light. The devices are placed in flat, bent-up and bent-down positions at a fixed distance of high and low power UV light sources. The I-V characteristic curves of ZnO thin films are obtained to study the changes in surface sheet conductivity results from UV light illumination.

The frequency responses of Lamb wave vibration modes A0, S0 and A1 are recorded at various UV light intensities. It is suggested that the frequency shift caused by using the high-power UV light is resulted from changes in conductivity as well as temperature, whereas, it is mainly due to changes in conductivity only when the low power is used.

Furthermore, the frequency responses of SAW devices of a wavelength of 160 µm with and without nanorods are also investigated in order to study the influence of nanorods on the enhancement of the sensitivity to UV light. Real-time cycling responses are obtained by illuminating the device by a fixed value of UV intensity for several cycles, which changes in temperature and humidity are also monitored.

6.2 I-V characteristic curve of ZnO thin film

ZnO thin film has variable resistivity since it is known to be a semiconducting material. Hence, the I-V characteristic curves of ZnO thin film-based SAW devices were investigated, and the results are shown in Figure 6.1. The ZnO thin film exhibited very high resistivity (ρ) when the voltage was varied from 0 to 6.5 V as there was no current flowing within this range. However, the current started to increase exponentially after this value, indicating that the film resistivity was decreasing. Hence, the voltage range was adjusted to between 0- 4 V to study the influence of UV light irradiation on the sheet conductivity (σ) of the ZnO thin film.

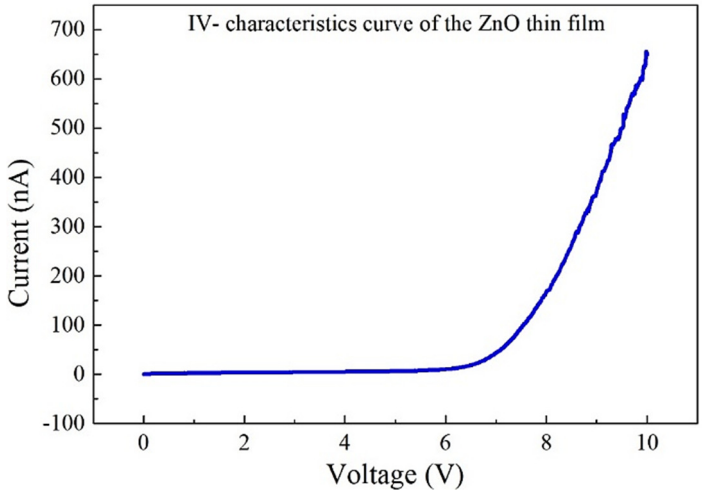

Figure 6.1 I-V characteristic curve of ZnO thin film

Figures 6.2a and 6.2b showed different I-V curves of ZnO thin film when it was illuminated with various UV light intensities using low and high UV power sources, respectively. This range of UV light intensities is frequently used in medical and environmental applications such as phototherapy (e.g. < 50 mW/cm^2), disinfection of microorganisms, and water treatment (e.g. up to ~0.5 W/cm^2) [353-355].

When the UV light was switched off (dark), the current change was insignificant at less than 6 nA because the ZnO thin film has a high resistivity or a low surface sheet conductivity.

This attributed to the presence of extra free electrons that originate due to the intrinsic defects in the ZnO thin film as a result of the fabrication process and the rough surface of the aluminium foil substrate. Therefore, oxygen molecules from the surrounding environment will be chemically adsorbed and confined those electrons. This eventually causes a decrease in the surface sheet conductivity (σ_s) of the thin film.

On the other hand, when UV light illuminated the top surface of the ZnO thin film, the current flow increased at various voltages suggesting that the surface sheet conductivity had increased. This is associated with the generation of electron-hole pairs due to the interaction of UV light with the surface of the ZnO film. Therefore, the confined electrons and generated holes will recombine and release the adsorbed oxygen back into the atmosphere.

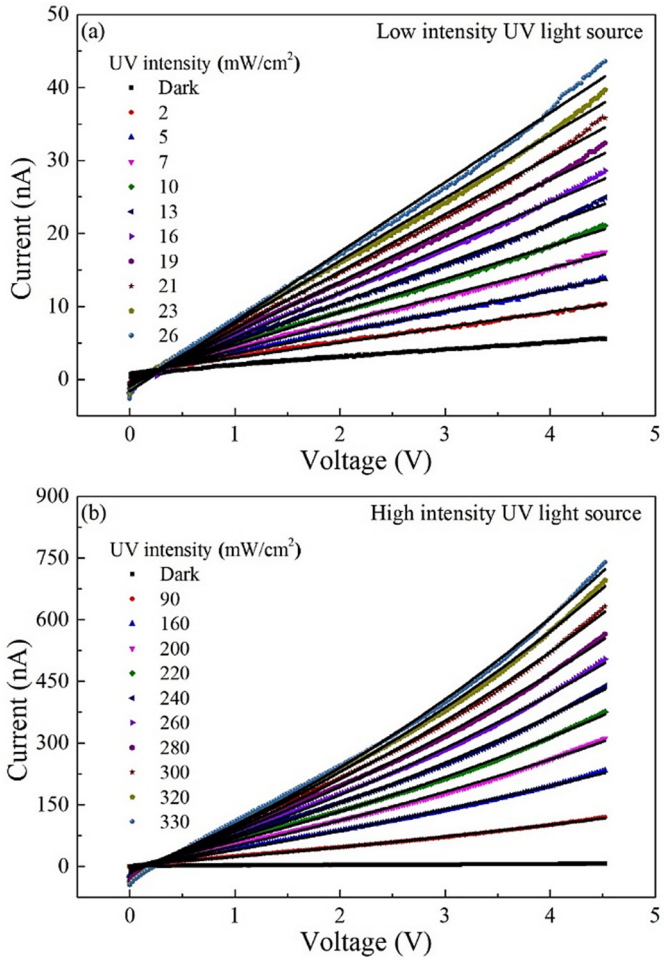

Figure 6.2 The relationship between current and voltage when ZnO thin film was illuminated with various UV light intensities using a) low and b) high power UV light sources

The current flow increased linearly with voltage when the low-power UV light source illuminated the surface of the ZnO thin film device, as seen in Figure 6.2a. Whereas during the early period of illuminating the device with high-power UV light, the current flow increased linearly and then it exhibited an exponential relationship with increasing further voltage, as shown in Figure 6.2b. This attributes to the heat generated (thermal influence) due to exposure of the UV light.

Moreover, the maximum value of current increased proportionally to the increase in UV light intensity. However, when the UV light was switched off, the current dropped immediately, suggesting a marked decrease in surface sheet conductivity. Hence, the change in surface sheet conductivity ($\Delta\sigma_s$) is calculated using equation 6.1, assuming that the thin film has a uniform sheet thickness [356].

$$\Delta\sigma_s = \frac{1}{\Delta R_s} = \frac{\Delta I}{\Delta V}\frac{L}{W} \tag{6.1}$$

where $\Delta\sigma_s$ is the change of the surface sheet conductivity, ΔR_s is the change of surface sheet resistance, ΔI is the change of the current, ΔV is the change of voltage, and L and W are the length and width of the device, respectively. The L×W dimensions are the area occupied by the IDTs which the UV irradiation was illuminated, and they are equal to 0.7×0.7 cm. The value ($\Delta I/\Delta V$) under UV light exposure can be obtained from the slopes of the curves in Figure 6.2a because the current varies linearly with the voltage. Thus, Figure 6.3 shows a linear relationship between the changes in surface sheet conductivity and the various UV light intensity where it is given by the formula in equation 6.2

$$\Delta\sigma_s = 1.32 + 0.31\, I_{UV}\ (nS) \tag{6.2}$$

where I_{UV} is the intensity of UV light in mW/cm^2. This equation is valid when the low power UV light source has been used, and the temperature increased to less than 1 ^{o}C.

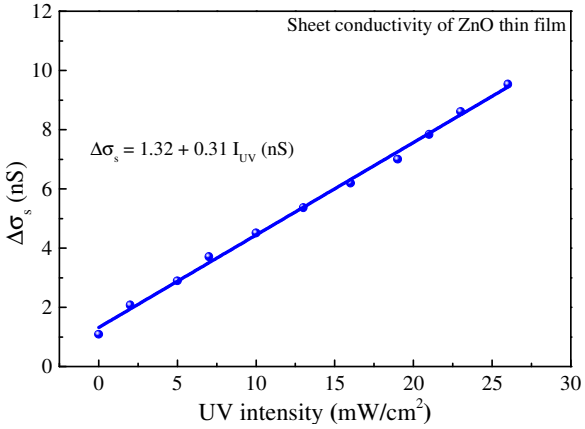

Figure 6.3 Change in surface sheet conductivity in response to various UV light intensities using low power source

6.3 The frequency response of flexible SAW devices in the flat position to UV irradiation

The frequency response of the SAW devices while kept in a flat position was then investigated. The S11 signal of the (A0) mode for the 200 µm and 160 µm SAW devices at different UV light power intensities are shown in Figure 6.4a and 6.4b, respectively. When the surfaces of the devices were illuminated with UV light, the resonant frequency shifted toward lower frequency values (downshift) as a result of the increasing surface sheet conductivity of the ZnO thin film. The insertion loss of the acoustic wave spectrum also increases with the UV light intensity indicating that the UV light caused signal attenuation.

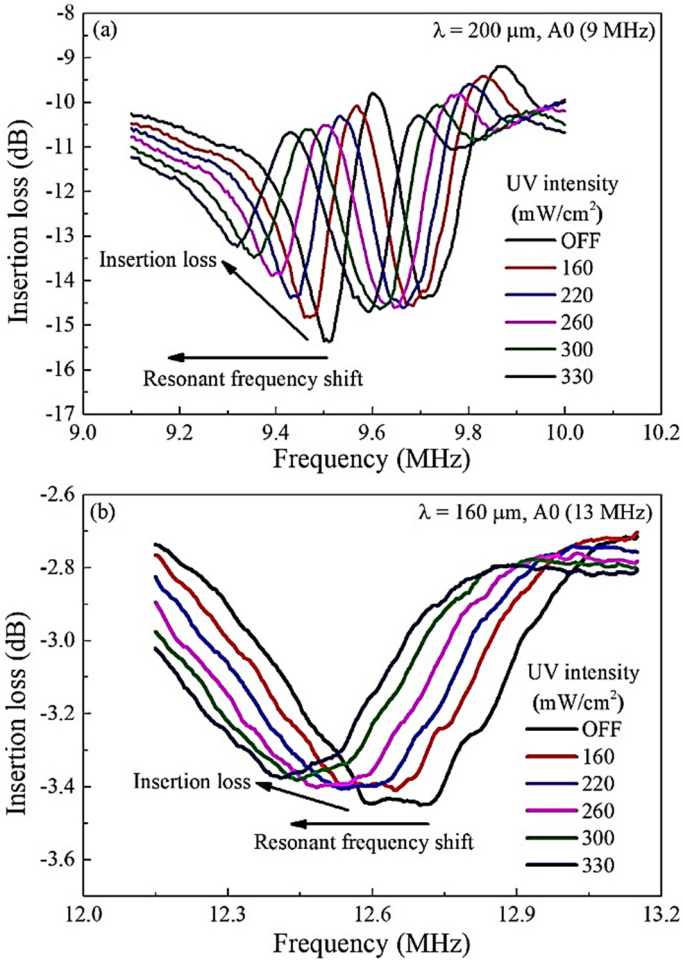

Figure 6.4 Frequency spectra showing increase in resonant frequency shifts with various UV light intensities of the SAW devices of wavelength a) λ = 200 µm and b) λ = 160 µm. S11 signal of A0 mode was used to determine resonant frequency.

The relationship between the change in acoustic wave velocity and insertion loss as well as surface sheet conductivity is given by equations 2.40 and 2.41. Thus, as the surface sheet conductivity of ZnO thin film increases, the acoustic wave velocity decreases and the insertion loss increases. Therefore, the UV light will eventually cause a decrease in resonant frequency due to the increase in the surface sheet conductivity of the ZnO thin film. This matches the frequency response obtained for these devices when illuminated with UV light.

The changes in the resonant frequency of the A0 mode for both SAW devices at various UV light intensities when using low and high-power UV sources are shown in Figure 6.5. The change in resonant frequency while the UV light was kept off for 20 seconds was insignificant, and this indicates sensor stability against external and environmental factors.

However, frequency change occurred very rapidly, and the resonant frequency markedly decreased (downshift) when the UV light was switched on. Besides, the resonant frequency's shifts increased with higher UV light power intensity. After switching UV light on, the response time of the sensors until reaching the maximum frequency shift was approximately 10-12 seconds, as shown in Figures 6.5a, 6.5b and 6.5d. The frequency shift was quite stable at this value as photon generated carriers started to be saturated, and there was no further change in the surface sheet conductivity of the thin film. In contrast, it is noticed in Figure 6.5c that the frequency shift continued to increase and did not reach a stable value within the period of exposure. This attributes to thermal effect and the high TCF value of this device, where frequency shift results from both the effect of the UV light interaction and the thermal influence. The resonant frequency was shifted to higher value immediately once the UV light was switched off, reaching about 65% of the maximum frequency shift. Then, for those devices illuminated by the low-power UV light source, it took 1-10 seconds to recover entirely depending on the value of UV light intensity. This phenomenon is likely resulted from film defects that influence electron-hole recombination and oxygen adsorption. Meanwhile, this process took much longer when the devices were irradiated with the high-power UV light source, and this is likely to be due to the thermal influence.

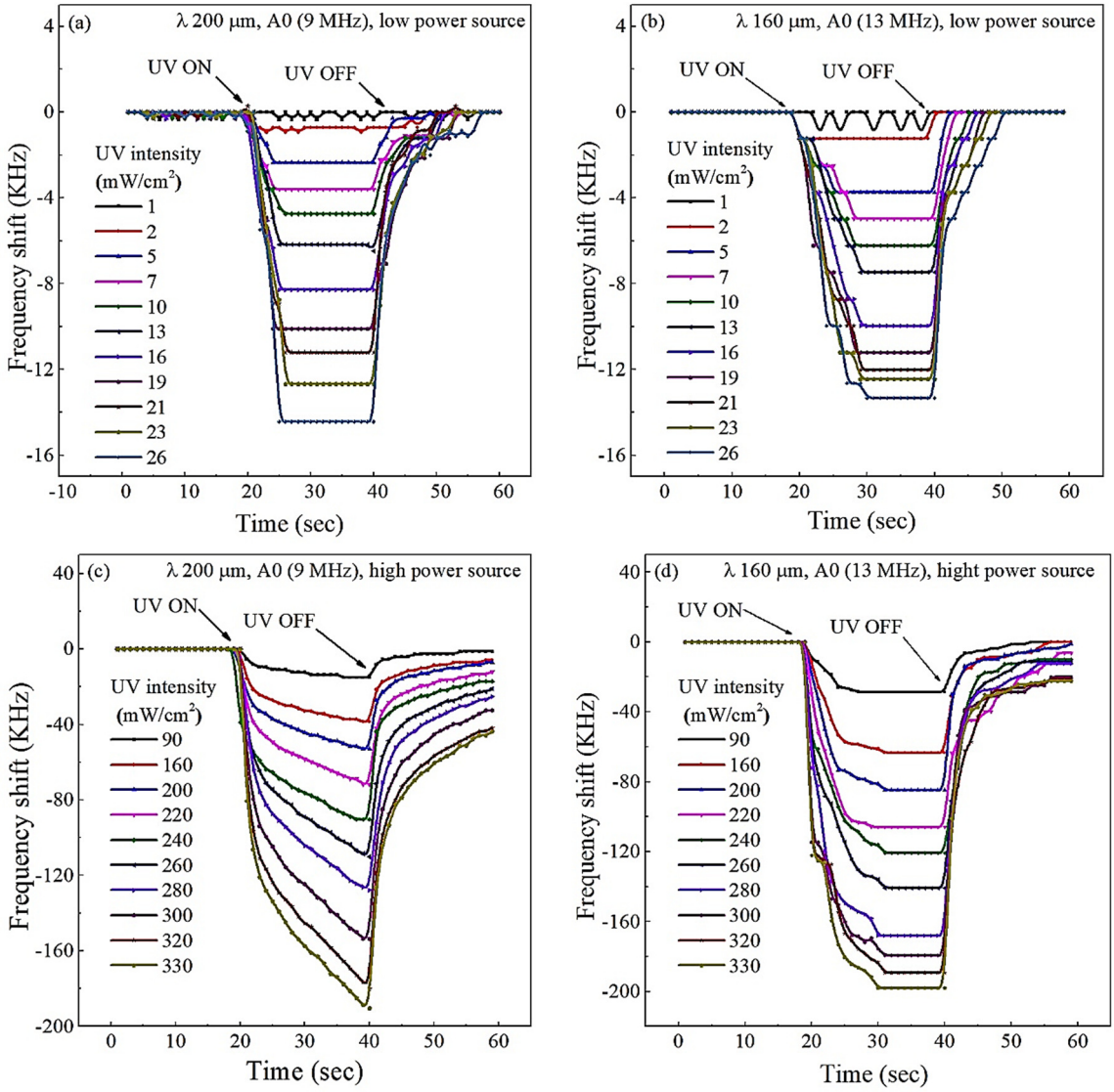

Figure 6.5 Frequency shifts of A0 mode in response to various UV light intensities for SAW devices with a) λ = 200 µm, f_0= 9 MHz, low power source, b) λ = 160 µm, f_0= 13 MHz, low power source, c) λ = 200 µm, f_0= 9 MHz, high power source and d) λ = 160 µm, f_0= 13 MHz, high power source

The frequency shift of other Lamb wave modes such as S0 and A1 vibration modes showed the same behaviour as in the A0 mode. Thus, the changes in the resonant frequency of different vibration modes at various UV light intensities are summarized in Figure 6.6, where the maximum frequency shift obtained for each mode is displayed.

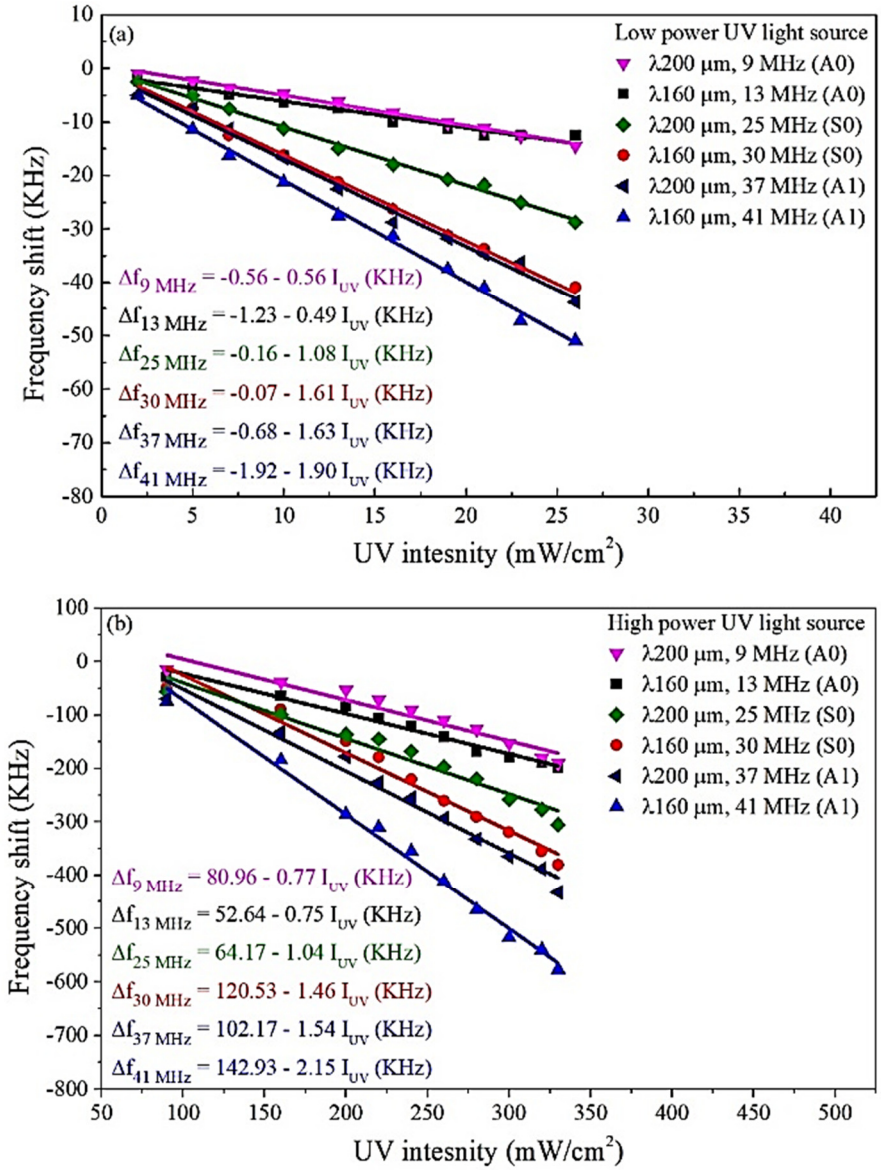

Figure 6.6 The relationship between frequency shift of different vibrating modes and various UV light intensities using a) low power and b) high power UV sources

The results show that the resonant frequency shift possesses a linear relationship with UV light intensity. However, the thermal effect happens due to the elevation of temperature during exposure to UV light, where the UV light-induced temperature increases with UV light intensity, as shown in Figure 6.7. The maximum temperature rise was 19 °C in 20 seconds when a high-power UV light source was used with an intensity of 330 mW/cm^2, while it was only 1.1 °C for the low power UV light source at 26 mW/cm^2.

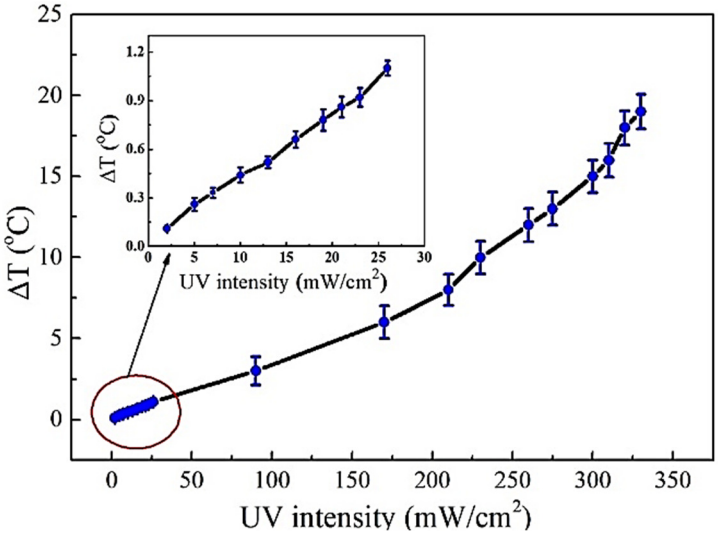

Figure 6.7 The change in temperature in response to the exposure to high power UV light. The insert plot shows the change in temperature in response to the exposure to low power UV light.

As discussed in section 2.5.1, the relationship between TCF and frequency shift is linear. The TCF values obtained for the various vibration modes of the λ=200 μm SAW device are much higher than those of the λ=160 μm devices, as shown in Table 5.1 and Figure 5.2. Therefore, the frequency shift caused by the thermal effect is minimal at low temperature and low values of TCF, and more significant when these values are higher. Figure 6.8 shows the calculated frequency shifts using the measured values during temperature change UV light exposure at various intensities.

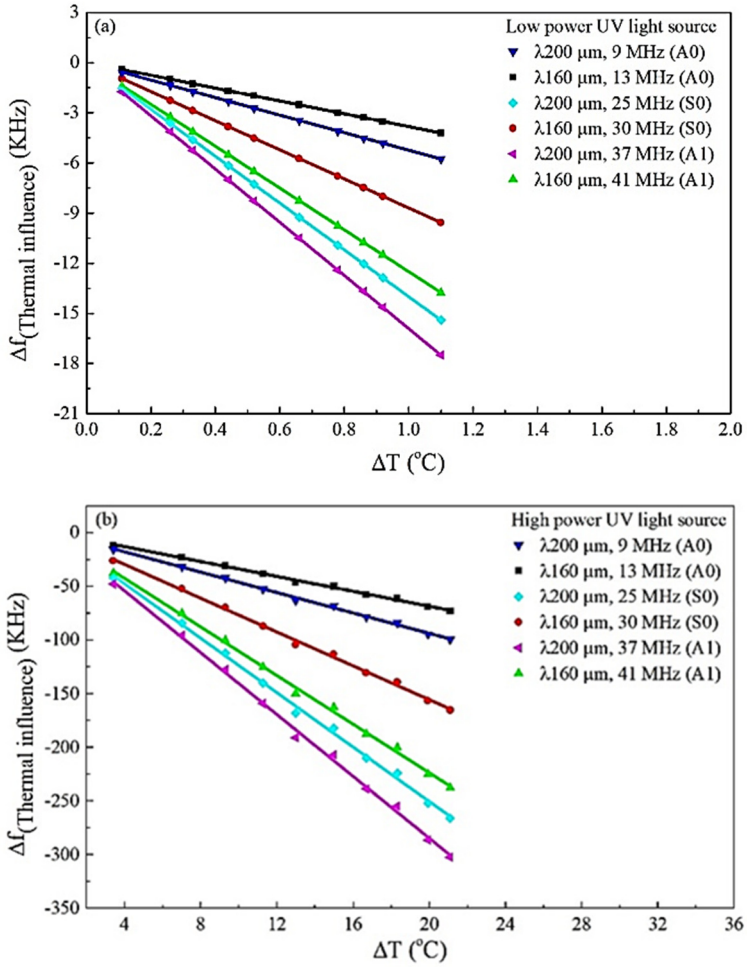

Figure 6.8 The calculated frequency shifts due to UV light induced temperature based on TCF values of the devices when using a) low power and b) high power UV sources

In the case of using low-power UV light, the maximum frequency shift calculated due to the thermal effect for the λ=160 µm device was 13.75 kHz at f_0 = 41 MHz (A1 mode), whereas, it was 17 kHz at f_0 = 37 MHz (S0 mode) for the λ=200 µm device. On the other hand, the maximum frequency shifts obtained when high-power UV light source was used are 237 kHz and 300 kHz corresponding to the λ=160 µm and λ=200 µm devices, respectively and for the first-order mode A1. Thus, the frequency shifts in Figures 6.6a and 6.6b result from a combination of light interaction and thermal influence as represented by the following equation:

$$\Delta f_0 = \Delta f_{(UV\ light)} + \Delta f_{(Thermal\ influence)} \tag{6.3}$$

Hence, the frequency shift caused by UV light ($\Delta f_{(UV\ light)}$) can be calculated by substituting the values of frequency shifts in Figures 6.6 and 6.8 in the above equation. Thus, the corrected frequency shifts due to various UV light intensities are shown in Figure 6.9a and 6.9b for low and high-power UV sources.

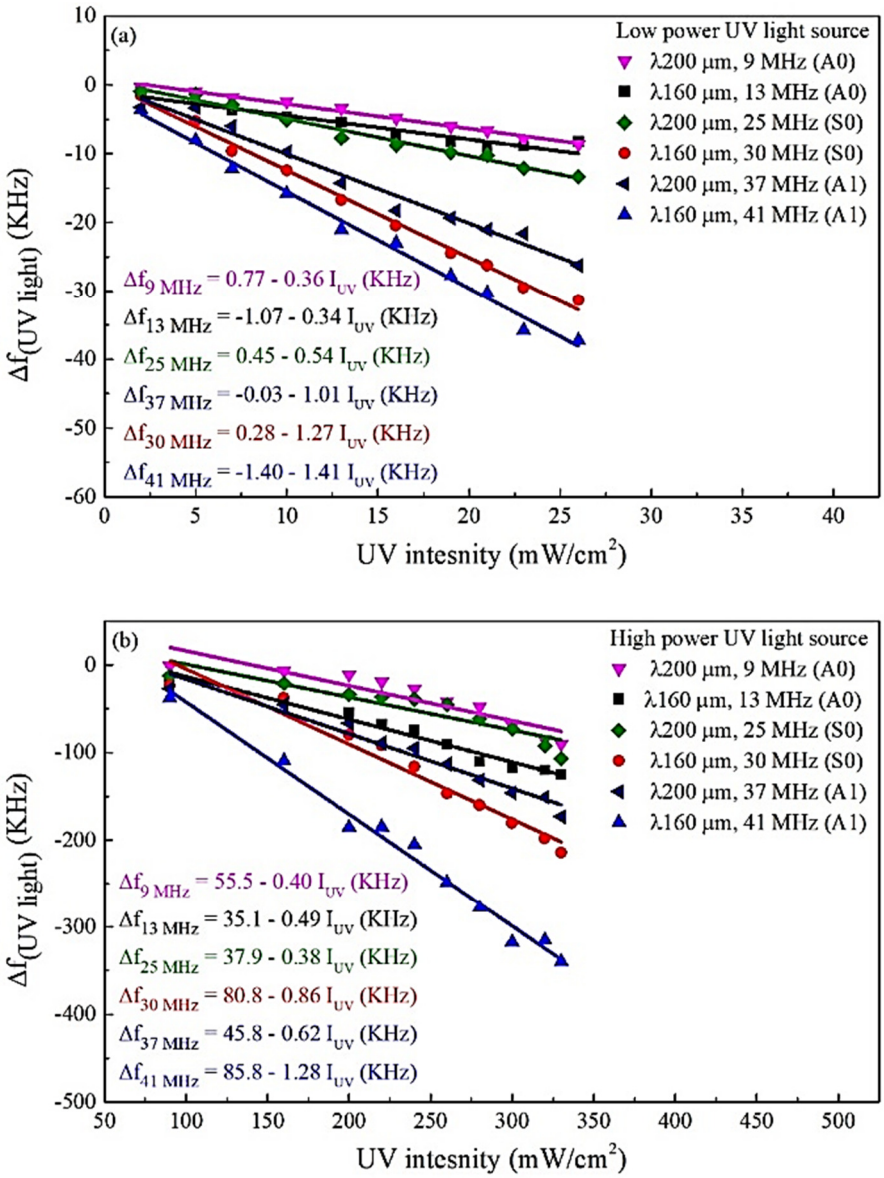

Figure 6.9 The relationship between frequency shifts and UV light intensities after subtracting shifts due to induced temperature when using a) low power and b) high-power UV sources

The relationship between frequency shift and UV light intensity is nearly linear after eliminating the thermal effect. This attributes to the linear correlation between the concentration of the generated electron-hole pairs and the light intensity. This ratio is

expressed as a percentage which represents the contribution of UV light to the frequency shift for various resonant frequencies, as illustrated in Figure 6.10.

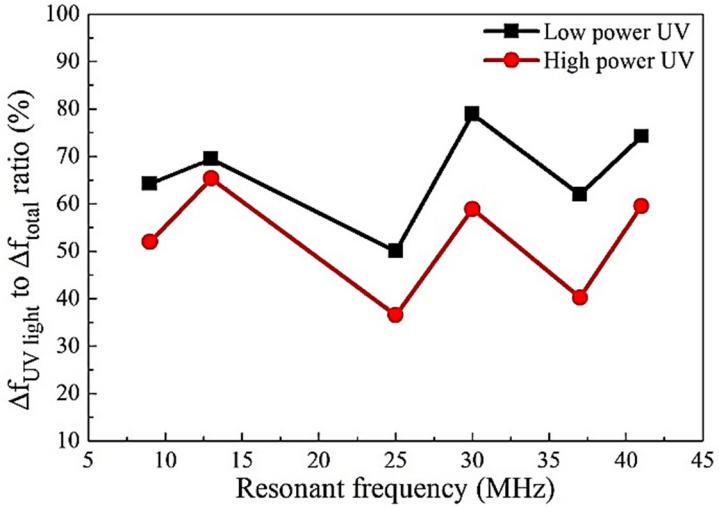

Figure 6.10 The ratio of frequency shift in response to UV light to the total frequency shift (including thermal effect) for various resonant frequencies

The figure shows that the maximum frequency shift caused by UV light is about 80% of the total shift at f_0 = 30 MHz (λ=160 µm device) and the minimum is 50% at f_0 = 25 MHz (λ=200 µm device) when low-power UV was used. Whereas, for high-power UV, the maximum UV light contribution is 65% at f_0 = 13 MHz (λ=160 µm device) and the minimum is 37% at f_0 = 25 MHz (λ=200 µm device). Also, the λ=160 µm device exhibits a better overall response to UV light with minimal thermal effects compared to the λ=200 µm device because it has lower TCF values.

The real-time response was further investigated to demonstrate the repeatability during UV light cycling, as shown in Figure 6.11. The resonant frequency decreased immediately when the UV light was switched on. The response time remained almost the same in all cycles (~10 seconds), and in each cycle, the frequency shift reached a similar value or saturation level. Moreover, as the UV light was switched off, the resonant frequency was increased, and it reached the original baseline level within 8-10 seconds. The frequency response was stable, and the same readings were obtained after five cycles as the thermal effect is insignificant at low UV intensity levels

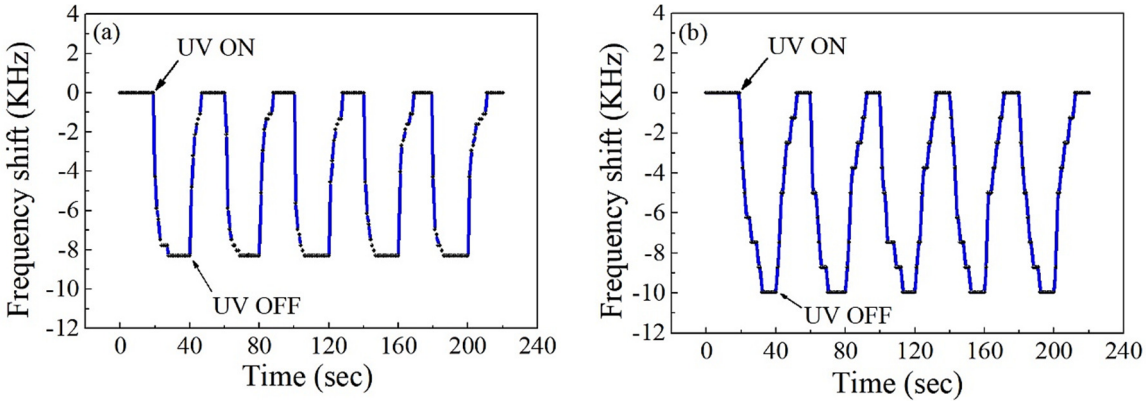

Figure 6.11 Cycling response to UV light intensity of 16 mW/cm^2 showing the change in frequency shifts of the SAW devices of a) λ=200 µm device, f_0 = 9 MHz and b) λ=160 µm device, f_0 = 13 MHz

In contrast, the resonant frequency continued to decrease and did not become saturated when the high intensity was used, as seen in Figures 6.12a and 6.12b. They show that, when the UV light switched on, the resonant frequency quickly decreased until it reached a particular frequency level where the UV light influence was dominant, and the thermal effect was minimal. As the temperature increased, the resonant frequency further decreased but only slowly and linearly due to the thermal influence. When the UV light was switched off, the interaction between the light and ZnO thin film stopped immediately, and the frequency increased quickly. However, the resonant frequency continued to increase slowly toward the original baseline value because of the thermal effect by which the time of cycling (20 seconds) was not enough to lower the temperature of the device. Therefore, when the UV light was switched on before the resonant frequency had fully recovered, the next cycle exhibited a higher frequency shift, and it continued to decrease further in the following cycles as noticed in Figure 6.12b.

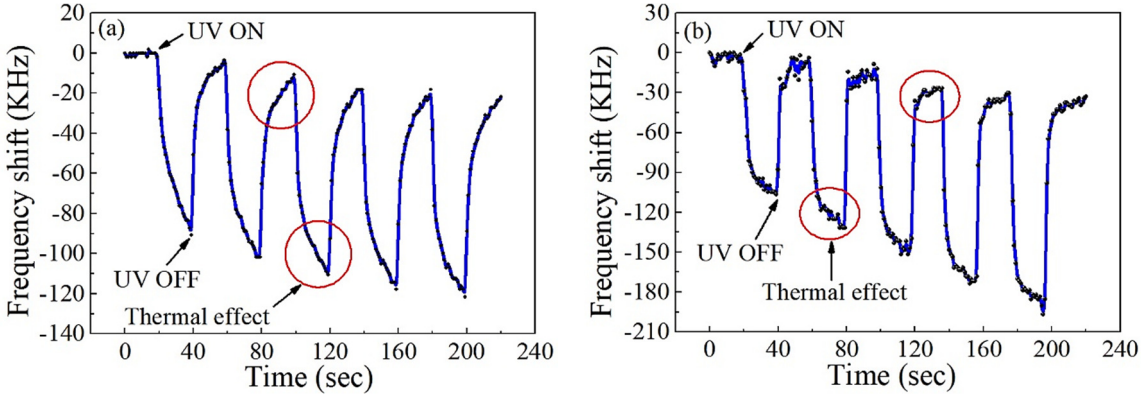

Figure 6.12 Cycling response to UV light intensity of 240 mW/cm^2 showing thermal effect and the change in frequency shifts of the SAW devices of a) λ=200 µm device, f_0 = 9 MHz and b) λ=160 µm device, f_0 = 13 MHz

6.4 The frequency response of flexible SAW devices in bent positions to UV irradiation

The sensing performance of the SAW devices was investigated in two different bent positions of down and up, as shown in Figure 3.12 in section 3.5. The low-power UV source only was used to illuminate the SAW devices, since the thermal influence is insignificant compared to that using the high-power source. Besides, when the devices are placed in bent positions, the temperature will change the radius of device curvature due to thermal expansion and contraction, causing changes in film stress and strain.

Figure 6.13 shows the changes in the resonant frequency of the A0 mode of the devices when irradiated with UV light when they were bent-down in Figures 6.13a and 6.13b, and when bent-up in Figures 6.13c and 6.13d. Reflection spectra (S11) were considered for the determination of the resonant frequency.

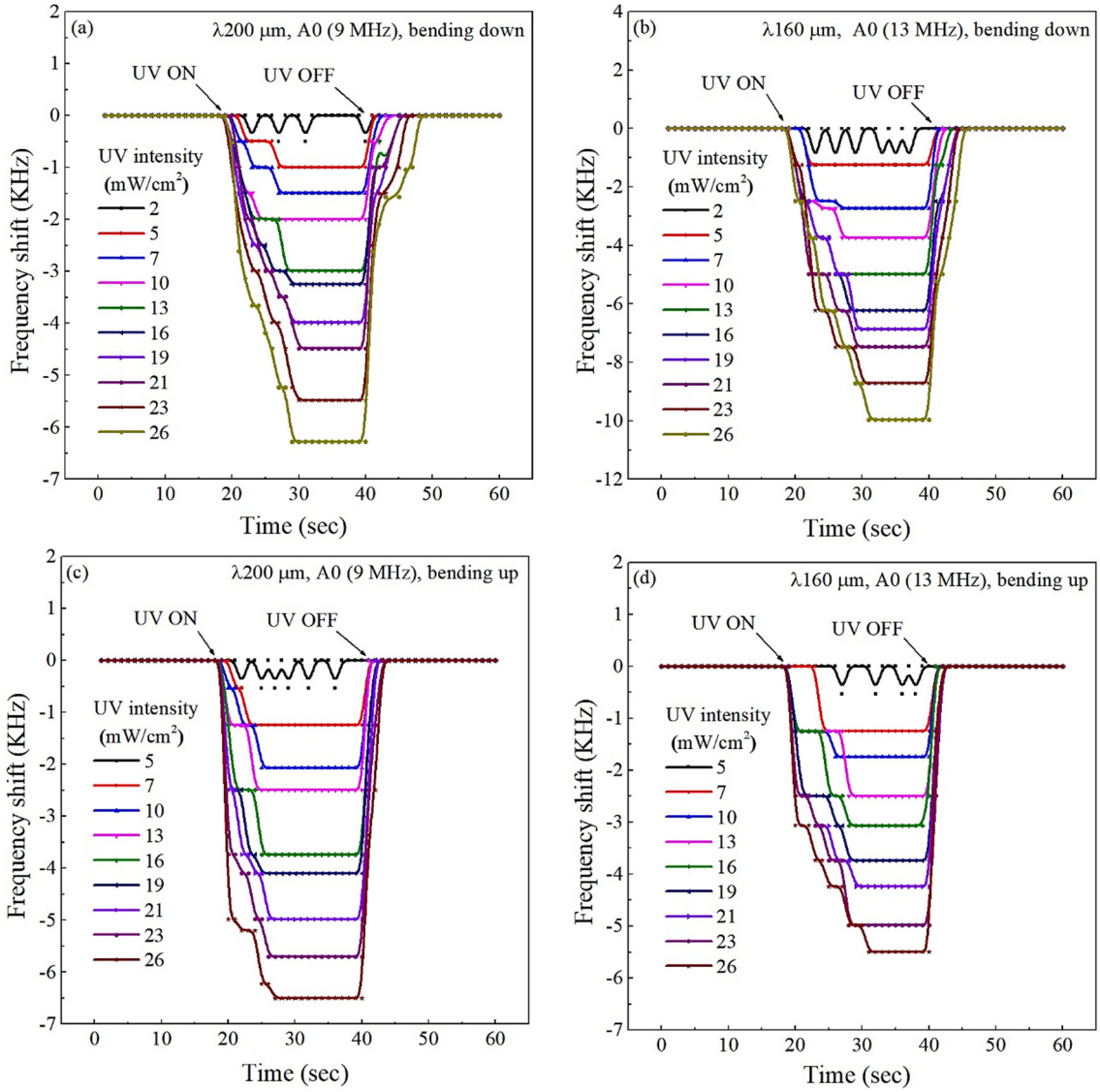

Figure 6.13 Frequency shifts of A0 mode in response to various UV light intensities for SAW devices with a) λ = 200 µm, f_0= 9 MHz, bent-down, b) λ = 160 µm, f_0= 13 MHz, bent-down, c) λ = 200 µm, f_0= 9 MHz, bent-up and d) λ = 160 µm, f_0= 13 MHz, bent-up

As noticed in these figures, the frequency response of the devices in the bent positions shows similar behaviour to that of the flat device. Therefore, when the UV light was switched on, the resonant frequencies downshifted immediately, and they continued to decrease until they reached the saturated level within 8-12 seconds. Also, the resonant frequency was increased quickly and reached to the original baseline level in 1-6 seconds when the UV light was switched off. Thus, the response and recovery times of the devices in the bent positions are comparable to those obtained when the device was kept flat.

However, the threshold value, which is the lowest UV light intensity that resulted in a significant frequency shift, when the devices were placed in the bent down position was 2 mW/cm^2. This value was increased to 5 mW/cm^2 when they were kept in the bent-up position, and this is higher than the minimum detectable limit of 1 mW/cm^2 devices in a flat position. It is suggested that bending the device generates strains and some defects in ZnO thin film that affect its surface sheet conductivity and increase the threshold UV intensity to produce a noticeable frequency shift.

Likewise, the S0 and A1 vibration modes were also investigated for both devices, and they exhibited the same behaviour like that in A0 mode. In addition, the change in resonant frequency possesses a linear relationship with UV light intensity for different resonant modes, as seen in Figure 6.14a and 6.14b.

In comparison to the flat position, the resonant frequency was shifted due to the strain induced as a result of bending the device and illumination of UV light. Hence, the rate of change ($\Delta f_0/\Delta I_{UV}$) decreased when the device was bent, and this is likely to be due to the defects and cracks generated during bending which influence the lattice structure of the thin film. Moreover, the rate of change was much less when the device was bent up since more cracks and film defects are likely to have occurred. However, the internal stress of the film has no significant effect because the flexible bimorph structure of the ZnO/Al-foil causes the relaxation of the film.

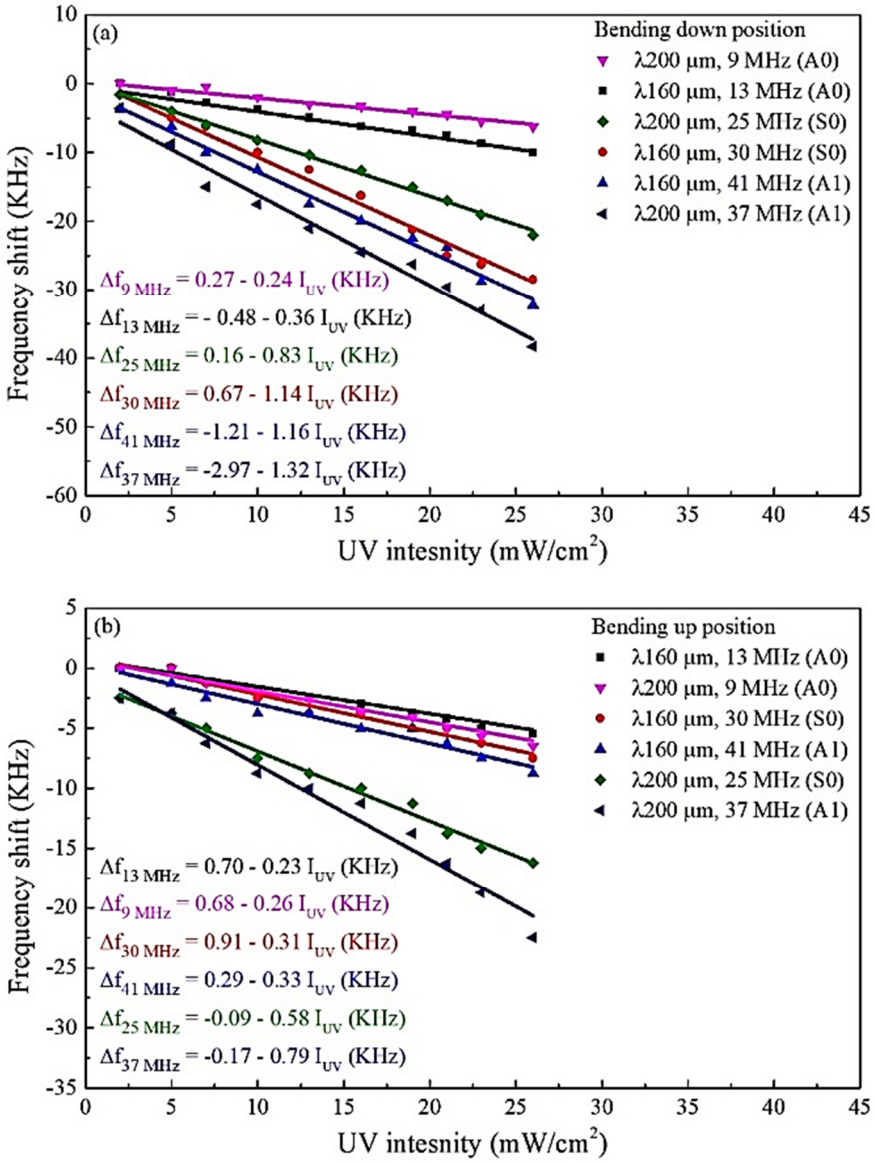

Figure 6.14 The relationship between frequency shift of different vibrating modes and various UV light intensities when the devices were kept in a) bent-down and b) bent-up positions

The real-time frequency response (cycling) of the devices in the bent down position is shown in Figure 6.15a and 6.15b, and the bent-up response can be seen in Figure 6.15c and 6.15d. The results show that the resonant frequency was decreased when the UV light was switched on until reached a maximum value where it was stable, and the same value was held. Then, the frequency was increased when the UV light was switched off and returned to its original level until the UV light was switched on again. This was observed for five cycles of real-time investigation.

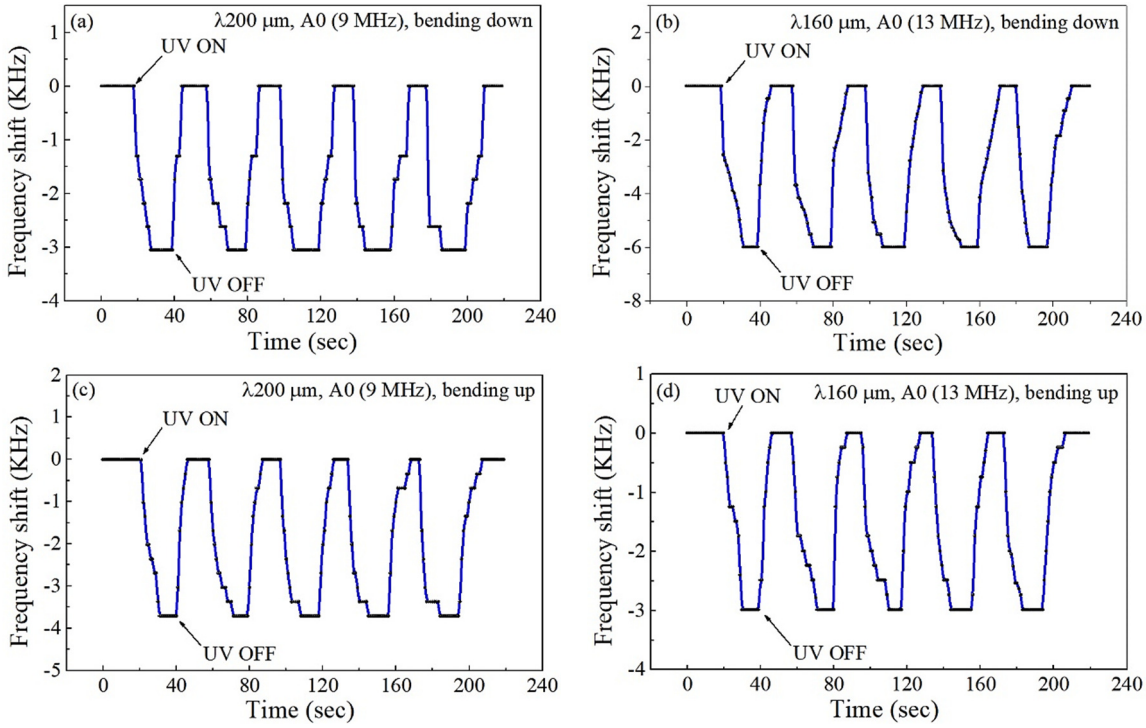

Figure 6.15 Cycling response to UV light intensity of 16 mW/cm^2 showing the change in frequency shifts of the SAW devices of a) λ = 200 µm, f_0= 9 MHz, bent-down, b) λ = 160 µm, f_0= 13 MHz, bent-down, c) λ = 200 µm, f_0= 9 MHz, bent-up and d) λ = 160 µm, f_0= 13 MHz, bent-up

6.5 Sensitivity analysis of flexible ZnO thin film-based SAW devices to UV irradiation

The sensitivity of the devices to UV light was calculated from the slopes ($\Delta f/\Delta I_{UV}$) obtained in Figures 6.6, 6.9 and 6.14, and it is given by equation 6.4 [312]:

$$Sensitivity\ (S_{UV}) = \frac{1}{f_0}\frac{\Delta f}{\Delta I_{UV}}\ ppm(mW/cm^2)^{-1} \tag{6.4}$$

where Δf is the frequency shift, ΔI_{UV} is the change in UV light intensity, and f_0 is the resonant frequency. The change in resonant frequency (Δf) is associated with both the influence of the light interaction and the thermal effect. The sensitivity of the SAW devices to UV light while the devices were kept flat is shown in Figure 6.16. It was estimated based on the corrected frequency shifts after eliminating the thermal influence.

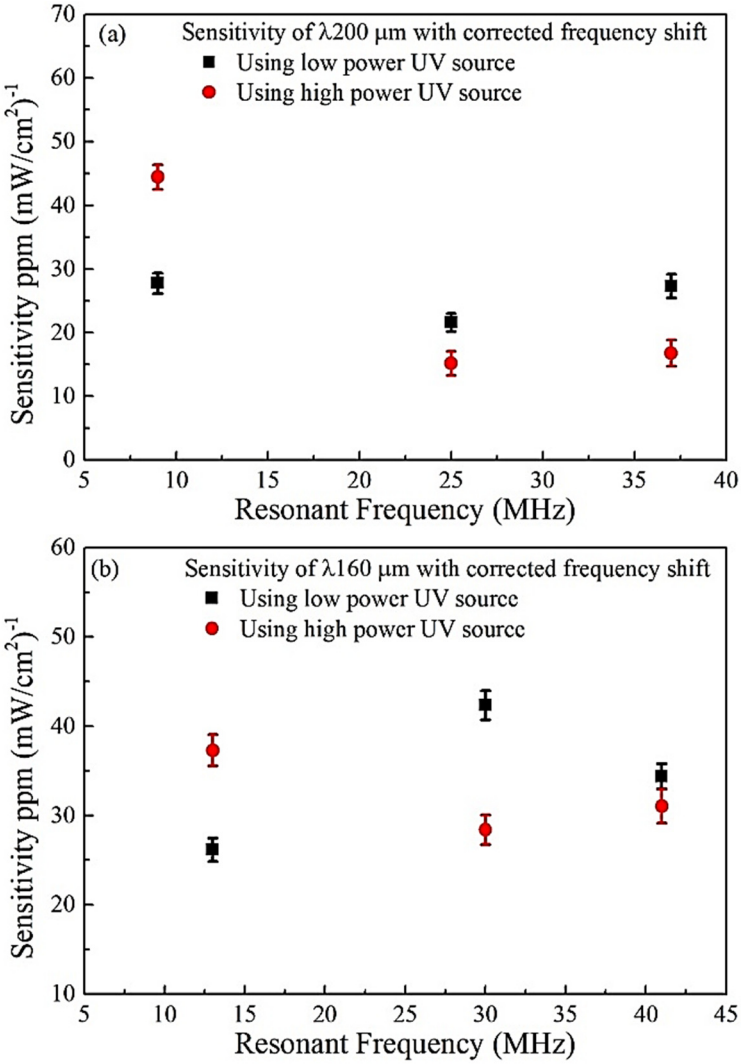

Figure 6.16 The sensitivity of various resonant frequencies to UV light after subtracting thermal effect for SAW devices of wavelengths a) λ=200 μm and b) λ=160 μm while the devices were kept in flat position

The highest sensitivity of the λ=200 μm device was 44.4 ppm $(mW/cm^2)^{-1}$ at 9 MHz (A0 mode), and the lowest value was 15.2 ppm $(mW/cm^2)^{-1}$ at 25 MHz S0 mode, both occurred when the high-power UV source was used as seen in Figure 6.16a. Whereas, the maximum sensitivity value of the λ=160 μm device was 42.3 ppm $(mW/cm^2)^{-1}$ at 30 MHz (S0 mode) and the minimum was 26 ppm $(mW/cm^2)^{-1}$ at 13 MHz (A0 mode) for the low-power UV source as seen in Figure 6.16b.

However, the two devices have different IDT designs as mentioned in section 3.2, and also, they are likely to have different patterns of defects in the ZnO thin film due to a non-uniform roughness of the foil surface. Thus, the vibration modes of both devices responded

differently to the various UV light sources. Besides, despite eliminating thermal influence from the calculations by using TCF values, it is likely to affect other parameters such as conductivity and film stress.

The sensitivity of the devices in various positions was calculated based on the total frequency shift resulting from both UV light and thermal influence. Figures 6.17a and 6.17b show the sensitivity of the λ=200 μm and λ=160 μm devices at the various resonant frequencies (vibration modes) and different positions of flat, bent down and bent up. The highest sensitivity was obtained when both devices were placed in the flat position, and it decreased when they were bent due to film defects and cracks. Also, it is evident that the sensitivity values of the bent-down position were higher than those in the bent-up position as in the latter case, more cracks and film defects were likely to occur.

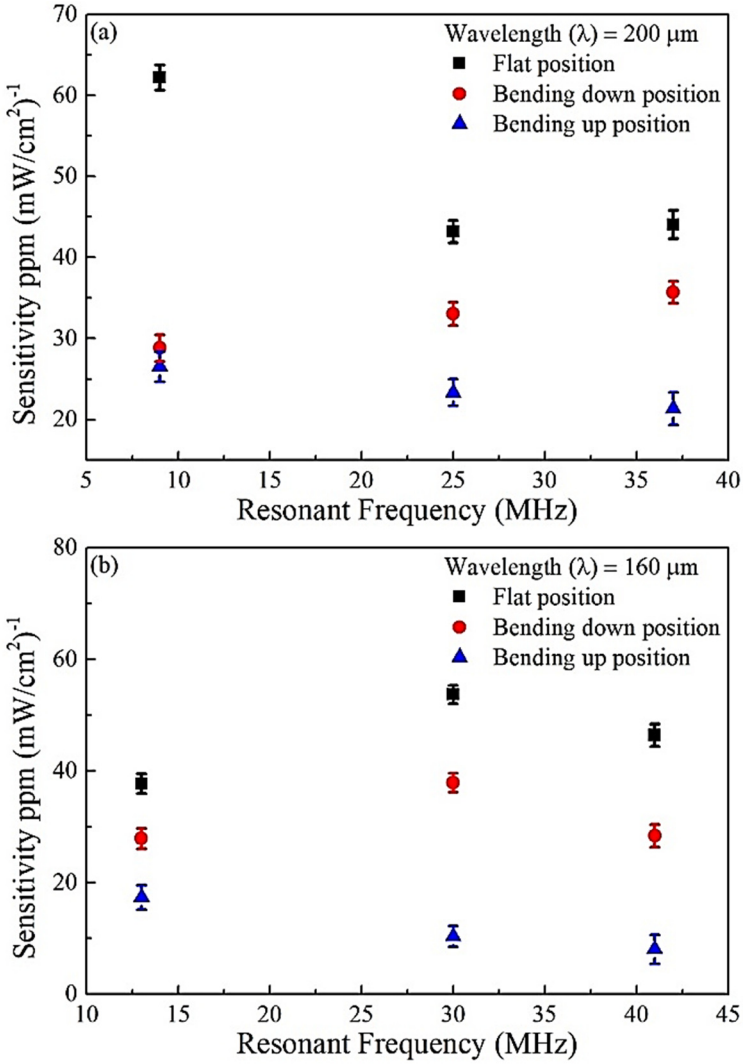

Figure 6.17 The sensitivity of various resonant frequencies to UV light for SAW devices of wavelengths of a) λ=200 μm and b) λ=160 μm while the devices were placed in flat, bent up and bent down positions

The maximum value of sensitivity of the λ=200 μm device was 63 ppm $(mW/cm^2)^{-1}$ at 9 MHz (A0 mode), and this value dropped to 27 ppm $(mW/cm^2)^{-1}$ when the device was bent up, as seen in Figure 6.17a. This remarkable decrease in sensitivity probably results from the thermal influence and the film defects caused by bending the device. These influence the propagation of acoustic waves, and A0 vibration mode has the highest TCF value ~580 ppm/K among all other modes. The TCF value is associated with the linear expansion coefficient of ZnO thin film, which is likely to change when the film is deformed. However, the minimum sensitivity was 21 ppm $(mW/cm^2)^{-1}$ at 37 MHz (A1 mode) when the device was bent-up. This indicates that more defects had been generated in the ZnO thin film which affected the surface acoustic wave properties. In contrast, the maximum and the minimum

sensitivity values of the λ=160 µm device were 53 and 8 ppm $(mW/cm^2)^{-1}$ at 30 MHz (S0 mode) when the device was kept flat and at 41 MHz (A1 mode) for the bent-up position, respectively. However, the values of sensitivity for the bent-down devices are intermediate between those of the flat and bent-up positions indicating that the performance of the device in flat and bent-down positions is better than in the bent-up position.

Thus, several factors likely affect the sensitivity of ZnO thin film-based SAW devices, such as film quality, intrinsic defects, TCF values, vibration modes, and acoustic signal quality.

6.6 The frequency response of flexible SAW device with enhanced nanorods to UV irradiation

ZnO nanorods were grown on the top surface of the ZnO thin film using a simplified hydrothermal method, as explained in section 3.3. The λ=160 µm device was selected because it has a relatively shorter distance between the input and output IDTs, and this minimises the insertion loss of the S21 signal S21. The frequency responses of the SAW device before and after growing the nanorods were obtained and discussed in section 4.5.

The device was illuminated with the low-power UV light source only that generates low UV intensity levels in order to study the enhancement of device sensitivity to UV light with less thermal interference. Thus, the sensing performance to UV light of the λ=160 µm device with and without enhanced nanorods was investigated. The frequency responses of the S21 signal S21 were recorded before and after the growth of the nanorods to determine the change of resonant frequency as a result of exposure of UV light. This change is shown in Figure 6.18a for the device without nanorods and in Figure 6.18b for the enhanced nanorods device.

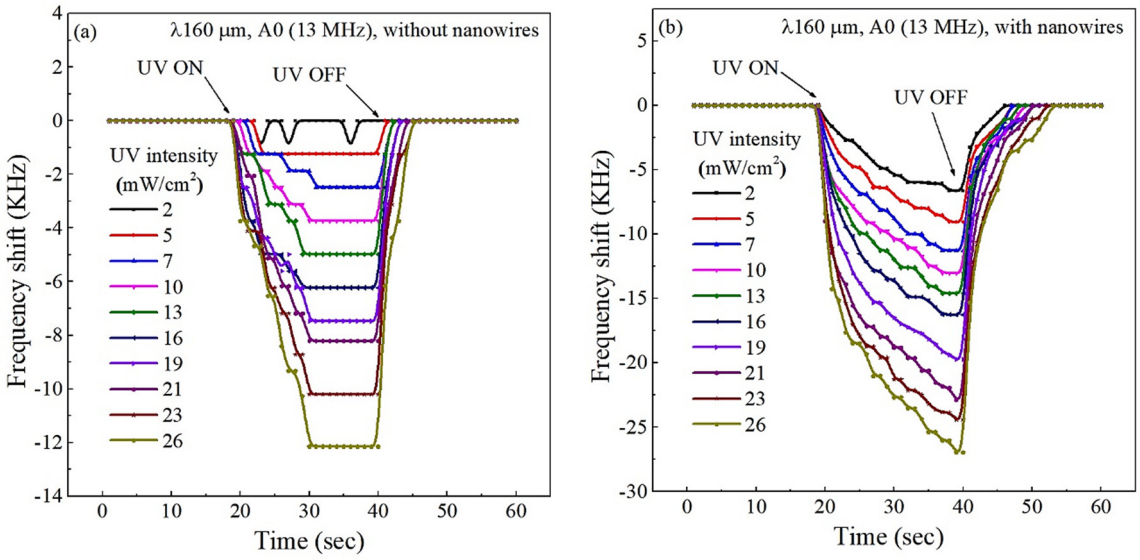

Figure 6.18 Frequency shifts of A0 mode in response to low power UV light for SAW device of wavelength of 160 µm a) without nanorods and b) enhanced with nanorods

It shows that the change in the resonant frequency of the S21 signal of the A0 mode follows the same trend as the S11 signal discussed in Sections 6.3 and 6.4. The signal decreased immediately when the UV light was switched on and decreased with increasing UV light intensity. However, it is noticed in Figure 6.18a that the frequency change was reached to saturated level in 10-12 seconds where the maximum shift obtained was 12 kHz. This value is comparable to the change in the resonant frequency of the same mode (A0) for the S11 signal, as shown in Figure 6.5b. In addition, the minimum frequency shift was 1.2 kHz when the device was illuminated with a UV light intensity of 5 mW/cm^2.

On the other hand, the resonant frequency shown in Figure 6.18b did not reach a steady-state level, and it continued to decrease further, but slowly until it reached the maximum shift. Also, it decreased substantially when the UV light was switched off, and then it changed slowly toward the original frequency level. This indicates that the interaction between the UV light and ZnO nanorods/ZnO film continued to generate more photo-carriers when the UV light was switched on.

The maximum frequency shift recorded was 27 kHz, and it is 2.25 times the maximum shift obtained for the device without growing the nanorods. Moreover, the minimum change in frequency was 6.6 kHz when the device was illuminated by UV light at 2 mW/cm^2, whereas,

there was no shift at this intensity for the non-enhanced device. In addition, it was found that the lowest UV intensity that resulted in a significant frequency shift was 0.45 mW/cm^2, which caused a change in the resonant frequency of 1.9 kHz. Thus, growing the nanorods on the top surface of the sensing region or the delay line of the SAW device enhanced both the frequency shift and the limits of detection.

The other vibration modes S0 and A1 were also investigated, and they exhibited a similar response trend as the A0 mode. Figure 6.19a and 6.19b show the changes in the resonant frequencies for different vibration modes as a result of various UV light intensities before and after growing the nanorods. The frequency shift has a nearly linear relationship with UV light intensity with and without nanorods. However, the change in frequency shift has been enhanced by 75%, 70% and 135% for the A0, S0, and A1 modes respectively when the nanorods were grown on the top surface of the device. This is mainly attributed to the fact that the nanorods have a large surface-area-to-volume ratio that can enhance the absorption of UV light and increase the number of photo-generated carriers, eventually influencing the surface sheet conductivity and thus causing significant frequency shifts [306].

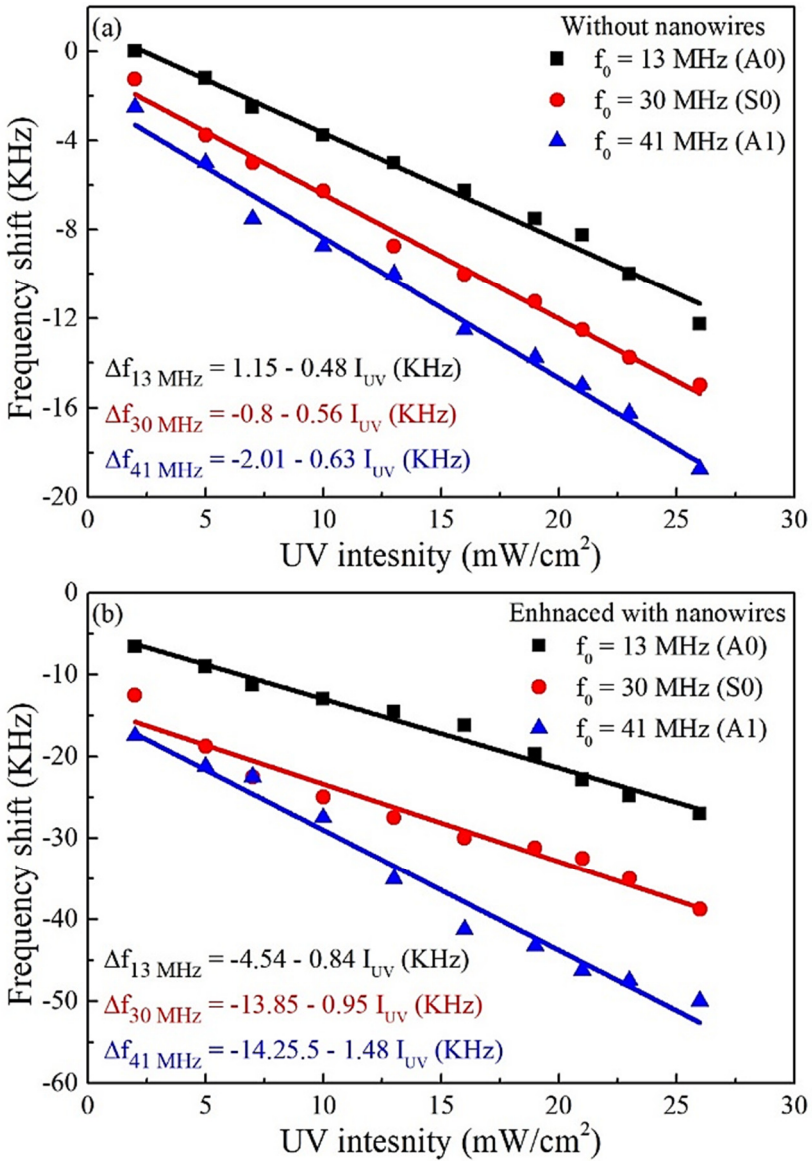

Figure 6.19 The relationship between frequency shift of various vibrating modes and UV light intensities for the device of wavelength 160 μm a) without nanorods and b) enhanced with nanorods

The real-time response of the nanostructured device exhibits excellent repeatability and stability after five cycles, as shown in Figure 6.20. The resonant frequency did not reach a saturation level, and it was slowly shifted until it reached the maximum shift value before the UV light was switched off. Similarly, it shifted upward slowly toward the original baseline level during the recovery stage.

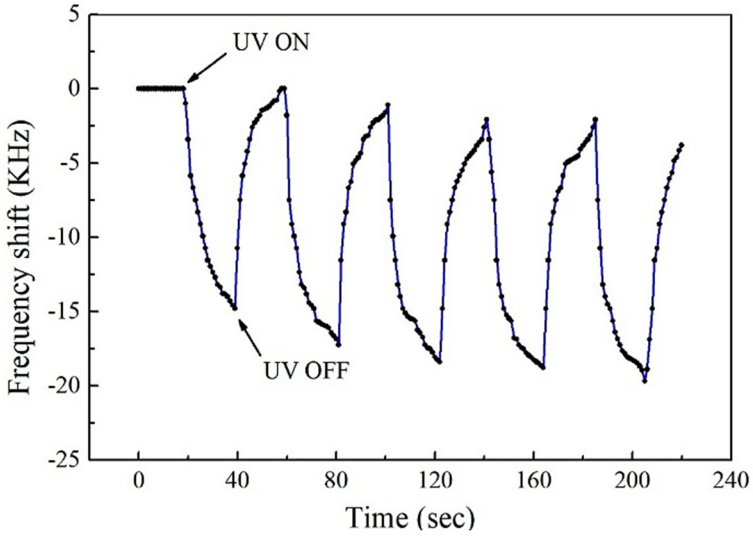

Figure 6.20 Cycling response to UV light intensity of 16 mW/cm^2 showing the change in frequency shifts of the nanorods-enhanced SAW devices

The sensitivity of the device has been calculated using equation 6.4, where the slopes in Figure 6.19 represent the rate of resonant frequency changes at various values of UV light intensities ($\Delta f/\Delta I_{UV}$). Thus, the highest sensitivity for this device is 65 ppm (mW/cm^2)$^{-1}$ corresponding to A0 mode enhanced with nanorods as seen in Figure 6.21. This value is 1.76 times as high as the sensitivity of the same mode for the device without nanorods. However, it can be noticed that there is a significant drop of the sensitivity for the S0 mode (at 30 MHz) in both devices, but it is followed by a slight increase for the A1 mode (at 41 MHz) for the enhanced nanorods device.

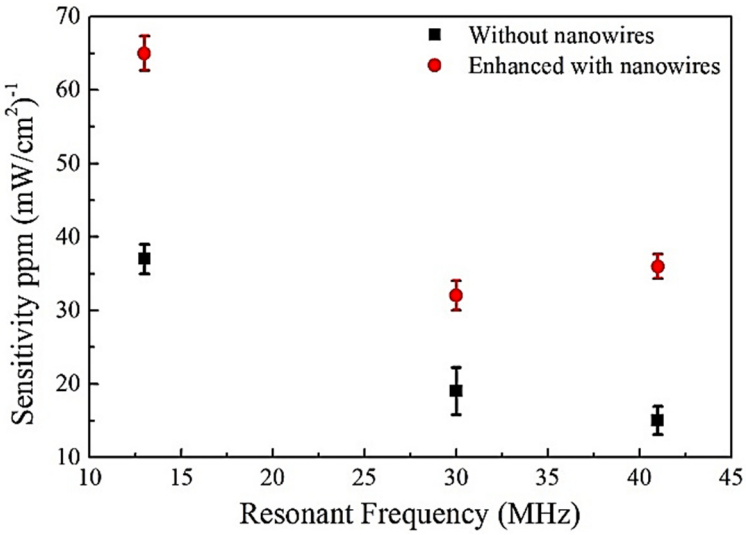

Figure 6.21 The sensitivity of various resonant frequencies to UV light for SAW device of wavelength of 160 µm with and without nanorods

The proposed flexible ZnO thin on aluminium foil-based SAW UV sensors showed less sensitivity, limit of detection, and response time compared to other detectors such as thermopile and Schottky photodiode. For example, thermopile has a dynamic range of 0.001 – 100 mW/cm^2, whereas the detection limit for the proposed sensors was about 2 mW/cm^2. However, these detectors are well-developed, and they have been used as UV light sensors for more that fifty years. Besides, the proposed devices have an advantage of flexibility and bendability as well as they have a great potential for further development.

On the other hand, the sensitivity of these devices exhibited lower values compared to rigid SAW devices such as ZnO/Si which showed a maximum sensitivity of 2190 ppm (mW/cm^2)$^{-1}$ as shown in Table 2.3 in section 2.5.2. This attributes to the high frequency by which this device was operated (842.8 MHz), while the proposed devices are operated in much lower frequencies (3 – 41 MHz) which are limited by the design of the IDTs due to the high surface roughness of aluminium foil. Furthermore, the sensitivity of the proposed device is comparable to those of the flexible devices made by polyamide substrate where the sensitivity of the Lamb wave mode was 55.8 (mW/cm^2)$^{-1}$.

6.7 Summary

Flexible SAW devices based on ZnO thin film on aluminium foil substrate have been investigated for the first time as UV light sensors while the devices were placed in flat and bending (curved) positions.

The I-V characteristics curves showed that the surface sheet conductivity of ZnO thin film was increased with the increase in UV light intensity. These changes in conductivity resulted in frequency shifts where the resonant frequency was decreased linearly with UV light intensity. Thermal effect had markedly influenced the changes in the resonant frequency when the high-power UV light source was used, whereas it was insignificant when using the

low power source. Moreover, the device of a wavelength of 200 μm possessed high TCF values as discussed in the previous chapter, which makes it more sensitive to changes in temperature.

The maximum value of sensitivity of the λ=200 μm device was 63 ppm $(mW/cm^2)^{-1}$ when the device was kept in a flat position, whereas it was 53 ppm $(mW/cm^2)^{-1}$ for the λ=160 μm device. These values were decreased when the devices were bent due to the defects and cracks generated in ZnO film. The value of sensitivity was enhanced by 1.76 folds when nanorods were grown on the surface of the device. Real-time cycling response showed excellent repeatability for several cycles when the devices were placed in flat and bent positions.

The sensitivity, limit of detection, and response of the flexible SAW UV sensors was much lower than that of the well-developed UV light detectors such as thermopile and Schottky photodiode. Also, their sensitivity was less than that of other ZnO thin film-based SAW devices made on rigid substrate such as silicon, and it was comparable to those fabricated on flexible polyamide substrate and operated by Lamb wave modes. However, the significant advantage of the proposed devices is performing sensing in bendable and flexible (curved) positions, besides, they have a potential for further development.

Chapter Seven

Humidity and Breath detection using the flexible ZnO thin film-based SAW device

7.1 Introduction

Humidity is one of the most commonly measured parameters in environmental, biomedical, and industrial applications as well as in research and controlled processes. SAW devices have been employed in humidity sensing as part of gravimetric-based devices which utilises the change in mass loading of humidity on the surface of the sensor. It is also suggested that changes in surface sheet conductivity and density due to the adsorption of water molecules at the surface of ZnO thin film are likely to be contributed to the change in acoustic velocity.

Flexible ZnO thin film-based SAW devices with a wavelength of 160 μm with and without nanorods are selected to perform humidity sensing using various operating modes. The device without nanorods is used to investigate flexible sensing performance in flat and bent down positions. The nanorods-enhanced device is exploited to study the enhancement in sensitivity compared to that of the device without nanorods. The S11 and S21signals are used to determine the resonant frequencies. Real-time cycling response is conducted by changing the humidity continuously for several cycles and recording the frequency response at the same time.

The sensors are also investigated in breath rate and apnoea detection by exploiting changes in humidity and temperature during inhalation and exhalation. The device is placed in flat and bent-up positions to study sensing performance in flexible conditions as well as when using nanorods. A volunteer is instructed to breathe normally in a rate of 12-20 breaths/min, slowly in a rate below 12 breaths/min, and fast in a rate above 20 breaths/min as well as to hold breathing for few seconds for detection of apnoea.

7.2 The frequency response of flexible SAW device to humidity change

The performance of the flexible SAW device-based humidity sensor was investigated. The device has a wavelength of 160 µm and was placed inside a humidity chamber where the relative humidity (RH) was controlled by adjusting the flow rate of dry nitrogen that passed through a bottle filled with DI water. The device was kept flat as well as bent down on a semi-circular holder with a radius of 50 mm.

Figures 7.1a and 7.1b show the changes in relative humidity and temperature inside the chamber as measured by the commercial reference sensor. The relative humidity was increased slowly from 1% to 90%, and the corresponding temperature change was ± 0.5 °C.

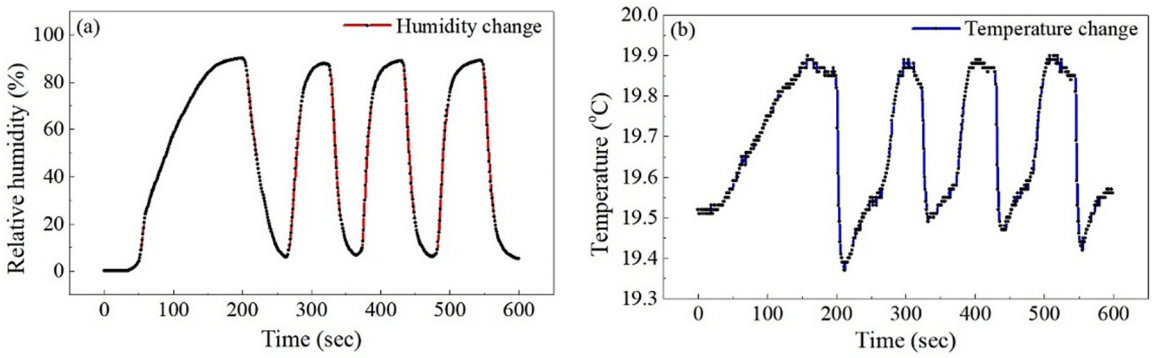

Figure 7.1 Changes in humidity and temperature inside the humidity chamber due to flowing nitrgoen gas carrying vapour at varied flowrates, a) humidity and b) temperature changes

Thus, the temperature change is insignificant and has only a slight effect on the propagation of the surface acoustic wave. However, the change in acoustic wave velocity caused by humidity is mainly due to other factors such as mass loading due to the condensation of vapour and changes in surface sheet conductivity and film density.

The changes in resonant frequency as a function of relative humidity for the different Lamb wave vibration modes (A0, S0, A1) are shown in Figure 7.2. The measurements were obtained while the device was kept in a flat and bent down positions, and the (S11) signal was recorded to determine the resonant frequency.

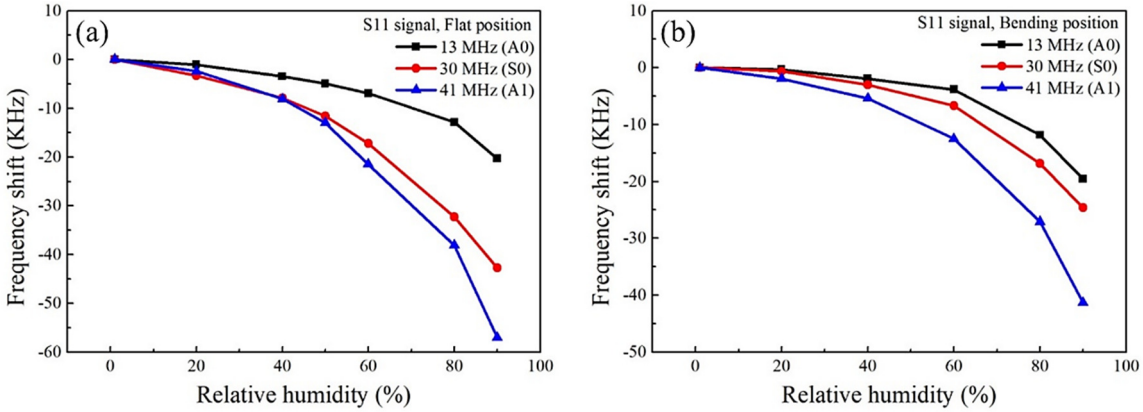

Figure 7.2 Frequency shifts of various vibrating modes in response to changes of relative humidity of the SAW device of the wavelength of 160 µm while the device was kept a) flat and b) bent down positions. S11 signal was used for the determination of the resonant frequency

Figure 7.2a shows that the change in resonant frequency has a nonlinear relationship (monotonic trend) with the increase in relative humidity. The frequency shift also increased with humidity. The maximum shift obtained was -57 kHz at RH 90% for the higher-order mode (A1), and the minimum shift was -20 kHz for the A0 mode. Hence, the higher resonant frequency caused a more substantial frequency shift. Moreover, the change in resonant frequency increased slowly in the range of RH 1-50% after which it increased dramatically for high RH values above 60%. The maximum resonant frequency shift for the A1 mode was decreased by 28% when the device was bent down due to existence of film crack and defects compared to the shift obtained for this mode when the device was kept flat, as shown in Figure 7.2b.

In contrast, the maximum frequency shift of the A0 mode was slightly less than that of the shift of the A0 mode when the device was kept flat. This could have been due to the characteristics of the Lamb waves where the higher-ordered modes are confined to the surface of the device, and they propagate mainly in the ZnO thin film which the defects existed because the device was bent. Therefore, the A1 mode was more influenced than the A0 mode by bending the device. The relationship between the shift in resonant frequency and relative humidity remained monotonic nonlinear, and the shift of frequency was remarkably increased when humidity was increased above 60%.

Likewise, when the S21 signal was used to determine the resonant frequency, the frequency shift increased as humidity increased, and it possessed a nonlinear relationship with humidity as seen in Figure 7.3. It is noticed that the frequency shifts of the three vibration modes showed slight variations when the humidity was changed from 1-60%. However, the resonant frequency decreased remarkably at RH 90%, and the maximum frequency shift of the A0 mode was 31 kHz, whereas, for other S0 and A1 modes, the shifts were ~41 kHz for both, as shown in Figure 7.3a.

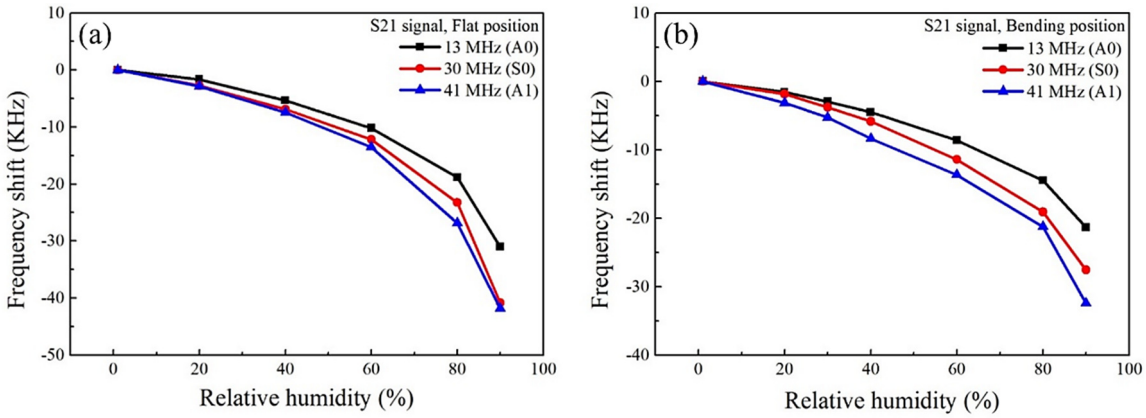

Figure 7.3 Frequency shifts of various vibrating modes in response to changes of relative humidity of the SAW device of the wavelength of 160 µm while the device was kept a) flat and b) bent down positions. S21 signal was used for the determination of the resonant frequency

However, when the device was bent down, the maximum frequency shifts of all the vibration modes were decreased by 25% compared to values for the device in a flat position, as shown in Figure 7.3b. This attributes to film defects, particularly in the delay line region where the transmission signal is propagating.

Table 7.1 presents a summary of the values of frequency shift at 90%RH of various vibration modes when the device was kept flat and bent-down positions.

Table 7.1 Summary of frequency shifts of various vibration modes at 90%RH

Mode	f_0 (MHz)	Δf (Hz) S11 (flat)	Δf (kHz) S11 bent down)	Δf (kHz) S21 (flat)	Δf (kHz) S21 (bent down)	Δf (kHz) S21 with nanorods
A0	13	-20.3	-19.6	-31	-21.3	-41.82
S0	30	-42.7	-24.6	-40.8	-27.6	-52.72
A1	41	-57	-41.3	-41.8	-32.4	-107

Hence, when the S11 signal was used to record the resonant frequency, the measurements were obtained from one port of the SAW device (resonator configuration) underneath the IDTs. Meanwhile, in the case of the S21 signal, the resonant frequency was recorded from the two ports of the device where the acoustic signal propagates from one to another through the delay line region. Thus, the S21signal is influenced by several factors. These include the mismatching of IDTs between the two ports due to the lithography process and the surface roughness of aluminium foil. Besides, the intrinsic defects in the ZnO thin film and the non-uniform cracks that occurred in the thin film when the device was bent. Therefore, some variation in the performance of the device for the S11 and S21 signals was noticed as well as in both flat and bent positions where the S11 signal exhibited higher frequency shifts than the S21 signal.

7.3 The frequency response of flexible SAW device with enhanced nanorods to humidity change

Nanorods were grown on the top surface of the device in the delay line region using the hydrothermal process to enhance the sensitivity of the device. The nanorods-enhanced SAW device was investigated as a humidity sensor. Figure 7.4 shows the frequency shift of the nanorods-enhanced device as a function of change in relative humidity. The maximum change in resonant frequency was 107 kHz for the A1 mode representing a significant enhancement of ~255% compared to that of the same mode of the device without nanorods, as shown in Table 7.1. The changes in the resonant frequencies of the A0 and S0 modes

showed fewer improvements compared to those values of the A1 mode, where the enhancement of the frequency shift was only about ~132%.

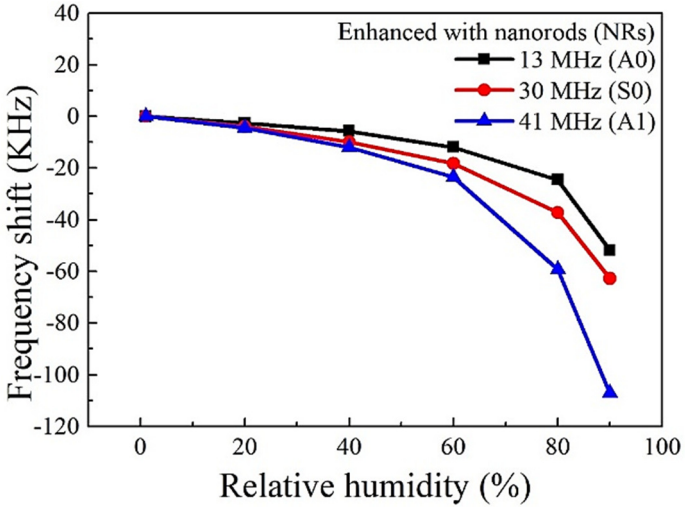

Figure 7.4 Frequency shifts of various vibrating modes in response to changes in relative humidity of the nanorods-enhanced SAW device.

The significant enhancement in the frequency shift of the higher-order (A1) mode results from the propagation characteristics of the Lamb waves. In general, Lamb wave travels through the whole device thickness in both the ZnO thin film and the aluminium foil substrate. Therefore, it exhibited less sensitivity to mass loading compared to the Rayleigh wave that travels along the surface of the device. Hence, the higher vibration modes of the Lamb wave have better performance in detecting any change on the surface of the device because they are more converging to the Rayleigh wave and have higher values of the resonant frequency. Besides, the nanorods increase the surface area of the sensing region where more water vapour is expected to be trapped on the surface of the device. This increases the mass loading, which eventually causes a significant change in acoustic wave velocity.

7.4 Sensitivity analysis of flexible ZnO thin film-based SAW devices to humidity change

The sensitivity of the flexible SAW device-based humidity sensor is defined by the following formula [357]:

$$S = \frac{\Delta f}{\Delta RH} \tag{7.1}$$

where Δf is the shift in resonant frequency and ΔRH is the change in relative humidity. The calculated sensitivities for various resonant frequencies when the device was kept in flat and in bent positions are shown in Figure 7.5. The frequency shift is considered when the humidity changed by 10%RH at 90%RH.

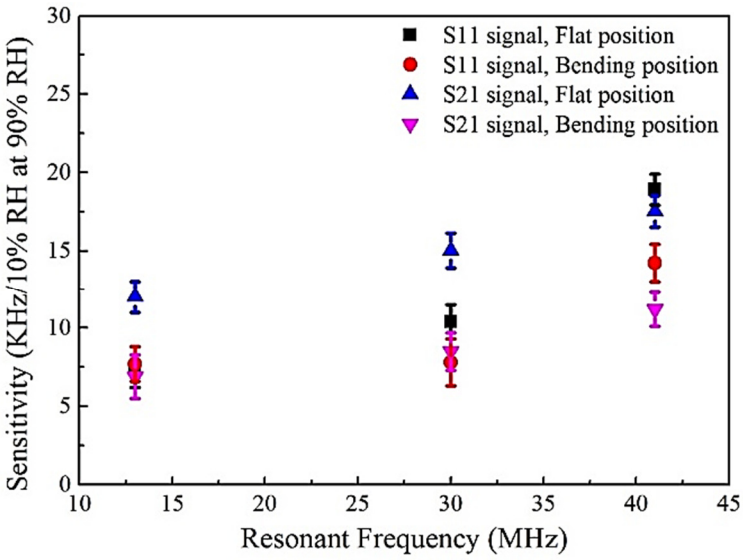

Figure 7.5 The sensitivity of various resonant frequencies to change in relative humidity of 10% RH (80-90%) when the device was placed in flat and bending positions.

The maximum sensitivity was ~19 kHz/10% RH for the higher-order mode (A1) at the resonant frequency 41 MHz (S11 signal) and when the device was kept in a flat position. This is attributed to the relatively high-frequency value where this mode is propagating close to the surface (converges to Rayleigh wave) as discussed. Besides, the S11 signal is used to determine the resonant frequency recorded from a single port where the acoustic wave is excited and measured. Therefore, it is more sensitive to mass loading as some of the water

molecules condensate directly over the IDTs area. In contrast, although the humidity level affected the acoustic velocity of the S21 signal, the water molecules on the surface of the device caused more signal damping than to the reflection signal. This mainly applies to the higher vibration mode as the acoustic wave is confined to the surface.

In addition, the SAW device exhibited less sensitivity when the sensor was bent compared to the flat position, due to cracks and defects in the film. Therefore, the lowest sensitivity was ~7.0 kHz/10% RH for the fundamental mode (A0) at 13 MHz when the device was in a bent position and for the S21 signal. This obviously results from the low frequency of this mode, as well as film cracks and defects and the slight damping of the S21 signal

The sensitivity of the nanorods-enhanced SAW humidity sensor was further studied, and the results are shown in Figures 7.6a and 7.6b for the device without nanorods and the nanorod-enhanced sensor, respectively. Sensitivity was calculated for different humidity change intervals from 1% to 80% with steps of 20% and for various vibration modes. The sensitivity of the device increased with relative humidity.

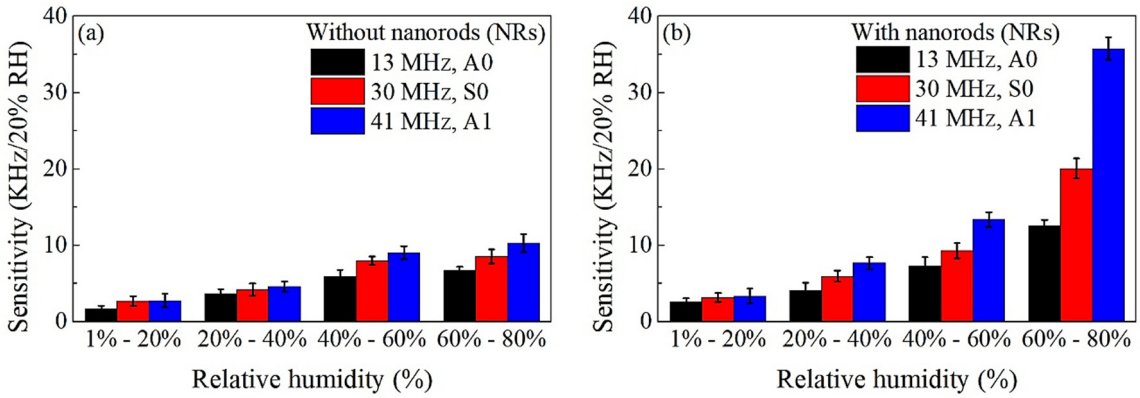

Figure 7.6 The sensitivity of various vibrating modes to changes in relative humidity at intervals of 20% RH of the SAW device a) without nanorods and b) with nanorods

The results show that the nanorods improved the sensitivity of the SAW device significantly when the relative humidity was above 60%. The maximum sensitivity of the nanorods-enhanced device was ~36 kHz/20%RH corresponding to the A1 mode at the resonant frequency of 41 MHz. This value is 3.6 times the sensitivity of the same mode of the device

without nanorods where the value was 10.4 kHz/20%RH. The calculated percentages enhancements in sensitivity for various humidity change intervals are shown in Figure 7.7.

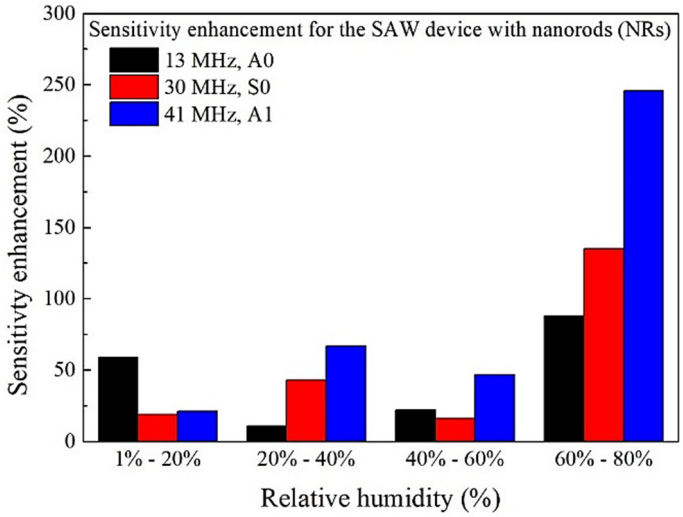

Figure 7.7 The sensitivity enhancement in percentage of various vibrating modes to changes in relative humidity at intervals of 20% RH of the nanorods-enhanced SAW device

There was a substantial enhancement of sensitivity when the change in humidity was between 60-80%, where the maximum enhancement was 246% for the A1 mode. However, the A0 and S0 modes also showed enhancements of 88% and 135%, respectively, for the same humidity change and interval. However, the values of sensitivity for the different vibration modes of the SAW device for humidity intervals from 1-60% were enhanced by 10-60%.

Moreover, the sensitivity for the A1 mode when humidity was changed from 80-90% was 47.7 kHz/10%RH for the nanorods-enhanced device. This value is 2.7 times the sensitivity of the same mode for the device without nanorods and 1.3 times higher than when humidity was changed from 60-80%.

The sensitivity and/or the frequency shift achieved in response to humidity change of the proposed devices exhibited higher values compared to those devices operated in lower operating frequency or in bulk mode (e.g. quartz-based devices) as mentioned in Table 2.5 in section 2.5.3. Whereas, they showed lower values compared to the SAW devices which

is mainly attributing to the lower operating frequency where the maximum resonant frequency of the proposed devices was 41 MHz, and this value is much lower than that of the highest frequency used in the literature (~395 MHz). However, the sensitivity of the flexible ZnO/Aluminium foil was greater than that of the flexible ZnO/polyimide where it is the only flexible device with similar structure found in the literature for humidity sensing. This indicates that the proposed flexible devices showed better performance than that of the flexible ZnO thin film-based SAW devices.

On the other hand, the limit of detection and resolution of the flexible device was 10% RH which is 10 times less than that of the capacitive humidity sensors. Also, the dynamic range of detection of flexible sensors was 1% - 90% while it was 0% - 100% for the capacitive sensors.

However, the significance of these sensors is the flexibility where the devices were performing humidity sensing in flat and bending (curved) positions. Besides, ZnO/Al foil-based SAW devices are investigated for the first time as humidity sensors and they exhibited a good potential for the detection of humidity, and they are subject for future development.

7.5 Real-time cycling response of flexible SAW device to humidity change

The real-time responses of the SAW device were further investigated to show repeatability during humidity cycling, as shown in Figure 7.8. The relative humidity increased and decreased between 1% and 90% in several cycles and the resulting changes in resonant frequency were recorded. The S11 signal was used to determine the resonant frequency and Figures 7.8a and 7.8b show the frequency response of A0 and S0 modes when the device was kept flat. Meanwhile, Figures 7.8c and 7.8d show the frequency response in humidity cycling for A0 and S0 modes when the device was bent down.

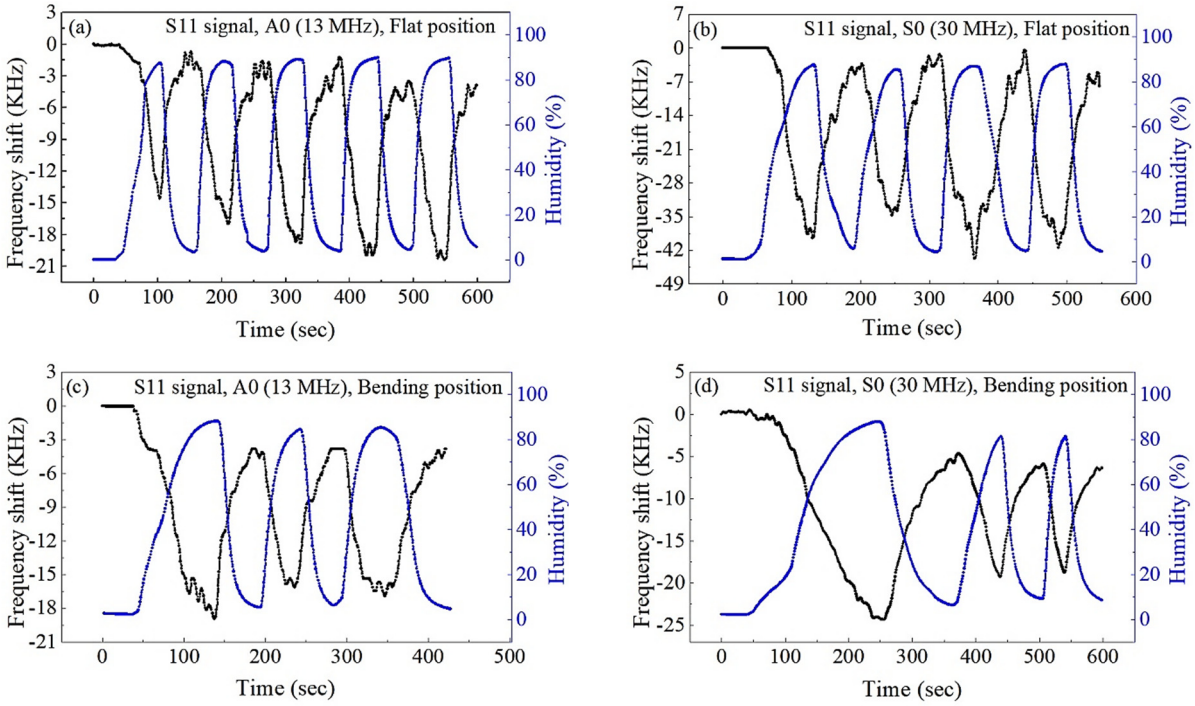

Figure 7.8 Cycling response to changes in humidity showing the change in frequency shifts of a) A0 mode in the flat position, b) S0 mode in the flat position, c) A0 mode in the bent down position and d) S0 mode in a bent down position. S11 signal was used for the determination of the resonant frequency

The results show that the resonant frequency decreased when the humidity increased due to the accumulation of water vapour on the surface of the device, and it increased when the humidity was decreased as the water evaporated.

However, it is suggested that some of the water molecules have remained on the surface of the device while cycling due to the very rough surface, and this allowed the diffusion of these molecules into the thin film. This probably resulted in changes in the surface sheet conductivity of the ZnO thin film, hence causing the fluctuations in the frequency shift. In addition, the resonant frequency did not move back toward the baseline level when the humidity was decreased.

However, the overall cycling response of the A0 and the S0 modes exhibited excellent repeatability when the SAW device was kept in flat and bent positions, as shown in Figure 7.9.

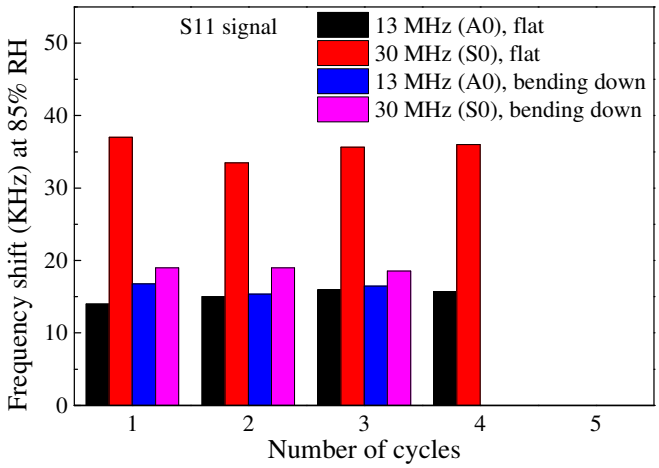

Figure 7.9 The reproducibility and reliability of humidity sensing of A0 and S0 vibrating modes of S11 signals while the SAW device was kept in flat and bent-down positions

Likewise, the cycling response of the device obtained when the transmission signal was used to determine the resonant frequency showed similar behaviour compared to the response of the reflection signal, as seen in Figure 7.10. It shows that the resonant frequency shifted downward when the humidity was increased and moved upward when the humidity was decreased by purging more dry nitrogen into the chamber.

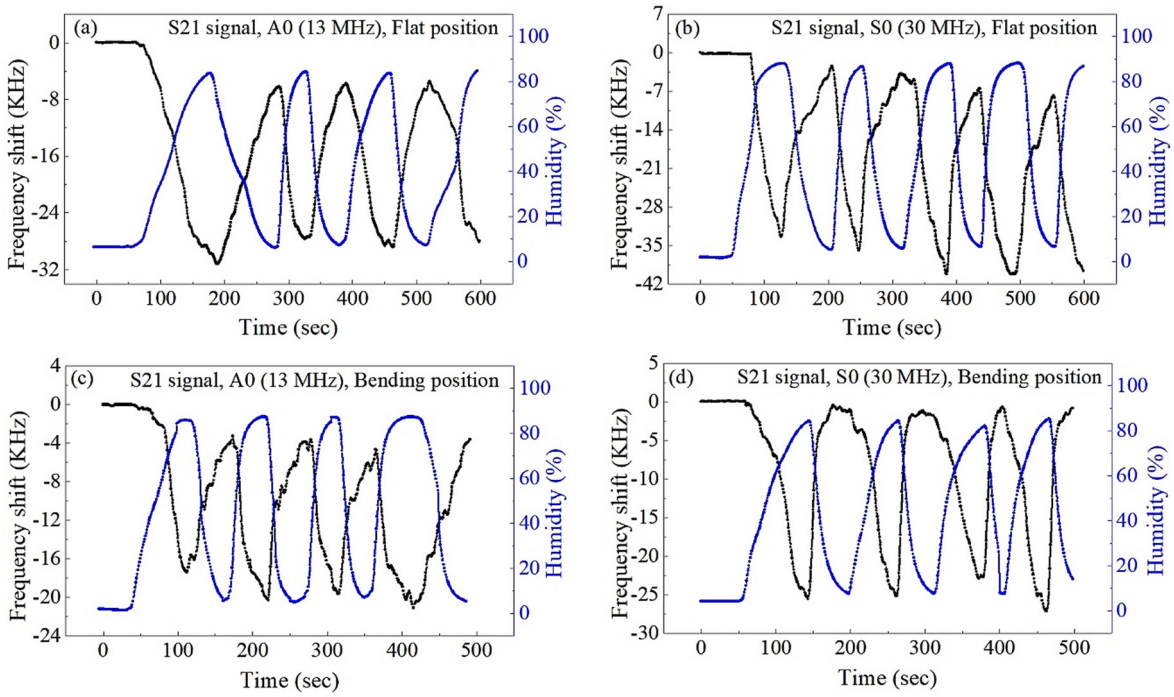

Figure 7.10 Cycling response to changes in humidity showing the change in frequency shifts of a) A0 mode in the flat position, b) S0 mode in the flat position, c) A0 mode in a bent down position and d) S0 mode in a bent down position. S21 signal was used for the determination of the resonant frequency

Thus, the sensing performance for the reflection (S11) and transmission (S21) signals were comparable, and the overall frequency response exhibited excellent repeatability when the device was kept in both flat and bent down positions as shown in Figures 7.9 and 7.11.

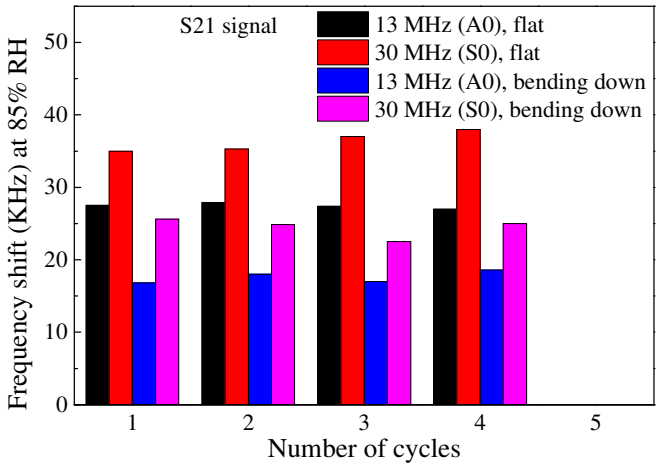

Figure 7.11 The reproducibility and reliability of humidity sensing of A0 and S0 vibrating modes of S21 signals while the SAW device was kept in flat and bent-down positions

Furthermore, the real-time response to humidity change of the nanorod-enhanced SAW device was further studied, and the results are shown in Figure 7.12a and 7.12b for the A0 and S0 modes, respectively.

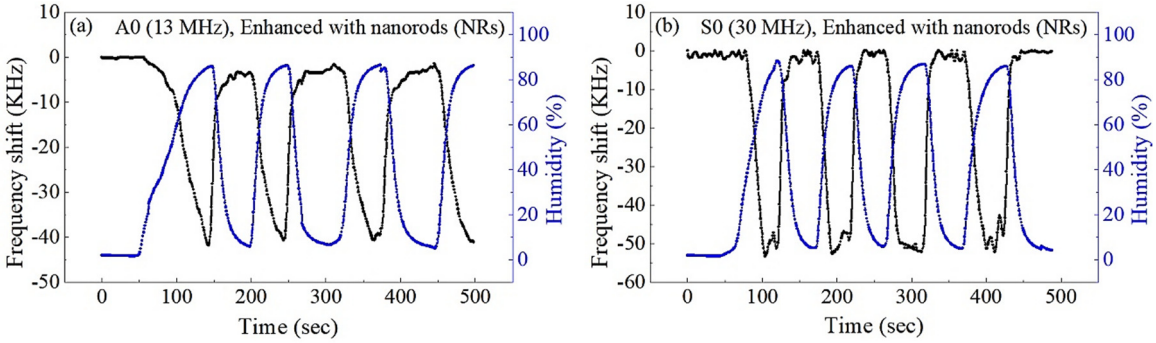

Figure 7.12 Cycling response to changes in humidity showing the change in frequency shifts of the nanorods-enhanced SAW device for a) A0 mode and b) S0 mode

The resonant frequency decreased the humidity was increased. Then. It was fully recovered, and it showed the same stable level in the four cycles when the humidity was decreased to the original value before it started to decrease again when the humidity was increased. The

frequency response of the device to humidity cycling showed better stability and repeatability than that of the device without nanorods, as shown in Figure 7.13.

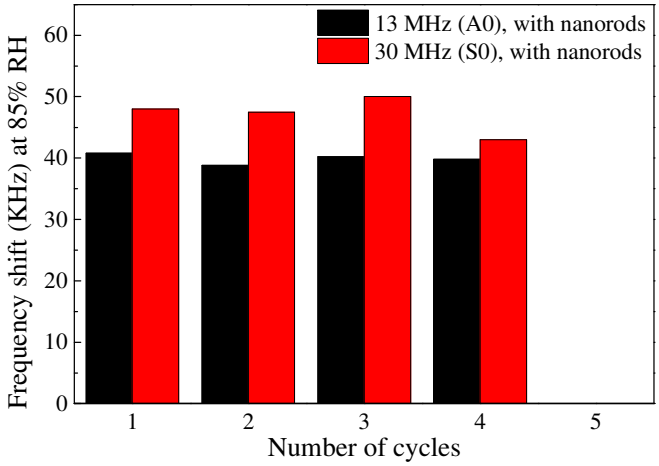

Figure 7.13 The reproducibility and reliability of humidity sensing of A0 and S0 vibrating modes of nanorods-enhanced SAW device

7.6 The frequency response of the flexible SAW device to various breath patterns

The flexible ZnO thin film-based SAW device was further investigated for respiratory rate monitoring and apnoea detection. Exhaled air carries humidity and other gases such as oxygen and carbon dioxide. Therefore, changes in humidity and the temperature during the breath cycle were exploited to monitor respiratory status, as these variables strongly influence the acoustic wave velocity. The SAW device was placed at a distance of approximately ~5.0 cm away from the mouth where the exhaled air comes into contact with the sensor. A commercial reference sensor was fixed to the top surface of the device to measure the change in humidity and temperature continuously. The humidity changes during inspiration and expiration are shown in Figure 7.14 as measured by the commercial reference sensor.

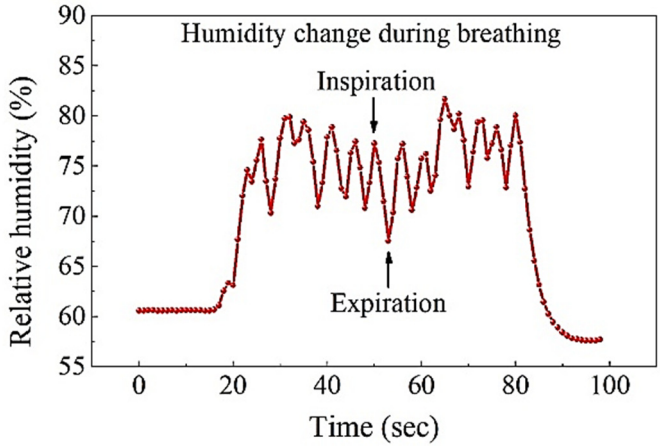

Figure 7.14 The changes in relative humidity as a result of breath cycling (inspiration and expiration)

The humidity increased from ~60 % to 80 % as a result of the moisture air in exhalations, and it fluctuated between 70 % and 80 % during the breathing cycles. These changes in humidity were sufficient to cause a significant frequency shift, as discussed in the previous section. Humidity was increased during the expiratory phase and decreased during the inspiration phase. However, it is noticed that humidity levels did not reach the original baseline because the time required to dry all the water vapour is not long enough, and the humidity is kept accumulated on the sensor.

On the other hand, the temperature was increasing continuously during the process where it was varied from 26.0 – 28.5 ^{o}C within one minute of breathing cycles, as seen in Figure 7.15. Although the temperature increased, there was a slight difference between inspiration and expiration where the difference in temperature during one breath cycle from the beginning of expiration until the end of inspiration was only about ± 0.5 ^{o}C. The frequency shift caused by the temperature variation during a breath cycle is calculated using the TCF equation (2.36), and the results are ~2.0 kHz and 4.3 kHz corresponding to A0 and S0 modes, respectively.

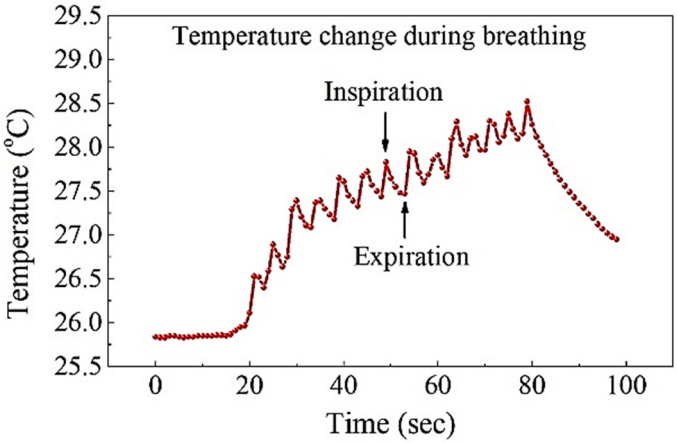

Figure 7.15 The changes in temperature as a result of breath cycling (inspiration and expiration)

The frequency responses of the SAW device as a function of time versus the change in the temperature and the humidity in one breath cycle are shown in Figures 7.16a and 7.16b, respectively.

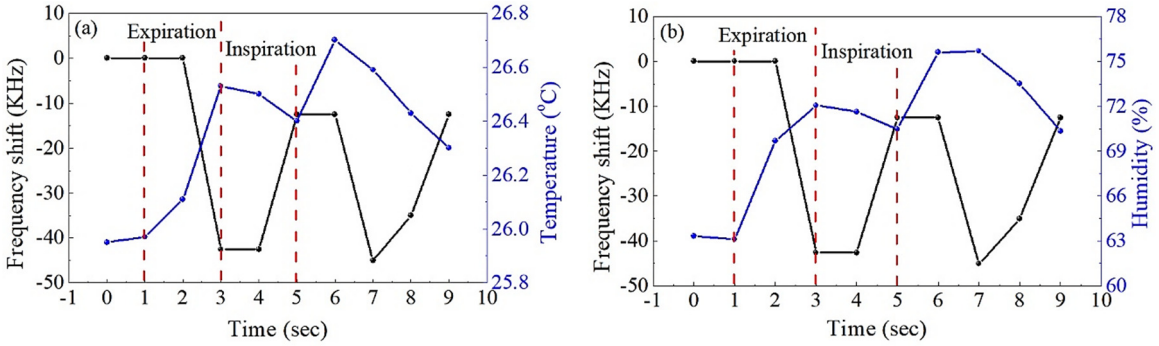

Figure 7.16 Frequency shift of SAW device in response to changes in a) temperature and b) humidity showing the time of inspration and expiration during one breath cycle

The temperature changed from ~26.0 to 26.5 °C during expiration, and humidity increased from 63% to 72%. The resonant frequency also decreased during the expiratory phase and increased during inspiration, where the maximum frequency shift was 42.6 kHz. The change in acoustic wave velocity has resulted from the combined effects of mass loading due to the accumulation of humidity at the surface of the sensor and the temperature changes during expiration and inspiration.

The response and recovery times of the device were about 2.0 seconds (1.0 second for each), and the total time of the breath cycle was 4.0 seconds. Therefore, the resonant frequency was not fully recovered to the original baseline, and instead held a value of ~12.45 kHz that could decrease further in the subsequent cycles. This is mainly attributed to the remaining water molecules at the surface of the device, which required more time to be entirely evaporated.

7.6.1 The frequency response of flexible SAW device to various breath patterns in a flat position

Figure 7.17 shows an example of the frequency response of the SAW device to several breath cycles involving an apnoea episode. The frequency shift decreased and increased with each expiration and inspiration breath cycle in a regular pattern. The estimated respiratory rate was 14 breaths per minute in the period from 20-80 seconds in one-minute breath cycles. The resonant frequency fully recovered when breathing paused (apnoea) at a time of 84 seconds and held the same value at the original baseline for 40 seconds before breathing resumed again for further regular breath cycles.

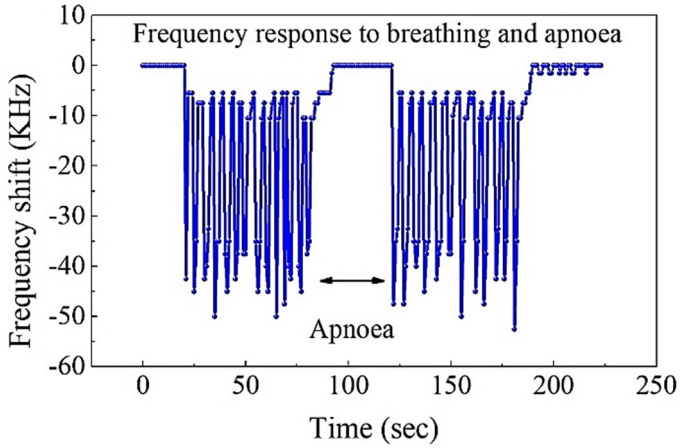

Figure 7.17 The response of SAW device showing frequency shifts due to regular breathing and apnoea episode

Figure 7.18a and 7.18b show the frequency response of the A0 and S0 modes to breathing cycles within one minute. The results show that the frequency shifts of the zero-order vibration modes of the Lamb wave were decreased and increased in response to the interchange between expiration and the inspiration. The respiratory rate can be estimated by counting the number of breath cycles in one minute. Thus, the respiratory rates detected by A0 and S0 modes were 13 and 17 breaths per minute, respectively. The respiration pattern was regular since the time between the two consecutive breath cycles was nearly similar

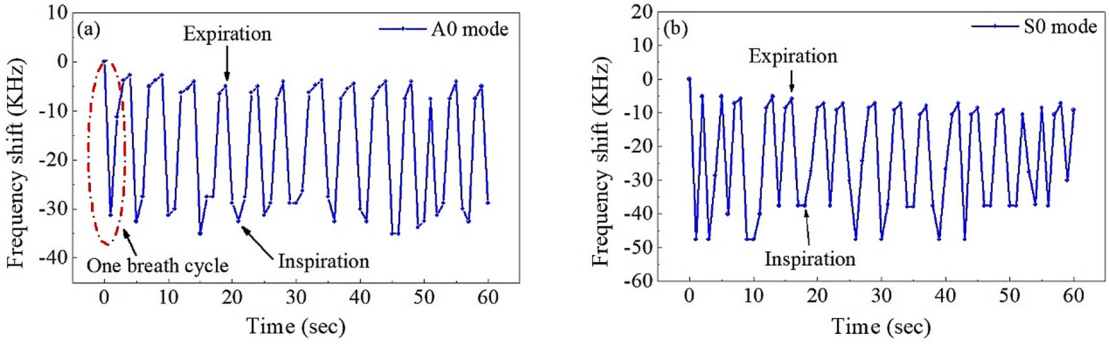

Figure 7.18 The response of SAW device showing frequency shifts due to regular breathing within one-minute cycle for a) A0 and b) S0 modes

Figures 7.19a and 7.19b show the frequency response of the fundamental modes A0 and S0, respectively, for slow breathing status (bradypnea) with apnoea episodes (cessation of breathing). The resonant frequency shifted immediately each time the device was exposed to the exhaled air, and it had fully recovered at the end of the inspiratory phase. The resonant frequency was stable and held the same original value during the apnoea interval, indicating that breathing had ceased.

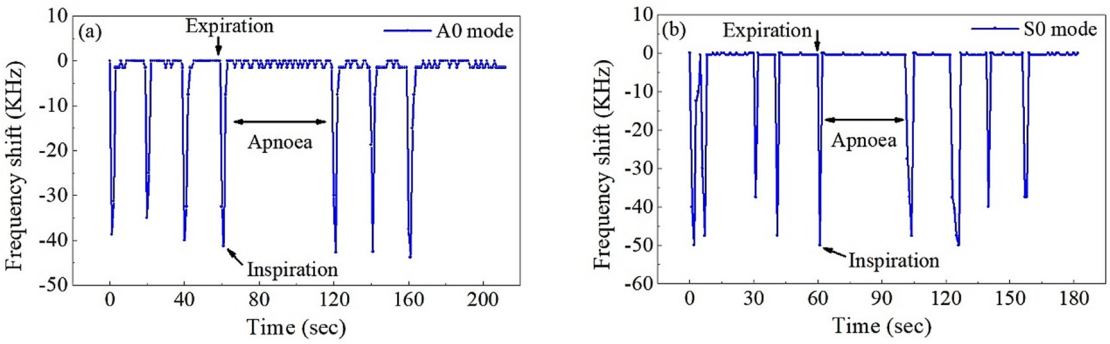

Figure 7.19 The response of SAW device showing frequency shifts due to bradypnea and apnoea episodes for a) A0 and b) S0 modes

However, the detection of tachypnoea, where the respiratory rate is higher than 20 breaths/min is more challenging than for bradypnea as it requires high response and recovery speeds to distinguish between the numbers of breaths. Therefore, the performance of the SAW device in detecting high respiratory rates was investigated. The frequency shifts of the A0 and S0 modes as a result of rapid breathing with alternating apnoea intervals are shown in Figures 7.20a and 7.20b, respectively. The resonant frequency of the SAW device exhibited excellent responsiveness to the high respiratory rate with a response time of 1.0 second, and it decreased and increased with each breath cycle. However, the resonant frequency was not recovered to the baseline during the inspiratory phase due to the accumulation of the humidity at the surface of the device. When breathing ceased, the resonant frequency fully recovered and became stable as this was allowed a longer time for any remained moistures to be dried. The respiratory rates detected by the A0 mode and S0 modes were 25 and 30 breaths per minute, respectively.

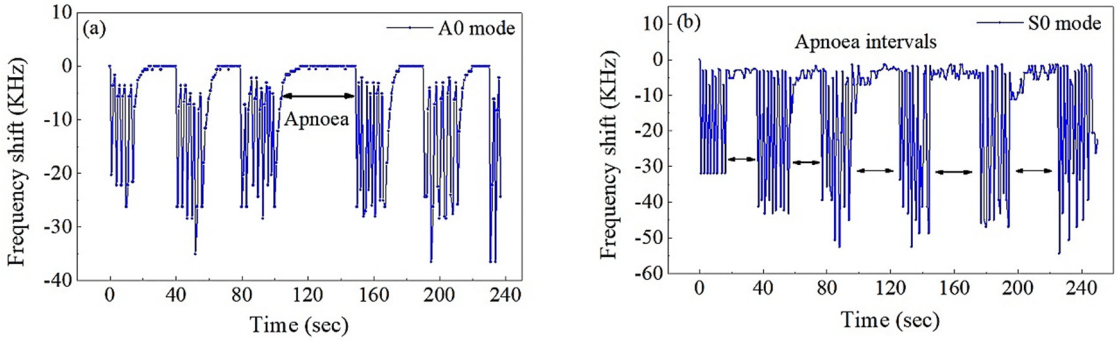

Figure 7.20 The response of SAW device showing frequency shifts due to tachypnea and apnoea episodes for a) A0 and b) S0 modes

7.6.2 The frequency response of flexible SAW device with enhanced nanorods to various breath patterns

The SAW device with enhanced-nanorods was also investigated for respiratory rate monitoring and apnoea detection. Figures 7.21a and 7.21b show the frequency shift of the A0 and S0 modes as a function of time in response to breathing cycles in one minute.

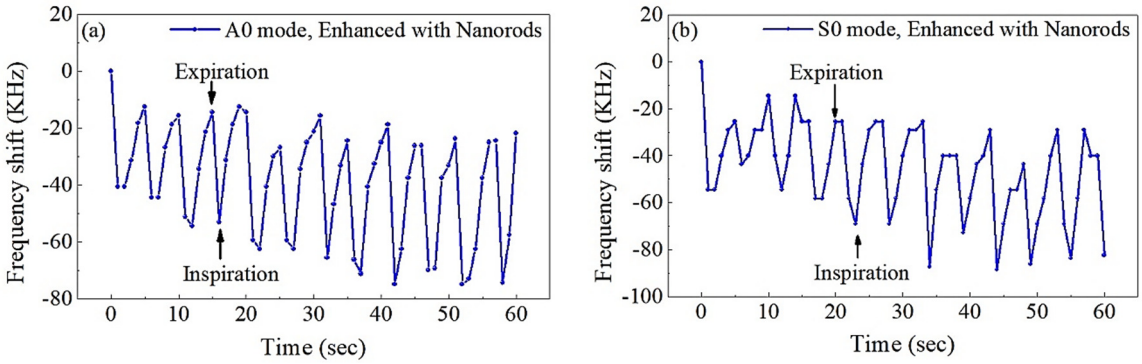

Figure 7.21 The response of the nanorods-enhanced SAW device showing frequency shifts due to regular breathing within one-minute cycle for a) A0 and b) S0 modes

The frequency shift continuously decreased with each breathing cycle, and it showed a long recovery time of 3-4 seconds due to the trapped moistures within the nanorods and on the surface of the device. However, the values of the changed resonant frequencies have been increased compared to the device without nanorods. This is mainly attributed to the mass loading and the changes in the surface sheet conductivity of the ZnO thin film due to the interaction between the trapped humidity from one side, and the nanorods and the ZnO thin film from another side.

7.6.3 The frequency response of flexible SAW device position to various breath patterns in a bent position

The performance of the SAW device in monitoring respiratory status and detecting apnoea while the device was kept in a bent position was also investigated. The SAW device with a wavelength of 160 μm was bent-up on a semi-circular holder with a radius of 50 mm, as shown in Figure 3.15b in section 3.6. The frequency shifts in response to various respiratory cases, including regular, bradypnea, tachypnoea and apnoea, are shown in Figures 7.22a and 7.22b, for both A0 and S0 modes, respectively.

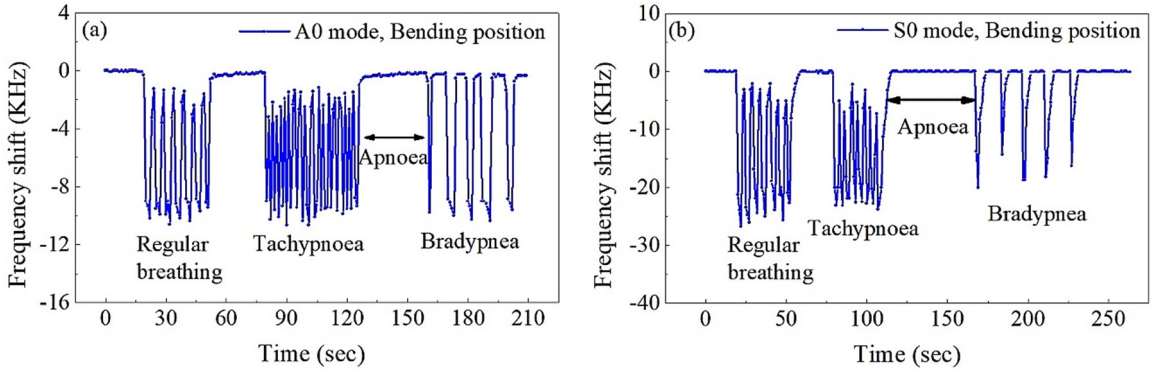

Figure 7.22 The response of SAW device showing frequency shifts due to regular breathing, tachypnea, bradypnea and apnoea episode while the device was kept in bent down position for a) A0 and b) S0 modes

The shifts in the resonant frequency of both modes decreased in response to expiration in the various breath patterns. They exhibited comparable performance to those of the flat device. However, the maximum change in the resonant frequency of A0 mode was 10.0 kHz, and it was 20.0-25.0 kHz in the case of the S0 mode. These values are significantly lower than the frequency shifts obtained for the same modes when the device was in a flat position. Moreover, the resonant frequency took a more prolonged time of 3.0-4.0 seconds to fully recover when breath had ceased (apnoea). These are attributed to the defects and cracks generated in the ZnO thin film as a result of bending of the device, where humidity was likely to have accumulated within those cracks, thus delaying in the recovery time.

7.7 Summary

Flexible SAW devices based on ZnO thin film on aluminium foil substrate have been investigated for the first time for humidity sensing as well as breath detection while the devices were placed in flat and bending (curved) positions.

Frequency responses to changes in relative humidity for the flexible SAW devices with a wavelength of 160 μm with and without nanorods were obtained. Relative humidity was changed in a range of 1-90% inside a humidity-controlled chamber where the devices were

placed in flat and bent down positions with a curvature radius of 50 mm. An external reference sensor was used to measure the changes in humidity and temperature.

The results showed that the maximum frequency shift was -57 kHz at 90%RH for the higher-order A1 mode when the value of S11 was used to determine resonant frequency, whereas the lowest value was -19.6 kHz for the A0 mode when the device was bent. These readings are corresponding to sensitivity values of 19 and 7 kHz/10%RH at 90%RH for the A1 and A0 modes, respectively. This attributes to (1) the high resonant frequency of the A1 mode which converges toward Rayleigh wave where it is confined on the surface of the device, and (2) to defects and cracks generated due to bending of the device. On the other hand, the maximum value of sensitivity of the nanorod-enhanced device was 47.7 kHz/10%RH at 90%RH, and this is resulted in a maximum enhancement by 3.6 folds. The real-time cycling response showed excellent repeatability over several cycles when the device was kept in flat and bent positions.

The values of sensitivity of flexible devices are lower than that of the SAW based humidity sensors in the literature due to the low operating frequency and the cracks generated due to bending the devices. Besides, the resolution of the flexible device was 10% RH and the dynamic range was 1% - 90% RH which they are lower than that of the capacitive humidity sensors. However, ZnO/Al foil-based SAW devices are investigated for the first time as humidity sensors and they exhibited better performance compared to the flexible ZnO thin film-based SAW devices. Besides, they possessed good potential for the detection of humidity in flat and bending position which makes them an interesting candidate for future development.

Furthermore, the sensing performance of the flexible SAW devices was obtained for various breathing patterns. The results showed that the devices exhibited excellent performance and responsiveness to various breathing patterns. The resonant frequency was shifted immediately in response to inhalation and exhalation. The response and recovery time was 1 second, and the maximum respiratory rate detected was 30 breaths/minutes, which was limited by the sampling rate of the LabVIEW applications. Therefore, the proposed sensor exhibited the capability to detect apnoea in one second, which makes it a potential candidate for early detection of apnoea related problems.

Chapter Eight

Conclusions and future work

8.1 Conclusions

Flexible ZnO thin film on aluminium foil-based SAW devices have been investigated for the first time as sensors for temperature, UV light, and humidity as well as breath and apnoea detection, and these devices were performing sensing while they were placed in flat and bending (curved) positions.

The devices were fabricated by depositing ZnO thin film ~5 μm thick on a commercial and low-cost aluminium foil 50 μm thick using DC reactive magnetron sputtering method. The depositing parameters were; DC power 400 W and flow rates of Ar and O_2 were 6.5 and 13 sccm, respectively. The as-deposited ZnO thin film was characterised using SEM, XRD and AFM. The results showed that the surface morphology of ZnO thin film exhibited a dense granular pattern composed of large ZnO grain-like structures with an average diameter of ~350 nm. The ZnO nanocrystals were vertically aligned in highly oriented columnar structures perpendicular to the aluminium substrate. They have also possessed wurtzite or hexagonal crystalline structure with a textured orientation in the (0002) plane along the c-axis and perpendicular to the substrate, which texture coefficient was 98.5%. Low compressive stress of -0.52 GPa was observed as well as a relatively high RMS value of surface roughness of 261.1 nm. The ZnO thin film possessed a high quality and the desired structural and physical properties for good piezoelectric performance.

Various types of IDTs structures were designed using analytical and finite-element method-based models to excite Lamb waves. Accordingly, flexible SAW sensors were made by patterning two different structures of IDTs (Cr/Au) using lithography and lift-off processes. The designed wavelengths used for sensing studies were 100 μm, 160 μm, 200 μm, 300 μm, and 400 μm. Frequency response was obtained and compared with simulation results, and

they were in good agreement. Frequency spectra were also measured for selected devices when they were placed in bent-down and bent-up positions by which the acoustic signal was still detectable and maintained good quality.

ZnO nanorods were further grown on the surface of a SAW device with a wavelength of 160 μm in order to enhance the sensitivity during sensing performance. The growth of the nanorods was conducted using a modified hydrothermal technique which a precursor solution of zinc nitrate 25 mM was prepared, and its pH was adjusted to 10.3 by adding ammonium hydroxide. The solution was placed in a sealed container and heated to about 85 ^{o}C for 4 hours. An isolation layer of SiO_2 was used to separate the thin film from nanorods and followed by depositing a seed layer of ZnO of 30 nm thick. The nanorods were evaluated, and the results showed that nanorods were aligned vertically in columnar structures perpendicular to the ZnO thin film with an average length of 900 nm and a diameter of 65 nm.

The flexible SAW devices were used for temperature, UV light, humidity, and breath sensing and the key findings are:

- TCF was obtained for all devices in which TCF values were among the highest values compared to those published for flexible devices. The range of the measured TCF values was 288-773 ppm/K. It was suggested that the reason for the high TCFs is the high TEC value of aluminium foil and its elastic properties. However, although low-frequency Lamb waves such as A0 modes possessed higher TCF values than that of high frequency such as S0 and higher-order modes, the latter exhibited better performance and more significant frequency shift, and hence higher sensitivity to temperature. The real-time cycling response showed that the devices had excellent linearity and repeatability when they were placed in flat and bent positions.

- The frequency shift of SAW devices possessed a linear relationship with various UV light intensity when they were placed in flat, bent down and bent up positions. A more substantial shift was observed when a high-power UV light irradiation was used due to UV light interaction and thermal effects as well as for higher frequency vibration modes, and when the devices were placed in flat positions. The highest and the lowest sensitivity values to low power UV light, which thermal effect is insignificant, were 63 and 8 $(mW/cm^2)^{-1}$, respectively. These results are corresponding to the device with a wavelength of the 200 μm in a flat position, and the 160 μm in bent-up position, respectively. However, the sensitivity to UV light was enhanced 1.76 times when nanorods-enhanced SAW device with was used.

- The frequency shift of the SAW device of a wavelength of 160 μm, exhibited a monotonic but non-linear relationship with the change in relative humidity when the device was placed in flat and bent positions. The highest and lowest sensitivity values were 19 and 7 kHz/10% at 90%RH for the A1 and A0 modes, respectively. The nanorods-enhanced SAW device showed maximum enhancement in sensitivity by 3.6-fold compared to the device without nanorods. The real-time cycling response of the SAW device in flat and bent positions exhibited acceptable repeatability.

- The frequency response of the SAW device to various breathing patterns was also investigated when the device was kept in flat and bent-up positions. The results showed that the device exhibited excellent responsiveness to normal, slow, and fast respiratory rates as well as apnoea detection. The response and recovery time were both one second which was limited by the recorded sampling rate of the LabVIEW application, and therefore, the highest rate detected was 25-30 breaths/minute.

8.2 Future work

Significant progress has been reported on various flexible SAW sensors with high sensitivity and excellent physical properties as well as low cost with the capability for integration with other technologies such as nanotechnology, microfluidics, and lab-on-a-chip. The main challenge of flexible SAW devices is selecting a substrate material which can withstand bending and deformation and considered to be a suitable medium for acoustic wave propagation without causing damping or attenuation to the signal. Depositing high-quality ZnO thin film is also another requirement for maximum piezoelectric performance, hence transduction excellence. Besides, the high resonant frequency and Q factor of the sensors are very crucial parameters for high sensitivity and reliability.

Thus, the suggested future work includes further improvements to the fabrication process to overcome the high rough surface of aluminium foil. This could be achieved by optimising the process parameters or introducing intermediate materials to decrease surface roughness such using nanoparticles on the surface.

The design of IDTs is another crucial factor in developing high-performance SAW sensors. Therefore, a focused IDT design with internal reflectors and optimised wavelength and dimensions could make an improvement in generating a high-quality signal with high Q factor, reduce power loss, and enhance coupling coefficients.

Besides, further studies using different sensitive layers are recommended to improve the sensitivity of the SAW sensors. In this thesis, ZnO nanorods were used as a sensing layer. However, further work is needed to improve the growth process or using sensing materials decorated nanorods such as Cu or Ag nanoparticles.

Moreover, studies have been conducted in using ZnO thin film on aluminium foil in microfluidics applications. Therefore, it would be an interesting field for developing an integrated sensing-microfluidics platform as a flexible lab-on-a-chip where one part is used

for acoustofluidics, and another part is utilised for sensing. Furthermore, finite element analysis can be used to study the Lamb wave modes and wave propagation into the liquid.

It is also suggested to conduct a comparative study on the influence of surface roughness, substrate type, and film properties (various thickness, grain size, and texture) on surface acoustic wave characteristics and sensing performance.

References

[1] R. Tao, W. Wang, J. Luo, S. A. Hasan, H. Torun, P. Canyelles-Pericas*, et al.*, "Thin film flexible/bendable acoustic wave devices: Evolution, hybridization and decoupling of multiple acoustic wave modes," *Surface and Coatings Technology,* vol. 357, pp. 587-594, 2019.

[2] A. Nag, S. C. Mukhopadhyay, and J. Kosel, "Wearable Flexible Sensors: A Review," *IEEE Sensors Journal,* vol. 17, pp. 3949-3960, 2017.

[3] M. Pohanka, "The Piezoelectric Biosensors: Principles and Applications," *Int. J. Electrochem. Sci,* vol. 12, pp. 496-506, 2017.

[4] M. Pohanka, "Overview of Piezoelectric Biosensors, Immunosensors and DNA Sensors and Their Applications," *Materials (Basel, Switzerland),* vol. 11, pp. 448, 2018.

[5] K. Uchino, "Chapter 1 - The Development of Piezoelectric Materials and the New Perspective," in *Advanced Piezoelectric Materials (Second Edition)*, K. Uchino, Ed., ed: Woodhead Publishing, 2017, pp. 1-92.

[6] A. Manbachi and R. S. C. Cobbold, "Development and Application of Piezoelectric Materials for Ultrasound Generation and Detection," *Ultrasound,* vol. 19, pp. 187-196, 2011.

[7] K. K. Sappati and S. Bhadra, "Piezoelectric Polymer and Paper Substrates: A Review," *Sensors (Basel, Switzerland),* vol. 18, pp. 3605, 2018.

[8] U. Ozgur, D. Hofstetter, and H. Morkoc, "ZnO devices and applications: a review of current status and future prospects," *Proceedings of the IEEE,* vol. 98, pp. 1255-1268, 2010.

[9] S. K. Arya, S. Saha, J. E. Ramirez-Vick, V. Gupta, S. Bhansali, and S. P. Singh, "Recent advances in ZnO nanostructures and thin films for biosensor applications," *Analytica chimica acta,* vol. 737, pp. 1-21, 2012.

[10] Y. Q. Fu, J. Luo, X. Du, A. Flewitt, Y. Li, G. Markx*, et al.*, "Recent developments on ZnO films for acoustic wave based bio-sensing and microfluidic applications: a review," *Sensors and Actuators B: Chemical,* vol. 143, pp. 606-619, 2010.

[11] T. Lim, G. Ico, K. Jung, K. Bozhilov, J. Nam, and A. Martinez-Morales, "Crystal growth and piezoelectric characterization of mechanically stable ZnO nanostructure arrays," *CrystEngComm,* vol. 20, pp. 5688-5694, 2018.

[12] D. Lee, Y. Fu, S. Maeng, X. Du, S. Tan, J. Luo*, et al.*, "Integrated ZnO surface acoustic wave microfluidic and biosensor system," in *2007 IEEE International Electron Devices Meeting*, 2007, pp. 851-854.

[13] Y. Q. Fu, J. Luo, N.-T. Nguyen, A. Walton, A. J. Flewitt, X.-T. Zu*, et al.*, "Advances in piezoelectric thin films for acoustic biosensors, acoustofluidics and lab-on-chip applications," *Progress in Materials Science,* vol. 89, pp. 31-91, 2017.

[14] C. Yoon, B. Jeon, and G. Yoon, "A Feasibility Study of Fabrication of Piezoelectric Energy Harvesters on Commercially Available Aluminum Foil," *Energies,* vol. 12, pp. 2797, 2019.

[15] Y. Liu, Y. Li, A. M. el-Hady, C. Zhao, J. Du, Y. Liu*, et al.*, "Flexible and bendable acoustofluidics based on ZnO film coated aluminium foil," *Sensors and Actuators B: Chemical,* vol. 221, pp. 230-235, 2015.

[16] S. H. Yoon and D.-J. Kim, "Fabrication of piezoelectric ZnO and PZT films for FPW device," *MRS Online Proceedings Library Archive,* vol. 966, 2006.

[17] T. M. A. Gronewold, "Surface acoustic wave sensors in the bioanalytical field: Recent trends and challenges," *Analytica Chimica Acta,* vol. 603, pp. 119-128, 2007.

[18] D. B. Go, M. Z. Atashbar, Z. Ramshani, and H.-C. Chang, "Surface acoustic wave devices for chemical sensing and microfluidics: a review and perspective," *Analytical Methods,* vol. 9, pp. 4112-4134, 2017.

[19] Y. Fu, "Zno Thin Films and Nanostructures for Acoustic Wave-Based Microfluidic and Sensing Applications," in *Functional Materials and Electronics*, ed: Apple Academic Press, 2018, pp. 195-262.

[20] H. Liu, J. Zhong, C. Lee, S.-W. Lee, and L. Lin, "A comprehensive review on piezoelectric energy harvesting technology: Materials, mechanisms, and applications," *Applied Physics Reviews,* vol. 5, p. 041306, 2018.

[21] M. Kim, Y. Wu, E. Kan, and J. Fan, "Breathable and flexible piezoelectric ZnO@ PVDF fibrous nanogenerator for wearable applications," *Polymers,* vol. 10, p. 745, 2018.

[22] V. Coleman and C. Jagadish, "Basic properties and applications of ZnO," in *Zinc oxide bulk, thin films and nanostructures*, ed: Elsevier, 2006, pp. 1-20.

[23] "Fundamentals of Piezoelectricity," in *Piezoelectric Transducers for Vibration Control and Damping*, S. O. R. Moheimani and A. J. Fleming, Eds., ed London: Springer London, 2006, pp. 9-35.

[24] K. Kao, "Ferroelectrics, piezoelectrics and pyroelectrics," *Dielectric Phenomena in Solids,* pp. 213-282, 2004.

[25] D. Damjanovic, "Ferroelectric, dielectric and piezoelectric properties of ferroelectric thin films and ceramics," *Reports on Progress in Physics,* vol. 61, pp. 1267-1324, 1998.

[26] K. Uchino and P. S. U. U. P. U. "*Introduction to Piezoelectric Actuators and Transducers,"* pennsylvania state univ university park, 2003.

[27] Y.-C. Chen, C.-K. Cheng, and S.-C. Shen, "Design and Fabrication of a Displacement Sensor Using Screen Printing Technology and Piezoelectric Nanofibers in d33 Mode," *Sensors and Materials,* vol. 31, pp. 233-244, 2019.

[28] K. Uchino, "Introduction to piezoelectric actuators and transducers," pennsylvania state univ university park, 2003.

[29] K. M. Ok, E. O. Chi, and P. S. Halasyamani, "Bulk characterization methods for non-centrosymmetric materials: second-harmonic generation, piezoelectricity, pyroelectricity, and ferroelectricity," *Chemical Society Reviews,* vol. 35, pp. 710-717, 2006.

[30] L. B. Kong, H. Huang, and S. Li, "Fundamentals of Ferroelectric Materials," *Ferroelectric Materials for Energy Applications,* pp. 1-31, 2018.

[31] J. Valasek, "Piezo-Electric and Allied Phenomena in Rochelle Salt," *Physical Review,* vol. 17, pp. 475-481, 1921.

[32] W. P. Mason, "Piezoelectricity, its history and applications," *The Journal of the Acoustical Society of America,* vol. 70, pp. 1561-1566, 1981.

[33] A. Lüker, "A short history of ferroelectricity," *Instituto Superior Técnico Departamento de Física,* 2011.

[34] S. Guerin, S. A. M. Tofail, and D. Thompson, "Organic piezoelectric materials: milestones and potential," *NPG Asia Materials,* vol. 11, p. 10, 2019.

[35] E. Fukada, "Piezoelectricity of Wood," *Journal of the Physical Society of Japan,* vol. 10, pp. 149-154, 1955.

[36] E. Fukada, "On the Piezoelectric Effect of Silk Fibers," *Journal of the Physical Society of Japan,* vol. 11, pp. 1301A-1301A, 1956.

[37] E. Fukada and I. Yasuda, "On the Piezoelectric Effect of Bone," *Journal of the Physical Society of Japan,* vol. 12, pp. 1158-1162, 1957.

[38] E. Fukada and I. Yasuda, "Piezoelectric Effects in Collagen," *Japanese Journal of Applied Physics,* vol. 3, pp. 117-121, 1964.

[39] E. Fukada and Y. Ando, "Piezoelectricity in oriented DNA films," *Journal of Polymer Science Part A-2: Polymer Physics,* vol. 10, pp. 565-567, 1972.

[40] M. Chen-Glasser, P. Li, J. Ryu, and S. Hong, "Piezoelectric materials for medical applications," in *Piezoelectricity-Organic and Inorganic Materials and Applications*, ed: IntechOpen London, 2018, pp. 125-145.

[41] A. H. Rajabi, M. Jaffe, and T. L. Arinzeh, "Piezoelectric materials for tissue regeneration: A review," *Acta Biomaterialia,* vol. 24, pp. 12-23, 2015.

[42] A. L. Kholkin, N. A. Pertsev, and A. V. Goltsev, "Piezoelectricity and Crystal Symmetry," in *Piezoelectric and Acoustic Materials for Transducer Applications*, A. Safari and E. K. Akdoğan, Eds., ed Boston, MA: Springer US, 2008, pp. 17-38.

[43] W. Heywang, K. Lubitz, and W. Wersing, *Piezoelectricity: evolution and future of a technology* vol. 114: Springer Science & Business Media, 2008.

[44] A. Vazquez Carazo, "Piezoelectric Transformers: An Historical Review," *Actuators,* vol. 5, 2016.

[45] M. Vijatović, J. Bobić, and B. Stojanović, "History and Challenges of Barium Titanate: Part I," *Science of Sintering,* vol. 40, 2008.

[46] M. Vijatović, J. Bobić, and B. Stojanović, "History and Challenges of Barium Titanate: Part II," *Science of Sintering,* vol. 40, 2008.

[47] X. Zhu, *Piezoelectric ceramic materials: processing, properties, characterization, and applications*: Nova Science Publishers, 2010.

[48] X. Xing, X. Zhu, and J. Li, "Structure of Pb(Zr,Ti)O3(PZT) for Power Ultrasonic Transducer," *Journal of Wuhan University of Technology-Mater. Sci. Ed.,* vol. 33, pp. 884-887, 2018.

[49] G. H. Haertling, "Ferroelectric ceramics: history and technology," *Journal of the American Ceramic Society,* vol. 82, pp. 797-818, 1999.

[50] M. Siddiqui, J. J. Mohamed, and Z. A. Ahmad, "Structural, piezoelectric, and dielectric properties of PZT-based ceramics without excess lead oxide," *Journal of the Australian Ceramic Society,* pp. 1-7, 2019.

[51] E. Suaste-Gomez, *Piezoelectric Ceramics*, IntechOpen London, 2010.

[52] N. Setter, D. Damjanovic, L. Eng, G. Fox, S. Gevorgian, S. Hong*, et al.*, "Ferroelectric thin films: Review of materials, properties, and applications," *Journal of Applied Physics,* vol. 100, p. 051606, 2006.

[53] Q. Zhao, J. Zhao, and X. Tan, "Classification, preparation process and its equipment and applications of piezoelectric ceramic," *Materials Physics and Chemistry,* vol. 1, 2018.

[54] M. D. Maeder, D. Damjanovic, and N. Setter, "Lead Free Piezoelectric Materials," *Journal of Electroceramics,* vol. 13, pp. 385-392, 2004.

[55] D. Damjanovic, N. Klein, J. I. N. Li, and V. Porokhonskyy, "WHAT CAN BE EXPECTED FROM LEAD-FREE PIEZOELECTRIC MATERIALS?," *Functional Materials Letters,* vol. 03, pp. 5-13, 2010.

[56] B. T. Matthias and J. P. Remeika, "Ferroelectricity in the Ilmenite Structure," *Physical Review,* vol. 76, pp. 1886-1887, 1949.

[57] R. Weis and T. Gaylord, "Lithium niobate: summary of physical properties and crystal structure," *Applied Physics A,* vol. 37, pp. 191-203, 1985.

[58] I. U. S. Kuz′minov and Y. S. Kuz'minov, *Lithium niobate crystals*: Cambridge Int Science Publishing, 1999.

[59] H. Liang, R. Luo, Y. He, H. Jiang, and Q. Lin, "High-quality lithium niobate photonic crystal nanocavities," *Optica,* vol. 4, pp. 1251-1258, 2017.

[60] V. Shur, "Lithium niobate and lithium tantalate-based piezoelectric materials," *Advanced Piezoelectric Materials: Science and Technology,* pp. 204-238, 2010.

[61] V. Y. Shur, "Nano-and microdomain engineering of lithium niobate and lithium tantalate for piezoelectric applications," in *Advanced Piezoelectric Materials*, ed: Elsevier, 2017, pp. 235-270.

[62] S. Zhang, Y. Zheng, H. Kong, J. Xin, E. Frantz, and T. R. Shrout, "Characterization of high temperature piezoelectric crystals with an ordered langasite structure," *Journal of Applied Physics,* vol. 105, p. 114107, 2009.

[63] H. Fritze and H. L. Tuller, "Langasite for high-temperature bulk acoustic wave applications," *Applied Physics Letters,* vol. 78, pp. 976-977, 2001.

[64] I. Hyoung Jung and K. Ho Auh, "Crystal growth and piezoelectric properties of langasite (La3Ga5SiO14) crystals," *Materials Letters,* vol. 41, pp. 241-246, 1999.

[65] C. Dagdeviren, P. Joe, O. L. Tuzman, K.-I. Park, K. J. Lee, Y. Shi*, et al.*, "Recent progress in flexible and stretchable piezoelectric devices for mechanical energy harvesting, sensing and actuation," *Extreme Mechanics Letters,* vol. 9, pp. 269-281, 2016.

[66] S. Inthong, S. Eitssayeam, J. Tontrakoon, and T. Tunkasiri, "Piezoceramic-polymer and piezoceramic-cement composites: A brief review," *Journal of Metals, Materials and Minerals,* vol. 29, 2019.

[67] J. Harrison and Z. Ounaies, "Piezoelectric polymers," *Encyclopedia of polymer science and technology,* vol. 3, 2002.

[68] H. Kawai, "The Piezoelectricity of Poly (vinylidene Fluoride)," *Japanese Journal of Applied Physics,* vol. 8, pp. 975-976, 1969.

[69] Y. Hu, W. Kang, Y. Fang, L. Xie, L. Qiu, and T. Jin, "Piezoelectric Poly (vinylidene fluoride)(PVDF) Polymer-Based Sensor for Wrist Motion Signal Detection," *Applied Sciences,* vol. 8, p. 836, 2018.

[70] K. S. Ramadan, D. Sameoto, and S. Evoy, "A review of piezoelectric polymers as functional materials for electromechanical transducers," *Smart Materials and Structures,* vol. 23, p. 033001, 2014.

[71] A. Jain, P. K. J, A. K. Sharma, A. Jain, and R. P.N, "Dielectric and piezoelectric properties of PVDF/PZT composites: A review," *Polymer Engineering & Science,* vol. 55, pp. 1589-1616, 2015.

[72] H. Wei, H. Wang, Y. Xia, D. Cui, Y. Shi, M. Dong*, et al.*, "An overview of lead-free piezoelectric materials and devices," *Journal of Materials Chemistry C,* vol. 6, pp. 12446-12467, 2018.

[73] V. L. Stuber, D. B. Deutz, J. Bennett, D. Cannel, D. M. de Leeuw, S. van der Zwaag*, et al.*, "Flexible Lead-Free Piezoelectric Composite Materials for Energy Harvesting Applications," *Energy Technology,* vol. 7, pp. 177-185, 2019.

[74] J. H. Lee, S. Zhang, Y. Bar-Cohen, and S. Sherrit, "High Temperature, High Power Piezoelectric Composite Transducers," *Sensors,* vol. 14, 2014.

[75] A. Safari, "Development of piezoelectric composites for transducers," *J. Phys. III France,* vol. 4, pp. 1129-1149, 1994.

[76] J. Holterman and P. Groen, *An introduction to piezoelectric materials and components*: Stichting Applied Piezo, 2012.

[77] X. Du, Y. Q. Fu, S. Tan, J. Luo, A. Flewitt, W. Milne*, et al.*, "ZnO film thickness effect on surface acoustic wave modes and acoustic streaming," *Applied Physics Letters,* vol. 93, p. 094105, 2008.

[78] G. Shilpa, K. Sreelakshmi, and M. Ananthaprasad, "PZT thin film deposition techniques, properties and its application in ultrasonic MEMS sensors: A review," in *IOP Conference Series: Materials Science and Engineering*, 2016, p. 012190.

[79] P. Muralt, "AlN Thin Film Processing and Basic Properties," in *Piezoelectric MEMS Resonators*, H. Bhugra and G. Piazza, Eds., ed Cham: Springer International Publishing, 2017, pp. 3-37.

[80] M. Kundakçı, A. Mantarcı, and E. Erdoğan, "Growth and characterization of GaN thin film on Si substrate by thermionic vacuum arc (TVA)," *Materials Research Express,* vol. 4, p. 016410, 2017.

[81] V. Edon, D. Rèmiens, and S. Saada, "Structural, electrical and piezoelectric properties of LiNbO3 thin films for surface acoustic wave resonators applications," *Applied Surface Science,* vol. 256, pp. 1455-1460, 2009.

[82] M. Ishihara, T. Nakamura, F. Kokai, and Y. Koga, "Preparation of AlN and LiNbO3 thin films on diamond substrates by sputtering method," *Diamond and Related Materials,* vol. 11, pp. 408-412, 2002.

[83] K. S. Kao, C. C. Cheng, Y. C. Chen, and Y. H. Lee, "The characteristics of surface acoustic waves on AlN/LiNbO3 substrates," *Applied Physics A,* vol. 76, pp. 1125-1127, 2003.

[84] F. Guido, A. Qualtieri, L. Algieri, E. D. Lemma, M. De Vittorio, and M. T. Todaro, "AlN-based flexible piezoelectric skin for energy harvesting from human motion," *Microelectronic Engineering,* vol. 159, pp. 174-178, 2016.

[85] P. Muralt, "Recent progress in materials issues for piezoelectric MEMS," *Journal of the American Ceramic Society,* vol. 91, pp. 1385-1396, 2008.

[86] P. Dutheil, J. C. Orlianges, A. Crunteanu, A. Catherinot, and C. Champeaux, "AlN, ZnO thin films and AlN/ZnO or ZnO/AlN multilayer structures deposited by PLD for surface acoustic wave applications," *physica status solidi (a),* vol. 212, pp. 817-825, 2015.

[87] A. M. Roji M, J. G, and A. B. Raj T, "A retrospect on the role of piezoelectric nanogenerators in the development of the green world," *RSC Advances,* vol. 7, pp. 33642-33670, 2017.

[88] M. Sumets, V. Dybov, and V. Ievlev, "LiNbO 3 films: Potential application, synthesis techniques, structure, properties," *Inorganic Materials,* vol. 53, pp. 1361-1377, 2017.

[89] Y. Yoshino, "Piezoelectric thin films and their applications for electronics," *Journal of Applied Physics,* vol. 105, p. 061623, 2009.

[90] H. Morkoç and Ü. Özgür, *Zinc oxide: fundamentals, materials and device technology*: John Wiley & Sons, 2008.

[91] M. Laurenti and V. Cauda, "Porous Zinc Oxide Thin Films: Synthesis Approaches and Applications," *Coatings,* vol. 8, 2018.

[92] C. Klingshirn, "ZnO: From basics towards applications," *physica status solidi (b),* vol. 244, pp. 3027-3073, 2007.

[93] Ü. Özgür, Y. I. Alivov, C. Liu, A. Teke, M. Reshchikov, S. Doğan*, et al.*, "A comprehensive review of ZnO materials and devices," *Journal of applied physics,* vol. 98, p. 041301, 2005.

[94] W. C. contributors. (20 September). *Wurtzite polyhedra.png*. Available: https://commons.wikimedia.org/w/index.php?title=File:Wurtzite_polyhedra.png&oldid=161320121

[95] W. C. contributors. (2015, 20 September 2019). *Sphalerite-unit-cell-depth-fade-3D-balls.png*.Available: https://commons.wikimedia.org/w/index.php?title=File:Sphalerite-unit-cell-depth-fade-3D-balls.png&oldid=149521174

[96] C. Tang, M. J. Spencer, and A. S. Barnard, "Activity of ZnO polar surfaces: an insight from surface energies," *Physical Chemistry Chemical Physics,* vol. 16, pp. 22139-22144, 2014.

[97] E.-S. Jang, "Recent progress in synthesis of plate-like ZnO and its applications: a review," *Journal of the Korean Ceramic Society,* vol. 54, pp. 167-183, 2017.

[98] N. Fujimura, T. Nishihara, S. Goto, J. Xu, and T. Ito, "Control of preferred orientation for ZnOx films: control of self-texture," *Journal of Crystal Growth,* vol. 130, pp. 269-279, 1993.

[99] C. F. Klingshirn, A. Waag, A. Hoffmann, and J. Geurts, *Zinc oxide: from fundamental properties towards novel applications* vol. 120: Springer Science & Business Media, 2010.

[100] W. Chebil, "Comparison of ZnO thin films on different substrates obtained by sol-gel process and deposited by spin-coating technique," *Indian Journal of Pure & Applied Physics (IJPAP),* vol. 53, pp. 521-529, 2015.

[101] E. Lifshin and E. Lifshin, *X-ray Characterization of Materials* vol. 38: Wiley Online Library, 1999.

[102] C. Malgrange, C. Ricolleau, and M. Schlenker, *Symmetry and Physical Properties of Crystals*: Springer, 2014.

[103] P. Bindu and S. Thomas, "Estimation of lattice strain in ZnO nanoparticles: X-ray peak profile analysis," *Journal of Theoretical and Applied Physics,* vol. 8, pp. 123-134, 2014.

[104] D. Tromans, "Elastic anisotropy of HCP metal crystals and polycrystals," *Int. J. Res. Rev. Appl. Sci,* vol. 6, pp. 462-483, 2011.

[105] Ü. Özgür, Y. I. Alivov, C. Liu, A. Teke, M. Reshchikov, S. Doğan*, et al.*, "A comprehensive review of ZnO materials and devices," *Journal of applied physics,* vol. 98, p. 11, 2005.

[106] A. Dal Corso, M. Posternak, R. Resta, and A. Baldereschi, "Ab initio study of piezoelectricity and spontaneous polarization in ZnO," *Physical Review B,* vol. 50, p. 10715, 1994.

[107] K.-m. Zhang, Y.-p. Zhao, F.-q. He, and D.-q. Liu, "Piezoelectricity of ZnO films prepared by sol-gel method," *Chinese Journal of Chemical Physics,* vol. 20, p. 721, 2007.

[108] G. Sauerbrey, "Use of quartz vibrator for weighting thin films on a microbalance," *Zeitschrift fur Physik,* vol. 155, pp. 206-212, 1959.

[109] B. P. Zhang, K. Wakatsuki, N. T. Binh, N. Usami, and Y. Segawa, "Effects of growth temperature on the characteristics of ZnO epitaxial films deposited by metalorganic chemical vapor deposition," *Thin Solid Films,* vol. 449, pp. 12-19, 2004.

[110] M. Abinaya, K. M. Dhanisha, M. Manoj Cristopher, P. Deepak Raj, K. Jeyadheepan, and M. Sridharan, "Reactive DC Magnetron Sputtered ZnO Thin Films for

Piezoelectric Application," *International Journal of Nanoscience,* vol. 17, p. 1760047, 2018.

[111] P. Y. Dave, K. H. Patel, K. V. Chauhan, A. K. Chawla, and S. K. Rawal, "Examination of Zinc Oxide Films Prepared by Magnetron Sputtering," *Procedia Technology,* vol. 23, pp. 328-335, 2016.

[112] R. Tao, W. B. Wang, J. T. Luo, S. Ahmad Hasan, H. Torun, P. Canyelles-Pericas*, et al.*, "Thin film flexible/bendable acoustic wave devices: Evolution, hybridization and decoupling of multiple acoustic wave modes," *Surface and Coatings Technology,* vol. 357, pp. 587-594, 2019.

[113] G.-S. Chung and D.-T. Phan, "Finite element modeling of surface acoustic waves in piezoelectric thin films," *Journal of the Korean Physical Society,* vol. 57, pp. 446-450, 2010.

[114] K. Ellmer and R. Wendt, "D.c. and r.f. (reactive) magnetron sputtering of ZnO:Al films from metallic and ceramic targets: a comparative study," *Surface and Coatings Technology,* vol. 93, pp. 21-26, 1997.

[115] G. Kiriakidis, M. Suchea, S. Christoulakis, P. Horvath, T. Kitsopoulos, and J. Stoemenos, "Structural characterization of ZnO thin films deposited by dc magnetron sputtering," *Thin Solid Films,* vol. 515, pp. 8577-8581, 2007.

[116] V. Kutiš, G. Gálik, V. Královič, I. Rýger, E. Mojto, and T. Lalinský, "Modelling and simulation of SAW sensor using FEM," *Procedia Engineering,* vol. 48, pp. 332-337, 2012.

[117] Y. J. Lee, E.-S. Cho, and S. J. Kwon, "Pulsed-DC magnetron sputtering of intrinsic ZnO film and its application to CIS solar cell," *Vacuum,* vol. 126, pp. 91-100, 2016.

[118] J. Zhou, H.-F. Pang, L. Garcia-Gancedo, E. Iborra, M. Clement, M. De Miguel-Ramos*, et al.*, "Discrete microfluidics based on aluminum nitride surface acoustic wave devices," *Microfluidics and Nanofluidics,* vol. 18, pp. 537-548, 2015.

[119] S. Singh, R. S. Srinivasa, and S. S. Major, "Effect of substrate temperature on the structure and optical properties of ZnO thin films deposited by reactive rf magnetron sputtering," *Thin Solid Films,* vol. 515, pp. 8718-8722, 2007.

[120] D. Zhang, P. Fan, X. Cai, J. Huang, L. Ru, Z. Zheng*, et al.*, "Properties of ZnO thin films deposited by DC reactive magnetron sputtering under different plasma power," *Applied Physics A,* vol. 97, pp. 437-441, 2009.

[121] Q.-B. Ma, Z.-Z. Ye, H.-P. He, L.-P. Zhu, J.-R. Wang, and B.-H. Zhao, "Influence of Ar/O2 ratio on the properties of transparent conductive ZnO:Ga films prepared by DC reactive magnetron sputtering," *Materials Letters,* vol. 61, pp. 2460-2463, 2007.

[122] J.-B. Lee, M.-H. Lee, C.-K. Park, and J.-S. Park, "Effects of lattice mismatches in ZnO/substrate structures on the orientations of ZnO films and characteristics of SAW devices," *Thin Solid Films,* vol. 447-448, pp. 296-301, 2004.

[123] R. Ghosh, D. Basak, and S. Fujihara, "Effect of substrate-induced strain on the structural, electrical, and optical properties of polycrystalline ZnO thin films," *Journal of Applied Physics,* vol. 96, pp. 2689-2692, 2004.

[124] Z. Chen, T. Salagaj, C. Jensen, K. Strobl, M. Nakarmi, and K. Shum, "ZnO Thin Film Deposition on Sapphire Substrates by Chemical Vapor Deposition," *MRS Proceedings,* vol. 1167, pp. 07-09, 2011.

[125] L. Han, F. Mei, C. Liu, C. Pedro, and E. Alves, "Comparison of ZnO thin films grown by pulsed laser deposition on sapphire and Si substrates," *Physica E: Low-dimensional Systems and Nanostructures,* vol. 40, pp. 699-704, 2008.

[126] Y.-S. Shih, P.-Y. Lin, L.-L. Wei, and L. Chang, "Orientations of ZnO grown on GaN," *physica status solidi (RRL) – Rapid Research Letters,* vol. 9, pp. 92-94, 2015.

[127] H. I. Efkere, A. Tataroglu, S. S. Cetin, N. Topaloglu, M. P. Gonullu, and H. Ates, "The effect of thickness on the optical, structural and electrical properties of ZnO thin film deposited on n-type Si," *Journal of Molecular Structure,* vol. 1165, pp. 376-380, 2018.

[128] S. Islam, K. M. A. Hussain, and M. J. Rashid, "Deposition and Optical Characterization of ZnO Thin films on Glass Substrate," *Journal of Physics: Conference Series,* vol. 1086, p. 012009, 2018.

[129] Y. Wang, X. Chen, L. Wang, S. Yang, and Z. Feng, "Properties of ZnO thin film on Al2O3 substrate prepared by pulsed laser deposition under different substrate temperature," *Physics Procedia,* vol. 18, pp. 85-90, 2011.

[130] J. F. Felix, M. Aziz, C. I. L. de Araujo, W. M. de Azevedo, V. Anjos, E. F. da Silva, *et al.*, "Zinc oxide thin films on silicon carbide substrates (ZnO/SiC): electro-optical properties and electrically active defects," *Semiconductor Science and Technology,* vol. 29, p. 045021, 2014.

[131] M. Mekhnache, A. Drici, L. Saad Hamideche, H. Benzarouk, A. Amara, L. Cattin, *et al.*, "Properties of ZnO thin films deposited on (glass, ITO and ZnO:Al) substrates," *Superlattices and Microstructures,* vol. 49, pp. 510-518, 2011.

[132] Y. R. Ryu, S. Zhu, J. D. Budai, H. R. Chandrasekhar, P. F. Miceli, and H. W. White, "Optical and structural properties of ZnO films deposited on GaAs by pulsed laser deposition," *Journal of Applied Physics,* vol. 88, pp. 201-204, 2000.

[133] Y. Wang, H. Wang, S. Li, S. Zhou, Y. Hang, J. Xu*, et al.*, "Annealing effect on properties of Zno thin films grown on LiNbO3 substrates by MOCVD," *Journal of Crystal Growth,* vol. 284, pp. 319-323, 2005.

[134] G. H. Lee, "Optical properties of ZnO thin films on LiNbO3 and LiTaO3 substrates grown by pulsed laser deposition," *Solid State Communications,* vol. 128, pp. 351-354, 2003.

[135] L. Zhao, J. Lian, Y. Liu, and Q. Jiang, "Structural and optical properties of ZnO thin films deposited on quartz glass by pulsed laser deposition," *Applied Surface Science,* vol. 252, pp. 8451-8455, 2006.

[136] J. J. Chen, F. Zeng, D. M. Li, J. B. Niu, and F. Pan, "Deposition of high-quality zinc oxide thin films on diamond substrates for high-frequency surface acoustic wave filter applications," *Thin Solid Films,* vol. 485, pp. 257-261, 2005.

[137] M. Matsumura and R. P. Camata, "Pulsed laser deposition and photoluminescence measurements of ZnO thin films on flexible polyimide substrates," *Thin Solid Films,* vol. 476, pp. 317-321, 2005.

[138] H.-H. Shieh, I.-C. Cheng, J. Z. Chen, C.-C. Hsiao, P.-C. Lin, and Y.-H. Yeh, "The electromechanical characteristics of ZnO grown on poly (ethylene terephthalate) substrates," *Journal of The Electrochemical Society,* vol. 157, pp. H750-H754, 2010.

[139] C. Koidis, S. Logothetidis, D. Georgiou, and A. Laskarakis, "In-situ and real-time investigation of ZnO thin films growth onto rigid and flexible substrates," *physica status solidi c,* vol. 5, pp. 1366-1369, 2008.

[140] K. Tian, B. Tudu, and A. Tiwari, "Growth and characterization of zinc oxide thin films on flexible substrates at low temperature using pulsed laser deposition," *Vacuum,* vol. 146, pp. 483-491, 2017.

[141] M. Suchea, S. Christoulakis, K. Moschovis, N. Katsarakis, and G. Kiriakidis, "ZnO transparent thin films for gas sensor applications," *Thin solid films,* vol. 515, pp. 551-554, 2006.

[142] S. Youssef, P. Combette, J. Podlecki, R. A. Asmar, and A. Foucaran, "Structural and Optical Characterization of ZnO Thin Films Deposited by Reactive rf Magnetron Sputtering," *Crystal Growth & Design,* vol. 9, pp. 1088-1094, 2009.

[143] Z. H. Khan, ISLAMUDDIN, R. K. KUMAR, N. SALAH, S. HABIB, S. A. EL-HAMIDY*, et al.*, "Optical and Electrical Characterization of ZnO Thin Film," *International Journal of Nanoscience,* vol. 9, pp. 423-429, 2010.

[144] J. Z. Hashmi, K. Siraj, A. Latif, M. Murray, and G. Jose, "Study of deposition parameters for the fabrication of ZnO thin films using femtosecond laser," *Applied Physics A,* vol. 122, p. 763, 2016.

[145] Y.-H. Hu, Y.-C. Chen, H.-J. Xu, H. Gao, W.-H. Jiang, F. Hu*, et al.*, "Texture ZnO thin-films and their application as front electrode in solar cells," *Engineering,* vol. 2, p. 973, 2010.

[146] Y. Hu, W. L F, H. Xu, Y. Chen, and W. Jiang, "The low-cost preparation of pyramid-like texture ZnO thin films and the application as a front electrode in hydrogen amorphous silicon solar cells," in *5th International Symposium on Advanced Optical Manufacturing and Testing Technologies: Optoelectronic Materials and Devices for Detector, Imager, Display, and Energy Conversion Technology*, 2010, p. 76580D.

[147] A. Mahroug, S. Boudjadar, S. Hamrit, and L. Guerbous, "Structural, morphological and optical properties of undoped and Co-doped ZnO thin films prepared by sol–gel process," *Journal of Materials Science: Materials in Electronics,* vol. 25, pp. 4967-4974, 2014.

[148] S.-H. Baek, H.-J. Lee, and S.-N. Lee, "Thickness dependence of crystal and optical characterization on ZnO thin film grown by atomic layer deposition," *AIP Advances,* vol. 8, p. 065306, 2018.

[149] S. Al-Khawaja, B. Abdallah, S. Abou Shaker, and M. Kakhia, "Thickness effect on stress, structural, electrical and sensing properties of (0 0 2) preferentially oriented undoped ZnO thin films," *Composite Interfaces,* vol. 22, pp. 221-231, 2015.

[150] J. I. Langford and A. Wilson, "Scherrer after sixty years: a survey and some new results in the determination of crystallite size," *Journal of applied crystallography,* vol. 11, pp. 102-113, 1978.

[151] B. R. Nagabushana and M. Vishwas, "Low temperature synthesis and optical and electrical characterization of ZnO thin films," *Materials Today: Proceedings,* vol. 5, pp. 21285-21291, 2018.

[152] A. Vorokh, "Scherrer formula: estimation of error in determining small nanoparticle size," *Nanosystems: Physics, Chemistry, Mathematics,* vol. 9, pp. 364-369, 2018.

[153] W. Dang, Y. Q. Fu, J. Luo, A. Flewitt, and W. Milne, "Deposition and characterization of sputtered ZnO films," *Superlattices and Microstructures,* vol. 42, pp. 89-93, 2007.

[154] S. Saha, M. Tomar, and V. Gupta, "Influence of stress in ZnO thin films on its biosensing application," *Enzyme and Microbial Technology,* vol. 79-80, pp. 63-69, 2015.

[155] I. Ozen and M. A. Gülgün, "Residual stress relaxation and microstructure in ZnO thin films," in *Advances in Science and Technology*, 2006, pp. 1316-1321.

[156] J. Singh, S. Ranwa, J. Akhtar, and M. Kumar, "Growth of residual stress-free ZnO films on SiO2/Si substrate at room temperature for MEMS devices," *AIP Advances,* vol. 5, p. 067140, 2015.

[157] G. A. Kumar, M. V. R. Reddy, and K. N. Reddy, "Structural and Optical properties of ZnO thin films grown on various substrates by RF magnetron sputtering," *IOP Conference Series: Materials Science and Engineering,* vol. 73, p. 012133, 2015.

[158] Q. M. Al-Bataineh, A. Alsaad, A. Ahmad, and A. Al-Sawalmih, "Structural, Electronic and Optical Characterization of ZnO Thin Film-Seeded Platforms for ZnO Nanostructures: Sol–Gel Method Versus Ab Initio Calculations," *Journal of Electronic Materials,* Vol. 48, pp. 5028-5038, 2019.

[159] B. D. Cullity, "Elements of X-ray diffraction, Addison," *Wesley Mass,* 1978.

[160] A. Rosa, E. Da Silva, E. Amorim, M. Chaves, A. Catto, P. N. Lisboa-Filho*, et al.*, "Growth evolution of ZnO thin films deposited by RF magnetron sputtering," in *Journal of Physics: Conference Series*, 2012, p. 012020.

[161] A. Tarasenko, L. Jastrabik, and N. Tarasenko, "Effect of roughness on the elastic surface wave propagation," *The European Physical Journal-Applied Physics,* vol. 24, pp. 3-12, 2003.

[162] C. Flannery and H. Von Kiedrowski, "Effects of surface roughness on surface acoustic wave propagation in semiconductor materials," *Ultrasonics,* vol. 40, pp. 83-87, 2002.

[163] Z. L. Wang, "Zinc oxide nanostructures: growth, properties and applications," *Journal of physics: condensed matter,* vol. 16, p. R829, 2004.

[164] A. Wei, L. Pan, and W. Huang, "Recent progress in the ZnO nanostructure-based sensors," *Materials Science and Engineering: B,* vol. 176, pp. 1409-1421, 2011.

[165] A. Albanese, P. S. Tang, and W. C. W. Chan, "The Effect of Nanoparticle Size, Shape, and Surface Chemistry on Biological Systems," *Annual Review of Biomedical Engineering,* vol. 14, pp. 1-16, 2012.

[166] G.-C. Yi, C. Wang, and W. I. Park, "ZnO nanorods: synthesis, characterization and applications," *Semiconductor Science and Technology,* vol. 20, p. S22, 2005.

[167] Q. Wan, Q. Li, Y. Chen, T.-H. Wang, X. He, J. Li*, et al.*, "Fabrication and ethanol sensing characteristics of ZnO nanowire gas sensors," *Applied Physics Letters,* vol. 84, pp. 3654-3656, 2004.

[168] J. Yu and X. Yu, "Hydrothermal synthesis and photocatalytic activity of zinc oxide hollow spheres," *Environmental science & technology,* vol. 42, pp. 4902-4907, 2008.

[169] P. J. P. Espitia, N. d. F. F. Soares, J. S. dos Reis Coimbra, N. J. de Andrade, R. S. Cruz, and E. A. A. Medeiros, "Zinc oxide nanoparticles: synthesis, antimicrobial

activity and food packaging applications," *Food and bioprocess technology,* vol. 5, pp. 1447-1464, 2012.

[170] K. Anand, O. Singh, M. P. Singh, J. Kaur, and R. C. Singh, "Hydrogen sensor based on graphene/ZnO nanocomposite," *Sensors and Actuators B: Chemical,* vol. 195, pp. 409-415, 2014.

[171] T. Kong, Y. Chen, Y. Ye, K. Zhang, Z. Wang, and X. Wang, "An amperometric glucose biosensor based on the immobilization of glucose oxidase on the ZnO nanotubes," *Sensors and Actuators B: Chemical,* vol. 138, pp. 344-350, 2009.

[172] J. Zhang, B. Zhao, Z. Pan, M. Gu, and A. Punnoose, "Synthesis of ZnO Nanoparticles with Controlled Shapes, Sizes, Aggregations, and Surface Complex Compounds for Tuning or Switching the Photoluminescence," *Crystal Growth & Design,* vol. 15, pp. 3144-3149, 2015.

[173] S. Chaudhary, A. Umar, K. Bhasin, and S. Baskoutas, "Chemical sensing applications of ZnO nanomaterials," *Materials,* vol. 11, p. 287, 2018.

[174] R. Kumar, O. Al-Dossary, G. Kumar, and A. Umar, "Zinc Oxide Nanostructures for NO2 Gas–Sensor Applications: A Review," *Nano-Micro Letters,* vol. 7, pp. 97-120, 2015.

[175] M. Krasovska, V. Gerbreders, I. Mihailova, A. Ogurcovs, E. Sledevskis, A. Gerbreders*, et al.*, "ZnO-nanostructure-based electrochemical sensor: Effect of nanostructure morphology on the sensing of heavy metal ions," *Beilstein journal of nanotechnology,* vol. 9, pp. 2421-2431, 2018.

[176] Z. Yang, Z. Ye, Z. Xu, and B. zhao, "Effect of the morphology on the optical properties of ZnO nanostructures," *Physica E: Low-dimensional Systems and Nanostructures,* vol. 42, pp. 116-119, 2009.

[177] A. Umar, B. Karunagaran, E. Suh, and Y. Hahn, "Structural and optical properties of single-crystalline ZnO nanorods grown on silicon by thermal evaporation," *Nanotechnology,* vol. 17, p. 4072, 2006.

[178] R. A. Rani, S. A. Ghafar, A. S. Zoolfakar, and M. Rusop, "Growth of ZnO nanorods on glass substrate deposited using dip coating method," in *AIP Conference Proceedings*, 2018, p. 020072.

[179] L. Wang, G. Yang, W. Huang, T. Xing, Y. Chen, and S. Ge, "A simple method to grow up ZnO nanorods," in *IOP Conference Series: Materials Science and Engineering*, 2019, p. 022003.

[180] R. Shabannia, "Fast UV detection by Cu-doped ZnO nanorod arrays chemically deposited on PET substrate," *International Journal of Nano Dimension,* vol. 10, pp. 313-319, 2019.

[181] J. J. Wu and S. C. Liu, "Low-temperature growth of well-aligned ZnO nanorods by chemical vapor deposition," *Advanced materials,* vol. 14, pp. 215-218, 2002.

[182] Q. Zhao, P. Klason, and M. Willander, "Growth of ZnO nanostructures by vapor–liquid–solid method," *Applied Physics A,* vol. 88, pp. 27-30, 2007.

[183] Z. Yin, S. Wu, X. Zhou, X. Huang, Q. Zhang, F. Boey, *et al.*, "Electrochemical deposition of ZnO nanorods on transparent reduced graphene oxide electrodes for hybrid solar cells," *small,* vol. 6, pp. 307-312, 2010.

[184] S. E. Ahn, J. S. Lee, H. Kim, S. Kim, B. H. Kang, K. H. Kim, *et al.*, "Photoresponse of sol-gel-synthesized ZnO nanorods," *Applied Physics Letters,* vol. 84, pp. 5022-5024, 2004.

[185] Y. Sun, G. M. Fuge, and M. N. Ashfold, "Growth of aligned ZnO nanorod arrays by catalyst-free pulsed laser deposition methods," *Chemical Physics Letters,* vol. 396, pp. 21-26, 2004.

[186] N. T. Son, J.-S. Noh, and S. Park, "Role of ZnO thin film in the vertically aligned growth of ZnO nanorods by chemical bath deposition," *Applied Surface Science,* vol. 379, pp. 440-445, 2016.

[187] S. Worasawat, T. Masuzawa, Y. Hatanaka, Y. Neo, H. Mimura, and W. Pecharapa, "Synthesis and characterization of ZnO nanorods by hydrothermal method," *Materials Today: Proceedings,* vol. 5, pp. 10964-10969, 2018.

[188] L. V. Podrezova, S. Porro, V. Cauda, M. Fontana, and G. Cicero, "Comparison between ZnO nanowires grown by chemical vapor deposition and hydrothermal synthesis," *Applied Physics A,* vol. 113, pp. 623-632, 2013.

[189] M. A. Vergés, A. Mifsud, and C. J. Serna, "Formation of rod-like zinc oxide microcrystals in homogeneous solutions," *Journal of the Chemical Society, Faraday Transactions,* vol. 86, pp. 959-963, 1990.

[190] L. Vayssieres, K. Keis, S.-E. Lindquist, and A. Hagfeldt, "Purpose-Built Anisotropic Metal Oxide Material: 3D Highly Oriented Microrod Array of ZnO," *The Journal of Physical Chemistry B,* vol. 105, pp. 3350-3352, 2001.

[191] S. Baruah and J. Dutta, "Effect of seeded substrates on hydrothermally grown ZnO nanorods," *Journal of sol-gel science and technology,* vol. 50, p. 456, 2009.

[192] R. B. Kale, Y.-J. Hsu, Y.-F. Lin, and S.-Y. Lu, "Hydrothermal synthesis, characterizations and photoluminescence study of single crystalline hexagonal ZnO nanorods with three dimensional flowerlike microstructures," *Superlattices and Microstructures,* vol. 69, pp. 239-252, 2014.

[193] H. Wang, J. Xie, K. Yan, and M. Duan, "Growth Mechanism of Different Morphologies of ZnO Crystals Prepared by Hydrothermal Method," *Journal of Materials Science & Technology,* vol. 27, pp. 153-158, 2011.

[194] G. Amin, M. H. Asif, A. Zainelabdin, S. Zaman, O. Nur, and M. Willander, "Influence of pH, Precursor Concentration, Growth Time, and Temperature on the Morphology of ZnO Nanostructures Grown by the Hydrothermal Method," *Journal of Nanomaterials,* vol. 2011, p. 9, 2011.

[195] J. L. Gomez and O. Tigli, "Zinc oxide nanostructures: from growth to application," *Journal of Materials Science,* vol. 48, pp. 612-624, 2013.

[196] K. H. Tam, C. K. Cheung, Y. H. Leung, A. B. Djurišić, C. C. Ling, C. D. Beling*, et al.*, "Defects in ZnO Nanorods Prepared by a Hydrothermal Method," *The Journal of Physical Chemistry B,* vol. 110, pp. 20865-20871, 2006.

[197] S. Baruah and J. Dutta, "Hydrothermal growth of ZnO nanostructures," *Science and Technology of Advanced Materials,* vol. 10, p. 013001, 2009.

[198] H. Xu, H. Wang, Y. Zhang, W. He, M. Zhu, B. Wang*, et al.*, "Hydrothermal synthesis of zinc oxide powders with controllable morphology," *Ceramics International,* vol. 30, pp. 93-97, 2004.

[199] S. Walley and J. Field, "Elastic wave propagation in materials," *Encyclopedia of Materials: Science and Technology',(ed. KHJ Buschow et al.),* pp. 2435-2439, 2001.

[200] J. Kankare, "Sauerbrey equation of quartz crystal microbalance in liquid medium," *Langmuir,* vol. 18, pp. 7092-7094, 2002.

[201] A. Alassi, M. Benammar, and D. Brett, "Quartz crystal microbalance electronic interfacing systems: A review," *Sensors,* vol. 17, p. 2799, 2017.

[202] X. Huang, Q. Bai, J. Hu, and D. Hou, "A Practical Model of Quartz Crystal Microbalance in Actual Applications," *Sensors (Basel, Switzerland),* vol. 17, p. 1785, 2017.

[203] G. Rughoobur, M. DeMiguel-Ramos, T. Mirea, M. Clement, J. Olivares, B. Díaz-Durán*, et al.*, "Room temperature sputtering of inclined c-axis ZnO for shear mode solidly mounted resonators," *Applied Physics Letters,* vol. 108, p. 034103, 2016.

[204] Y. Zhang, J. Luo, A. J. Flewitt, Z. Cai, and X. Zhao, "Film bulk acoustic resonators (FBARs) as biosensors: A review," *Biosensors and Bioelectronics,* vol. 116, pp. 1-15, 2018.

[205] N. G. Durmuş, R. L. Lin, M. Kozberg, D. Dermici, A. Khademhosseini, and U. Demirci, "Acoustic-Based Biosensors," in *Encyclopedia of Microfluidics and Nanofluidics*, D. Li, Ed., ed New York, NY: Springer New York, 2015, pp. 28-40.

[206] B. Drafts, "Acoustic wave technology sensors," *IEEE Transactions on microwave theory and techniques,* vol. 49, pp. 795-802, 2001.

[207] S. Martin, A. Ricco, T. Niemczyk, and G. Frye, "Characterization of SH acoustic plate mode liquid sensors," *Sensors and actuators,* vol. 20, pp. 253-268, 1989.

[208] R.-C. Lin, Y.-C. Chen, W.-T. Chang, C.-C. Cheng, and K.-S. Kao, "Highly sensitive mass sensor using film bulk acoustic resonator," *Sensors and Actuators A: Physical,* vol. 147, pp. 425-429, 2008.

[209] K. Tukkiniemi, A. Rantala, M. Nirschl, D. Pitzer, T. Huber, and M. Schreiter, "Fully integrated FBAR sensor matrix for mass detection," *Procedia Chemistry,* vol. 1, pp. 1051-1054, 2009.

[210] A. Flewitt, J. Luo, Y. Q. Fu, L. Garcia-Gancedo, X. Du, J. Lu*, et al.*, "ZnO based SAW and FBAR devices for bio-sensing applications," *Journal of Non-Newtonian Fluid Mechanics,* vol. 222, pp. 209-216, 2015.

[211] L. García-Gancedo, J. Pedros, X. Zhao, G. Ashley, A. Flewitt, W. Milne*, et al.*, "Dual-mode thin film bulk acoustic wave resonators for parallel sensing of temperature and mass loading," *Biosensors and Bioelectronics,* vol. 38, pp. 369-374, 2012.

[212] L. Rayleigh, "On Waves Propagated along the Plane Surface of an Elastic Solid," *Proceedings of the London Mathematical Society,* vol. s1-17, pp. 4-11, 1885.

[213] P. Hess, "Surface acoustic waves in materials science," *Physics Today,* vol. 55, pp. 42-47, 2002.

[214] J. D. N. Cheeke, *Fundamentals and applications of ultrasonic waves*: CRC press, 2016.

[215] R. White and F. Voltmer, "Direct piezoelectric coupling to surface elastic waves," *Applied physics letters,* vol. 7, pp. 314-316, 1965.

[216] R. Banupriya, T. Venkatesan, G. Pandiyarajan, and H. M. Pandya, "SAW devices–a comprehensive review," *Journal of Environmental Nanotechnology,* vol. 3, pp. 106-115, 2014.

[217] F. S. Hickernell, "Surface acoustic wave devices: a rewarding past, a significant present, and a promising future," in *12th International Conference on Microwaves and Radar. MIKON-98. Conference Proceedings (IEEE Cat. No.98EX195)*, 1998, pp. 159-168 vol.4.

[218] A. V. Mamishev, K. Sundara-Rajan, F. Yang, Y. Du, and M. Zahn, "Interdigital sensors and transducers," *Proceedings of the IEEE,* vol. 92, pp. 808-845, 2004.

[219] D. Mishra, "Modeling of Interdigital Transducer Surface Acoustic Wave Device - Design and Simulation," in *2015 Fifth International Conference on Communication Systems and Network Technologies*, 2015, pp. 1327-1331.

[220] W. Soluch and E. Brzozowski, "Effect of Metal Electrodes on Surface Acoustic Wave Properties in Bulk Z-Cut GaN Crystal," *IEEE Transactions on Electron Devices,* vol. 61, pp. 3395-3398, 2014.

[221] T. Aubert, O. Elmazria, B. Assouar, L. Bouvot, M. Hehn, S. Weber*, et al.*, "Behavior of platinum/tantalum as interdigital transducers for SAW devices in high-temperature environments," *IEEE Transactions on Ultrasonics, Ferroelectrics, and Frequency Control,* vol. 58, pp. 603-610, 2011.

[222] T. Palacios, F. Calle, J. Grajal, E. Monroy, M. Eickhoff, O. Ambacher*, et al.*, "High frequency SAW devices on AlGaN: fabrication, characterization and integration with optoelectronics," in *2002 IEEE Ultrasonics Symposium, 2002. Proceedings.*, 2002, pp. 57-60 vol.1.

[223] U. C. Kaletta, D. Wolansky, M. F. C. Wipf, and C. Wenger, "Crosstalk suppression of CMOS compatible AlN based SAW devices on low resistive Si(100)," *physica status solidi c,* vol. 11, pp. 249-252, 2014.

[224] R. Gupta, L. Rana, A. Sharma, V. Gupta, and M. Tomar, "Fabrication of micro-cantilever and its theoretical validation for energy harvesting applications," *Microsystem Technologies,* 2019.

[225] H. Wu, H. Zu, J. H. C. Wang, and Q.-M. Wang, "A study of Love wave acoustic biosensors monitoring the adhesion process of tendon stem cells (TSCs)," *European Biophysics Journal,* vol. 48, pp. 249-260, 2019.

[226] M. F. Hribšek, D. V. Tošić, and M. R. Radosavljević, "Surface acoustic wave sensors in mechanical engineering," *FME transactions,* vol. 38, pp. 11-18, 2010.

[227] I. Voiculescu and A. N. Nordin, "Acoustic wave based MEMS devices for biosensing applications," *Biosensors and Bioelectronics,* vol. 33, pp. 1-9, 2012.

[228] O. Tigli and M. E. Zaghloul, "Design and fabrication of a novel SAW bio/chemical sensor in CMOS," in *SENSORS, 2005 IEEE*, 2005, p. 4 pp.

[229] M. Zakaria, U. Hashim, and M. M. Amin, "Design and fabrication of IDT saw by using conventional lithography technique," *Middle-East J. Sci. Res.,* vol. 18, pp. 1281-1285, 2013.

[230] T. Hoang, "SAW parameters analysis and equivalent circuit of SAW device," in *Acoustic Waves-From Microdevices to Helioseismology*, ed: IntechOpen, 2011.

[231] K.-y. Hashimoto and K.-Y. Hashimoto, *Surface acoustic wave devices in telecommunications*: Springer, 2000.

[232] K. Hanma and B. J. Hunsinger, "A Triple Transit Suppression Technique," in *1976 Ultrasonics Symposium*, 1976, pp. 328-331.

[233] X. Sun, W. Liu, X. Shao, S. Zhou, W. Wang, and D. Lin, "Surface Acoustic Wave Gyroscopic Effect in an Interdigital Transducer," *Sensors,* vol. 19, p. 106, 2019.

[234] W. Connacher, N. Zhang, A. Huang, J. Mei, S. Zhang, T. Gopesh*, et al.*, "Micro/nano acoustofluidics: materials, phenomena, design, devices, and applications," *Lab on a Chip,* vol. 18, pp. 1952-1996, 2018.

[235] J. Devkota, R. P. Ohodnicki, and W. D. Greve, "SAW Sensors for Chemical Vapors and Gases," *Sensors,* vol. 17, 2017.

[236] A. Baracu, A. Gurban, I. Giangu, F. Craciunoiu, V. Buiculescu, A. Dinescu*, et al.*, "Selective chemical sensor for liquid specimens based on lithium tantalate surface acoustic wave devices," in *2015 International Semiconductor Conference (CAS)*, 2015, pp. 271-274.

[237] A. Mujahid and L. F. Dickert, "Surface Acoustic Wave (SAW) for Chemical Sensing Applications of Recognition Layers," *Sensors,* vol. 17, 2017.

[238] C. Caliendo and M. Hamidullah, "A Theoretical Study of Love Wave Sensors Based on ZnO-Glass Layered Structures for Application to Liquid Environments," *Biosensors,* vol. 6, p. 59, 2016.

[239] J. Luo, A. Quan, C. Fu, and H. Li, "Shear-horizontal surface acoustic wave characteristics of a (110) ZnO/SiO2/Si multilayer structure," *Journal of Alloys and Compounds,* vol. 693, pp. 558-564, 2017.

[240] M. Link, M. Schreiter, J. Weber, R. Gabl, D. Pitzer, R. Primig*, et al.*, "c-axis inclined ZnO films for shear-wave transducers deposited by reactive sputtering using an additional blind," *Journal of Vacuum Science & Technology A,* vol. 24, pp. 218-222, 2006.

[241] H. F. Pang, Y. Q. Fu, R. Hou, K. J. Kirk, D. Hutson, X. T. Zu*, et al.*, "Annealing effect on the generation of dual mode acoustic waves in inclined ZnO films," *Ultrasonics,* vol. 53, pp. 1264-1269, 2013.

[242] T. Yanagitani, N. Morisato, S. Takayanagi, M. Matsukawa, and Y. Watanabe, "c-Axis Zig-Zag ZnO film ultrasonic transducers for designing longitudinal and shear wave resonant frequencies and modes," *IEEE Transactions on Ultrasonics, Ferroelectrics, and Frequency Control,* vol. 58, pp. 1062-1068, 2011.

[243] H. Lamb, "On waves in an elastic plate," *Proceedings of the Royal Society of London. Series A, Containing Papers of a Mathematical and Physical Character,* vol. 93, pp. 114-128, 1917.

[244] D. C. Worlton, "Experimental Confirmation of Lamb Waves at Megacycle Frequencies," *Journal of Applied Physics,* vol. 32, pp. 967-971, 1961.

[245] M.-I. Rocha-Gaso, C. March-Iborra, Á. Montoya-Baides, and A. Arnau-Vives, "Surface Generated Acoustic Wave Biosensors for the Detection of Pathogens: A Review," *Sensors,* vol. 9, 2009.

[246] V. Yantchev and I. Katardjiev, "Thin film Lamb wave resonators in frequency control and sensing applications: a review," *Journal of Micromechanics and Microengineering,* vol. 23, p. 043001, 2013.

[247] L. Ge, "Theory of Lamb Wave Transducers and Their Applications for Gas and Liquid Sensing," in *2013 IEEE International Conference on Green Computing and Communications and IEEE Internet of Things and IEEE Cyber, Physical and Social Computing*, 2013, pp. 1714-1717.

[248] S. Torkamani, S. Roy, M. E. Barkey, E. Sazonov, S. Burkett, and S. Kotru, "A novel damage index for damage identification using guided waves with application in laminated composites," *Smart Materials and Structures,* vol. 23, p. 095015, 2014.

[249] M. Liu, M. Xue, J. Li, and X. Li, "A MEMS Lamb wave microdevice based on ZnO thin film," in *Proceedings of the 2010 Symposium on Piezoelectricity, Acoustic Waves and Device Applications*, 2010, pp. 455-459.

[250] S. W. Wenzel and R. M. White, "A multisensor employing an ultrasonic Lamb-wave oscillator," *IEEE Transactions on Electron Devices,* vol. 35, pp. 735-743, 1988.

[251] M. J. Vellekoop, "Acoustic wave sensors and their technology," *Ultrasonics,* vol. 36, pp. 7-14, 1998.

[252] M. Reusch, K. Holc, A. Žukauskaitė, V. Lebedev, N. Kurz, and O. Ambacher, "Flexural plate wave sensors with buried IDT for sensing in liquids," in *2017 IEEE SENSORS*, 2017, pp. 1-3.

[253] J. C. Pyun, H. Beutel, J. U. Meyer, and H. H. Ruf, "Development of a biosensor for E. coli based on a flexural plate wave (FPW) transducer," *Biosensors and Bioelectronics,* vol. 13, pp. 839-845, 1998.

[254] Z. Su and L. Ye, "Fundamentals and Analysis of Lamb Waves," *Lecture Notes in Applied and Computational Mechanics,* vol. 48, 2009.

[255] A. K. Pantazis, E. Gizeli, and G. Konstantinidis, "A high frequency GaN Lamb-wave sensor device," *Applied Physics Letters,* vol. 96, p. 194103, 2010.

[256] J. Bjurström, I. Katardjiev, and V. Yantchev, "Lateral-field-excited thin-film Lamb wave resonator," *Applied Physics Letters,* vol. 86, p. 154103, 2005.

[257] L. Rana, R. Gupta, A. Sharma, M. Tomar, and V. Gupta, "Fabrication of ZnO/Si lamb wave acoustic devices," *Ferroelectrics,* vol. 535, pp. 41-46, 2018.

[258] J. Pepper, R. Noring, M. Klempner, B. Cunningham, A. Petrovich, R. Bousquet, *et al.*, "Detection of proteins and intact microorganisms using microfabricated flexural plate silicon resonator arrays," *Sensors and Actuators B: Chemical,* vol. 96, pp. 565-575, 2003.

[259] I. Y. Huang and M. C. Lee, "Development of a FPW allergy biosensor for human IgE detection by MEMS and cystamine-based SAM technologies," *Sensors and Actuators B: Chemical,* vol. 132, pp. 340-348, 2008.

[260] Q.-Y. Cai, J. Park, D. Heldsinger, M.-D. Hsieh, and E. T. Zellers, "Vapor recognition with an integrated array of polymer-coated flexural plate wave sensors," *Sensors and Actuators B: Chemical,* vol. 62, pp. 121-130, 2000.

[261] B. Cunningham, M. Weinberg, J. Pepper, C. Clapp, R. Bousquet, B. Hugh, *et al.*, "Design, fabrication and vapor characterization of a microfabricated flexural plate resonator sensor and application to integrated sensor arrays," *Sensors and Actuators B: Chemical,* vol. 73, pp. 112-123, 2001.

[262] J.-W. Lan, I. Y. Huang, Y.-C. Lin, C.-Y. Lin, J.-L. Chen, and C.-H. Hsieh, "Development of an FPW Biosensor with Low Insertion Loss and High Fabrication Yield for Detection of Carcinoembryonic Antigen," *Sensors (Basel, Switzerland),* vol. 16, p. 1729, 2016.

[263] N. Wilkie-Chancellier, L. Martinez, S. Serfaty, and P. Griesmar, "Lamb Wave Sensor for Viscous Fluids Characterization," *IEEE Sensors Journal,* vol. 9, pp. 1142-1147, 2009.

[264] T. Laurent, F. O. Bastien, J.-C. Pommier, A. Cachard, D. Remiens, and E. Cattan, "Lamb wave and plate mode in ZnO/silicon and AlN/silicon membrane: Application to sensors able to operate in contact with liquid," *Sensors and Actuators A: Physical,* vol. 87, pp. 26-37, 2000.

[265] J. Nam, H. Choi, J. Y. Kim, W. Jang, and C. S. Lim, "Lamb wave-based blood coagulation test," *Sensors and Actuators B: Chemical,* vol. 263, pp. 190-195, 2018.

[266] J. Nam, W. S. Jang, J. Kim, H. Lee, and C. S. Lim, "Lamb wave-based molecular diagnosis using DNA hydrogel formation by rolling circle amplification (RCA) process," *Biosensors and Bioelectronics,* vol. 142, p. 111496, 2019.

[267] J. Zhou, X. He, W. Wang, N. Hu, H. Jin, Y. Xu, *et al.*, "Flexible surface acoustic wave devices and its applications in microfluidics," *MRS Online Proceedings Library Archive,* vol. 1659, pp. 27-33, 2014.

[268] L. Lamanna, F. Rizzi, F. Guido, L. Algieri, S. Marras, V. M. Mastronardi, *et al.*, "Flexible and Transparent Aluminum-Nitride-Based Surface-Acoustic-Wave Device

on Polymeric Polyethylene Naphthalate," *Advanced Electronic Materials,* vol. 5, p. 1900095, 2019.

[269] H. Jin, J. Zhou, X. He, W. Wang, H. Guo, S. Dong*, et al.*, "Flexible surface acoustic wave resonators built on disposable plastic film for electronics and lab-on-a-chip applications," *Scientific Reports,* vol. 3, p. 2140, 2013.

[270] H. Boukabache, C. Escriba, and J.-Y. Fourniols, "Toward smart aerospace structures: Design of a piezoelectric sensor and its analog interface for flaw detection," *Sensors,* vol. 14, pp. 20543-20561, 2014.

[271] W. Xuan, J. Chen, X. He, W. Wang, S. Dong, and J. Luo, "Flexible surface acoustic wave humidity sensor with on chip temperature compensation," *Procedia engineering,* vol. 120, pp. 364-367, 2015.

[272] N. Promsawat, W. Wichaiwong, P. Pimpawat, K. Changsarn, K. Phimol, M. Promsawat*, et al.*, "A study of flexible piezoelectric generators by sputtering ZnO thin film on PET substrate," *Integrated Ferroelectrics,* vol. 195, pp. 220-229, 2019.

[273] X. He, H. Guo, J. Chen, W. Wang, W. Xuan, Y. Xu*, et al.*, "Bendable ZnO thin film surface acoustic wave devices on polyethylene terephthalate substrate," *Applied Physics Letters,* vol. 104, p. 213504, 2014.

[274] J. Chen, H. Guo, X. He, W. Wang, W. Xuan, H. Jin*, et al.*, "Development of flexible ZnO thin film surface acoustic wave strain sensors on ultrathin glass substrates," *Journal of Micromechanics and Microengineering,* vol. 25, p. 115005, 2015.

[275] J. Chen, X. He, W. Wang, W. Xuan, J. Zhou, X. Wang*, et al.*, "Bendable transparent ZnO thin film surface acoustic wave strain sensors on ultra-thin flexible glass substrates," *Journal of Materials Chemistry C,* vol. 2, pp. 9109-9114, 2014.

[276] Y. Liu, J. T. Luo, C. Zhao, J. Zhou, S. A. Hasan, Y. Li*, et al.*, "Annealing effect on structural, functional, and device properties of flexible ZnO acoustic wave sensors based on commercially available Al foil," *IEEE Transactions on Electron Devices,* vol. 63, pp. 4535-4541, 2016.

[277] R. Hou, Y. Q. Fu, D. Hutson, C. Zhao, E. Gimenez, and K. J. Kirk, "Use of sputtered zinc oxide film on aluminium foil substrate to produce a flexible and low profile ultrasonic transducer," *Ultrasonics,* vol. 68, pp. 54-60, 2016.

[278] Q. Li, L.-N. Zhang, X.-M. Tao, and X. Ding, "Review of Flexible Temperature Sensing Networks for Wearable Physiological Monitoring," *Advanced Healthcare Materials,* vol. 6, p. 1601371, 2017.

[279] M. Srilata and K. Jayaram, "Chapter 35 - Hypothermia," in *Complications in Neuroanesthesia*, H. Prabhakar, Ed., ed San Diego: Academic Press, 2016, pp. 331-344.

[280] P. Kyriacou, "Temperature sensor technology," 2010.

[281] Q. Liu, H. Tai, Z. Yuan, Y. Zhou, Y. Su, and Y. Jiang, "A High-Performances Flexible Temperature Sensor Composed of Polyethyleneimine/Reduced Graphene Oxide Bilayer for Real-Time Monitoring," *Advanced Materials Technologies,* vol. 4, p. 1800594, 2019.

[282] G. A. Salvatore, J. Sülzle, F. Dalla Valle, G. Cantarella, F. Robotti, P. Jokic*, et al.*, "Biodegradable and Highly Deformable Temperature Sensors for the Internet of Things," *Advanced Functional Materials,* vol. 27, p. 1702390, 2017.

[283] P. Zhu, Y. Wang, M. Sheng, Y. Wang, Y. Yu, and Y. Deng, "A flexible active dual-parameter sensor for sensitive temperature and physiological signal monitoring via integrating thermoelectric and piezoelectric conversion," *Journal of Materials Chemistry A,* vol. 7, pp. 8258-8267, 2019.

[284] Y. Liu, H. Wang, W. Zhao, M. Zhang, H. Qin, and Y. Xie, "Flexible, Stretchable Sensors for Wearable Health Monitoring: Sensing Mechanisms, Materials, Fabrication Strategies and Features," *Sensors,* vol. 18, 2018.

[285] J. Zhou, X. Wu, D. Xiao, H. Jin, S. Dong, Y. Fu*, et al.*, "Transparent ZNO/glass surface acoustic wave devices with aluminum doped ZNO electrode," in *2017 IEEE 30th International Conference on Micro Electro Mechanical Systems (MEMS)*, 2017, pp. 691-695.

[286] R. Fachberger and A. Erlacher, "Applications of wireless SAW sensing in the steel industry," *Procedia Engineering,* vol. 5, pp. 224-227, 2010.

[287] R. M. White, "Surface Acoustic Wave Sensors," in *IEEE 1985 Ultrasonics Symposium*, 1985, pp. 490-494.

[288] C. Huck, H. P. Zidek, T. Ebner, K. C. Wagner, and A. Wixforth, "Thermal characterization of Surface Acoustic Wave devices," in *2013 IEEE International Ultrasonics Symposium (IUS)*, 2013, pp. 1089-1092.

[289] J. H. Kuypers, C.-M. Lin, G. Vigevani, and A. P. Pisano, "Intrinsic temperature compensation of aluminum nitride Lamb wave resonators for multiple-frequency references," in *2008 IEEE International Frequency Control Symposium*, 2008, pp. 240-249.

[290] R. Tao, S. A. Hasan, H. Z. Wang, J. Zhou, J. T. Luo, G. McHale*, et al.*, "Bimorph material/structure designs for high sensitivity flexible surface acoustic wave temperature sensors," *Scientific Reports,* vol. 8, p. 9052, 2018.

[291] M. Hoummady and D. Hauden, "Acoustic wave thermal sensitivity: temperature sensors and temperature compensation in microsensors," *Sensors and Actuators A: Physical,* vol. 44, pp. 177-182, 1994.

[292] X.-G. Tian, H. Liu, L.-Q. Tao, Y. Yang, H. Jiang, and T.-L. Ren, "High-resolution, high-linearity temperature sensor using surface acoustic wave device based on LiNbO3/SiO2/Si substrate," *Aip Advances,* vol. 6, p. 095317, 2016.

[293] T. M. Reeder and D. E. Cullen, "Surface-acoustic-wave pressure and temperature sensors," *Proceedings of the IEEE,* vol. 64, pp. 754-756, 1976.

[294] G. A. Borrero, J. P. Bravo, S. F. Mora, S. Velásquez, and F. E. Segura-Quijano, "Design and fabrication of SAW pressure, temperature and impedance sensors using novel multiphysics simulation models," *Sensors and Actuators A: Physical,* vol. 203, pp. 204-214, 2013.

[295] P. Zheng, T.-L. Chin, D. W. Greve, I. J. Oppenheim, and L. Cao, "Pulse-mode temperature sensing with langasite SAW devices," in *2010 IEEE International Frequency Control Symposium*, 2010, pp. 297-300.

[296] F. Bartoli, T. Aubert, M. Moutaouekkil, J. Streque, P. Pigeat, S. Zhgoon*, et al.*, "AlN/GaN/Sapphire heterostructure for high-temperature packageless acoustic wave devices," *Sensors and Actuators A: Physical,* vol. 283, pp. 9-16, 2018.

[297] C. Li, X. Liu, L. Shu, and Y. Li, "AlN-based surface acoustic wave resonators for temperature sensing applications," *Materials Express,* vol. 5, pp. 367-370, 2015.

[298] K.-S. Kao, Y.-C. Chen, Y.-H. Lee, and C.-C. Cheng, "Temperature coefficients of SAW velocity for AlN thin film sputtered on ST-X quartz," in *2002 IEEE Ultrasonics Symposium, 2002. Proceedings.*, 2002, pp. 239-242.

[299] H. Chen, K. Liu, L. Hu, A. A. Al-Ghamdi, and X. Fang, "New concept ultraviolet photodetectors," *Materials Today,* vol. 18, pp. 493-502, 2015.

[300] B. Diffey, "Ultraviolet radiation physics and the skin," *Physics in Medicine & Biology,* vol. 25, p. 405, 1980.

[301] B. Diffey, "Ultraviolet Radiation Dosimetry and," *Radiation Dosimetry: Physical and Biological Aspects,* p. 243, 2013.

[302] Y. Zou, Y. Zhang, Y. Hu, and H. Gu, "Ultraviolet detectors based on wide bandgap semiconductor nanowire: A review," *Sensors,* vol. 18, p. 2072, 2018.

[303] L. Shi and S. Nihtianov, "Comparative Study of Silicon-Based Ultraviolet Photodetectors," *IEEE Sensors Journal,* vol. 12, pp. 2453-2459, 2012.

[304] Y. Zhao, J. Qi, C. Biswas, F. Li, K. Zhang, X. Li*, et al.*, "Local irradiation effects of one-dimensional ZnO based self-powered asymmetric Schottky barrier UV photodetector," *Materials Chemistry and Physics,* vol. 166, pp. 116-121, 2015.

[305] Y. Xu, C. Cheng, S. Du, J. Yang, B. Yu, J. Luo*, et al.*, "Contacts between Two- and Three-Dimensional Materials: Ohmic, Schottky, and p–n Heterojunctions," *ACS Nano,* vol. 10, pp. 4895-4919, 2016.

[306] S. Wang, Z.-J. Li, X. Zhou, C. Zhao, X.-T. Zu, and Y. Q. Fu, "Advances in Nanostructured Acoustic Wave Technologies for Ultraviolet Sensing," *Nanoscience and Nanotechnology Letters,* vol. 7, pp. 169-192, 2015.

[307] T. Saha, N. Guo, and N. Ramakrishnan, "Zinc oxide nanostructure-based langasite crystal microbalance ultraviolet sensor," *IEEE Sensors Journal,* vol. 16, pp. 2964-2970, 2016.

[308] A. J. Gimenez, J. Yanez-Limon, and J. M. Seminario, "ZnO– paper based photoconductive UV sensor," *The Journal of Physical Chemistry C,* vol. 115, pp. 282-287, 2010.

[309] S. Ghosh, K. Das, N. Tripathy, G. Bose, D. Kim, T. Lee*, et al.*, "Ultraviolet photodetection characteristics of Zinc oxide thin films and nanostructures," in *IOP Conference Series: Materials Science and Engineering*, 2016, p. 012035.

[310] A. J. Ricco, S. J. Martin, and T. E. Zipperian, "Surface acoustic wave gas sensor based on film conductivity changes," *Sensors and Actuators,* vol. 8, pp. 319-333, 1985.

[311] P. Sharma and K. Sreenivas, "Highly sensitive ultraviolet detector based on ZnO/LiNbO 3 hybrid surface acoustic wave filter," *Applied physics letters,* vol. 83, pp. 3617-3619, 2003.

[312] Y. Guo, C. Zhao, X. Zhou, Y. Li, X.-T. Zu, D. Gibson*, et al.*, "Ultraviolet sensing based on nanostructured ZnO/Si surface acoustic wave devices," *Smart Materials and Structures,* vol. 24, p. 125015, 2015.

[313] S. Kumar, G.-H. Kim, K. Sreenivas, and R. Tandon, "ZnO based surface acoustic wave ultraviolet photo sensor," *Journal of electroceramics,* vol. 22, pp. 198-202, 2009.

[314] N. W. Emanetoglu, J. Zhu, Y. Chen, J. Zhong, Y. Chen, and Y. Lu, "Surface acoustic wave ultraviolet photodetectors using epitaxial ZnO multilayers grown on r-plane sapphire," *Applied physics letters,* vol. 85, pp. 3702-3704, 2004.

[315] C.-L. Wei, Y.-C. Chen, C.-C. Cheng, K.-S. Kao, D.-L. Cheng, and P.-S. Cheng, "Highly sensitive ultraviolet detector using a ZnO/Si layered SAW oscillator," *Thin Solid Films,* vol. 518, pp. 3059-3062, 2010.

[316] W. Li, Y. Guo, Q. Tang, X. Zu, J. Ma, L. Wang*, et al.*, "Highly sensitive ultraviolet sensor based on ZnO nanorod film deposited on ST-cut quartz surface acoustic wave devices," *Surface and Coatings Technology,* vol. 363, pp. 419-425, 2019.

[317] P. Sharma, S. Kumar, and K. Sreenivas, "Interaction of surface acoustic waves and ultraviolet light in ZnO films," *Journal of Materials Research,* vol. 18, pp. 545-548, 2011.

[318] W.-B. Wang, H. Gu, X.-L. He, W.-P. Xuan, J.-K. Chen, X.-Z. Wang*, et al.*, "Transparent ZnO/glass surface acoustic wave based high performance ultraviolet light sensors," *Chinese Physics B,* vol. 24, p. 057701, 2015.

[319] D. Ciplys, R. Rimeika, M. S. Shur, S. Rumyantsev, R. Gaska, A. Sereika*, et al.*, "Visible–blind photoresponse of GaN-based surface acoustic wave oscillator," *Applied Physics Letters,* vol. 80, pp. 2020-2022, 2002.

[320] X. L. He, J. Zhou, W. B. Wang, W. P. Xuan, X. Yang, H. Jin*, et al.*, "High performance dual-wave mode flexible surface acoustic wave resonators for UV light sensing," *Journal of Micromechanics and Microengineering,* vol. 24, p. 055014, 2014.

[321] C.-Y. Lee and G.-B. Lee, "Humidity sensors: a review," *Sensor Letters,* vol. 3, pp. 1-15, 2005.

[322] H. Farahani, R. Wagiran, and M. N. Hamidon, "Humidity sensors principle, mechanism, and fabrication technologies: a comprehensive review," *Sensors,* vol. 14, pp. 7881-7939, 2014.

[323] T. A. Blank, L. P. Eksperiandova, and K. N. Belikov, "Recent trends of ceramic humidity sensors development: A review," *Sensors and Actuators B: Chemical,* vol. 228, pp. 416-442, 2016.

[324] J. Xu, M. Bertke, H. S. Wasisto, and E. Peiner, "Piezoresistive microcantilevers for humidity sensing," *Journal of Micromechanics and Microengineering,* vol. 29, p. 053003, 2019.

[325] Z. Chen and C. Lu, "Humidity sensors: a review of materials and mechanisms," *Sensor letters,* vol. 3, pp. 274-295, 2005.

[326] L. Bo, C. Xiao, C. Hualin, M. A. Mohammad, T. Xiangguang, T. Luqi*, et al.*, "Surface acoustic wave devices for sensor applications," *Journal of Semiconductors,* vol. 37, p. 021001, 2016.

[327] T. Nomura, T. Yasuda, and S. Furukawa, "Humidity sensor using surface acoustic waves propagating along polymer/LiNbO 3 structures," in *1993 Proceedings IEEE Ultrasonics Symposium*, 1993, pp. 417-420.

[328] C. Caliendo, E. Verona, A. D'Amico, A. Furlani, G. Iucci, and M. V. Russo, "Surface acoustic wave humidity sensor," *Sensors and Actuators B: Chemical,* vol. 16, pp. 288-292, 1993.

[329] Y. Li, P. Li, M. Yang, S. Lei, Y. Chen, and X. Guo, "A surface acoustic wave humidity sensor based on electrosprayed silicon-containing polyelectrolyte," *Sensors and Actuators B: Chemical,* vol. 145, pp. 516-520, 2010.

[330] Y. Guo, J. Zhang, C. Zhao, J.-Y. Ma, H.-F. Pang, P. A. Hu, *et al.*, "Characterization and humidity sensing of ZnO/42 YX LiTaO3 Love wave devices with ZnO nanorods," *Materials Research Bulletin,* vol. 48, pp. 5058-5063, 2013.

[331] H.-S. Hong and G.-S. Chung, "Surface acoustic wave humidity sensor based on polycrystalline AlN thin film coated with sol–gel derived nanocrystalline zinc oxide film," *Sensors and Actuators B: Chemical,* vol. 148, pp. 347-352, 2010.

[332] H.-S. Hong, D.-T. Phan, and G.-S. Chung, "High-sensitivity humidity sensors with ZnO nanorods based two-port surface acoustic wave delay line," *Sensors and Actuators B: Chemical,* vol. 171-172, pp. 1283-1287, 2012.

[333] X. Le, X. Wang, J. Pang, Y. Liu, B. Fang, Z. Xu, *et al.*, "A high performance humidity sensor based on surface acoustic wave and graphene oxide on AlN/Si layered structure," *Sensors and Actuators B: Chemical,* vol. 255, pp. 2454-2461, 2018.

[334] W. Xuan, M. He, N. Meng, X. He, W. Wang, J. Chen, *et al.*, "Fast response and high sensitivity ZnO/glass surface acoustic wave humidity sensors using graphene oxide sensing layer," *Scientific reports,* vol. 4, p. 7206, 2014.

[335] I. E. Kuznetsova, V. I. Anisimkin, S. P. Gubin, S. V. Tkachev, V. V. Kolesov, V. V. Kashin, *et al.*, "Super high sensitive plate acoustic wave humidity sensor based on graphene oxide film," *Ultrasonics,* vol. 81, pp. 135-139, 2017.

[336] W. Xuan, X. He, J. Chen, W. Wang, X. Wang, Y. Xu, *et al.*, "High sensitivity flexible Lamb-wave humidity sensors with a graphene oxide sensing layer," *Nanoscale,* vol. 7, pp. 7430-7436, 2015.

[337] M. Sato and T. Yamamoto, "Sensitivity of phase velocity of a composite ZnO plate to humidity," *Sensors and Actuators B: Chemical,* vol. 13, pp. 96-99, 1993.

[338] X. He, D. Li, J. Zhou, W. Wang, W. Xuan, S. Dong, *et al.*, "High sensitivity humidity sensors using flexible surface acoustic wave devices made on nanocrystalline ZnO/polyimide substrates," *Journal of Materials Chemistry C,* vol. 1, pp. 6210-6215, 2013.

[339] C. Massaroni, A. Nicolò, D. Lo Presti, M. Sacchetti, S. Silvestri, and E. Schena, "Contact-Based Methods for Measuring Respiratory Rate," *Sensors,* vol. 19, 2019.

[340] F. Q. Al-Khalidi, R. Saatchi, D. Burke, H. Elphick, and S. Tan, "Respiration rate monitoring methods: A review," *Pediatric Pulmonology,* vol. 46, pp. 523-529, 2011.

[341] Y. Pang, J. Jian, T. Tu, Z. Yang, J. Ling, Y. Li, *et al.*, "Wearable humidity sensor based on porous graphene network for respiration monitoring," *Biosensors and Bioelectronics,* vol. 116, pp. 123-129, 2018.

[342] J. Luis, L. Roa Romero, J. Gómez-Galán, D. Hernández, M. Estudillo-Valderrama, G. Barbarov-Rostán, *et al.*, "Design and implementation of a smart sensor for respiratory rate monitoring," *Sensors,* vol. 14, pp. 3019-3032, 2014.

[343] S. Milici, A. Lázaro, R. Villarino, D. Girbau, and M. Magnarosa, "Wireless Wearable Magnetometer-Based Sensor for Sleep Quality Monitoring," *IEEE Sensors Journal,* vol. 18, pp. 2145-2152, 2018.

[344] S. K. Kundu, S. Kumagai, and M. Sasaki, "A Wearable Capacitive Sensor for Monitoring Human Respiratory Rate," *Japanese Journal of Applied Physics,* vol. 52, p. 04CL05, 2013.

[345] M. Chu, T. Nguyen, V. Pandey, Y. Zhou, H. N. Pham, R. Bar-Yoseph, *et al.*, "Respiration rate and volume measurements using wearable strain sensors," *npj Digital Medicine,* vol. 2, p. 8, 2019.

[346] Y.-Y. Chiu, W.-Y. Lin, H.-Y. Wang, S.-B. Huang, and M.-H. Wu, "Development of a piezoelectric polyvinylidene fluoride (PVDF) polymer-based sensor patch for simultaneous heartbeat and respiration monitoring," *Sensors and Actuators A: Physical,* vol. 189, pp. 328-334, 2013.

[347] J. Jeong, Y. Jang, I. Lee, S. Shin, and S. Kim, "Wearable respiratory rate monitoring using piezo-resistive fabric sensor," in *World Congress on Medical Physics and Biomedical Engineering, September 7-12, 2009, Munich, Germany*, 2009, pp. 282-284.

[348] H. Alshaer, G. R. Fernie, and T. D. Bradley, "Monitoring of breathing phases using a bioacoustic method in healthy awake subjects," *Journal of clinical monitoring and computing,* vol. 25, p. 285, 2011.

[349] A. S. Sezen, S. Sivaramakrishnan, S. Hur, R. Rajamani, W. Robbins, and B. J. Nelson, "Passive Wireless MEMS Microphones for Biomedical Applications," *Journal of Biomechanical Engineering,* vol. 127, pp. 1030-1034, 2005.

[350] R. Selyanchyn, S. Korposh, S. Wakamatsu, and S.-W. Lee, "Respiratory Monitoring by Porphyrin Modified Quartz Crystal Microbalance Sensors," *Sensors,* vol. 11, 2011.

[351] H. Jin, X. Tao, S. Dong, Y. Qin, L. Yu, J. Luo, *et al.*, "Flexible surface acoustic wave respiration sensor for monitoring obstructive sleep apnea syndrome," *Journal of Micromechanics and Microengineering,* vol. 27, p. 115006, 2017.

[352] R. Tao, S. Hasan, H. Z. Wang, J. Zhou, J. T. Luo, G. McHale, *et al.*, "Bimorph material/structure designs for high sensitivity flexible surface acoustic wave temperature sensors," *Scientific reports,* vol. 8, p. 9052, 2018.

[353] T. Mudigonda, T. S. Dabade, and S. R. Feldman, "A review of targeted ultraviolet B phototherapy for psoriasis," *Journal of the American Academy of Dermatology,* vol. 66, pp. 664-672, 2012.

[354] H. Moseley, D. Allan, H. Amatiello, A. Coleman, H. du Peloux Menagé, C. Edwards*, et al.*, "Guidelines on the measurement of ultraviolet radiation levels in ultraviolet phototherapy: report issued by the British Association of Dermatologists and British Photodermatology Group 2015," *British Journal of Dermatology,* vol. 173, pp. 333-350, 2015.

[355] K. Johnson, M. A. Kumar, P. Ponmurugan, and B. M. Gananamangai, "Ultraviolet radiation and its germicidal effect in drinking water purification," *Journal of Phytology,* 2010.

[356] M. B. Heaney, "Electrical conductivity and resistivity," *The measurement, instrumentation and sensors handbook,* CRC Press, pp. 1332-1345, 2000.

[357] H. Jin, X. Tao, B. Feng, L. Yu, D. Wang, S. Dong*, et al.*, "A humidity sensor based on quartz crystal microbalance using graphene oxide as a sensitive layer," *Vacuum,* vol. 140, pp. 101-105, 2017.